THESE

Pour l'obtention du Grade de
DOCTEUR DE L'ECOLE NATIONALE SUPERIEURE DE MECANIQUE ET D'AEROTECHNIQUE
(Diplôme National – Arrêté du 25 mai 2016 Modifié par l'Arrêté du 26 Août 2022)

Ecole Doctorale :
MIMME_ Mathématiques, Informatique, Matériaux, Mécanique, Energétique

Secteur de Recherche : Mécanique des solides, des matériaux, des structures et des surfaces

Présentée par :

Kushal Gowda JAYARAM

****

Understanding the influence of thermal aging and PWR primary water environment on the low-cycle fatigue behavior of Alloy 690TT

****

Directeur de thèse : Gilbert HENAFF
Co-encadrants : Jonathan QUIBEL
Joseph HURET

****

Soutenue le 17 Décembre 2025

devant la Commission d'Examen

****

JURY

Rapporteurs :		
AUBIN Véronique	Professeure	CentraleSupélec, Paris-Saclay
CICERO Sergio	Professeur	Universidad de Cantabria, Spain
Membres du jury :		
BUFFIERE Jean-Yves	Professeur	INSA Lyon
LE ROUX Jean-Christophe	Ingénieur de Recherche	EDF Lab les Renardières
CHITTY Walter-John	Ingénieur de Recherche	Newcleo, Lyon
HENAFF Gilbert	Professeur	ISAE-ENSMA, Poitiers
QUIBEL Jonathan	Ingénieur de Recherche	ASNR, Cadarache

Acknowledgements

I would first like to sincerely thank the members of my jury for accepting to review my thesis and for the time and interest they devoted to evaluating my work: Véronique Aubin, Sergio Cicero, Jean-Yves Buffière, and Jean-Christophe Le Roux.

From the bottom of my heart, I thank my tutors Jonathan Quibel, Joseph Huret, and Walter-John Chitty for their constant guidance, support, and encouragement throughout this PhD journey. My special and deepest gratitude goes to my thesis director, Professor Gilbert Henaff, for his trust, invaluable advice, and continuous support during these years.

I would also like to warmly thank Alexis Landureau for his support during his alternance period and for his help with different aspects of this thesis. My sincere thanks to Armel Descamps Mandine for his expertise in TEM, to Claudie Josse for her precious assistance with FIB experiments, to Olga Smerdova for her support with nanoindentation measurements, and to Florence Hamon for carrying out the vacuum testing.

I am very grateful to all the members of my laboratory who contributed, directly or indirectly, to this work. In particular, I would like to thank the technicians Alice Virreto, Pauline Lacote, and Nicolas Cillieres for their constant availability and technical assistance, as well as the senior researchers Jean Desquines, Séverine Guilbert, and Christina Dominguez for their valuable advice and fruitful discussions. I also express my sincere thanks to the head of the laboratory, Jacques Di Salvo, and to the head of the service, Laurence Rigollet, for their support and for providing an excellent working environment during this thesis.

A very special thank you goes to my dear colleagues and friends Martial, Fouzia, Youcef, Enida, Léa, Julie, Menes, Keymoon, Anaïs, João, Soufiane, Marek, Myriam, Mouna, and many others, for the wonderful moments, stimulating discussions, and friendship that made these years truly memorable.

I would like to express my deepest gratitude to my dear Grai for being there throughout this entire journey, for the constant support, patience, and encouragement.

Finally, I dedicate my greatest gratitude to my parents, who have supported me unconditionally from the very beginning and without whom this achievement would not have been possible.

Table of Contents

Introduction and context

The continuous growth in global energy demand has reinforced the importance of nuclear power as a stable and low-carbon energy source. As of May 2023, the International Atomic Energy Agency (IAEA) reported 410 nuclear power reactors in operation worldwide, providing a total electrical capacity of 369 GW. In France, the second-largest nuclear fleet worldwide, there are currently 57 operational reactors producing about 63 GW of electricity and the nuclear power share accounts for 67% of national electricity production. In addition, 59 reactors are under construction worldwide (66 GW), 100 are planned (102 GW), and 325 more have been proposed, reflecting the ongoing commitment to nuclear energy as a cornerstone of future electricity generation. Among the existing and planned reactors, light-water reactor (LWRs) designs dominate, with Pressurized Water Reactors (PWRs) and Boiling Water Reactors (BWRs) constituting the vast majority of the global nuclear fleet.

However, in 2022, nearly 40% of the world's nuclear reactors had already exceeded 40 years of operation and projections suggest that by 2030 this figure will rise to almost 67%. This trend underscores the challenge of extending the service life of existing nuclear plants while maintaining the highest levels of safety and reliability. Therefore, Long-Term Operation (LTO) programs focus on understanding and mitigating material degradation mechanisms such as fatigue, corrosion, and thermal aging, which directly affect the structural integrity of the components.

In France, this issue is particularly significant given the country's reliance on nuclear power, where Electricité de France (EDF) has accordingly launched a major program to extend the lifetime of its 900 MWe reactors beyond 40 years, requiring extensive safety reviews and in-depth studies of material behavior under service conditions. Operational feedback from French nuclear power plants has shown that structural components in service are subjected to various degradation mechanisms. Among these, flow-accelerated corrosion dominates, accounting for 58% of reported cases, followed by pitting corrosion (18%), fatigue (16%), general corrosion (4%) and stress corrosion cracking (3%). This distribution clearly indicates that fatigue is a major contributor to long-term aging and maintenance costs of PWRs.

Most of the materials used in PWRs (**Figure 1**) are low-alloy steels, stainless steels (SS) and nickel-based alloys. Indeed, some components such as reactor pressure vessel, pressurizer, steam generator, steam lines are made of carbon or low-alloy steel while core structural and piping of the primary circuit are made of austenitic stainless steels (Types 304, 304L, 316,

316L). In addition, nickel-based alloys (Types 718, 600, 690) are used for components where a high-strength and good stress corrosion cracking resistance are required such as springs, Control Rod Drive Mechanism (CRDM) housing and steam generator tubes.

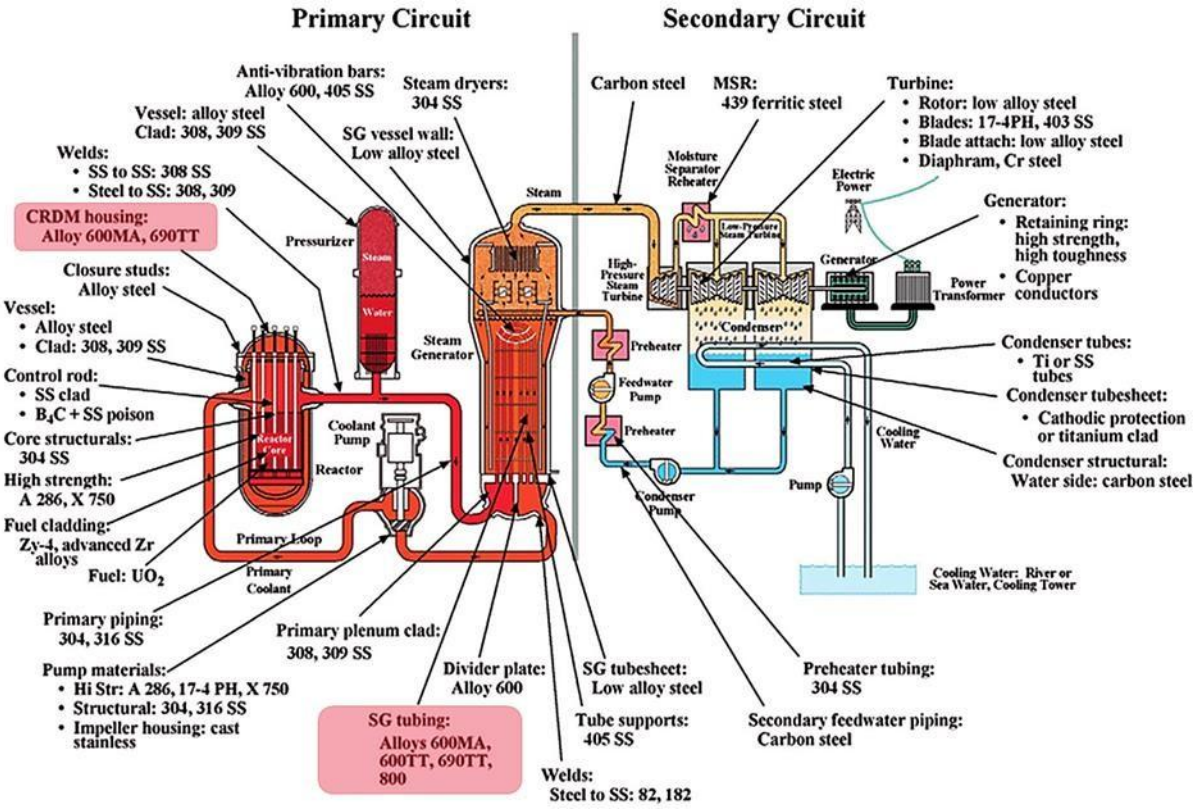

Figure 1: Diagram of the primary circuit and the secondary circuit of a PWR type nuclear power plant. In red, parts having nickel alloys in the primary circuit [Andresen et al., 2016].

In service, these metallic components of the PWR primary circuit are subjected to repeated thermal transients leading to a fatigue loading. The most significant occur during start-up and shutdown operations, when the coolant temperature is cycled between ambient and ~300 °C, producing expansion and contraction that impose thermomechanical stresses on piping, and nozzles for example. Although less frequent, power adjustments and emergency shutdowns can also generate temperature gradients in the primary loop, contributing to fatigue loading. In addition to this mechanical loading, the primary water coolant itself contains chemical additives such as lithium hydroxide and boric acid, which are used to control pH and reactivity but can act as a corrosive medium for structural alloys. The combined action of cyclic mechanical stresses and the exposure to corrosive primary water environment is referred to as Environmentally Assisted Fatigue (EAF), a phenomenon recognized as a penalizing factor that reduces the fatigue life of reactor materials compared to air.

Currently, the majority of studies on Environmentally Assisted Fatigue have been performed on austenitic stainless steels, such as 304L. In comparison, relatively little attention has been given to nickel-based alloys, such as Alloy 690, including its thermally treated (TT) version. Indeed, Alloy 600 is progressively replaced by Alloy 690 due to its well-documented susceptibility to stress corrosion cracking (SCC), a phenomenon widely studied and supported by extensive scientific research. Alloy 690, introduced as a new generation of alloy has also been the subject of significant research regarding its SCC resistance. However, in contrast, only limited investigations have addressed the EAF behavior of Alloy 690.

Beyond environmental effects, another important factor for the long-term performance of Alloy 690TT is thermal aging. During service in PWR primary circuits, components operate for decades (>40 years) at elevated temperatures (≈ 300-350 °C). Under such conditions, thermal exposure could cause microstructural changes, which would affect key mechanical properties such as strength and hardness, and potentially impact fatigue resistance. Despite the central role of Alloy 690TT in PWRs, the influence of thermal aging on its fatigue behavior has received no attention at all.

Considering these gaps in the research, the present thesis is structured around three main objectives:

1. To characterize the fatigue behavior of as-received Alloy 690TT under low-cycle fatigue conditions in different environments (vacuum, air, and simulated PWR primary water), in order to establish both baseline and environmentally assisted fatigue responses.
2. To investigate the microstructural evolution of Alloy 690TT during long-term thermal aging by performing accelerated thermal aging which is equivalent to service conditions.
3. To evaluate the effect of accelerated thermal aging on the fatigue behavior of Alloy 690TT, by comparing the performance of aged and as-received samples and establishing correlations between microstructural changes and fatigue resistance.

To achieve this goal, the manuscript is composed of three chapters:

The first chapter presents the material Alloy 690TT and provides a state-of-the-art review of its fatigue behavior. It discusses the influence of key parameters such as temperature and strain rate in air, as well as environmental factors including dissolved oxygen and dissolved hydrogen

in PWR primary water. In addition, it reviews damage mechanisms reported for Alloy 690TT and comparable austenitic alloys.

The second chapter describes the material investigated in this study and the experimental approaches employed. It details the testing machines and specimen geometries used to evaluate fatigue behavior in different environments (air, PWR water, and vacuum). The chapter also presents the techniques applied to quantify damage in tested samples, as well as the methodologies developed to monitor microstructural evolution during accelerated thermal aging. Characterization tools such as SEM, FIB, and TEM were used for microstructural observations, while mechanical property changes were assessed through hardness measurements performed using Vickers microhardness and nanoindentation techniques.

The third chapter focuses on the fatigue behavior of Alloy 690TT in the as-received condition. It examines the influence of parameters such as strain amplitude (±0.3, ±0.45, ±0.6%), temperature (room temperature and 300 °C), strain rate (0.4, 0.02, 0.004%/s) and the medium of testing (vacuum, air and PWR environment).

The fourth chapter is dedicated to the effect of accelerated thermal aging at 420 °C for up to 6000 hours. A quantitative analysis of microstructural evolution was carried out, focusing on the characteristics of intergranular and intragranular precipitates, the possible formation of secondary phases, and the impact of these changes on hardness.

The fifth chapter addresses the influence of thermal aging on the fatigue behavior of Alloy 690TT. Fatigue tests were conducted on aged samples at different strain amplitudes (±0.3, ±0.45, ±0.6%) and at 300 °C under varying strain rates (0.4, 0.02, 0.004%/s) in both air and PWR environments. The results were then compared with those obtained on the as-received alloy to highlight changes in fatigue performance induced by thermal aging.

Finally, a general conclusion summarizes the main findings of this study and perspectives for future research.

I. State of the Art

This section provides an overview of the current knowledge, key findings, and existing gaps related to the fatigue behavior of Alloy 690TT and its response to environmental and microstructural factors. It summarizes the main advances reported in the literature concerning cyclic deformation mechanisms, thermal aging effects, and environmentally assisted fatigue in nuclear reactor environments. The objective is to establish a scientific foundation for the present study by identifying the mechanisms that govern fatigue performance, highlighting the limitations of existing approaches, and defining the motivation for the experimental work developed in the subsequent chapters.

Contents

I.1. ALLOY 690TT

I.1.1. Composition

Alloy 690 (commercially known as Inconel™ 690) is a nickel-based alloy that was developed to replace Alloy 600, which exhibited strong susceptibility to stress corrosion cracking (SCC) in both the primary and secondary water circuits of PWRs.

In the ternary Ni–Cr–Fe phase diagram, Alloy 690 lies fully within the austenitic (face-centered cubic, FCC) stability region (**Figure 2**), ensuring a single-phase structure under typical PWR operating conditions. Alloy 690 is characterized by its high chromium content (~30 wt.%), which provides excellent corrosion resistance, particularly in oxidizing environments such as PWR primary water. Nickel (>58 wt.%) ensures a stable austenitic (FCC) matrix, enhancing toughness and resistance to stress corrosion cracking. Iron (~9 wt.%) balances phase stability and cost, while still maintaining the alloy's desirable mechanical properties. Additionally, minor alloying elements such as titanium and aluminum are added to promote carbide stabilization and enhance grain boundary strength. The compositional ranges specified by RCC-M (M-4109) and those of the ASTM B166 standard are summarized in **Table 1** [AFCEN. RCC-M, 2022].

Content	C	Si	Mn	P	S	Cr	Ni	Al	Ti	Co	Cu	Fe
RCC- M (M-4109)	0.01 - 0.04	<0.5	<0.5	<0.015	<0.01	28-31	>58	<0.5	<0.5	<0.1	<0.5	8-11
ASTM (B166)	0.05	<0.5	<0.5	-	<0.015	27-31	>58	-	-	-	<0.5	7-11

Table 1: Chemical composition in wt% of the Alloy 690TT required by RCC-M and ASTM [AFCEN. RCC-M, 2022, ASTM B166, 2023].

In Alloy 690, the higher chromium content contributes to the formation of a stable and protective Cr_2O_3 passive film, which provides superior corrosion and SCC resistance [Kuang et al., 2017, Zhai et al., 2019]. Iron plays a role in stabilizing the FCC austenitic matrix and reduces the likelihood of ordering transformations during long-term service [Song et al., 2018]. The resulting stable austenitic phase is critical to maintaining both corrosion resistance and mechanical stability under reactor operating conditions.

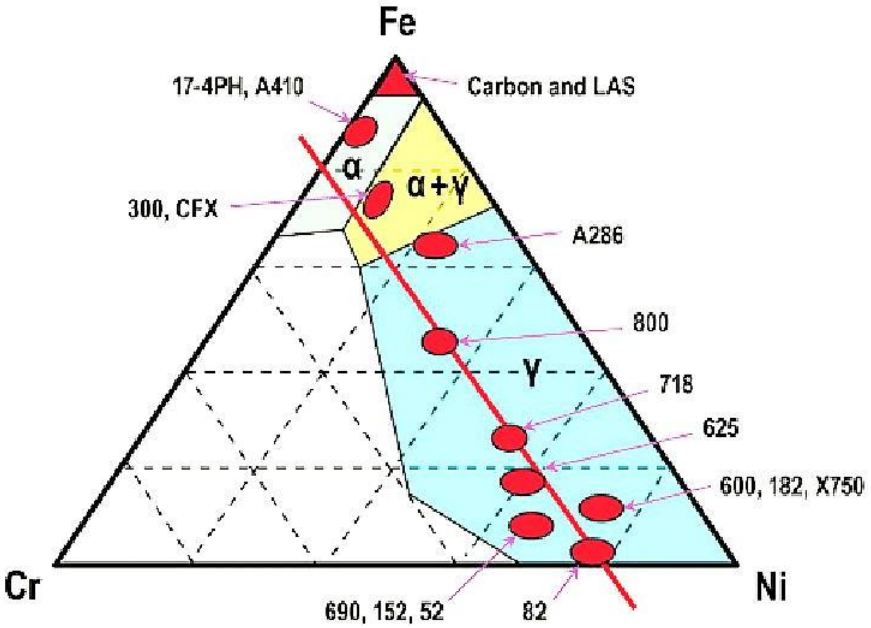

Figure 2: Ternary diagram for the Fe-Cr-Ni system at 400°C [Rudling, 2007].

I.1.2. Thermal treatment and microstructure

Alloy 690 is first subjected to mill annealing (MA), a high-temperature heat treatment carried out under reducing conditions within the RCC-M [AFCEN. RCC-M, 2022] specified temperature range of 950–1050 °C. This treatment promotes recrystallisation and dissolves pre-existing carbides. Rapid cooling, typically by water quenching (or air cooling for thinner gauges), is then used to lock in carbon and alloying elements such as chromium in solid solution. This process creates a uniform initial microstructure by maximising solute in the matrix and removing pre-existing precipitates [MRP-241, 2008].

Subsequently, a thermal treatment (TT) is performed at 705–715 °C for a minimum of 5 hours to release the residual stresses and promote a controlled grain boundary carbide precipitation, which enhances stress corrosion cracking resistance by stabilizing grain boundaries and mitigating intergranular attack [Lim et al., 2014].

After thermal treatment, Alloy 690TT typically exhibits a microstructure consisting of a single austenitic (FCC) phase, which is the stable high-temperature phase of the alloy (Figure 2). Annealing twins are often observed within the grains and contribute to the structural stability of the matrix. Although some intragranular carbides remain dispersed within the grains, precipitation occurs predominantly at grain boundaries (**Figure 3**), where carbides may form in different morphologies. Two main types are commonly observed: discrete carbides, which are isolated particles decorating grain boundaries, and cellular carbides, which grow in colonies

and form a more extended, semi-continuous network along the boundary [Dutta and Tewari, 1999, Matt, 2011]. The main precipitate phase is chromium-rich $M_{23}C_6$, favored by the high chromium content of Alloy 690TT. These $M_{23}C_6$ carbides typically nucleate early during thermal exposure, preferentially at grain boundaries, twin boundaries, and in association with pre-existing intragranular particles such as TiN [Lee et al., 2016]. This tailored carbide distribution is one of the objectives of the thermal treatment, as it contributes to improved resistance against stress corrosion cracking (SCC) in primary water environments [H. Xu, 2004].

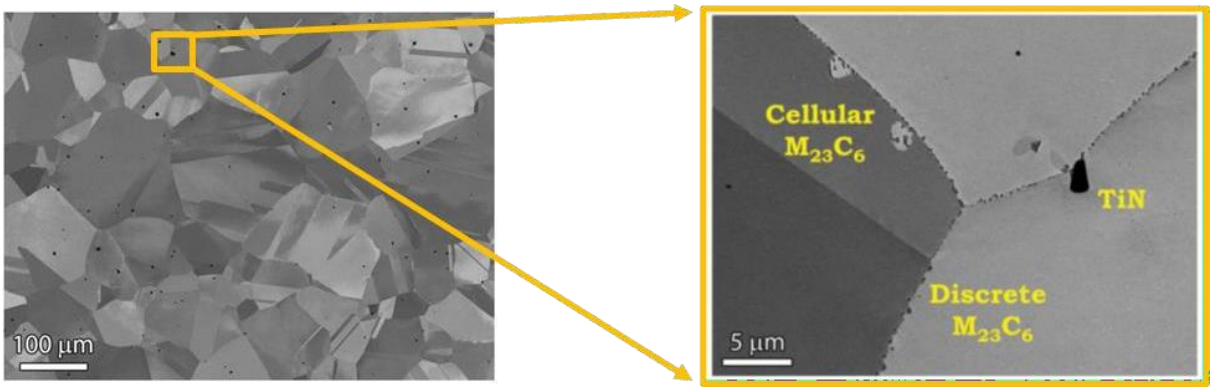

Figure 3: General microstructure and grain boundary carbides in alloy 690TT [Matt, 2011].

I.2. EFFECT OF THERMAL AGING ON ALLOY 690TT

I.2.1. Introduction to thermal aging

In nuclear reactors, the structural materials used in the primary circuit are exposed to high temperatures, ranging from 290 to 350°C for extended periods, often exceeding several decades. This prolonged thermal exposure could lead to gradual changes in the microstructure and the associated mechanical properties of these materials, a phenomenon commonly referred to as thermal aging.

To simulate the thermal aging of a component during decades at a nominal temperature (300-350°C), an accelerated thermal aging at higher temperature is usually performed [Mouginot et al., 2017a]. This approach relies on the principle of time–temperature equivalence (TTE), applicable to diffusion controlled phenomena like bulk diffusion of chromium in Alloy 690TT such as precipitation, segregation, or ordering, are diffusion-controlled [Aerne et al., 2023, Bullens et al., 2018, Huotilainen and Que, 2022, Mouginot et al., 2017b] and thus follow an Arrhenius-type relation (**Eq. I.1**).

where t(T) is the time required for aging at the accelerating temperature T, t_0 is the reference

$$t(T) = t_0 \times \left[\frac{e^{Q/RT}}{e^{Q/RT_0}}\right] \qquad \textbf{Eq. I.1}$$

service time at operating temperature T_0, R is the ideal gas constant (8.3145 $J.mol^{-1}.K^{-1}$) and Q the activation energy.

The selection of an accelerated aging temperature, therefore, represents a compromise between ensuring a reasonable acceleration of the phenomena occurring at nominal temperature (even if their exact nature is not fully known) and preventing the emergence of parasitic phenomena such as grain growth or the formation of phases that would not realistically develop under reactor operating conditions.

I.2.2. Microstructural evolution during thermal aging

I.2.2.1. Evolution of precipitates in the microstructure

One significant consequence of thermal aging is the microstructural evolution of the material. Indeed, an increase in the size of the intergranular carbides as well as the formation of α-Cr precipitates along the grain boundaries have been observed qualitatively [Lee et al., 2015, Lim et al., 2014, Mouginot et al., 2017b].

The micrographs in **Figure 4** show the qualitative evolution of the intergranular carbides in Alloy 690TT after 10,000 hours of accelerated thermal aging at different temperatures. The as-received material (TT) shows a fine and uniform distribution of grain boundary carbides with minimal coarsening. After aging at 420 °C, the carbides remain relatively fine and closely spaced, with only slight evidence of growth compared to the as-received state.

After 10,000 h at 475 °C, the precipitates appear noticeably coarser, with an increase in their width and spacing along grain boundaries, suggesting the onset of significant carbide coarsening. Aging at 550 °C produces the most pronounced changes, with carbides becoming substantially larger and more irregular in shape, and in some cases forming continuous or semi-continuous films along grain boundaries. This progression confirms that higher temperatures accelerate precipitate growth and morphological changes in Alloy 690TT, consistent with thermally activated diffusion-controlled coarsening mechanisms.

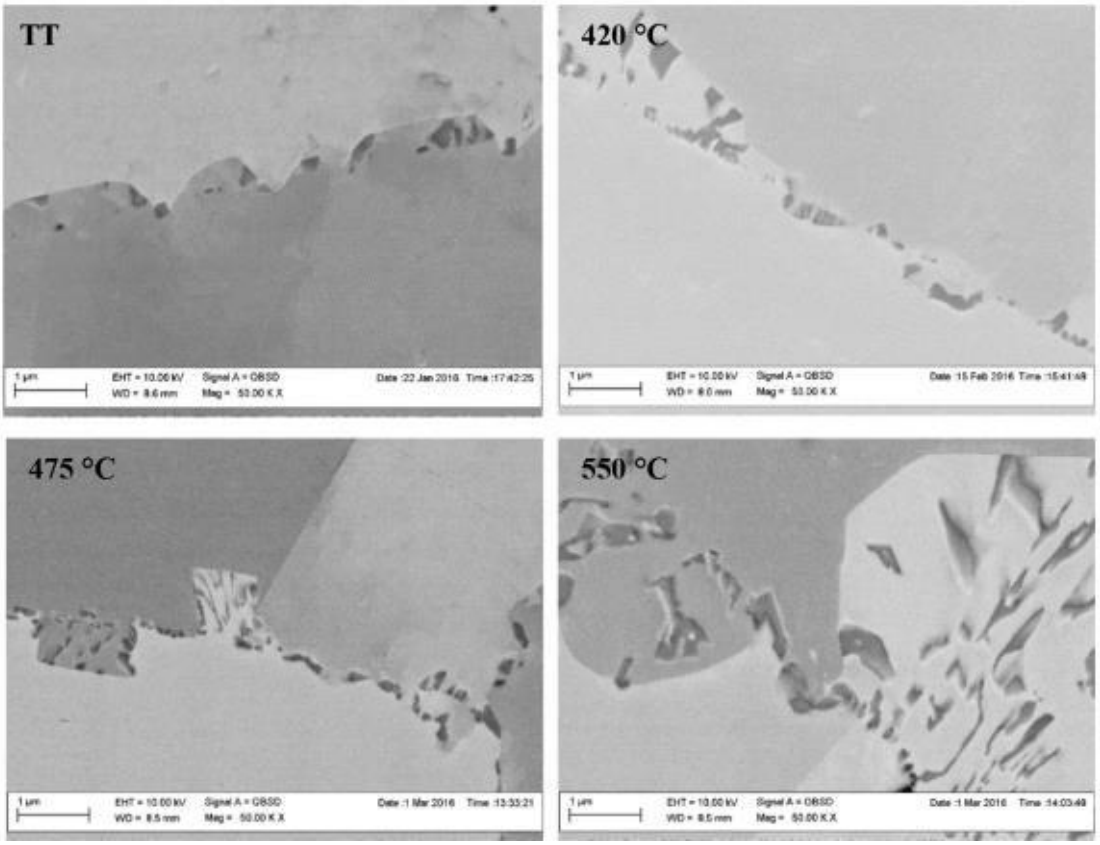

Figure 4: Evolution of Alloy 690TT's intergranular carbides before (TT) and after aging at 420, 475 and 550 °C for 10 000 h [Mouginot et al., 2017b].

These changes in precipitate evolution can have an impact on the mechanical properties of Alloy 690TT. A study conducted by Lee et al. [Lee et al., 2016] also revealed the growth of intergranular $M_{23}C_6$ precipitates during aging at 700°C for 50 hours, primarily near high-angle grain boundaries. The formation of these precipitates negatively impacted the ultimate tensile strength and yield strength of the Alloy 690TT, mainly due to the weak bond strength between the coarsened intergranular carbide and the matrix, which led to intergranular cracking. Intergranular precipitate coarsening during thermal aging is a common phenomenon observed in various nickel-based alloys, impacting their mechanical properties. In Alloy 617B, $M_{23}C_6$ carbides precipitate along grain boundaries at 725°C, reducing ductility and affecting creep resistance [Song et al., 2017]. Similarly, in Re-containing Ni-based single-crystal superalloys, γ′ precipitates coarsen at 900–1000°C, altering the microstructure and potentially weakening the alloy [Zhang et al., 2021]. In Ni-Al-Cr-Co model superalloys, γ′ precipitate coarsening is influenced by cobalt additions, which refine the microstructure, slow the coarsening rate, and improve hardness [Atas et al., 2024].[Alexandreanu et al., 2021]. The literature also states that the formation of SRO is accompanied by intergranular carbide precipitation during thermal

aging at 420°C [Mouginot et al., 2017a]. These findings indicate that intergranular precipitate evolution affects the mechanical behavior of the nickel-based alloy.

I.2.2.2. Ordering phenomenon

Definition of ordering

The ordering phenomenon in metals refers to the tendency of atoms to adopt a specific arrangement resulting in a local organization that is distinct from the random distribution found in a disordered state. When this phenomenon occurs over short distances (1-2 nm/ 3-6 unit cells [Wang et al., 2019a]), it is referred to as Short-Range Ordering (SRO). If the ordering extends over longer distances, it is typically called Long-Range Ordering (LRO).

The ordering phenomenon is characterized by the chemical nature of atoms at specific lattice sites. In the case of an alloy based on a disordered Ni-Cr solution such as Alloy 690TT, chromium and nickel atoms are initially distributed randomly over the lattice sites (**Figure 5**). However, during the ordering process due to a long time at high temperature, this randomness is altered. This can lead to the formation of a Short-Range Ordered state (**Figure 5**). Here, SRO can result from the diffusion of specific elements, such as nickel and chromium, which leads to the formation of ordered clusters or regions within the alloy matrix, like the Ni_2Cr phase [Bullens et al., 2018, Stephan et al., 2019].

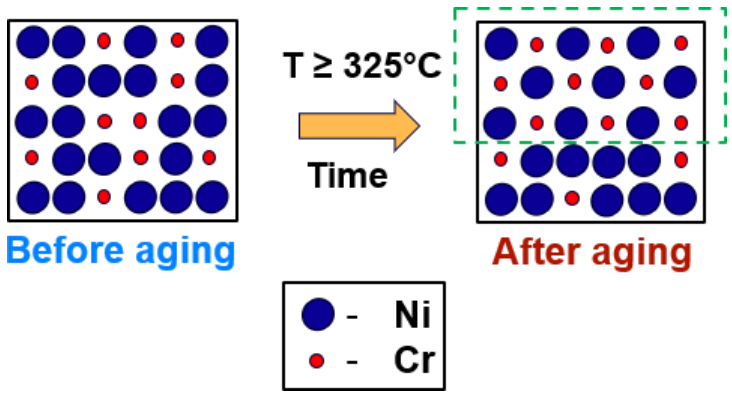

Figure 5: Schematic of Ni_2Cr short-range ordering in Alloy 690 during aging at T ≥ 325 °C. The blue dots are Ni atoms, the red dots are Cr atoms, and the green square represents SRO.

With a longer time of exposure and/or higher temperature, this SRO can evolve into Long-Range Ordering with the formation of Ni_2Cr on a larger scale. This process can impact

mechanical properties such as hardness and fracture toughness of the Ni-Cr-Fe model alloys [Aerne et al., 2023].

The **Figure 6** illustrates the kinetics of Ni_2Cr precipitation in Ni–Cr and Ni–Cr–Fe alloys. In the binary Ni–Cr system, precipitation occurs relatively rapidly at intermediate temperatures (400–500 °C), following an incubation period associated with short-range ordering. The addition of Fe significantly slows down the precipitation kinetics, shifting the onset of Ni_2Cr nucleation to longer timescales. Under PWR operating conditions (thermal exposure 290–350 °C over decades), this implies that in Alloy 690TT, which contains ~9 wt.% Fe, Ni_2Cr formation is strongly delayed, and the alloy is more likely to exhibit only early-stage ordering phenomena rather than fully developed ordered phases during service lifetimes.

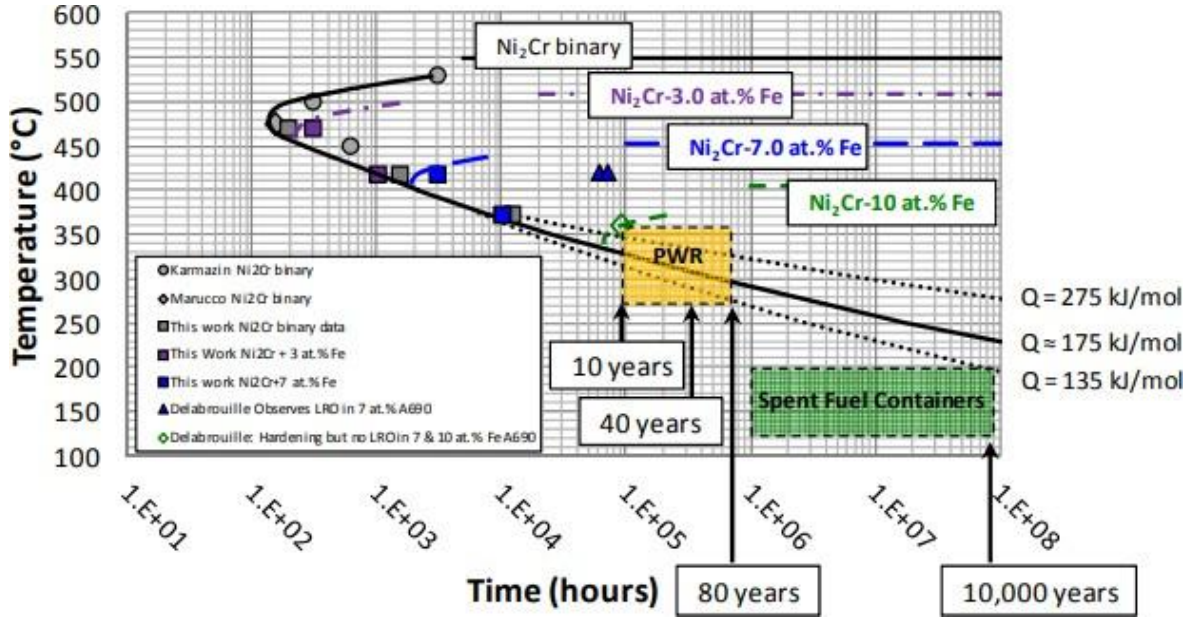

Figure 6: The kinetics of Ni_2Cr precipitation in the Ni-Cr binary and Ni-Cr-Fe ternary systems, exhibit an incubation period for precipitation [Young and Tucker, 2013].

In the binary Ni–Cr alloy, the onset of Ni_2Cr ordering is observed relatively early, typically after ~10^2–10^3 hours at 400–450 °C, owing to the higher mobility of Cr atoms. By contrast, the addition of 3–10 at. % Fe, as in ternary alloys representative of Alloy 690, significantly retards this process, shifting the initiation of ordering to longer times (≥10^5 hours) and requiring slightly higher temperatures (> 450 °C). The overlay of service-relevant time-temperature conditions reveals that at typical PWR operating temperatures (~325-350 °C), only short-range ordering (SRO) is expected to develop gradually over decades. In contrast, higher aging temperatures

accelerate the kinetics and promote the transition to long-range order within shorter experimental timescales.

The activation energy for SRO/LRO was determined to lie withing the range of 135 to 275 kJ/mol for Ni-Cr and Ni-Cr-Fe alloys. This wide range can be attributed to the influence of multiple parameters such as the alloy chemical composition, prior cold work and quenching conditions.

For example, water-quenched alloys show a lower activation energy (135 kJ/mol), whereas furnace-cooled alloys exhibit a higher activation energy (155 kJ/mol) [Young and Tucker, 2013]. The highest value of activation energy (205 kJ/mol) is reported for cold-worked alloys, in which additional defects are introduced [Kim et al., 2000]. The local strain fields created by coldwork increase the lattice distortions that modify local solubility, creating a lower chemical driving force for diffusion and affecting the measured activation energy [Huotilainen and Que, 2022, Kim et al., 2000]. It has been seen in the literature that the iron content of the alloy has also an influence on the activation energy of SRO [Young, G. A. and Eno, D. R., 2014]. The Ni-Cr-1Fe furnace-cooled (FC) alloy has an activation energy of 140 kJ/mol, while the Ni-Cr-3Fe FC alloy has an activation energy of 160 kJ/mol [Young and Tucker, 2013]. Moreover, a previous study by Alexandreanu et al. [Alexandreanu et al., 2021] on the Alloy 690SA (solution-annealed) and air-cooled uses an activation energy of 125 kJ/mol. In the specific case of Alloy 690TT, an activation energy of 177 kJ/mol has been reported for bulk chromium diffusion in an air-cooled alloy [Huotilainen and Que, 2022]. Furthermore, all these parameters like Iron content and cold work affecting the activation energy of SRO can also have an effect on its kinetics [Young and Tucker, 2013].

Experimental approaches to characterize SRO

Several techniques, direct or indirect, have been employed in the literature to detect the SRO in nickel-based alloys.

SRO in Ni-based alloys can be detected using **Transmission Electron Microscopy (TEM) techniques combined with diffraction analysis**. It has been shown in a commercial alloy Ni-20Cr-3.2Al-2.5Fe that imaging techniques such as bright-field and dark-field (**Figure 7 (a) and (d)**) are not able to detect SRO as they reveal a homogeneous single-phase solid solution without the presence of secondary phases [Wang et al., 2019a].

However, Selected Area Electron Diffraction (SAED) provides a more sensitive technique for distinguishing ordered from disordered states. For the as-quenched sample, SAED patterns acquired along the [001] and [11$\bar{2}$] zone axes exhibit only the fundamental FCC diffraction spots, indicating the absence of any long- or short-range ordering. In contrast, after thermal aging, additional weak diffraction spots appear at halfway positions between the fundamental reflections in SAED patterns for the same zone axes [Wang et al., 2019a]. These half-order reflections are characteristic of an $L1_2$-type superlattice, indicating the formation of SRO domains during the aging process (**Figure 7 (e) and (f)**). The lattice parameters measured from the reciprocal lattice vectors were 0.366 nm for the disordered matrix and 0.365 nm for the SRO domains, suggesting minimal lattice mismatch.

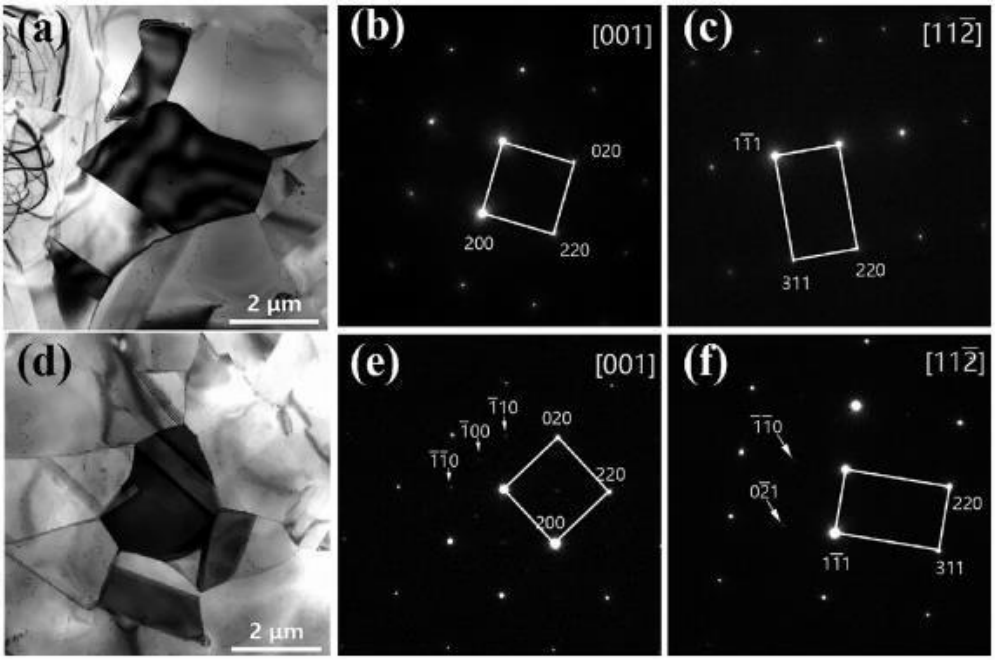

Figure 7: (a) Bright-field TEM image of as-quenched sample, (b) and (c) for its SAED patterns along [001] and [11–2] zone, respectively; (d) bright-field TEM image of as-aged sample, and (e) and (f) for its SAED patterns along [001] and [11$\bar{2}$] zone, respectively [Wang et al., 2019a].

High-resolution TEM (HRTEM) can provide atomic-scale information on ordering, although SRO domains often lack strong contrast in direct images due to their coherent interface with the surrounding matrix (**Figure 8**). In this case, Fast Fourier Transform (FFT) analysis of HRTEM images of aged samples revealed additional weak $L1_2$ superlattice spots, similar to those observed in SAED patterns [Diánez et al., 2016]. The interplanar spacings for the (200) reflections were 0.184 nm for the disordered matrix and 0.181 nm for the SRO microdomains, corresponding to lattice parameters of 0.368 nm and 0.362 nm, respectively — a difference of

only ~1.6%. This small mismatch explains the absence of distinct SRO contrast in bright-field or HRTEM images [Hata et al., 2000].

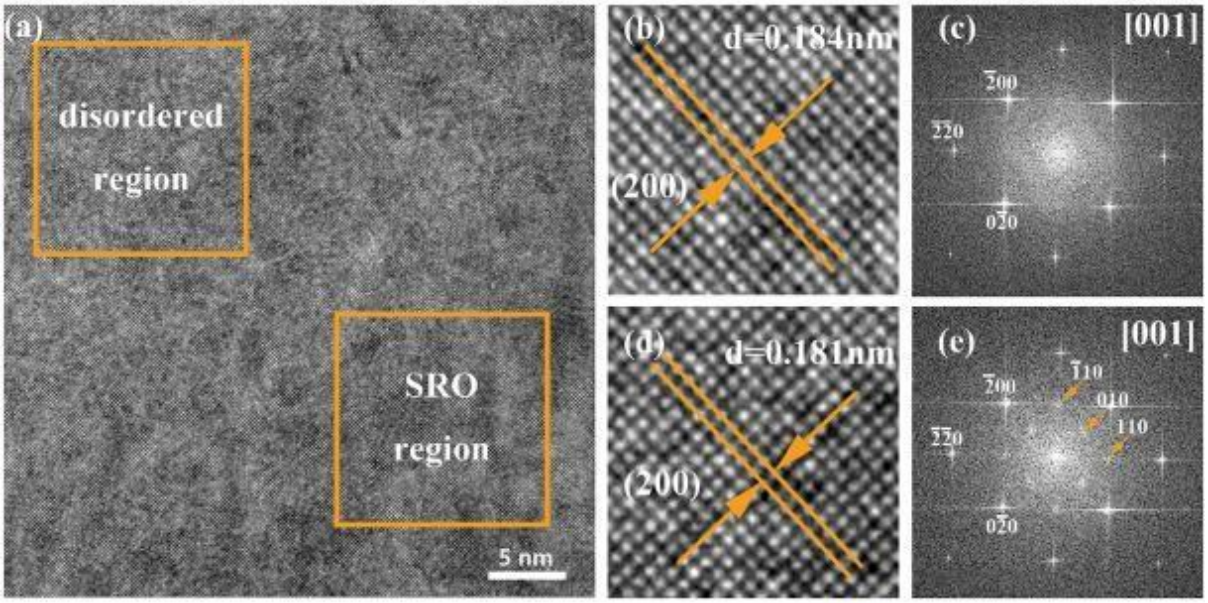

Figure 8: HRTEM observation revealing SRO microdomain dispersed in random matrix. (a) Low magnification HRTEM image of as-aged sample. (b) High magnification image of disordered region. (c) FFT pattern of disorder region (d) High magnification image of SRO region. (e) FFT pattern of SRO region [Wang et al., 2019a].

This combination of TEM, SAED, and FFT analysis from HRTEM images thus provides a robust method for detecting SRO, even when direct imaging contrast is minimal, and highlights the sensitivity of diffraction techniques to subtle ordering phenomena in Ni-based alloys.

Atom Probe Tomography (APT) is a state-of-the-art analytical technique that enables three-dimensional characterization of materials at near-atomic resolution, providing detailed compositional mapping with sub-nanometer precision [Gault et al., 2012]. In the context of identifying SRO in alloys, APT offers unique advantages because it detects the spatial positions and chemical identities of individual atoms, allowing direct analysis of local atomic arrangements that deviate from randomness, evident signs of SRO (**Figure 9**). By statistically evaluating the frequencies and preferences of atomic pairs in the reconstructed volume, it can quantify the tendency for certain elements to cluster or anti-cluster within their first few atomic neighbors, which are conventionally described by Warren–Cowley SRO parameters [Cowley, 1950, Schönfeld, 1999].

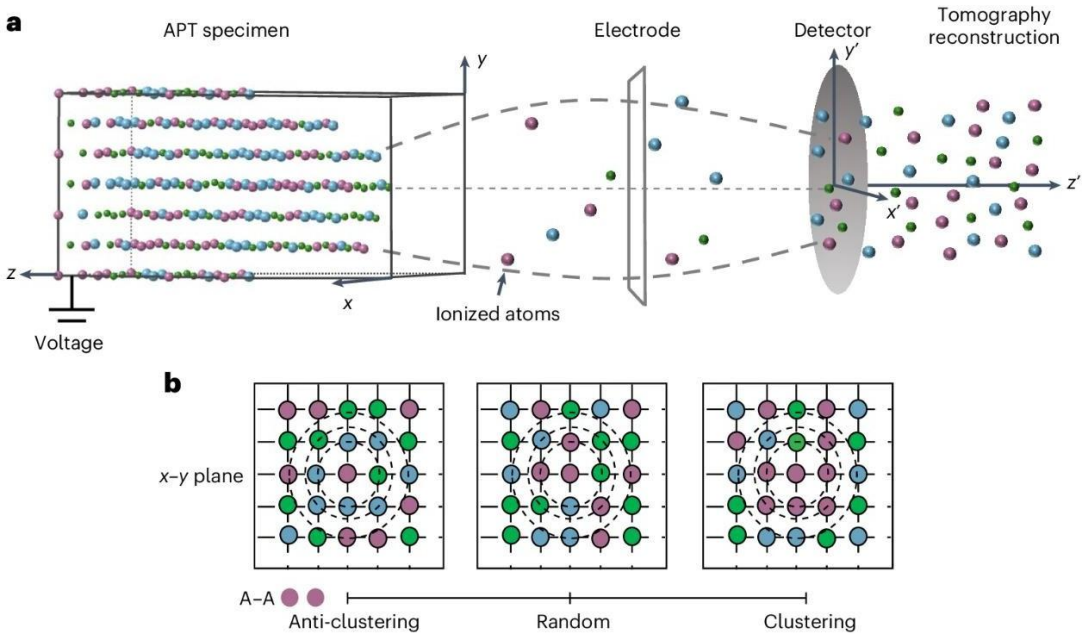

Figure 9: APT technique to identify the SRO clustering [He et al., 2024].

However, the efficiency of APT in detecting and quantifying SRO is influenced by intrinsic limitations such as finite detection efficiency, typically 50–60% for contemporary instruments, and trajectory uncertainties that reduce spatial resolution, particularly in the lateral direction. These limitations tend to systematically underestimate true SRO intensity, especially in complex or highly concentrated alloys and can challenge the detection of weak SRO signals [Marceau et al., 2015]. Nevertheless, for moderate to strong SRO signals, systematic data analysis methods and computational corrections (e.g., via Monte Carlo simulations and statistical reconstitution) enable reliable quantification and even mapping of SRO parameters [He et al., 2024]. The technique is especially powerful when the mass spectrum allows clear elemental distinction (as in many medium- and high-entropy alloys), and its combination with methods such as spatial distribution maps (SDMs) and radial distribution functions further highlights subtle ordering phenomena [Li et al., 2023a].

APT is the most direct atomic-scale probe for SRO, with recent advances in resolution, analysis, and machine learning improving its sensitivity. While quantification of weak or highly localized SRO remains challenging, combining APT with complementary techniques like TEM or scattering provides clear insight into how atomic order influences alloy structure and properties.

In addition to direct imaging and diffraction-based techniques, several indirect methods have been developed and applied to characterize SRO in nickel-based alloys, particularly when direct observation proves challenging due to the subtle nature of SRO.

Another widely used approach is **electrical resistivity measurements**. Electrical resistivity measurements have quantitatively shown that short-range order influences resistivity in nickel alloys by a few percent compared to a random atomic distribution. For example, in Ni-Al alloys, SRO reduces the electrical resistivity by about 3–7% relative to the value for a random configuration, indicating less electron scattering in more ordered local atomic environments [Ikram and Shaukat, 1993]. In complex solid solutions like NiCoCr, SRO involving preferential bonding of Cr atoms to Ni and Co contributes to lower electrical and thermal conductivities, as confirmed by correlated structural and resistivity analyses, although precise resistivity change percentages for NiCoCr are less commonly reported [Zhang et al., 2017]. Typical experimental protocols involve annealing at fixed temperatures to promote SRO formation, then measuring resistivity changes that correlate directly with the degree of SRO evolution. In a study on a commercial precision resistance Ni-Cr alloy, the as-quenched sample showed a resistivity of 1.22 Ω·m, which was below the required 1.30 Ω·m. After aging treatment, the resistivity increased to 1.36 Ω·m, confirming the formation of SRO in the alloy during aging [Marucco, 1991]. While resistivity measurements provide a highly sensitive but indirect probe of SRO formation, they do not allow a precise quantification of its extent or spatial characteristics. For this reason, they are most effective when combined with direct structural techniques.

X-ray diffraction (XRD) has been widely employed to investigate the effect of thermal aging on Alloy 690TT. For example, studies on material heats similar to the present work (notably Heat C) showed that aging up to 10,000 h at 400 °C produced no significant change in lattice parameter, indicating that the long-range crystal structure remains essentially stable (**Figure 10**) [Huotilainen and Que, 2022]. Nevertheless, non-negligible peak broadening was detected after aging, which has been interpreted as an indirect indication of short-range ordering (SRO), in agreement with complementary resistivity measurements. Importantly, no superlattice reflections, which would confirm the presence of long-range order, were observed.

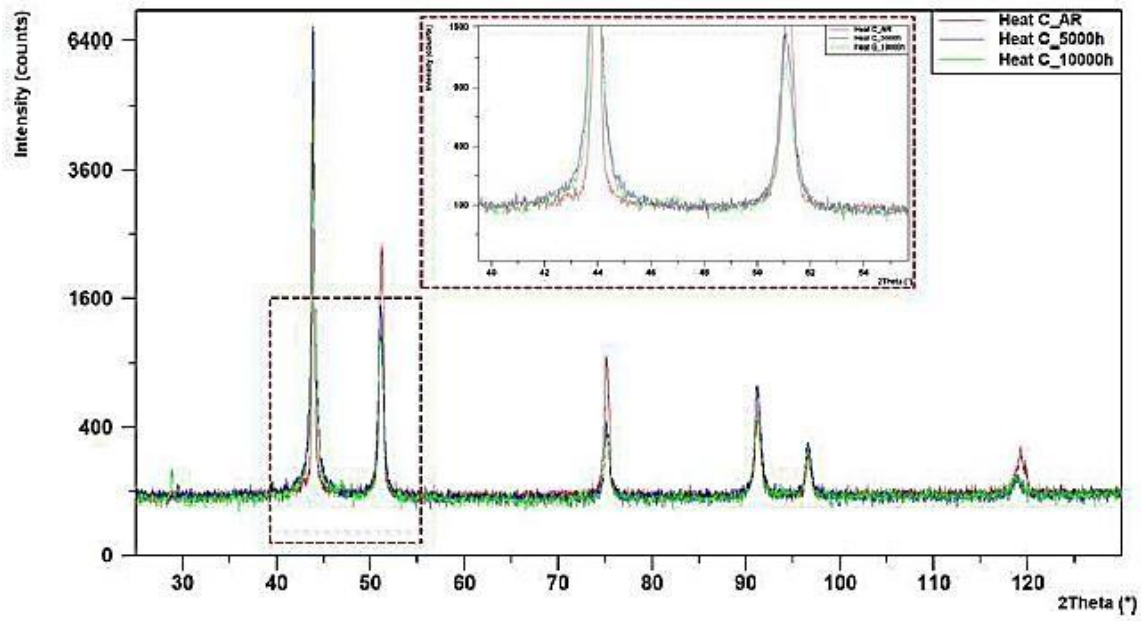

Figure 10: XRD patterns of an aged Alloy 690TT at 400°C after 10,000 hours [Huotilainen and Que, 2022].

Similar observations were made in Ni–Cr model alloys, where XRD revealed only fundamental fcc peaks in both as-quenched and aged conditions, with nearly identical lattice parameters before and after aging (0.3570 nm vs. 0.3568 nm) [Wang et al., 2019a].

Literature review of SRO/LRO in Alloy 690TT

The below **Table 2** compiles key studies investigating SRO and LRO phenomena in Alloy 690 and similar Ni–Cr–Fe compositions. The occurrence of ordering has been examined through various techniques, including electron diffraction (ED), X-ray diffraction (XRD), hardness evolution, electrical resistivity (ER), and thermoelectric power (TEP), under different thermal-aging conditions, with results strongly dependent on Fe content, cold work, and aging duration.

References	Alloy chemistry (wt%)	Cold work (%)	Aging temp. (°C)	Aging time (h)	Evidence of SRO/LRO	Methods used	Notes
[Marucco, 1991]	Cr 29.2, Fe 8.85	0	475	32,000	Yes	ED	Identified SRO in TT Alloy 690
[Mouginot et al., 2017b]	Cr 28.7, Fe 9.18	0, 20	350–550	~10,000	Yes	XRD, HV, ED	Suggested SRO, strongest at 420 °C
[Huotilainen et al., 2019]	Cr 29.0, Fe 9.3	0	400	~10,000	No	HV, TEM	HV ↑ but no SRO seen
[Stephan, 2018]	Cr 29.4–30, Fe 0.06–3	0	400–500	~10,000	Yes: SRO No: LRO	XRD, HV, ER, TEP	LRO: Some indirect signals but inconclusive
[Delabrouille et al., 2009]	Cr 29–30, Fe 10.4	0, 20	420	60,000–70,000	No	ED	LRO/SRO excluded for Fe ≥ 9%

Table 2: Summary of key studies on the occurrence of short-range ordering (SRO) and long-range ordering (LRO) in Alloy 690.

Overall, the literature remains divided between pro-SRO and no-SRO findings (**Table 2**), with results strongly dependent on Fe content, cold work, and aging duration.

I.2.2.3. Evolution of grain boundary geometry

During thermal aging, a significant microstructural evolution involves changes in grain boundary chemistry and structure. This phenomenon, called Diffusion-Induced Grain Boundary Migration (DIGM) [Balluffi and Cahn, 1981], occurs when compositional gradients drive solute diffusion along the grain boundaries causing the boundaries themselves to migrate (**Figure 11**) [Xue and Marquis, 2022].

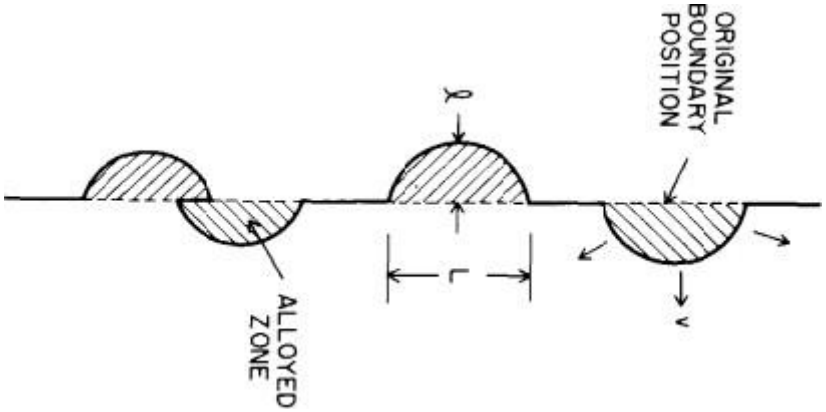

Figure 11: Schematic representation of grain boundary bulging during the early stages of DIGM [Balluffi and Cahn, 1981].

In Alloy 690, which is rich in nickel and chromium, thermal aging promotes chromium diffusion toward grain boundaries. This leads to chromium enrichment at the boundaries, facilitating precipitation of chromium-rich carbides, primarily $Cr_{23}C_6$. Simultaneously, chromium depletion occurs in the matrix adjacent to the grain boundaries, causing these boundaries to migrate and replace existing grains with new crystallographic orientations [Angeliu and Was, 1990, Lee et al., 2016]. This migration is anisotropic and creates zones near grain boundaries with lowered chromium concentration that can reduce local corrosion resistance.

The DIGM process can also leave behind “ghost” precipitates and sometimes subgrain structures. This evolution impacts carbide distribution [Xue and Marquis, 2022] and the grain boundary morphology. Recent studies on Alloy 600 have highlighted the role of DIGM as a key mechanism enhancing intergranular oxidation under high-temperature water and steam environments [Volpe et al., 2022]. During exposure at 320–400 °C, DIGM was observed through lateral shifts of grain boundaries relative to fixed carbides, revealing that solute-depleted zones formed ahead of migrating boundaries. This phenomenon significantly increases the effective diffusivity of Cr and O along moving boundaries, thereby accelerating the

penetration of intergranular oxides beyond what is expected from stationary grain-boundary diffusion alone. The degree of these changes depends on factors such as aging time, temperature, and whether secondary phases like intragranular precipitates or ordering phenomena like SRO are present [Mouginot et al., 2017b].

I.2.3. Impact of mechanical properties due to thermal aging

I.2.3.1. Hardness evolution

Thermal aging is known to influence the mechanical behavior of nickel-based alloys through various microstructural changes, particularly in the distribution and characteristics of precipitates and ordering phenomena. In Alloy 690TT, microhardness measurements have been used extensively to track the evolution of strength during aging. However, the results reported in the literature vary depending on the alloy heat, aging temperature, and exposure time.

Micro hardness

Huotilainen et al. [Huotilainen et al., 2019] evaluated the thermal aging response of four different industrial heats of Alloy 690 subjected to aging at 400 °C for 5,000 to 10,000 hours (**Figure 12**). For heats (A, B), the hardness increases only slightly with thermal aging, indicating relatively modest microstructural changes at this temperature over the studied time frame. For example, the hardness of Heat A increases from ~150 HV to ~165 HV over 10,000 h, while for Heat B it remains close to its initial hardness with a marginal increase.

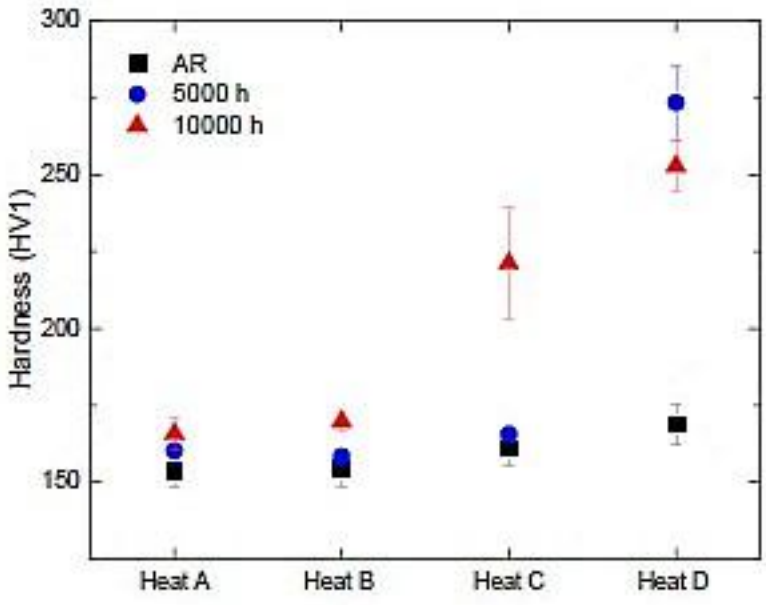

Figure 12: Evolution of microhardness of different Alloy 690TT for 5,000 to 10,000 hours [Huotilainen et al., 2019].

Heat C (Alloy 690 TT) shows a markedly different behavior. While the AR hardness is around ~160 HV, after 5,000 h it increases sharply to ~170 HV, and after 10,000 h it rises further to about ~225 HV, representing the largest hardness increase among the tested heats. This significant hardening suggests more pronounced microstructural evolution in Alloy 690TT under the same thermal exposure. The increase is consistent with processes such as thermal aging–induced microstructure modifications, including the formation of ordered phases (e.g., Ni_2Cr-type ordering), carbide precipitation and coarsening at grain boundaries and within the matrix, both of which can hinder dislocation motion and thereby increase hardness.

Complementary work by Mouginot et al. [Mouginot et al., 2017] investigated the response of Alloy 690 and Alloy 152 across aging temperatures from 350 °C to 550 °C (**Figure 13**). Their results demonstrated a typical hardness peak at around 420 °C, which aligns with the known thermodynamic stability range of SRO. This stability range is supported by prior studies indicating that ordering reactions in Ni–Cr alloys are maximized between 400 °C and 450 °C, depending on composition and Fe content [Marucco, 1991, Stephan et al., 2019] (**Figure 6**). At temperatures beyond 420 °C, the hardness was found to decrease, the hardness gradually decreases, indicating that increased atomic mobility promotes the dissolution or loss of stability of SRO.

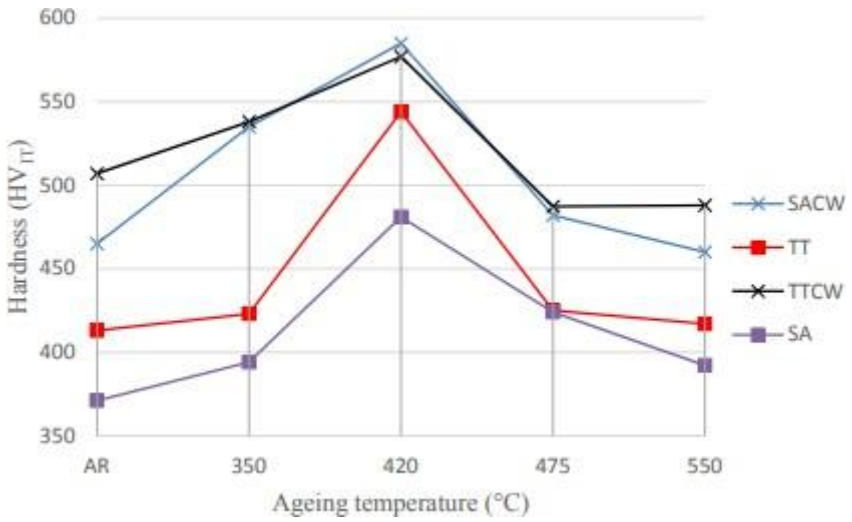

Figure 13: Evolution of the microhardness of Alloy 690 at different temperatures after aging for 10,000 hours [Mouginot et al., 2017b].

Nano hardness

While microhardness testing provides an averaged view of bulk mechanical properties, nanoindentation enables high-resolution probing of local variations in hardness and modulus—particularly useful for assessing grain boundary regions, matrix areas, and potential short-range ordering (SRO) effects. In thermally aged Alloy 690, nanoindentation studies have revealed important insights into localized hardening phenomena that may not be captured through conventional microhardness techniques.

Very few studies have used nanoindentation to assess the localized mechanical response of Alloy 690 aged at temperatures from 420°C to 550 °C. For example, Mouginot et al.[Mouginot et al., 2017] observed increased nano-hardness in regions near grain boundaries after aging treatments (**Figure 14**), linking this behaviour to the formation of SRO and compositional variations at the nanoscale. It should be underlined that, the presence of SRO was not proved in this study.

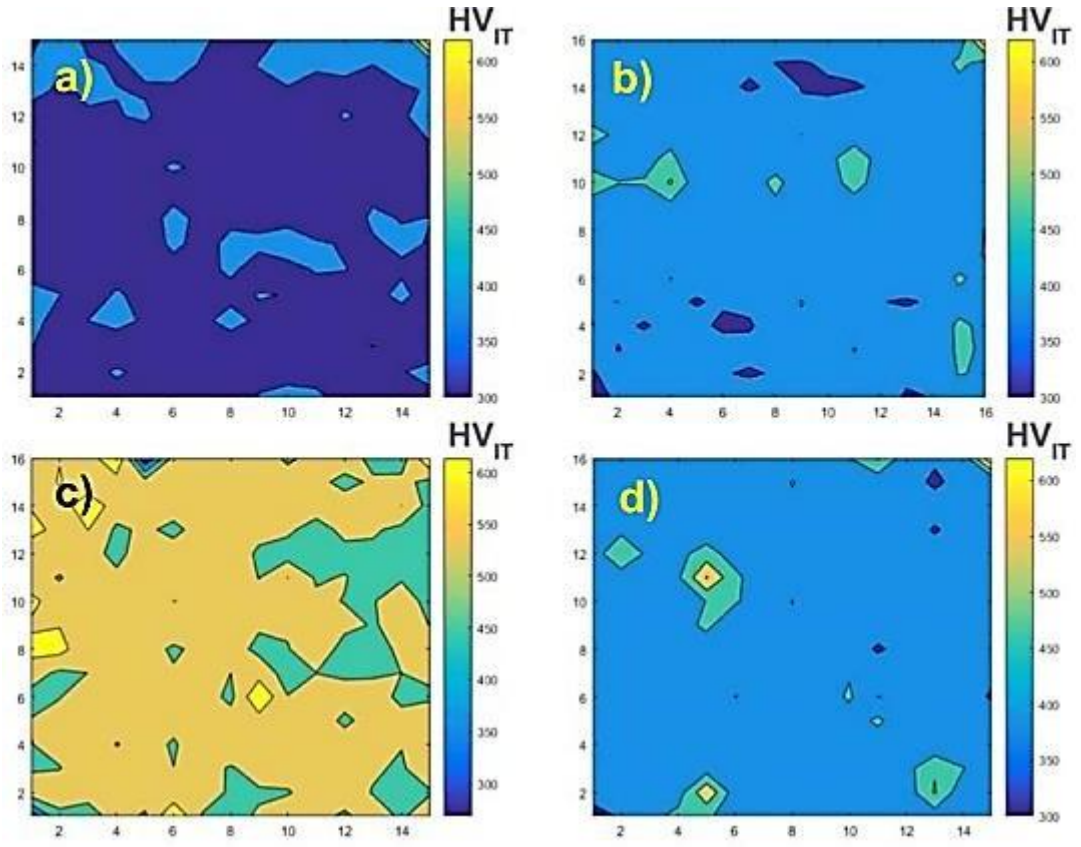

Figure 14: Hardness mapping of Alloy 690 aged for 10000 hours; (a) SA, (b) TT, (c) 420°C and (d) 550°C using data from the 1.5 mN load nanoindentation matrices (the indent spacing between two successive indentations was 5 µm) [Mouginot et al., 2019].

I.2.4. Summary of thermal aging effects and knowledge gaps

This bibliographic review showed that accelerated thermal aging can have an impact on the microstructure of the Alloy 690TT. Indeed, some authors showed qualitatively an increase in the size of the intergranular precipitates and the formation of α-Cr precipitates [Mouginot et al., 2017b]. However, no quantitative study either on intergranular or intragranular carbides has been conducted yet.

Short- and Long-Range Ordering are phenomena that may occur during aging in Alloy 690TT. however, the literature remains divided. While several studies have reported the presence of ordering after accelerated aging [Huotilainen and Que, 2022, Marucco, 1991, Mouginot et al., 2019], others conducted under comparable conditions found no clear evidence of such phenomena [Delabrouille et al., 2009, Huotilainen et al., 2019].

Another change in the microstructure of Alloy 690 is the apparition of tortuous grain boundaries during thermal aging due to Diffusion Induced Grain Boundary Migration (DIGM).

All these microstructural changes lead to a modification of the mechanical properties of the alloy. Hence, it has been shown an increase in hardness after aging depending on the heat and some authors found a peak after accelerated thermal aging at 420°C [Mouginot et al., 2017b].

In the literature, it remains unclear to what extent each consequence of thermal aging (i.e. increase in precipitates, SRO, DIGM) contributes to the increase in hardness. For example, Mouginot et al. [Mouginot et al., 2019] made the hypothesis of an increase in nano-hardness due to SRO without direct evidence.

Finally, it should be noted that most of the studies on accelerated thermal aging of Alloy 690TT are oriented onto the susceptibility to stress corrosion cracking due to the history of Alloy 600 [Guerre et al., 2016, Kim et al., 2000, 2015]. However, there is no study specifically dedicated to the impact of thermal aging on the fatigue and environmentally assisted fatigue behavior of the alloy.

I.3. GENERALITIES OF LOW CYCLE FATIGUE

I.3.1. Introduction to fatigue

Fatigue is a phenomenon in materials science and engineering where a material experiences damage and failure under cyclic loading, even when the applied stress levels are below its ultimate strength. Two common types of fatigue (**Figure 15**) are high-cycle fatigue and low-cycle fatigue [Schijve, 2009] :

- **High-cycle fatigue (HCF):** The cyclic stresses are generally in the elastic range and the fatigue lifetime of the material is usually between 10^5 and 10^7 cycles.
- **Low-cycle fatigue (LCF):** The cyclic stresses are high, and, in each cycle, macroscopic plastic deformation is induced. In **Figure 15**, the rupture in LCF occurs after less than $5x10^4$ cycles.

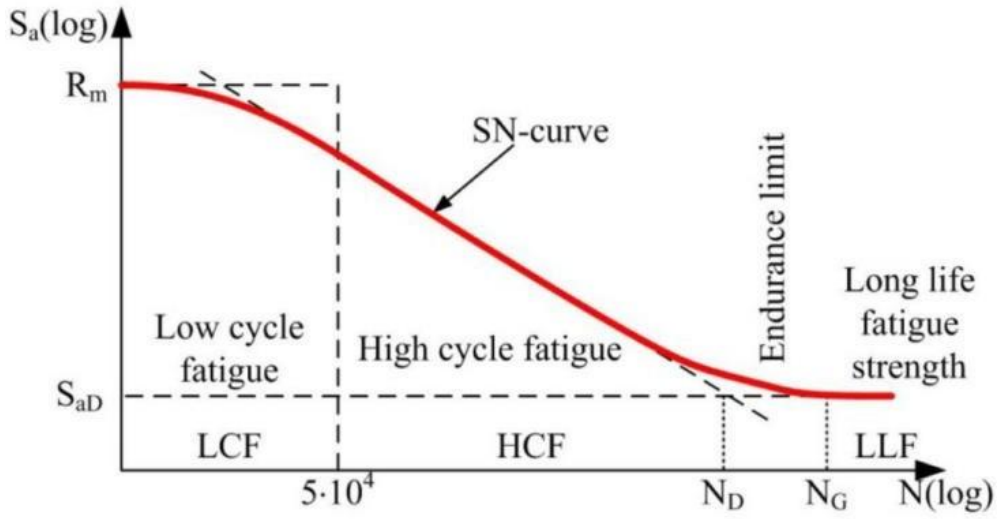

Figure 15: Schematic S-N curves for metallic materials [Stahlmann, 2013].

This study focuses on LCF, a regime marked by high strain amplitudes that influence the material stress–strain behavior. In this regime, several parameters define the loading conditions:

- **Strain amplitude ε_a (%) =** $\frac{\varepsilon_{max}-\varepsilon_{min}}{2}$
- **Strain rate $\dot{\varepsilon}$ (%/s):** the speed at which strain is applied and reversed within a cycle.
- **Strain ratio R_ε:** the ratio between the minimum and maximum strain in a cycle ($R_\varepsilon=\varepsilon_{min}/\varepsilon_{max}$); a value of –1 corresponds to fully reversed loading.

Indeed, the LCF regime is especially important for PWR components, which undergo thermal transients during start-up, shutdown, and load-following operations, resulting in large cyclic strains. Under these conditions, the cyclic stress–strain response becomes a critical parameter for assessing fatigue resistance and predicting component lifetime. The following sections first present the fundamentals of fatigue and fatigue design curves used for structural assessment, followed by energy-based fatigue life models. Finally, the initiation and propagation stages of fatigue cracks are discussed, providing a foundation for interpreting the experimental results of this study.

I.3.2. Fatigue design curve in air

The NUREG/CR-6909 report, published by the U.S. Nuclear Regulatory Commission (NRC) in 2007 [Chopra, 2007], provides a comprehensive evaluation of the environmental effects on fatigue life of light water reactor (LWR) materials, including austenitic stainless steels, low-alloy steels, and nickel-based alloys. The report compiles an extensive database of strain-controlled fatigue tests performed in air and simulated LWR water environments, under a wide range of temperatures, strain rates, and dissolved oxygen/hydrogen conditions.

Based on this database, NUREG/CR-6909 introduced the concept of the environmental correction factor (F_{en}), which quantifies the influence of reactor water environment on fatigue life relative to air. The methodology defines fatigue life in air as the reference baseline and applies the F_{en} factor to account for environmental degradation in design evaluations of primary circuit components. The fatigue design curves derived in the report remain the reference framework for assessing EAF in LWR component design and life extension analyses.

The **Figure 16** illustrates the procedure used to derive fatigue design curves for structural materials such as austenitic stainless steels and nickel-based alloys. The starting point is the mean air curve, obtained from extensive strain-controlled fatigue database established on polished specimens tested in air at different temperatures and strain rates, which represents the average fatigue life for a given strain amplitude.

To introduce conservatism, a design air curve is established by applying successive reduction factors accounting for the influence of various parameters: (A) material variability, (B) specimen-to-component size effects, (C) surface finish, (D) loading history, and finally (E) an additional factor of 2 on strain amplitude. The cumulative effect of these margins ensures that

the design curve is significantly lower than the experimental mean curve, thereby guaranteeing a conservative fatigue assessment under air conditions [ASME, RCC-M].

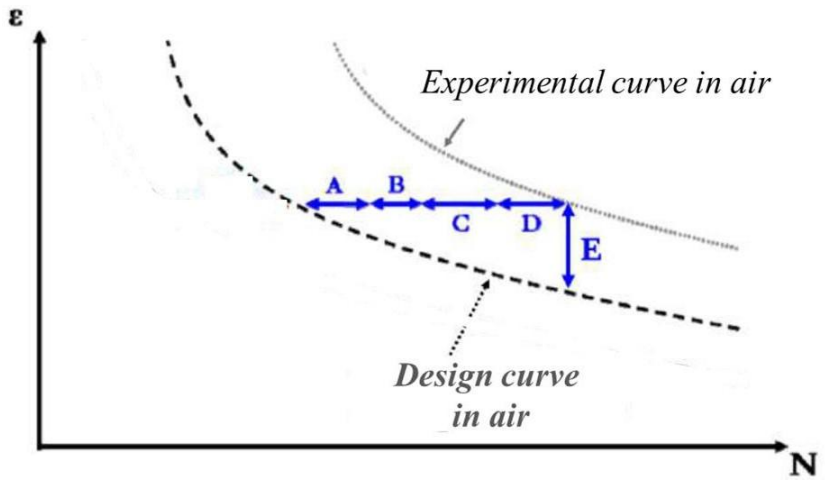

Figure 16: Design approach accounting for sub-factors.

While design curves offer a practical and conservative approach, they remain empirical and do not capture the underlying damage mechanisms. To better describe the material response in the low-cycle fatigue regime, energy-based models relate the dissipated plastic energy per cycle to fatigue life, offering a more physical interpretation of fatigue behavior.

I.3.3. Energy-based fatigue life models

Energy-based fatigue life models are a class of fatigue prediction approaches that relate the mechanical energy dissipated during cyclic loading to the fatigue life of a material [Liu et al., 2015, Zhang et al., 2023]. Instead of using only stress or strain amplitudes, as in traditional models like Basquin or Coffin-Manson [Coffin, 2022, Mitchell, 1996], these models consider the area enclosed by the hysteresis loop in a stress–strain curve, which reflects the energy the material absorbs (and dissipates) during each fatigue cycle. This approach is often considered more comprehensive because it typically accounts for both elastic and plastic contributions to deformation, thereby capturing the cumulative effect of cyclic loading on damage more directly than stress or strain-based parameters alone.

In energy-based fatigue analysis, two commonly used approaches are the total strain energy model and the plastic strain energy model, both of which relate the dissipated energy during cyclic loading to the fatigue life of the material.

I.3.3.1. Total Strain Energy Model (Wt)

The total strain energy per cycle, W_t, is defined as the area enclosed by the full hysteresis loop in a σ-ε plot, encompassing both elastic and plastic contributions:

$$W_t = \oint \sigma \, d\varepsilon = W_p + W_e \qquad \textbf{Eq. I.2}$$

$$W_t = W_0 . N_f^{-1/\beta} \qquad \textbf{Eq. I.3}$$

where:

W_t = total strain energy per cycle,

W_p = plastic strain energy per cycle (irreversible),

W_e = elastic strain energy per cycle (recoverable),

β = The fatigue damage exponent (or energy exponent),

N_f = The number of cycles to failure,

W_0 = The material fatigue toughness parameter, i.e. the total strain energy density per cycle corresponding to one cycle to failure.

This model has been used to correlate fatigue life over a wide range of strain amplitudes, especially when the elastic portion of deformation is not negligible, such as in the LCF-HCF transition regime [Zhang et al., 2023] [Ellyin, 1997]. It is considered more comprehensive and can accommodate effects such as cyclic hardening, softening, and elastic recovery.

I.3.3.2. Plastic Strain Energy Model (W_p)

In contrast, the plastic strain energy per cycle, W_p, considers only the irreversible energy dissipated through plastic deformation.

This model is particularly effective for classical low-cycle fatigue (LCF) applications, where plastic deformation is the primary damage parameter [Liu et al., 2015] [Wang et al., 2017]. It provides a more physically representative measure of fatigue damage for ductile materials under large strain amplitudes.

$$W_p = \oint \sigma \, d\varepsilon_p \qquad \textbf{Eq. I.4}$$

$$W_p = W_0 . N_f^{-1/\beta} \qquad \textbf{Eq. I.5}$$

where,

W_p: Energy dissipated per cycle by plastic deformation (represented by the Area under the hysteresis loop),

W_0: A material constant representing plastic energy at $N_f = 1$,

β: Fatigue exponent that defines the slope of the log-log W_p vs. N_f curve.

To calculate the strain energy for tests conducted at a strain amplitude of 0.6%, the plastic strain energy model (W_p) was adopted. This selection is based on the understanding that, under such high strain amplitudes, the majority of the energy dissipated during each cycle is attributed to plastic deformation. As a result, the W_p model offers a more suitable representation of fatigue damage compared to models incorporating total or elastic energy. This approach is consistent with classical LCF methodologies, where plastic work is the primary source of material degradation.

I.3.4. Initiation and propagation

There are usually three stages in fatigue life: crack initiation, crack propagation and final failure.

Initiation

During the initial stage, repeated plastic straining promotes the localization of damage, most often in the form of persistent slip bands or at microstructural heterogeneities acting as preferential sites for crack nucleation. The initiation stage is governed by cyclic plastic deformation, leading to the formation of intrusions and extrusions on the surface that evolve into microcracks once the local strain exceeds a critical threshold [Mu and Aubin, 2010, Suresh, 1998].

Propagation

Once a crack has formed, the second stage involves its progressive propagation under cyclic loading, ultimately leading to final fracture when the remaining cross-section can no longer sustain the applied stresses.

As the cracks extend beyond the grain scale, their propagation rate becomes more uniform and can be described using fracture mechanics relationships such as the Paris law , correlating crack growth rate with the applied stress intensity factor range [Paris and Erdogan, 1963].

This classical Paris law (**Eq. I.6**), expressed in terms of the stress intensity factor range ΔK, provides reliable predictions of fatigue crack growth only under small-scale yielding conditions, where plasticity remains confined at the crack tip.

$$\frac{da}{dN} = C \times (\Delta K)^m \qquad \textbf{Eq. I.6}$$

However, under low-cycle fatigue and large-scale yielding conditions, the parameter ΔK alone does not capture the role of extensive cyclic plastic deformation as a crack driving force.

To address this limitation, several authors have introduced strain-based intensity parameters [R. C. Boettner et al., 1965, Skelton and Haigh, 1978], such as ΔK_ε, which combines elastic and plastic strain amplitudes with crack length through the relation (**Eq. I.7**):

$$\Delta K_s = (\Delta\varepsilon_p + q\Delta\varepsilon_e)\sqrt{\pi a} \quad \textbf{Eq. I.7}$$

This approach enables crack growth data obtained under both confined and extensive plasticity to be correlated within a single power-law framework. In the present work, a simplified formulation using the total strain amplitude ($\Delta\varepsilon_{tot}$) is adopted, without introducing an additional weighting factor q, in line with previous studies [Kamaya, 2015], to evaluate fatigue crack growth rates in Alloy 690. The modified Paris law after considering the strain intensity factor range is given **Eq. I.8:**

$$\Delta K_s = F(a) \times \Delta\varepsilon_t \times \sqrt{\pi \times a} \quad \textbf{Eq. I.8}$$

I.4. LOW CYCLE FATIGUE OF ALLOY 690 IN AIR

I.4.1. Cyclic stress-strain behavior of Alloy 690

The cyclic stress–strain response of Alloy 690 has been far less studied compared to austenitic stainless steels, such as 304L, which are well-documented in the literature in terms of microstructural evolution during cyclic loading. **Figure 17** compares the cyclic behavior of the two alloys under similar strain amplitudes.

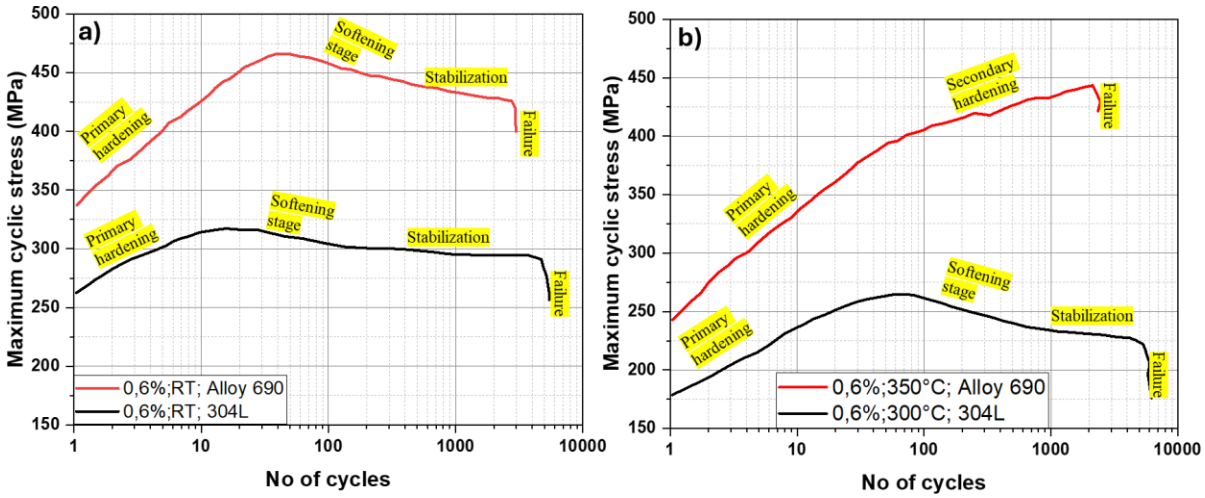

Figure 17 : Cyclic stress-strain behavior of Alloy 690 [Wang et al., 2022] and 304L [de Baglion, 2011] in air at RT and 300°C.

It can be seen different stages depending on the alloy, the temperature and the number of fatigue cycles :

- **Primary hardening:** At room temperature, both Alloy 690 and 304L exhibit a pronounced initial increase in stress, reflecting the multiplication and rearrangement of dislocations and their interactions with solute atoms in solid solution [Gerland et al., 1997, Poulain et al., 2016]. The extent of this stage is controlled by parameters such as strain amplitude, strain rate, and solute concentration, which govern the evolving dislocation density. At 300 °C, Alloy 690 maintains a strong primary hardening response [Wang et al., 2022], while 304L also exhibits hardening but to a lesser degree [de Baglion, 2011].
- **Softening:** At RT, Alloy 690 exhibits an initial hardening phase followed by a cyclic softening, similar in trend to austenitic stainless steels like 304L [Wang et al., 2022]. In 304L, this softening is associated with the annihilation of mobile dislocations and their rearrangement into stable substructures, together with the gradual localization of slip

within persistent slip bands [Gerland et al., 1997]. However, at 300–350 °C, Alloy 690 departs from this behavior: instead of softening, it continues to harden throughout life [Shi et al., 2023, Wang et al., 2022]. By contrast, 304L still shows cyclic softening and eventual stabilization at comparable conditions. Several hypotheses have been advanced to explain this persistent hardening in Alloy 690, including dislocation pinning by solute atoms associated with dynamic strain aging (DSA) [Wang et al., 2022], strong interactions with stacking faults [Li et al., 2022], and the possible activation of nano-twinning [Chai et al., 2013] and the formation of SRO [Shi et al., 2023], all of which could inhibit dislocation annihilation and sustain cyclic hardening. Nevertheless, microstructural evidence at 300 °C remains limited, and the precise mechanisms driving this continuous hardening in Alloy 690 are yet to be fully verified.

- **Stabilization:** At room temperature, both Alloy 690 and 304L exhibit a stabilization regime after the initial hardening/softening stages. During this stage in 304L, a balance is achieved between dislocation multiplication and annihilation, resulting in stable dislocation structures, such as cells or persistent slip bands [Gerland et al., 1997]. This results in a relatively constant cyclic stress level over a large number of cycles. However, at 300-350 °C, the behavior diverges. In 304L, a clear stabilization plateau is still present, reflecting the ability of the dislocation network to reorganize into stable configurations despite thermal activation. In contrast, Alloy 690 does not show a sustained stabilized regime; instead, it continues to harden throughout cycling, indicating that dislocation rearrangements do not reach equilibrium.

  This shows that while the CSS response of both alloys stabilize at RT, only 304L maintains stabilization at 300 °C, whereas Alloy 690 transitions into continuous hardening.

- **Secondary hardening:** This phenomenon has already been introduced in the softening section, where it was shown that Alloy 690 does not undergo cyclic softening at 300 °C as observed in 304L, but instead continues to harden. More specifically, the cyclic stress–strain response of Alloy 690 exhibits a distinct change in slope after ~100 cycles, after which the hardening persists but at a slower rate [Shi et al., 2023, Wang et al., 2022]. This secondary hardening stage contrasts sharply with the stabilization or softening regimes of 304L under similar conditions. The persistence of hardening in Alloy 690 suggests that additional deformation mechanisms are active beyond the initial dislocation multiplication, but their exact nature at 300 °C remains uncertain. This

continuous hardening behavior is a distinctive feature of Alloy 690 compared to austenitic stainless steels, and it highlights the need for further studies to establish clear links between the observed macroscopic cyclic response and the underlying microstructural mechanisms.

- **Failure:** In both materials, failure occurs after several thousand cycles depending on the strain amplitude. In 304L, failure follows the sequence of hardening–softening–stabilization, while in Alloy 690, it occurs after prolonged hardening without a clear plateau at 300°C.

I.4.2. Fatigue crack initiation and propagation in Alloy 690

I.4.2.1. Crack initiation

Crack initiation in Alloy 690 under LCF at high temperature in air has generally been associated with localized cyclic plasticity at the microstructural level. The available studies remain limited: most were conducted on tubular specimens [Shi et al., 2023], reflecting the historical application of Alloy 690 in steam generator tubing, while only a few investigations have been carried out on polished bulk specimens [Wang et al., 2022]. Within favorably oriented grains, persistent slip bands (PSBs) form due to repeated irreversible dislocation motion, resulting in surface intrusions and extrusions [Chai et al., 2013]. These features act as micro-notches, serving as predominant nucleation sites for fatigue cracks. In Alloy 690 and similar nickel-based alloys, such crack initiation is strongly localized. At high temperature, increased dislocation activity can further promote PSB formation and enhance local plasticity [Chai et al., 2013].

I.4.2.2. Fatigue crack propagation

Once initiated, cracks in Alloy 690TT typically propagate predominantly in a transgranular manner under high-temperature LCF in air. In the early propagation stage, microstructurally short cracks interact strongly with grain boundaries, precipitates, and local hardening regions, sometimes being momentarily deflected but ultimately advancing through the grain interiors. The crack path is strongly influenced by crystallographic orientation, with fracture surfaces often revealing fatigue striations characteristic of transgranular fatigue crack growth [Hong et al., 2014].

I.4.3. Factors influencing fatigue life in air

I.4.3.1. Effect of temperature

The effect of the testing temperature has been investigated and reported in the NUREG/CR-6909 rev1 [Chopra, 2018].

In this report (**Figure 18**), a comparison is done between the fatigue life of Alloy 690 tested in air at room temperature and at 315°C (a working point of PWRs). Moreover, the best-fit fatigue curve established by ANL for austenitic stainless steels in air is plotted.

The results indicate that no significant effect of temperature is visible between room temperature and 315°C in air. Plus, Alloy 690 exhibits fatigue lives broadly consistent with the ANL curve for stainless steels, although some scatter is observed.

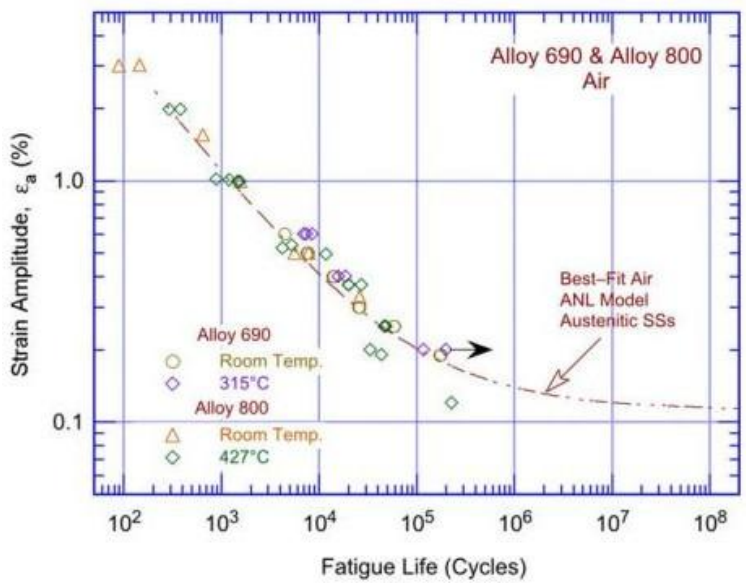

Figure 18 : Fatigue ε–N behavior for Alloys 600, 690 and 800 in air at temperatures between room temperature and 427°C [Chopra, 2018].

It is important to emphasise that these data are presented as general results for Alloy 690, without specifying the heat treatment condition (e.g., thermally treated, mill-annealed). Therefore, they should be interpreted with caution: while they offer a valuable reference for the overall fatigue response of Alloy 690, further research is needed to confirm the specific fatigue properties of individual microstructural states, such as TT or MA, under typical environments.

I.4.3.2. Effect of strain rate and input waveform

Strain rate effect

Due to limited available data regarding the influence of parameters, such as strain rate, on the fatigue life of Alloy 690TT, the NUREG/CR-6909 rev1 [Chopra, 2018] report relies on the data related to austenitic stainless steels (SSs) due to their mechanical property similarities.

Statistical analysis did reveal that fatigue lives of austenitic SSs in an air environment tend to decrease with decreasing strain rate within the temperature range of 400 to 430°C. However, it is worth noting that other studies, specifically those conducted by Électricité de France (EdF), suggested that variations in strain rate between 0.4 and 0.008%/s had no significant impact on the fatigue lives of SSs at temperatures up to 400°C [Chopra, 2018, de Baglion, 2011].

Consequently, the NUREG/CR-6909 [Chopra, 2018] assessment considered the effect of strain rate on the fatigue life of SSs in air to be negligible. It should be emphasized, however, that no equivalent data currently exist for Alloy 690TT, and the applicability of these conclusions to this specific alloy remains to be experimentally verified.

Waveform effect

The triangular waveform involves a linear increase and decrease in strain over time. It can represent loading conditions that gradually increase and decrease, such as temperature cycling or startup and shutdown procedures.

The research conducted by Nicolas Huin [Huin, 2013] explains the influence of strain rate and waveform on the hardening behavior of 304L. Notably, the 10% cold-worked material (**Figure 19**) exhibits distinct responses under different strain rates and waveforms when subjected to cyclic loading. Under high strain rates, the material displays limited hardening and predominantly exhibits softening during cyclic loading. This counterintuitive behavior is attributed to Dynamic Strain Aging (DSA) which is further explained in chapter 2.5.2.

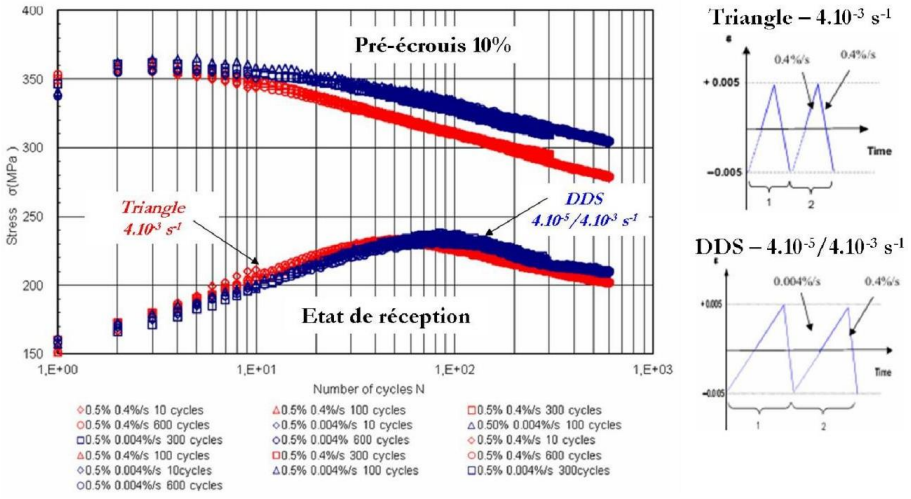

Figure 19 : Influence of the cold-work and the waveform on the cyclic behavior of a 304L at ε_a = 0.5%, $\dot{\varepsilon}$ = 0.4%/s and 0.004%/s, 300°C in air [Huin, 2013].

To date, however, no equivalent experimental data are available for Alloy 690TT, and it remains to be verified whether similar mechanisms operate in this alloy.

I.4.4. Deformation and damage mechanisms of Alloy 690 in air

I.4.4.1. Dynamic strain aging in Alloy 690

Dynamic Strain Aging (DSA) is a complex phenomenon arising from the interaction between moving dislocations and diffusing solute atoms [Hänninen et al., 2005]. Depending on the strain rate, temperature, and alloy chemistry, this interaction can lead to the temporary pinning of dislocations, followed by sudden unpinning. The resulting intermittent motion can produce serrated stress–strain curves, commonly referred to as the Portevin–Le Chatelier (PLC) effect [Shi et al., 2023]. Mechanistically, during cyclic loading, solute atoms diffuse to dislocations and temporarily lock them in place, which increases the stress required for further glide (**Figure 20**). When the dislocations eventually break free, abrupt stress drops occur, giving rise to flow serrations and stress fluctuations (**Figure 21**) [Sourabh and Singh, 2023].

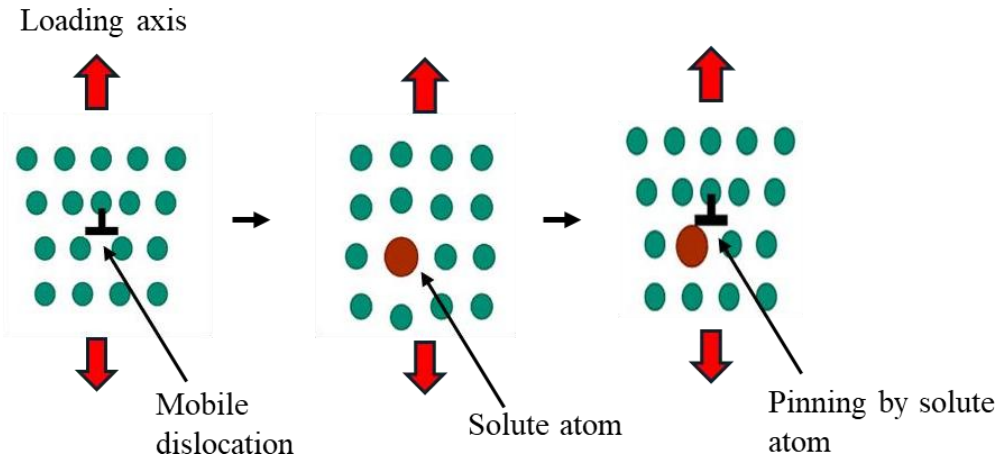

Figure 20 : Schematic of Dynamic Strain Aging (DSA) causing PLC effect.

Dynamic strain aging is particularly relevant to high-temperature applications, such as structural alloys in nuclear power plants, where components operate under cyclic stresses for extended periods [Hong et al., 2014, Hong and Lee, 2005, Shi et al., 2023]. In the case of Alloy 690, the principal solute atoms contributing to DSA are carbon, nitrogen, and chromium[Hong and Lee, 2005]. This phenomenon typically occurs in the temperature range of 200–600 °C, with the effect being more pronounced at low strain rates [Hong et al., 2014, Ivanchenko, 2010, Moss and Was, 2012].

In Alloy 690, DSA is manifested through cyclic hardening, strain localization, and dynamic stress fluctuations during fatigue tests, which significantly influence crack initiation and early crack propagation [Hong et al., 2014, Shi et al., 2023, Sourabh and Singh, 2023]. At lower strain rates and within the critical temperature window (**Figure 20**), DSA becomes more active, producing characteristic stress serrations and often a peak in work-hardening rate [Hänninen et al., 2005, Sourabh and Singh, 2023].

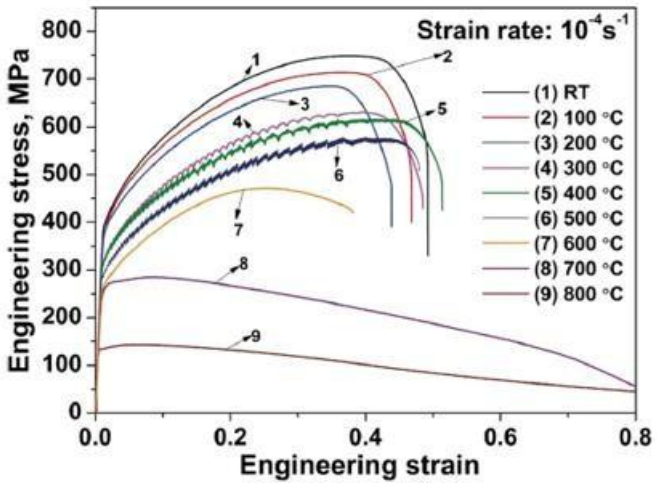

Figure 21: Influence of the temperature on the mechanical response of Alloy 690 during tensile test [Sourabh and Singh, 2023].

The consequences of DSA include a significant reduction in ductility, an increase in yield strength, and the promotion of strain localization that accelerates crack initiation and propagation under cyclic stresses [de Baglion, 2011].

I.4.5. Summary of LCF of Alloy 690 in air and knowledge gaps

At RT, Alloy 690TT exhibits a cyclic hardening/softening response comparable to austenitic stainless steels. However, at ~300 °C in air, the alloy consistently shows a distinctive continuous or secondary hardening, the origin of which is not well understood. The literature survey highlights discrepancies between authors regarding the influence of DSA, nano-twins, and stacking fault–dislocation interactions, all of which have been proposed as possible mechanisms for this behavior. The secondary hardening zone, however, has not been systematically investigated.

In stainless steels, strain rate and waveform have been shown to exert only a negligible influence on fatigue life. For Alloy 690TT, no systematic tests have been performed to confirm whether this trend holds true. The few available studies addressing DSA under cyclic loading were conducted at ~200 °C on solid bar specimens, whereas more data are required at ~300 °C to verify whether the phenomenon exists in Alloy 690TT.

I.5. LOW CYCLE FATIGUE BEHAVIOR IN THE PWR PRIMARY WATER ENVIRONMENT

I.5.1. Characteristics of the PWR Environment

The PWR primary water medium is made up of water at approximately 150 bars and 300°C. Its chemistry (**Table 3**) is particularly controlled and is composed of [Chopra, 2018]:

- Demineralized and deoxygenated water.
- Boric acid, as boron is used for neutron capture and thus be able to correctly control the nuclear reaction.
- Lithium hydroxide to optimize the pH_{300} of the medium at 7 (slightly alkaline) and to minimize the solubility of corrosion products of stainless steels and nickel-based alloys.
- Dissolved hydrogen to neutralize the oxidizing species resulting from the radiolysis of the water.

Properties and Contents	Typical values
Temperature	285 - 350°C
Pressure	150 bar
Dissolved oxygen	< 0.1 ppm
Hydrogen	25-35 cm^3 /kg
Chlorides, Fluorides, Sulphates	<0.15mg/Kg
Boron	1000 ppm ± 10% (By adding boric acid)
Lithium	2ppm ± 10%. (By adding lithium hydroxide)
pH	[6.8-7.4]
Electrical conductivity	2-40 µS/cm

Table 3: Representative properties and chemical composition of the simulated PWR primary water environment used in laboratory fatigue studies [Chopra, 2018].

I.5.2. Effect of PWR environment on fatigue life

The fatigue life of the Alloy 690 is affected by different parameters linked to the primary medium of PWRs.

I.5.2.1. Effect of temperature in PWR environment

The cyclic response and fatigue lives of Alloy 690TT steam generator (SG) tubes tested in low-oxygen water (< 5 ppb DO) under strain-controlled fatigue conditions are presented in **Figure 22**. As shown in **Figure 22a**, the maximum stress levels and fatigue life decrease progressively with increasing temperature, with the shortest lives observed at 325 °C. The average fatigue life plotted **Figure 22b** confirms this trend, showing a significant reduction as temperature increases above ~150 °C [Li et al., 2024].

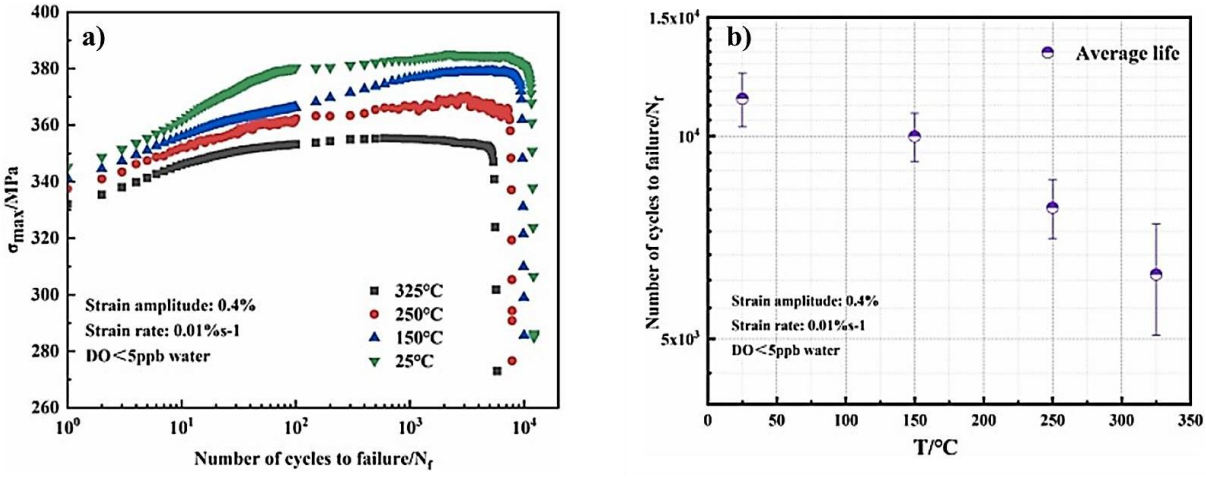

Figure 22: Effect of temperature on the corrosion fatigue behavior of Alloy 690TT steam generator tubes tested in simulated PWR primary water (DO < 5 ppb). (a) maximum cyclic stress evolution at a strain amplitude of 0.4% and strain rate of 0.01 s^{-1} for different test temperatures; (b) average fatigue life as a function of temperature [Li et al., 2024].

Detailed microstructural analyses in this study provided mechanistic explanations for these trends. First, temperature alters the dislocation structure during cyclic loading: at higher temperatures, planar slip bands and entanglements are more prevalent, leading to increased formation of persistent slip bands (PSBs) that act as multiple crack initiation sites [Li et al., 2024, Polák and Man, 2014]. Second, the crack initiation mechanism changes with temperature: at lower temperatures, initiation is governed primarily by PSBs and local stress concentrations, whereas at higher temperatures, it follows an oxide film rupture–PSB dissolution mechanism [Li et al., 2024]. Third, the fatigue crack propagation rate is also accelerated at elevated temperatures due to the combined effects of slip dissolution and local plasticity. Based on these

results, a model was proposed in which the environmental effect on fatigue life is negligible below 100 °C, while between 100 °C and 325 °C the life decreases exponentially with increasing temperature [Li et al., 2024].

These observations highlight the strong temperature sensitivity of Alloy 690TT under PWR-simulated water environments. However, it remains to be verified whether such mechanisms and quantitative trends are transferable across different specimen geometry, loading histories, and strain rates representative of in-service PWR conditions. This point is especially relevant because NUREG/CR-6909 rev-1 [Chopra, 2018] was largely established from fatigue data on austenitic stainless steels, with only limited tests available for nickel-based alloys such as Alloy 690TT. As a result, the applicability of the NUREG environmental penalty factors (Fen) to Alloy 690TT remains uncertain and requires further dedicated testing.

I.5.2.2. Effect of strain rate

The impact of strain rate on the fatigue life of Alloy 690 is illustrated in **Figure 23**. Lowering the strain rate under PWR conditions results in a linear decrease in the fatigue life of both alloys 690 and 600, owing to the influence of the environment on the fatigue damage.

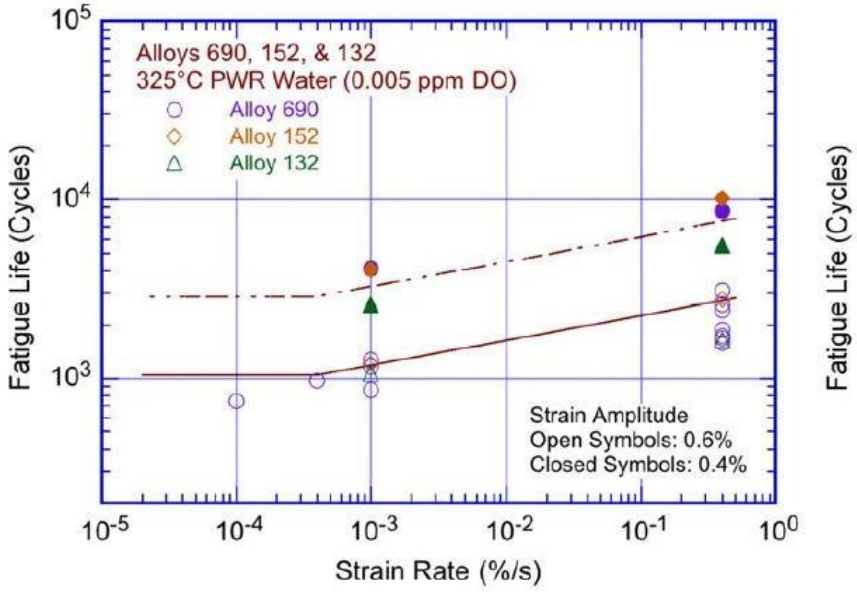

Figure 23 : Influence of strain rate on the fatigue life in PWR environment [Chopra, 2018].

Furthermore, a saturation in strain rate effect is observed on stainless steels for very slow strain rate ($\dot{\varepsilon} < 10^{-5}$ %/s) [Chopra, 2018, de Baglion, 2011]. Since very few tests have been performed on Alloy 690 (only one point at $\dot{\varepsilon} = 10^{-4}$ %/s, **Figure 23**), no saturation level has been properly

defined [Chopra, 2018]. In NUREG/CR-6909, the current threshold for strain-rate effects is defined as $\dot{\varepsilon} \leq 5\%$ /s, based on experimental data for austenitic stainless steels. Whether this threshold is directly applicable to Alloy 690TT in simulated PWR conditions remains to be experimentally verified.

I.5.2.3. Effect of strain amplitude

The fatigue life of Alloy 690 decreases with increasing strain amplitude, both in air and in PWR environments (**Figure 24**), as higher amplitudes impose greater cyclic plasticity and accelerate crack initiation and growth. While this general trend is well established, current studies do not provide clear evidence that the sensitivity to strain amplitude differs significantly between air and PWR water. Reported reductions in fatigue life in PWR environments therefore appear to be mainly associated with environmental effects superimposed on the plastic strain damage, rather than a fundamentally different strain-amplitude dependence [Chopra, 2018]. Further investigations are required to confirm whether Alloy 690TT exhibits any distinct amplitude–environment interaction.

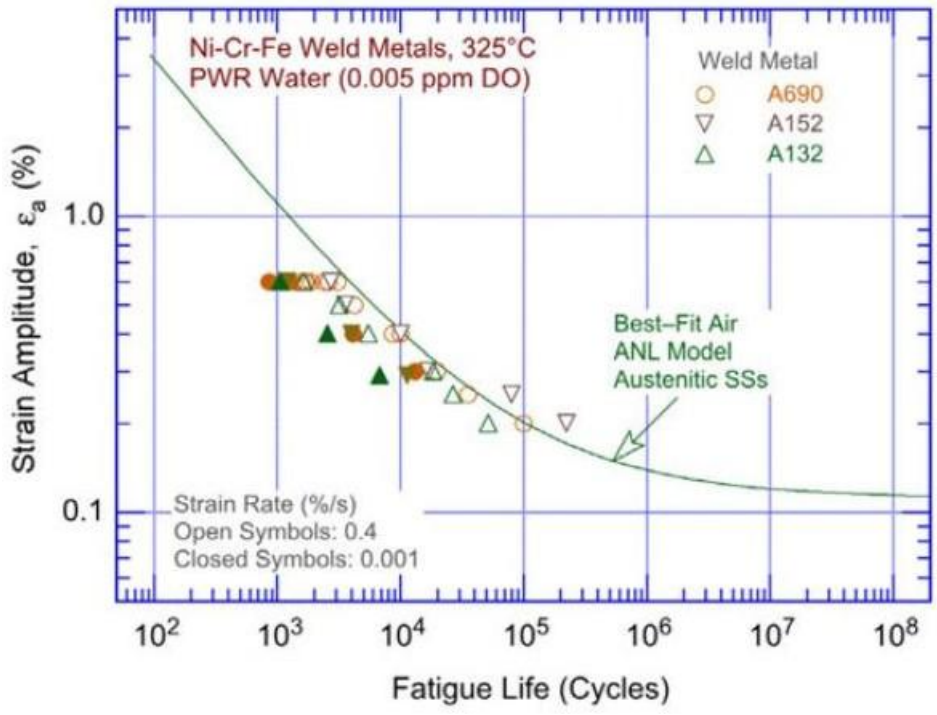

Figure 24 : Influence of Strain amplitude on the fatigue life of Alloy 690 in PWR environment [Chopra, 2018].

I.5.2.4. Effect of Dissolved Oxygen

The presence of dissolved oxygen within the environment where Alloy 690 operates can have a pronounced impact on its fatigue life. One of the primary consequences is the facilitation of corrosion. In the presence of dissolved oxygen, Alloy 690's surface is susceptible to the formation of oxides, which can compromise the material's surface integrity. These oxides may introduce stress concentrations, leading to localized corrosion [TAN ET AL., 2014, XIAO ET AL., 2015]. Such localized corrosion sites can act as initiation points for fatigue cracks, effectively accelerating the rate of fatigue damage. This phenomenon becomes particularly critical when Alloy 690 components are exposed to cyclic loading in oxygen-rich environments [Zhang et al., 2011].

However the research performed by Tan et al [Tan et al., 2016b] shows a contrasting result. The **Figure 25** illustrates the relationship between Fen (environmental factor) defined as the ratio of the number of cycles to failure in air to the number of cycles to failure in PWR environment **(I.5.2.6)**, at 325 °C and a strain rate of 0.001 %·s^{-1}, the average environmental correction factor (F_{en}) at DO = 10 ppb is ~1.59× higher than at DO = 200 ppb (**Figure 25a**). This is consistent with the boat-shaped specimens, whose fatigue life at high DO (200 ppb) is ~1.35× that obtained at low DO (10 ppb) (**Figure 25b**). Thus, within 10–200 ppb DO, increasing DO reduces the environmental penalty (lower F_{en}) and yields longer life for Alloy 690TT under these test conditions. A possible explanation is that higher dissolved oxygen levels promote the formation of a more stable chromia-rich oxide surface layer on Ni–Cr alloys, thereby reducing slip dissolution processes at the crack tip. In contrast, low-DO or hydrogenated conditions may favor less protective oxide films and/or hydrogen-related effects [Xu and Shoji, 2015]. Although dissolved hydrogen (DH) is known to influence oxide structure and stress corrosion cracking behavior in austenitic alloys, its role in corrosion fatigue has not yet been clearly established. In the absence of controlled DH data, it remains difficult to distinguish between ‘low-oxygen’ and ‘hydrogenated’ water conditions in corrosion-fatigue testing, underlining the need for dedicated investigations [Chopra, 2018],.

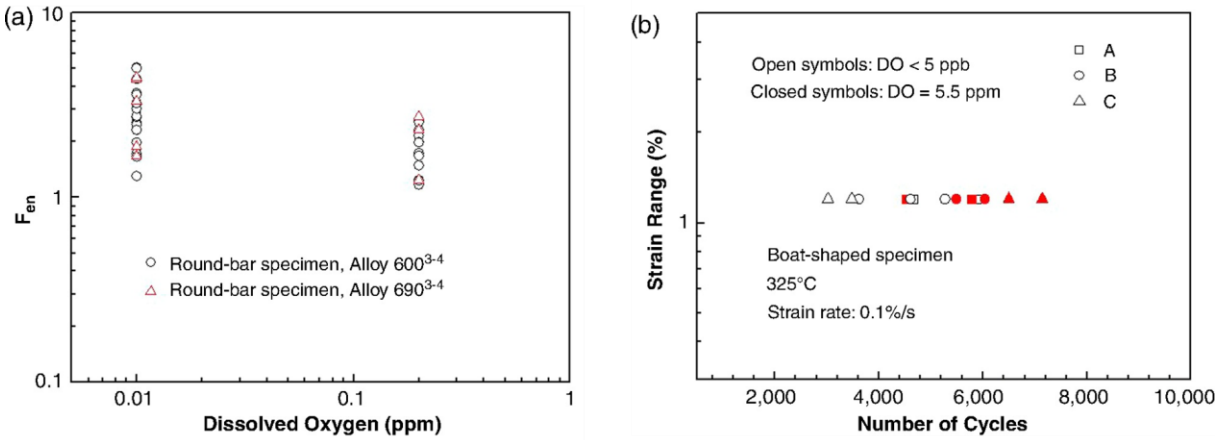

Figure 25: (a) Environmental fatigue correction factor (Fen) as a function of dissolved oxygen concentration in Alloy 600 and Alloy 690 round-bar specimens, (b) Fatigue life of Alloy 690 boat-shaped specimens tested at 325 °C under a strain rate of 0.1%/s, comparing low (< 5 ppb) and higher (5.5 ppm) dissolved oxygen concentrations [Tan et al., 2016a].

I.5.2.5. Effect of dissolved hydrogen

Dissolved hydrogen is critically important in stress corrosion cracking (SCC) of Alloy 690 in PWR environments because it controls the corrosion potential, maintaining reducing conditions that stabilize the protective passive film on the alloy surface. In EAF, the effect of dissolved hydrogen and thus the corrosion potential of the material is not clear. It is worth noting that the environmental fatigue penalty factor F_{en} does not take into account dissolved hydrogen as an influencing factor. However, it has been mainly established for austenitic stainless steels, and its applicability to nickel-based alloys such as Alloy 690 remains less well validated.

The **Figure 26** presents the relationship between dissolved hydrogen concentration (in cc/kg) and the fatigue life (in number of cycles) for Alloy 690 (black squares) and Alloy 52M (red circles) tested in simulated PWR primary water at 310 °C. The tests were conducted at a strain rate of 0.04%/s and a strain amplitude of 0.4%, representing LCF conditions relevant to nuclear plant components.

For Alloy 690, the fatigue life remains significantly lower compared to Alloy 52M across all hydrogen concentrations, generally ranging between ~4,000 and ~6,500 cycles. While the variation with hydrogen content appears minor, the overall negative influence of dissolved hydrogen is reflected in the fact that all Alloy 690 results lie well below the fatigue life predictions established by the Argonne National Laboratory (ANL) and JSME, plotted as horizontal dashed lines [Jang et al., 2013]. This indicates that, under these conditions, hydrogen

reduces the low-cycle fatigue resistance of Alloy 690. It should be noted, however, that these results concern general Alloy 690 and not specifically the thermally treated (TT) version.

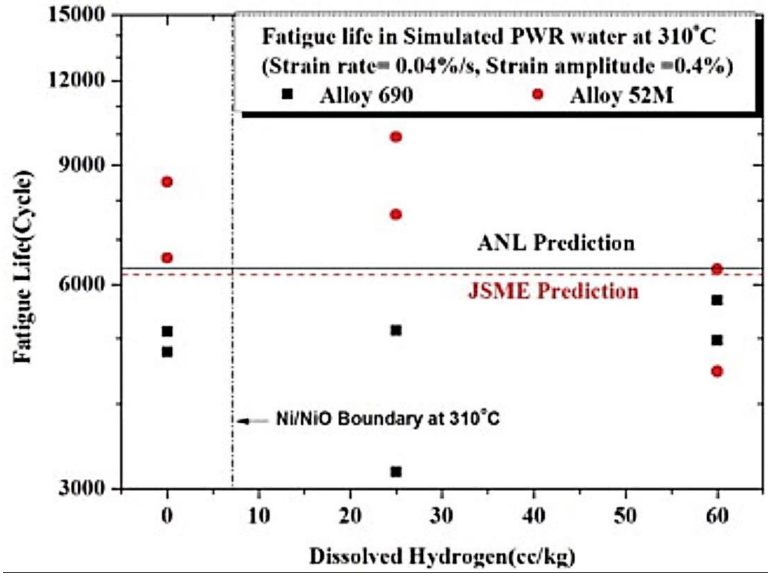

Figure 26 : Effect of dissolved hydrogen on the fatigue life of Alloy 690 [Jang et al., 2013].

I.5.2.6. Fatigue design curve in PWR environment

Environmental correction factor (F_{en})

The impact of the PWR environment on the fatigue durability of stainless steels and Ni-Cr-Fe alloys was described in terms of the F_{en} in the NUREG CR-6909 rev1 [Chopra, 2018]. However, due to limited available fatigue data, a dedicated fatigue life model specifically for Ni-Cr-Fe alloys, including Inconel 718, in LWR (Light Water Reactor) environments could not be developed. Additional data is necessary to establish a more precise F_{en} model.

Nonetheless, the environmental effect data available for these alloys exhibited similar trends as observed in austenitic stainless steels. Thus environmental effects were found to increase with higher temperatures and lower strain rates. Based on the existing fatigue ε-N data, the temperature effect was considered insignificant below 50°C and saturated at 325°C [Chopra, 2018]. A maximum temperature limit of 325°C was selected to encompass most anticipated LWR operating conditions. This is suitable for the expected operating LWR conditions, considering the use of average temperature. Similarly, the effects of strain rate were deemed insignificant at strain rates exceeding 5%/s and reached saturation at 0.0004%/s. Thus, the F_{en}

relationship for Ni-Cr-Fe alloys was expressed [Chopra, 2018] as the ratio of fatigue life in air

$$F_{en} = \frac{N_{air}}{N_{pwr}} = \exp(-T^* \dot{\varepsilon}^* O^*) \quad \textbf{Eq. I.10}$$

at room

temperature (25°C) to that in water at the service temperature as below,

where T*, ε̇*, and O* are transformed temperature, strain rate, and DO, respectively. The functional forms for these transformed parameters were obtained from the best fit of the experimental data and were defined as follows:

T* = 0	(T < 50°C)
T* = (T-50)/275	(50°C ≤ T ≤ 325°C)
ε̇* = 0	(ε̇ > 5.0%/s)
ε̇* = ln (ε̇/5.0)	(0.0004%/s ≤ ε̇ ≤ 5.0%/s)
ε̇* = ln (0.0004/5.0)	(ε̇ < 0.0004%/s)
O* = 0.06	(NWC BWR water (i.e., ≥ 0.1 ppm DO))
O* = 0.14	(PWR or BWR water (i.e., < 0.1 ppm DO)

It can be noticed that these equations from the NUREG/CR-6909 [Chopra, 2018] formed the basis for the French RCC-M environmental fatigue assessment procedure. However, rather than a direct adoption, RCC-M integrated the F_{en} approach into its design methodology and introduced specific adaptations, particularly for the austenitic stainless steel design curve.

The **Figure 27** shows how the fatigue design curve in a PWR environment is obtained by applying the F_{en} to the design curve in air. While the design curve in air already accounts for material scatter and loading conditions, the presence of primary water further reduces the allowable fatigue life. This downward shift reflects the environmental penalty specific to PWR conditions, where temperature, strain rate, and dissolved oxygen accelerate fatigue damage. Although this approach was first validated for austenitic stainless steels, its direct transferability

to Ni-Cr-Fe alloys such as Alloy 690TT remains less well established, underlining the need for additional dedicated data.

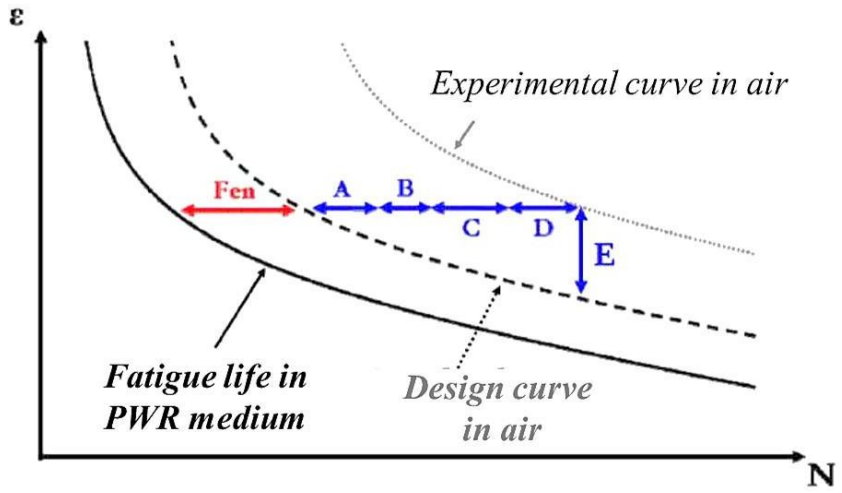

Figure 27: Design approach accounting for the environmental correction factor F_{en} in PWR environment.

I.5.3. Effect of PWR environment on fatigue crack initiation and propagation

I.5.3.1. Crack Initiation

Effect of TiN inclusion on fatigue crack initiation

The presence of inclusions in the alloy can significantly influence its mechanical properties and fatigue behavior in PWR environment. Large inclusions in particular are known to be preferential sites for fatigue crack initiation, potentially reducing the fatigue strength. The study by Tan et al. [Tan et al., 2014c] introduces a revised dislocation dipole accumulation model to explain fatigue crack initiation at TiN inclusions in Alloy 690 (**Figure 28**).

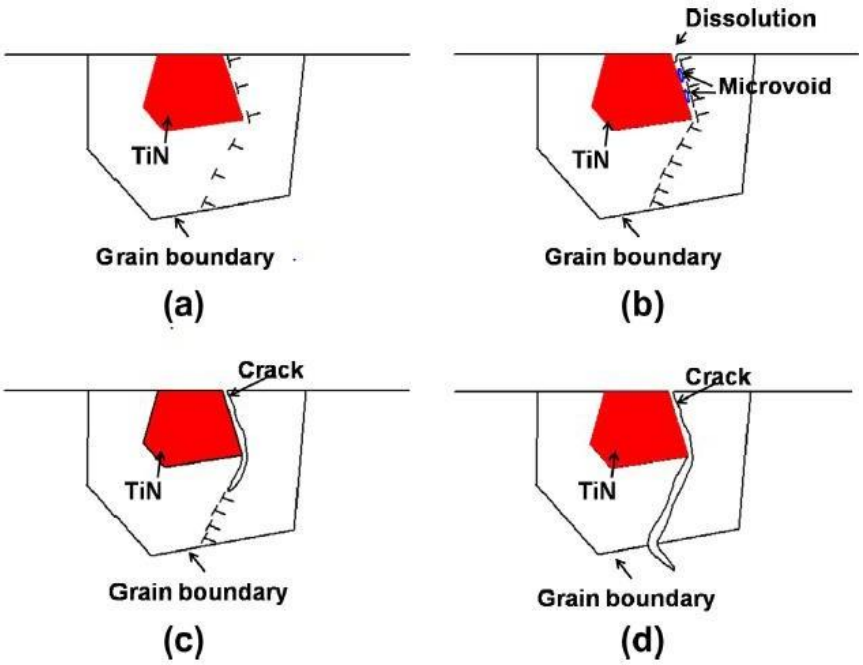

Figure 28 : Schematic of fatigue crack initated at large TiN inclusion on the surface [Tan et al., 2014c].

In this model, dislocations within the matrix are blocked by TiN inclusions, leading to the formation of microvoids at the inclusion/matrix interface due to cyclic loading. Meanwhile, the matrix surrounding the TiN inclusions accumulates dislocations and experiences plastic strain, increasing its electrochemical activity. This electrochemical activity results in the selective dissolution of the matrix in high-temperature water. As a result, the TiN inclusion eventually debonds from the metal matrix. The fatigue crack initiates along the interface and propagates along slip bands, changing direction when encountering grain boundaries [Tan et al., 2014c]. Clusters of fractured TiN inclusions, particularly those situated just beneath the surface, can act as preferential sites for fatigue crack initiation.

Environment-Dependent Crack Initiation Mechanisms in Austenitic Stainless Steels and Alloy 690TT

Fatigue crack initiation in austenitic stainless steels strongly depends on the environment. In air, initiation is linked to the modification of surface roughness by the emergence of three-dimensional dislocation structures on the most highly stressed grains. Cracks typically form along the most activated slip systems, corresponding to grains with the highest Schmid factors, as is common in FCC alloys [Huin, 2013, Poulain, 2015]. Vacuum tests on 304L further confirm this mechanism by eliminating oxidation effects, showing that crack initiation is controlled by slip activity rather than surface chemistry [de Baglion, 2011, Poulain, 2015]. Although some

oxidation occurs at the free surface, it does not significantly affect the underlying microstructure [Huang et al., 2013]. By contrast, in pressurized water reactor (PWR) primary water, initiation occurs at the metal–oxide interface. Here, the local growth and rupture of the passive Cr-rich film is promoted by dislocation activity and micro-twinning, leading to crack initiation. In both environments, initiation remains predominantly transgranular (>80%) on grains with Schmid factors above 0.41, showing that active slip is a key prerequisite, regardless of environment. However, in PWR primary water, cracks tend to reorient rapidly: after a short stage of growth along planes, they transition to directions perpendicular to the loading axis [Huin, 2013] (**Figure 29**).

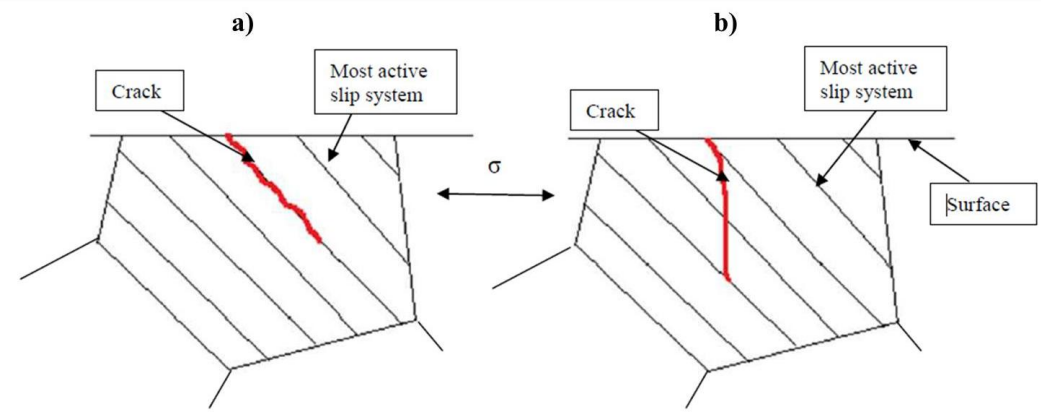

Figure 29: Crack initiation in austenitic SSs a) along emerging shearbands in air environment, b) along emerging shear bands and early transitioning at 90° from the surface in PWR primary environment [Huin, 2013].

The case of Alloy 690TT in high-temperature water environments shows both similarities and added complexity due to its corrosion resistance mechanisms. Recent work by Li et al [Li et al., 2023b] revealed that chromium from the inner oxide film undergoes continuous dissolution into solution during high-temperature oxidation. This conclusion was supported by cross-sectional TEM/EDS analyses of oxide films prepared by FIB, which revealed chromium-rich inner oxides adjacent to chromium-depleted alloy regions, together with Raman spectroscopy identifying $NiFe_2O_4$ and NiO in the outer oxide. The compositional gradient indicated that chromium diffuses outward and dissolves into the high-temperature water as CrO_4^{2-}, leading to continuous depletion of chromium from the inner oxide film during oxidation. The chromium loss lowers the local corrosion resistance and destabilizes the passive protection. Under cyclic mechanical loading, slip bands and persistent slip bands (PSBs) emerge as preferential sites for crack initiation. Their high dislocation density increases electrochemical activity, making them

prone to oxidation [Li et al., 2023b, Xiao et al., 2015]. As the oxide film grows within PSBs, stresses build within the film until rupture occurs, exposing fresh alloy to the aggressive aqueous environment. This rupture–repassivation cycle forms local corrosion couples and accelerates localized dissolution, providing the precursor for corrosion fatigue crack initiation (**Figure 30**).

Taken together, these studies demonstrate that in both austenitic stainless steels and Alloy 690TT, crack initiation is driven by the interplay between local slip activity and surface oxide dynamics. While in air environments initiation generally follows slip band emergence with minimal oxidation effects, in aqueous environments such as PWR water, the stability and rupture of Cr-rich oxides become decisive, leading to environmentally assisted crack initiation mechanisms coupled with plasticity.

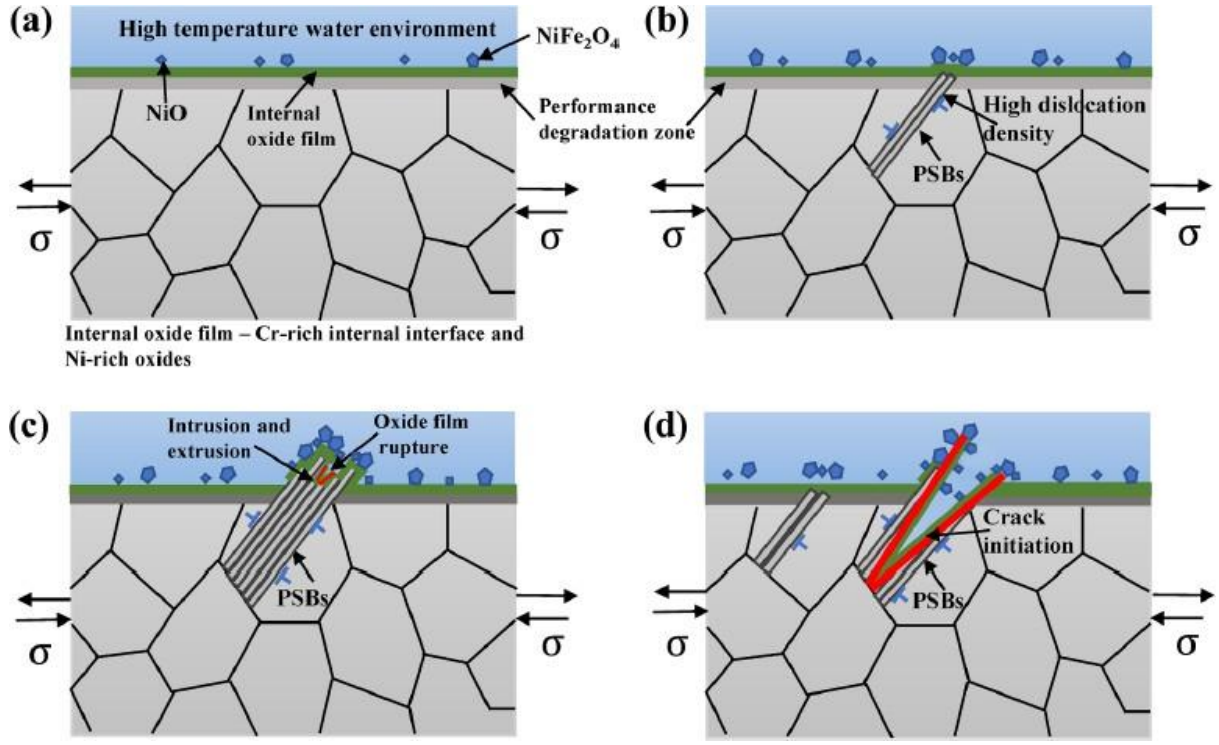

Figure 30 : Schematic diagram of microstructure degradation and corrosion fatigue crack initiation of Alloy 690TT in high temperature water: degradation of surface performance (a) surface oxidation and (b) slip bands or PSBs formed on the surface, (c) oxide film rupture at extrusion of PSBs, (d) deformed matrix dissolved and initiated cracks [Li et al., 2023b].

I.5.3.2. Crack Propagation

Effect of TiN inclusion on fatigue crack propagation

The presence of inclusions, especially the largest ones, can affect the fatigue crack growth rate in materials like Alloy 690 [Tan et al., 2014c]. Studies have shown that inclusions decrease the resistance to void nucleation and reduce the fracture toughness, leading to a reduction in critical crack size and decreased fatigue life [Dutta et al., 2007, Meng et al., 2010, Tan et al., 2014c]. In high-temperature water environments, the interaction between electrochemical factors and inclusions can further accelerate fatigue crack growth. For instance, the presence of sulfide inclusions can lead to the release of sulfur and sulfur-anions, which, in turn, may retard re-nucleation and repassivation after oxide film rupture, promoting anodic dissolution and hydrogen uptake [Tan et al., 2014c].

While TiN inclusions in austenitic alloy or low alloy steel are stable and do not dissolve in high-temperature water, their misfit with the matrix makes them stress concentration sites and preferential sites for hydrogen uptake. The absorbed hydrogen promotes Hydrogen Enhanced Localized Plasticity (HELP), a mechanism whereby hydrogen reduces the resistance to dislocation motion, facilitating dislocation glide and multiplication [Birnbaum and Sofronis, 1994].This localized softening accelerates the formation of voids and microcracks at inclusion–matrix interfaces or leads to their decohesion under cyclic loading (**Figure 31**) [Meng et al., 2010]. The linkage between voids/microcracks and the main crack ahead of the crack tip can enhance fatigue crack growth. In summary, the presence of inclusions, their interaction with hydrogen and oxygen, and their impact on stress concentrations collectively contribute to the acceleration of fatigue crack propagation in high-temperature water environments for materials like Alloy 690TT.

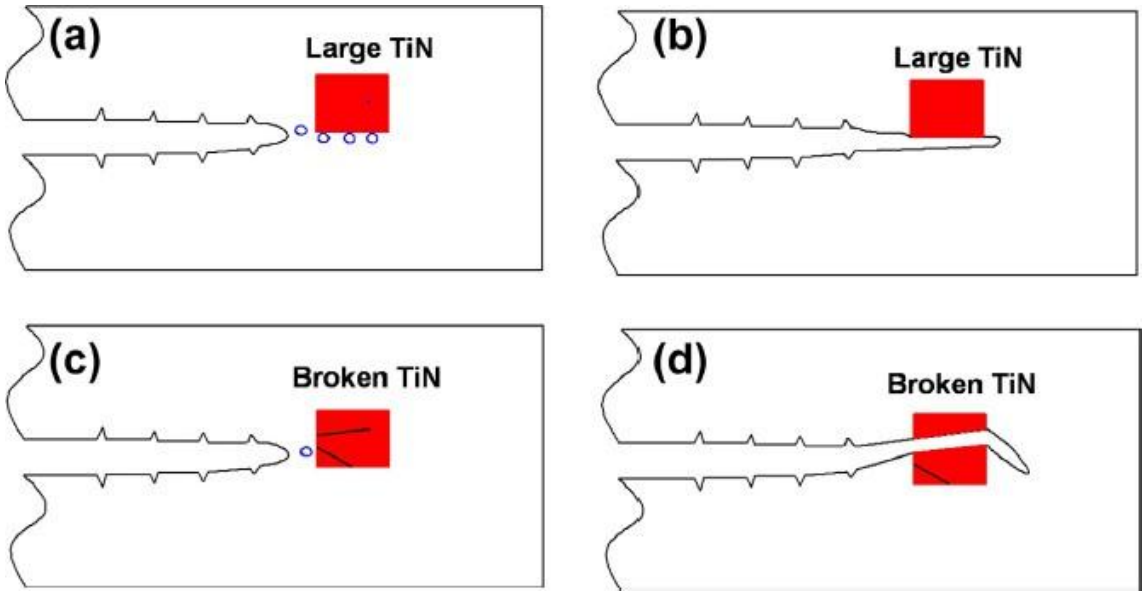

Figure 31 : Schematic representation of the role of the TiN inclusion on the fatigue crack propagation in Alloy 690 (a) Interaction of a propagating crack with a large TiN inclusion, showing stress concentration at the interface, (b) Crack bypassing a large TiN particle, leading to local deflection of the crack path, (c) Interaction of a propagating crack with a broken TiN inclusion, where cracks nucleate from the fractured particle, (d) Crack deflection and acceleration after crossing a broken TiN inclusion, demonstrating the role of fractured inclusions in promoting crack advance [Tan et al., 2014c].

I.5.3.3. Hydrogen embrittlement in austenitic alloys in PWR environment

In a study performed by Vainionpää et al. [Vainionpää et al., 2025], the authors highlight that hydrogen present in simulated PWR primary water plays a critical role in the EAF of 316L stainless steel by interacting with plastic deformation. Hydrogen, generated from corrosion reactions can absorb and diffuse interstitially into the alloy and accumulate at defects such as grain boundaries, dislocations, and deformation bands. This uptake affects the deformation substructure in several ways: (i) it reduces the stacking fault energy, widening the distance between partial dislocations and restricting cross-slip, which promotes planar slip and the emergence of pronounced slip steps that rupture the passive film; (ii) due to the slight difference in diffusivity between the austenite matrix and deformation bands, hydrogen tends to localize at these interfaces, weakening atomic bonding and promoting micro-crack nucleation under cyclic loading; and (iii) hydrogen can sharpen crack tips, allowing cracks to grow even before maximum load is reached, thereby enhancing fatigue crack growth rates. These combined effects explain why specimens tested in PWR water exhibited up to an order of magnitude more localized plastic deformation beneath fatigue cracks compared to air, with extensive shear

bands, ultrafine grains, and multiple secondary cracks. Collectively, the results demonstrate that the synergy between hydrogen uptake and localized plasticity drives the acceleration of crack initiation and propagation in PWR environments.

I.5.4. Summary of LCF of Alloy 690 in PWR environment and knowledge gaps

In the PWR environment, even the Fen environmental correction factors for Alloy 690TT in the NUREG reports are mainly derived from data on austenitic stainless steels rather than from Alloy 690 itself, raising questions about their applicability. Reliable fatigue life data for Alloy 690TT in PWR water are scarce, and no evaluation of the influence of strain rate has been carried out, even though this parameter is known to affect environmental fatigue. Moreover, most published results concern tubular geometries, while very limited data exist for round-bar specimens [Li et al., 2022, 2023b, Tan et al., 2014c, 2016b]. This lack of geometry-dependent data makes it difficult to generalize the fatigue response of Alloy 690TT. In addition, no fatigue studies in vacuum have been reported, although such tests are essential to establish a true baseline free of environmental effects against which air and PWR results can be compared. The influence of dissolved hydrogen on fatigue, although well established in the context of stress corrosion cracking, has not been clarified under fatigue loading conditions. Furthermore, while thermal aging is known to induce significant microstructural evolution in Alloy 690TT, its interaction with fatigue in PWR conditions remains unexplored.

I.6. OBJECTIVES OF THE THESIS

From the review presented above, several gaps in the current understanding of Alloy 690TT behavior have been identified. Although its fatigue properties have been partly investigated, especially in air, reliable data in PWR primary water remain scarce, and no systematic baseline studies in vacuum have been carried out to isolate purely mechanical effects from environmental contributions. This raises the need to better quantify the intrinsic fatigue resistance of the alloy and to clarify the penalizing role of the PWR environment.

Another open question concerns the unusual continuous hardening observed around 300 °C. While mechanisms such as dynamic strain aging (DSA), nano-twinning, and dislocation–fault interactions have been proposed, no clear microstructural evidence has yet been established. Understanding the physical origin of this phenomenon is essential to explain Alloy 690TT's distinct cyclic behavior compared to austenitic stainless steels.

In parallel, the long-term stability of the microstructure under service conditions remains insufficiently characterized. Thermal aging at ~420 °C is known to promote carbide coarsening, changes in precipitate distribution, and potentially the formation of short-range ordering (SRO). However, the kinetics and quantitative impact of these evolutions on mechanical properties are still not well defined.

Finally, how thermal aging influences fatigue performance under air and PWR conditions remains largely unexplored. Establishing links between microstructural changes (precipitate evolution, SRO) and macroscopic behavior (cyclic behavior, fatigue life) is a crucial step toward more accurate predictions of long-term behavior of alloy 690TT.

On this basis, the present thesis aims to (i) characterize the fatigue behavior of as-received Alloy 690TT in vacuum, air, and PWR environments, (ii) investigate the origin of continuous secondary hardening at ~300 °C, (iii) quantify microstructural changes during accelerated thermal aging at 420 °C, (iv) correlate these changes with hardness through advanced characterization techniques, and (v) evaluate the impact of thermal aging on fatigue resistance by comparing aged and as-received conditions in both air and PWR environments.

I.7. SUMMARY

- Alloy 690TT is a Ni–Cr–Fe austenitic alloy (Ni >58%, Cr ~30%, Fe ~9%) developed for improved stress corrosion cracking resistance in PWR environments.

- Its thermal treatment (TT) leads to a homogeneous FCC matrix stress-relieved with grain boundary carbides.

- Accelerated thermal aging modifies the alloy's microstructure, leading to carbide coarsening, possible short range ordering (SRO), and diffusion-induced grain boundary migration (DIGM). These microstructural changes are linked to increased hardness, but the relative contribution of carbides and SRO remains unclear.

- At room temperature, Alloy 690TT shows a cyclic hardening/softening response similar to austenitic stainless steels. At ~300 °C in air, Alloy 690TT exhibits continuous secondary hardening, unlike stainless steels, but the mechanisms remain debated and not extensively investigated so far.

- In PWR environments, the F_{en} correction factors for Alloy 690TT in NUREG CR/6909 rev1 report are based on stainless steels, not on Alloy 690, raising concerns about their validity. Fatigue data for Alloy 690TT in PWR are scarce, especially for round-bar specimens.

- No vacuum fatigue studies have been reported allowing the evaluation of the fatigue behavior of Alloy 690TT in absence of any environmental effect.

- The interaction between thermal aging–induced microstructural changes and fatigue behavior in Alloy 690TT under air and PWR conditions remains unexplored.

II. Materials and experimental methods

This chapter presents the material, experimental procedures, and characterization techniques used in this study. It describes the composition and microstructure of Alloy 690TT, the thermal aging treatment applied to simulate long-term service exposure, the fatigue testing conditions in air, vacuum, and simulated PWR environments, and the methods employed for microstructural and damage analysis.

Contents

II.1. MATERIAL: ALLOY 690TT

II.1.1. Composition

The material used for this study is an Alloy 690TT. Its composition given **Table 4** follows the RCC-M (M-4109) and the ASTM B166 requirements [AFCEN. RCC-M, 2022] [ASTM B166, 2023].

Content	C	Si	Mn	P	S	Cr	Ni	Al	Ti	Co	Cu	Fe
RCC- M (M-4109)	0.01-0.04	<0.5	<0.5	<0.015	<0.01	28-31	>58	<0.5	<0.5	<0.1	<0.5	8-11
ASTM (B166)	0.05	<0.5	<0,5	-	<0.015	27-31	>58	-	-	-	<0.5	7-11
Heat no. 335554	0.02	0.28	0.13	0.004	<0.002	28.8	60.7	0.28	0.3	0.01	<0.01	9.36

Table 4 : Chemical composition in wt% of the Alloy 690TT: Values required (RCC-M, ASTM), and measured by ICP-OES (VDM metals, Germany).

II.1.2. Properties of Alloy 690TT

The **Table 5** summarizes the key mechanical properties of Alloy 690TT used in this study at room temperature (RT) and at 350 °C.

Mechanical properties	Measured values
Tensile Strength (RT - 350°C)	608 MPa - 501 MPa
Youngs Modulus (RT - 350°C)	197 GPa – 150 GPa
Yield Strength (0.2%)(RT - 350°C)	269 MPa – 272 MPa
Elongation (RT - 350°C)	57% - 47%

Table 5: Measured mechanical properties of the studied Alloy 690TT.

II.1.3. Microstructure

The solid bar of Alloy 690 used in this study underwent a two-step heat treatment: a mill annealing at 1060 °C for 1 hour, followed by a thermal treatment at 715 °C for 5 hours (**Figure 32**). This process ensured full recrystallization of the matrix during the high-temperature anneal and subsequent carbide precipitation during the thermal treatment.

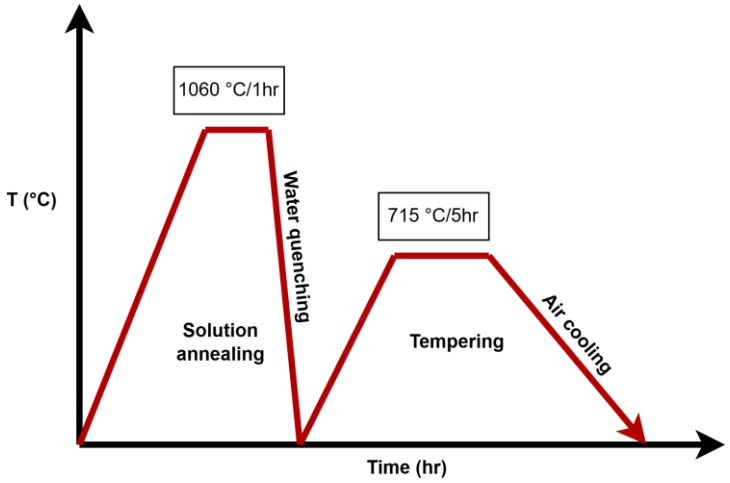

Figure 32 : Heat treatment procedure performed to transform Alloy 690 into Alloy 690TT.

The final microstructure obtained is typical from Alloy 690TT. Indeed, **Figure 33** shows austenitic grains with thermal twins accompanied with TiX titanium inclusions (mostly TiN) and intergranular/intragranular carbides.

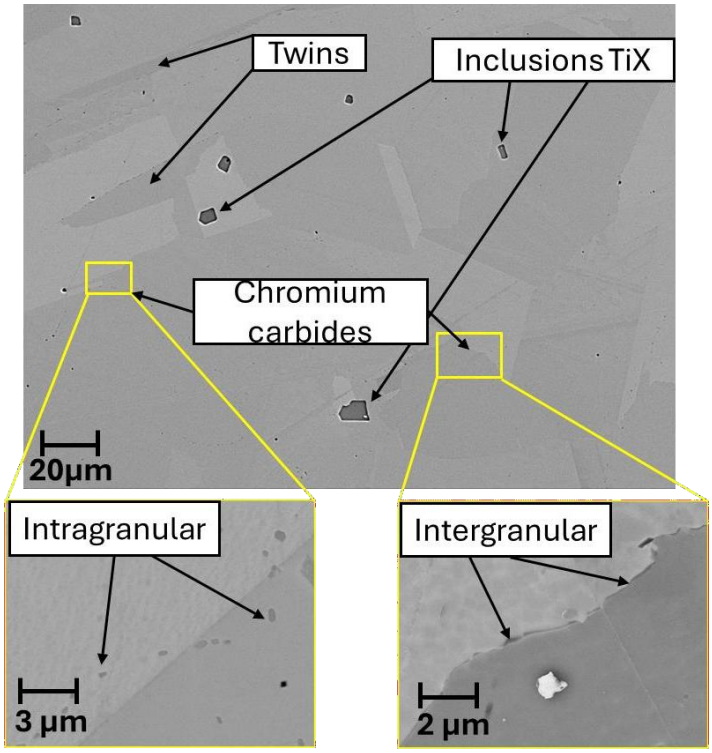

Figure 33 : SEM image of the Alloy 690TT microstructure studied.

EBSD maps of the alloy showed an average grain size of approximately 90 µm and a median grain size of 75 µm (**Table 6**). The grain boundary character distribution revealed a predominance of Σ3 twin boundaries (~84 %), while other coincidence site lattice (CSL) boundaries such as Σ5 (0.1 %), Σ7 (0.2 %), and Σ9 (≈8 %) were comparatively scarce. The high fraction of Σ3 boundaries is characteristic of thermally treated Alloy 690TT.

Sample	Average Grain size (µm)	Median Grain size (µm)	∑ 3 (%)	∑ 5 (%)	∑ 7 (%)	∑ 9 (%)
As-received	90	75	84	0.1	0.2	8

Table 6: Grain size and grain boundary angle of the As-received Alloy 690TT.

II.2. THEMAL AGING PROCEDURE

II.2.1. Accelerated thermal aging

To simulate the thermal aging process corresponding to 325 °C during the 0 to 80-years operating lifetime of a component, an accelerated aging approach was adopted. The aging process was conducted at an elevated temperature of 420°C, which was selected based on a previous study by [Mouginot et al., 2017a] showing the highest hardness during nano-indentation tests (550 HV). The time required for the aging at the elevated temperature can be estimated using the following Arrhenius-type equation (**Eq. I.1**)

where t(T) is the time required for aging (h), t_0 is the reference service time at operating temperature, T is the elevated aging temperature, namely 693K (420°C), T_0 is the operating temperature 598K, (325°C), R is the ideal gas constant (8.3145 $J.mol^{-1}.K^{-1}$) and for the activation energy Q_c, a chromium diffusion energy of 177 kJ/mol along the grain boundary was selected for the Ni-Cr-Fe based alloys, which is compatible with the iron content and the air cooling that follows TT [Huotilainen and Que, 2022, Yoo et al., 2016]. The aging process was conducted for durations equivalent to 10, 20, 30, 40, 50, 60, 70, and 80 years of operation at 325°C. Using the Arrhenius equation, these durations were translated into accelerated aging times at 420°C, as shown in **Table 7**.

Aging time at operational condition: 325°C (in years)	10	20	30	40	50	60	70	80
Aging time at accelerated condition: 420°C (in hours)	700	1400	2000	2700	3400	4000	4700	5400

Table 7: Equivalent aging durations: 325°C (operational) vs. 420°C (accelerated).

II.2.2. Sample preparation and aging environment

The Alloy 690TT samples were machined into pellets with a thickness of 4 mm and a diameter of 20 mm to ensure uniform heating and facilitate microstructural and hardness evaluations. The samples were aged in a high-temperature oven at 420°C under ambient conditions, ensuring precise control of temperature and aging duration for each time interval. The cylindrical bar specimens for fatigue testing were also polished after after aging.

II.3. FATIGUE SPECIMEN AND TESTING PROCEDURES

II.3.1. Fatigue testing in air

The fatigue machine used to perform the tests in air at RT and 300°C is an INSTRON 8862 with a load cell of 100kN and a resistive furnace regulated with 3 thermocouples (**Figure 34a**). The specimens were extracted from an initial round bar of 35 mm diameter. The specimens were machined from an initial round bar of 35 mm diameter. The cylindrical surfaces were then polished according to the surface finish criteria defined for LCF testing of austenitic alloys in the INCEFA-SCALE European program, achieving an average surface roughness of $R_a = 0.172$ µm and a total roughness height of $R_t = 1.929$ µm [Beswick et al., 2025]. The fatigue tests in air were performed on machined specimens with a constant cross-section area of 9 mm diameter in the gauge length of 13 mm (**Figure 34b**). To measure the specimen temperature during the test, two thermocouples were placed at the ends of the gauge length.

All the tests were performed under total strain-controlled conditions at $R_\varepsilon = -1$, meaning that the specimens were subjected to fully reversed tension–compression cycles. This loading mode reproduces the alternating mechanical strains induced by thermal transients in PWR components, where expansion and contraction during heating and cooling impose cyclic deformation rather than pure load control. To measure and control the strain amplitude in the gauge length, a ceramic knives extensometer was used.

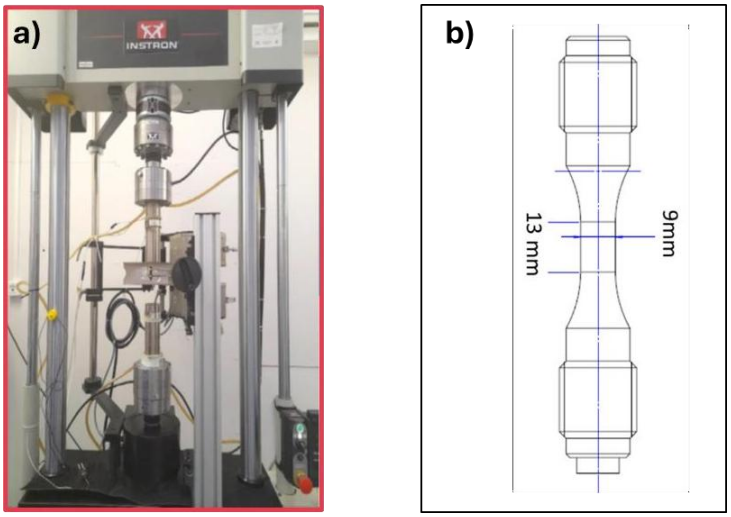

Figure 34: a) Fatigue testing machine in air and the b) specimen geometry associated.

II.3.2. Fatigue testing in the simulated PWR environment

For PWR environment testing, the fatigue tests were performed using a Walter+Bai servo-hydraulic low-cycle fatigue testing machine with a 100 kN load capacity (**Figure 35a**). The specimen used has a cylindrical gauge section (9 mm × 13.5 mm) with two shoulders 39 mm apart, designed to mount an eddy-current extensometer inside the autoclave (**Figure 35b**). This type of extensometer is necessary because no usual ceramic knives extensometer can operate in such demanding conditions (water at 300°C, 150 bar).

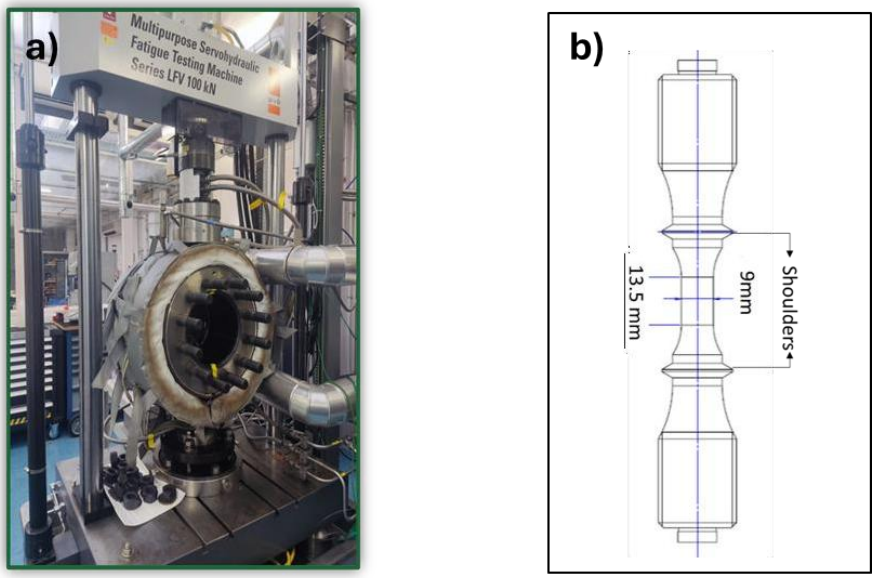

Figure 35: a) Fatigue testing machine in the PWR environment and the b) specimen geometry associated.

To ensure an accurate strain control during the fatigue test given the differences in specimen geometry and extensometer used in air and PWR environment, a transfer coefficient was determined to evaluate the applied strain in the gauge length while applying it at the shoulders.

This was achieved by conducting finite element simulations using CAST3M to simulate the cyclic behavior of Alloy 690TT on both the shoulder and the gauge section geometries of the specimen. The Chaboche constitutive model was utilized to model the cyclic behavior [Chaboche, 1989] of the alloy (**Annexe 1**). Its parameters were obtained by the hysteresis loops at $N_{25}/2$ (N_{25} refers to the number of cycles corresponding to the 25% of the peak stress during the maximum stress evolution) of tests conducted in air at 300°C, considering that the CSS is not affected by environment. However, for this alloy, these loops are not stabilized at this temperature, leading to a tendency to maximize strain at the beginning and minimize it towards the end. As the tests were strain-controlled, a uniaxial force was applied as displacement at the shoulder, with the corresponding displacement measured at the gauge length.

This allowed the derivation of a correction factor known as the "Shoulder to Gauge" (S2G) correction factor. This factor was verified by performing a test with two extensometers, one at the shoulders and one at the gauge length (A detailed explanation of the calculation of the S2G factor from both simulation and experimental methods is provided in the **Annexe 1**, along with the S2G values for each strain amplitudes).

The tests under PWR environment were performed on a dedicated test rig composed of a fatigue machine accompanied by a 11 litres autoclave filled with the PWR primary medium, which consists of a mixture of boric acid (~1000 ppm) and lithium hydroxide (~2 ppm) deaerated (< 1 ppb dissolved oxygen) at 300°C and 140 bar. The pH, conductivity and dissolved oxygen content were measured during all the tests.

In this study, the water was not intentionally hydrogenated, and dissolved hydrogen (DH) was therefore not controlled. However, as the NUREG/CR-6909 Rev.1 [Chopra, 2018] F_{en} formulation for Ni–Cr–Fe alloys considers only temperature, strain rate, and dissolved oxygen as impactful parameters, DH is not supposed to have any impact. The present results thus correspond to low-DO, non-hydrogenated primary water, with DH effects left for future investigation.

II.3.3. Fatigue testing in vacuum

The low-cycle fatigue tests in vacuum were performed using a high-vacuum chamber integrated into a servo-hydraulic fatigue testing machine (**Figure 36a**). The setup was equipped with a

resistive heating system and a temperature controller to maintain the specimen at 300 °C ± 2 °C throughout the test. The chamber operated under a vacuum of approximately 10^{-5} mbar, effectively preventing oxidation and ensuring that the measured response reflected only the intrinsic mechanical behavior of the material. A ceramic knife-edge extensometer was mounted directly on the gauge section to measure the imposed strain with high precision.

Cylindrical Alloy 690TT specimens similar as those tested in air (diameter 9 mm, gauge length 13.5 mm) were tested in total strain control at 300 °C under fully reversed loading ($R_\varepsilon = -1$) (**Figure 36b**). A triangular waveform with constant strain rates of 0.02 %/s and 0.4%/s was applied, and total strain amplitudes ranged from ±0.45% to ±0.6 %.

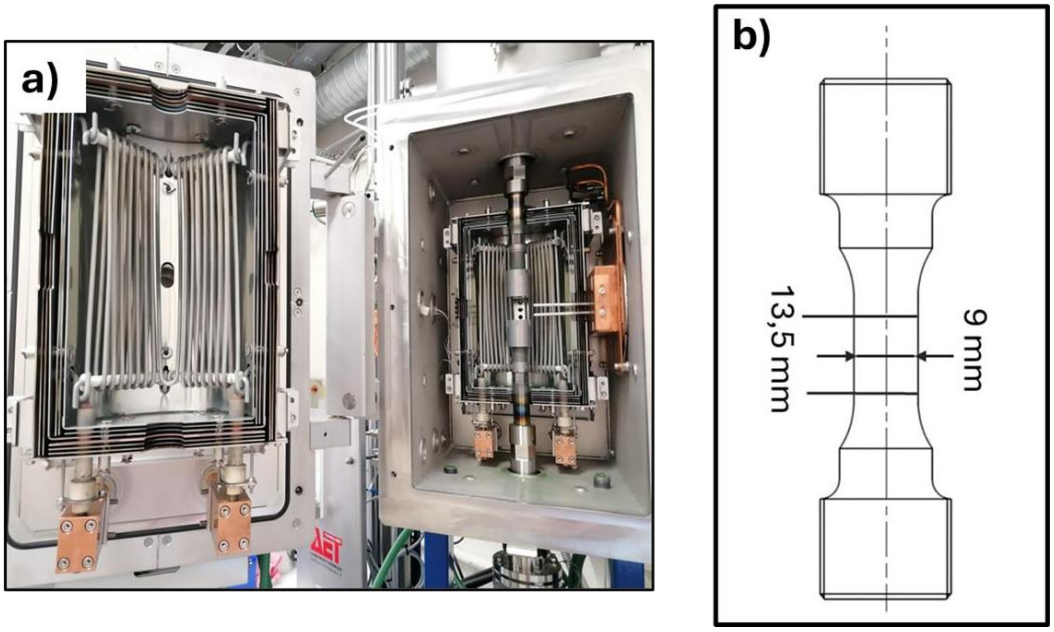

Figure 36: a) Fatigue testing machine under vacuum and the b) Specimen geometry associated.

II.4. MICROSTRUCTURAL AND DAMAGE CHARACTERIZATION

II.4.1. Methods to evaluate microstructural evolutions

II.4.1.1. Scanning Electron Microscopy (SEM)

To investigate the microstructural changes in Alloy 690TT due to thermal aging, Scanning Electron Microscopy (SEM) is employed as a primary characterization technique.

To examine the precipitate evolution in the Alloy 690TT resulting from the accelerated thermal aging, a Scanning Electron Microscopy (SEM) FEG-SEM SIGMA 500 from ZEISS was used. After aging, the material pieces were embedded in a conductive resin for further observation.

They are then polished using a semi-automatic polisher (Mecatech-334). The polishing process commences with coarse abrasive sheets—320, 600, and 1200 grit—followed by polishing with diamond suspensions of 9 µm and 3 µm. The final step utilizes an Optical Polishing Suspension (OPS) to achieve a near-mirror finish. Additionally, a vibratory polisher (Saphir Vibro) is employed for 24 hours to ensure a completely mirror-polished surface, which is essential for high-resolution imaging. A similar polishing protocol is applied to samples meant for microhardness and nano-hardness testing. Throughout the SEM imaging, consistent settings for brightness, contrast, scale, and magnification are maintained across all samples to ensure uniformity and comparability (**Figure 37**).

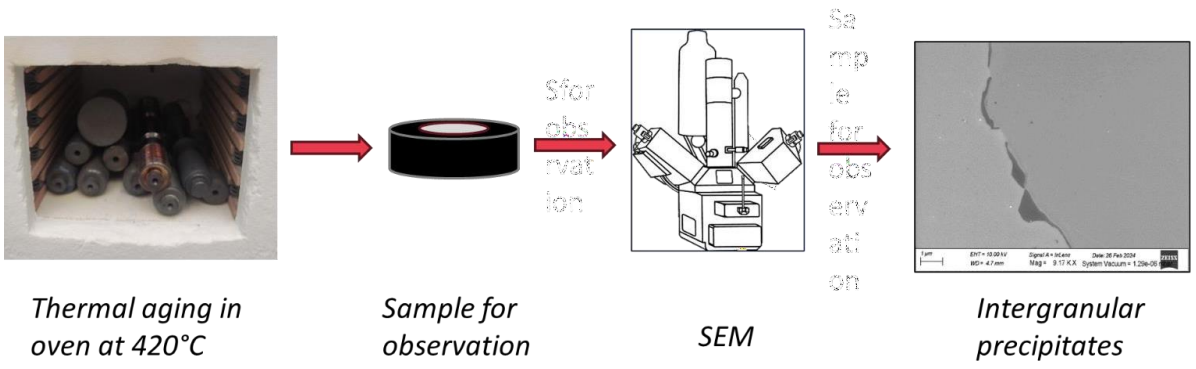

Figure 37: Process for observing intergranular precipitates in Alloy 690TT after thermal aging at 420°C using SEM.

II.4.1.2. Image acquisition and post-processing procedure

The SEM imaging focuses on capturing detailed images of intergranular precipitates around grain boundaries. For each aged sample, representing 10 years of aging, 20 images are systematically taken in a '+' pattern — 10 images in the vertical direction and 10 in the horizontal direction (**Figure 38**). The objective of this imaging pattern is to ensure a statistically representative analysis of the precipitates across the sample. The method helps capture the variability and distribution of precipitates within the microstructure.

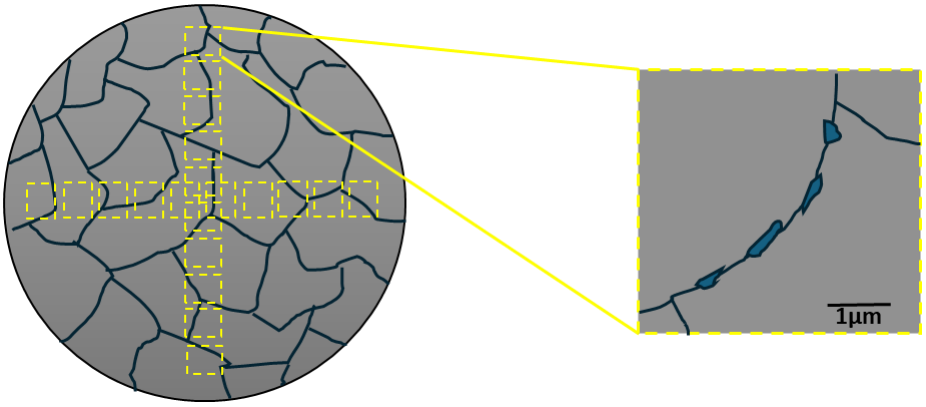

Figure 38 : Representation of image acquisition method using SEM.

The SEM images are thereafter analyzed using the ImageJ software. A semi-automated image processing method has been adopted to quantify the characteristics of the precipitates. Initially, an appropriate threshold is applied to each image to enhance the visibility of the precipitates. Following this, the images are binarized, and any noise present is eliminated manually. Once the noise is removed, the regions corresponding to the precipitates are selected to trace their dimensions (**Figure 39**).

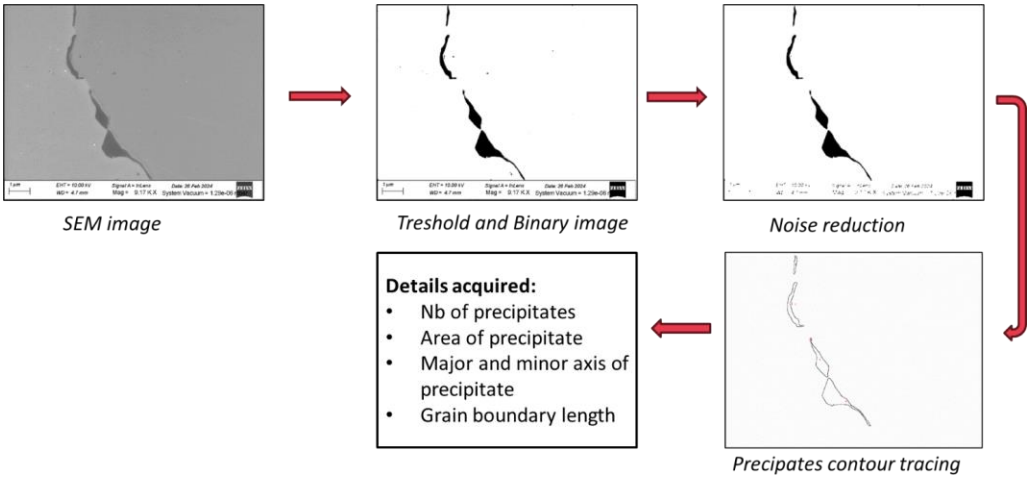

Figure 39: Image processing workflow using ImageJ to characterize the precipitates.

The subsequent post-processing of these images involves several steps. First, the individual areas of the precipitates (μm^2) are measured to monitor their growth over time. Additionally, the number of precipitates is counted to determine their density evolution, i.e., the total number of precipitates per unit length of the grain boundary (nb/µm), and their widths (µm) are measured to evaluate the size distribution. Furthermore, the ratio of the precipitate length to the grain boundary length is calculated to quantify the precipitate length fraction (**Figure 40**).

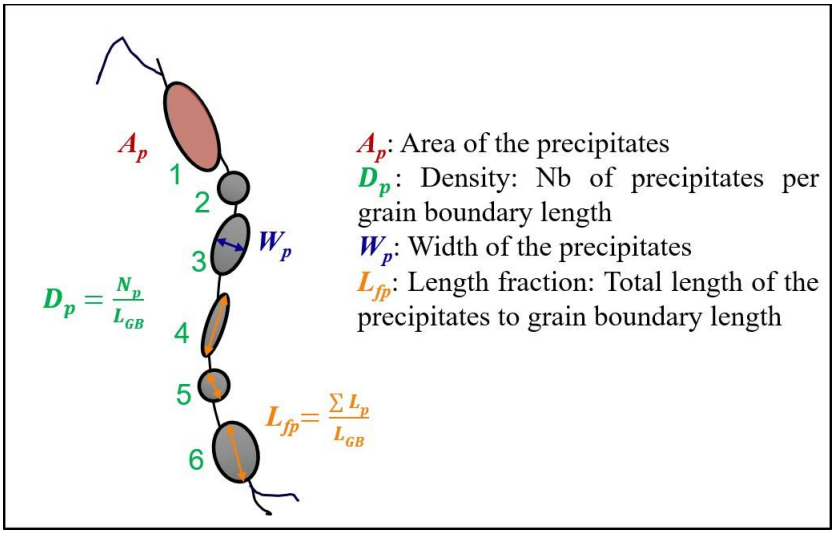

Figure 40 : Schematic of precipitates along a grain boundary, showing their area A_p, density D_p, width W_p, and length fraction L_{fp}.

The **Figure 41** describes the precipitates present within the grains (intragranular precipitates). By analyzing a single grain, the area of the precipitates (µm²) inside the grain and their density is measured by counting the number of precipitates present per scanned area (nb/mm²). To calculate the width and length of the precipitates, they are assumed to be elliptical in shape.

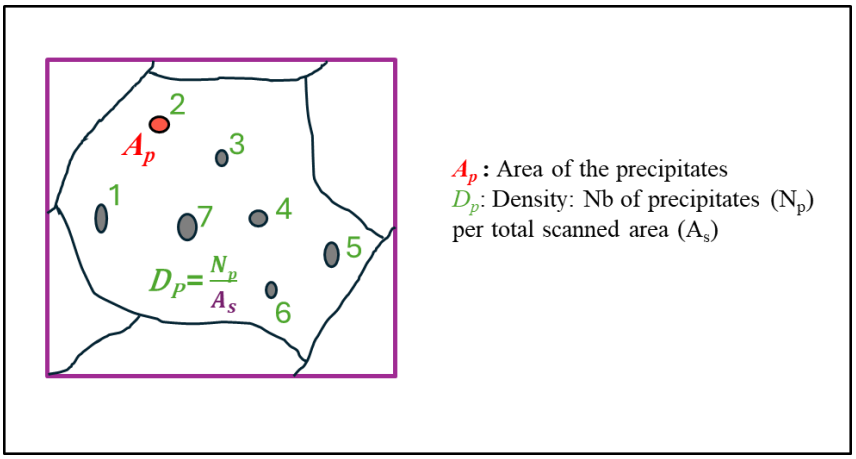

Figure 41 : Schematic of precipitates in a grain, showing their area A_p and density D_P.

II.4.1.3. Electron back scattered diffraction (EBSD)

Electron Backscatter Diffraction (EBSD) was employed to analyze the grain structure and crystallographic orientations of the as-received and thermally aged Alloy 690TT samples. The EBSD measurements were conducted using an eFlash FS detector by Bruker equipped on the SEM. The analysis was carried out at an accelerating voltage of 20 kV with a working distance

of 15 mm. To measure the grain size, approximately 5,000 grains were considered. Plotting the grain size distribution using EBSD data weighted by area fraction was preferred over number fraction, as smaller grains are overrepresented in number fraction due to their higher numbers than larger grains. By using area fraction, the distribution more accurately reflects the mechanical properties, such as strength and ductility, as larger grains contribute more significantly to the mechanical properties of an alloy [Toth et al., 2013]. A threshold of 5 μm grain size was used in this analysis to exclude smaller grains that may represent artifacts or noise from EBSD measurements. Identifying the grains using EBSD also requires defining a critical disorientation angle, so that all boundary segments with an angle higher than this defined critical angle are considered grain boundaries. Therefore, a minimum disorientation angle of 5° was used as recommended by the ASTM E2627 standard.

II.4.1.4. Transmission electron microscopy

To investigate the presence of short-range ordering in the microstructure near the hardened zone identified by nanoindentation, a small section of thermally aged Alloy 690TT was extracted. This section was selected in a region adjacent to the grain boundary (**Figure 42a**) after thermal aging at 420°C for 4,000 hours. Thin foils were prepared using a dual-beam Focused Ion Beam (FIB) system, FEI HELIOS 600, at Centre Castaing, Toulouse. A foil with a thickness of less than 100 nm was extracted from the selected area near the grain boundary by using a current of 5 nA and a voltage of 30 kV (**Figure 42b and c**). The milling process was followed by a low-energy ion polishing step at 5 kV (Figure 42d), which was applied to minimize ion damage and enhance surface quality, ensuring suitability for high-resolution imaging and Selected Area Electron Diffraction (SAED) analysis. The prepared samples were analyzed using a Transmission Electron Microscope (TEM) JEM-2100F from JEOL, operated at 200 kV. SAED patterns were collected from the hardened regions near the grain boundaries to examine the evidence of SRO.

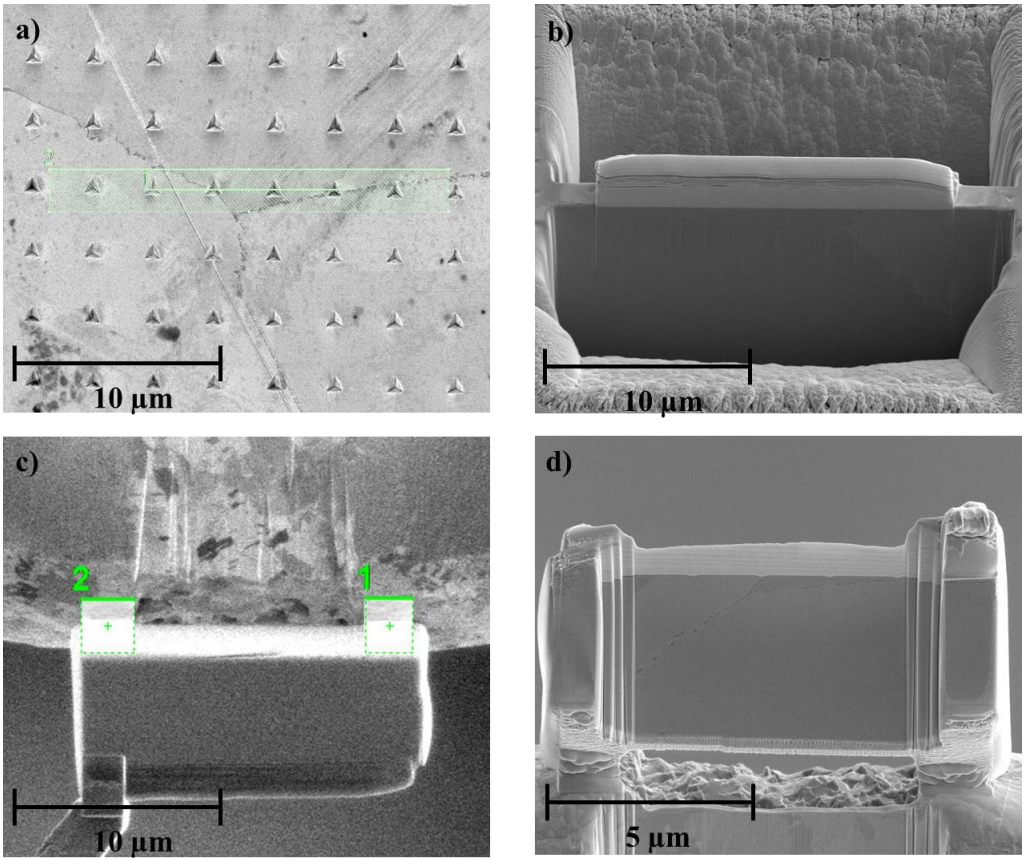

Figure 42: Sample preparation utilizing FIB: a) Area of interest; b) Platinum deposition and excavation around the ZOI; c) Placement of the extracted sample on the holder; and d) Polishing the sample to create a thin foil for TEM observations.

II.4.1.5. Hardness tests

Microhardness testing of the Alloy 690TT was performed using a Vickers hardness testing machine made by BUEHLER, which is equipped with an optical microscope for observing indentations. An indentation load of 100 g was applied for a duration of 15 seconds to ensure consistent indentations. The Vickers geometry was used, and the indentation speed was set at 0.1 N/s. To ensure statistical reliability and minimize measurement variability, at least 12 indentations per sample were performed.

Nano-indentation tests were performed using a nano-indenter from NanoTest Vantage (Micromaterials, UK), which is equipped with a Berkovich diamond tip. The indentations were carried out in displacement control mode, with the maximum penetration depth set to 100 nm to minimize substrate effects and ensure surface-sensitive measurements. The load was applied in a controlled manner to ensure a maximum penetration depth of 100 nm. A 20×20 grid matrix was employed, resulting in 400 indentations per sample. The indentations were spaced 3 µm

apart in both the X and Y directions to prevent interaction of plastic deformation zones. The overall length of the indentation matrix was approximately 60 µm. The hardness values obtained from the 400 indentations were plotted to create a nano-hardness map. The indentations were specifically conducted in regions with two or more grain boundaries as they are the seats of most of the microstructural changes.

II.4.2. Methods to evaluate damage evolution

II.4.2.1. Crack growth rate analysis

The fracture surface of Alloy 690TT specimens tested under LCF was examined using a FEG-SEM ZEISS Sigma 500 to quantify fatigue crack growth rates. To account for the cyclic plastic deformation, the strain intensity factor (ΔK_ε) was adopted instead of the classical stress intensity factor (ΔK_σ) (**I.3.4).**

The correction factor F(a) was determined using the Carpinteri formulation [Carpinteri, 1993], which relates the geometry of a semi-elliptical surface crack to its depth (a) and surface half-length (b) in a round-var sample. To simplify the analysis, the normalized crack depth (a/D, with D = 9 mm) was used instead of a/b, allowing direct evaluation of F(a) from measurable parameters. This approximation provides a conservative yet sufficiently accurate estimation of the strain intensity factor, as the a/D approach generally leads to a slight underestimation compared to the full a/b model while remaining consistent with the specimen geometry.

The da/dN value is obtained from striation spacing measurement. A brief overview of the procedure is given in the next part.

$$F(a) = 0.643 + 0.986\left(\frac{a}{D}\right) - 1.357\left(\frac{a}{D}\right)^2 + 4.172\left(\frac{a}{D}\right)^3 \qquad \textbf{Eq. II.12}$$

Several crack paths are visible on the fracture surface of the specimen (Error! Reference source not found.**(b)**). Only the main crack trajectory (Path 2) is studied to manage the data processing time. Therefore, the crack growth rate in a given specimen is understood to be the crack growth rate of the main crack. Along this main crack, several images of fatigue striations (about a dozen) were taken using the SEM (example: Error! Reference source not found.**(a)**). To minimize the influence of short crack effects and near-surface initiation scatter, striation measurements were considered only beyond a depth of ~200 µm from the free surface.

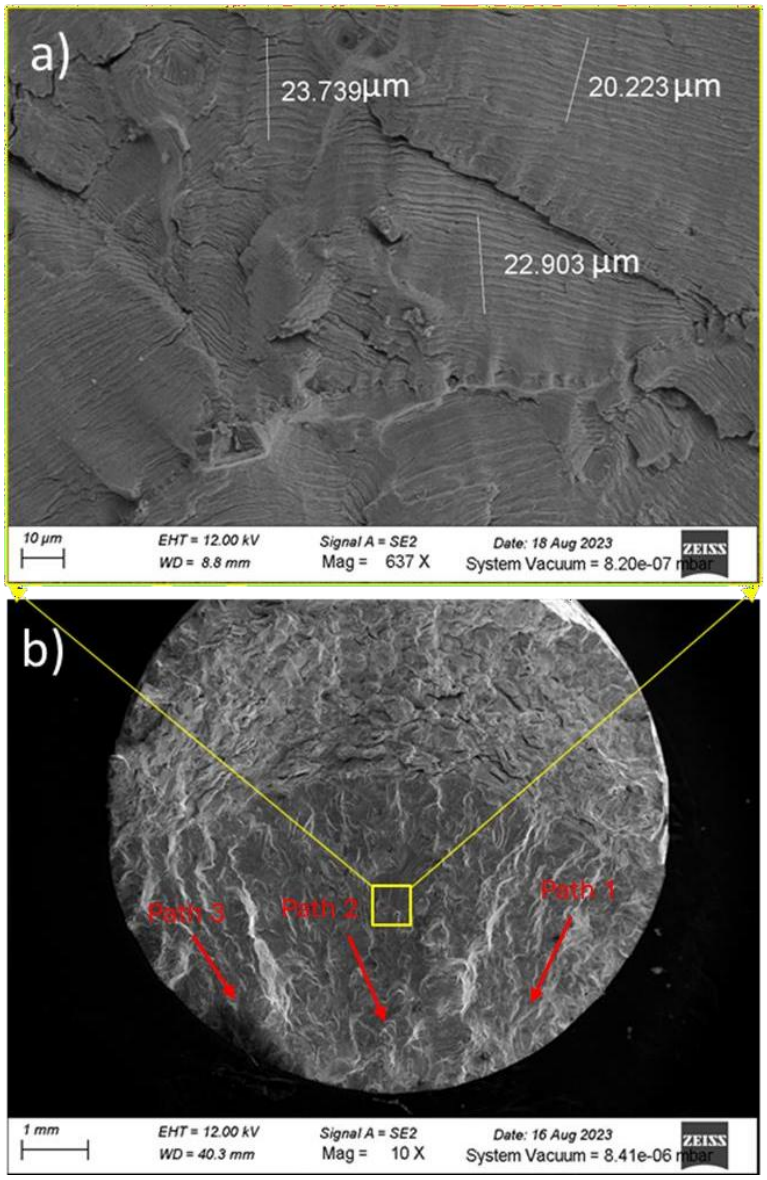

Figure 43: Morphology of a fracture surface and the striation measurements of test in air for a strain amplitude of 0.3%, strain rate of 0.02%/s at 300°C.

In this analysis, the assumption that one striation corresponds to one loading cycle has been considered. This means that each visible striation on the fracture surface is taken to represent a single loading cycle, thereby simplifying fatigue crack growth rate analysis. While this hypothesis provides a convenient means of linking fatigue loading to crack propagation, it does not always hold true. De Baglion's work [de Baglion, 2011], for instance, demonstrated on 316L stainless steels tested in air and in PWR environments at 300 °C that striation spacing does not systematically correspond to a one-to-one cycle marking. In air, striations often represented more than 1 cycle (1.3 cycle in average), leading to an overestimation of crack growth rates and initiation durations, while in PWR, interstriation spacings were 1.5 to 3 times

larger than in air but still insufficient to explain the observed life differences. These results highlight that the one-striation-per-cycle assumption can break down in complex loading scenarios or in environmentally assisted fatigue conditions, where crack closure, non-linear loading, or microstructural effects also play a significant role [Duarte et al., 2020].

To minimize measurement uncertainty, the inter-striation spacing was determined by measuring the distance over ten consecutive striations and then reducing it to an average value per striation. This approach, frequently employed in quantitative fractography [Howe et al., 2022], reduces the error associated with local irregularities in striation spacing.

II.4.2.2. Dislocation structure analysis

To observe the dislocation structures after interrupted fatigue tests, a transmission electron microscope (TEM) analysis was performed at Centre Castaing, Toulouse, by using a JOEL JEM 2100F with an acceleration voltage of 200kV. The specimens for TEM examination are extracted from the gauge length in the form of small pellets with 1 mm thickness, which are further polished manually up to 150µm. Later, a small piece of 3 mm diameter is cut from the polished pellet and introduced to electro-polishing with 5% perchloric acid in ethanol (Struers "A2"-type). The thinning was carried out at a voltage of ~30 V until a central perforation of approximately 100 nm thickness was obtained. Finally, these specimens are used to observe the dislocation structures using TEM (**Figure 44**).

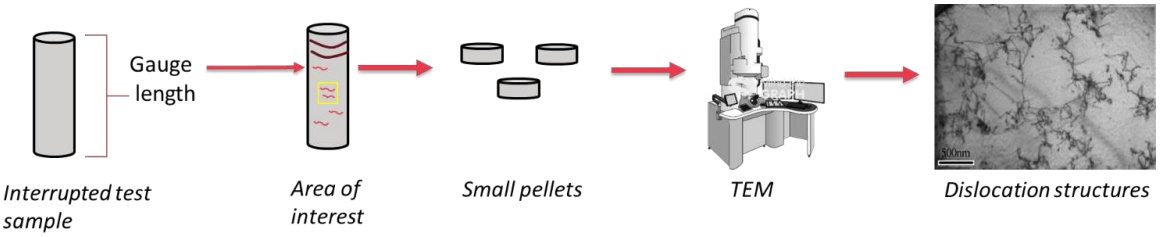

Figure 44 : Representation of sample preparation and to observe dislocations using TEM.

II.4.2.3. Damage evolution and strain localization analysis

To analyze the microstructural factors governing strain localization and crack propagation, the fractured samples were cut axially and examined using electron backscatter diffraction (EBSD) with an eFlash FS detector by Bruker. This approach provides insight into the role of environment, crystallographic orientation, and local deformation mechanisms near the crack path.

The specimen preparation procedure for EBSD analysis can be briefly summarized as follows (**Figure 45**): Firstly, the fractured samples were cut axially, taking the initiation point as a reference and cross-sectioning in the direction of the main crack path. One of the sectioned specimens was mounted and polished using a semi-automatic polisher up to a 1 µm diamond finish and then subjected to final polishing with colloidal silica (OPS) on a vibropolisher to achieve a mirror-like, deformation-free surface suitable for microstructural characterization.

EBSD measurements were carried out to investigate crystallographic orientation and its relation to crack path, including Schmid factor analysis for slip activity (**II.4.2.4**) and KAM (Kernel Average Misorientation) mapping for strain localization. Quantitative characterization of cracks included measurements of crack length, depth, initiation angle, and linear crack density (LCD) of secondary cracks (**II.4.2.5**). The EBSD analyses were performed at a working distance of 15 mm, an accelerating voltage of 20 kV, and under high-current mode with a 120 µm diaphragm, with an average of 9–10 indexed Kikuchi bands per pattern ensuring reliable orientation data.

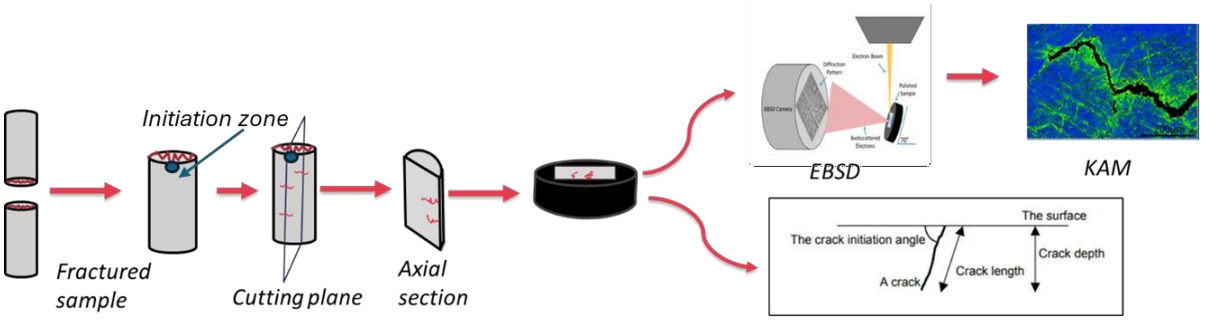

Figure 45 : Representation of sample preparation to quantify the damage evolution and strain localization using the SEM and EBSD.

II.4.2.4. Schmid factor analysis

Schmid factor analysis was performed on the EBSD orientation maps in order to assess the influence of crystallographic orientation on crack initiation. For each grain, the Schmid factor

(SF) was calculated for the primary slip system of FCC alloys, i.e., {111} <110>, considering the macroscopic loading axis. This analysis provides a measure of the resolved shear stress acting on the slip systems, with higher Schmid factors indicating a greater propensity for slip activation under the applied stress state.

II.4.2.5. Linear crack density

To quantify the extent of surface cracking, the linear crack density (LCD) was determined from axial sections of the fatigued specimens. LCD is defined as the number of cracks observed along the specimen surface per unit length, expressed in cracks per millimeter (**Figure 46a**). The measurement was carried out on metallographic cuts taken parallel to the loading axis after cyclic testing. Cracks intersecting the examined surface were counted, and the measured gauge length of the specimen section was normalized to the total number of cracks.

Along with the LCD, other crack characteristics include the crack length, defined as the surface dimension of the crack along the specimen surface; the crack depth, corresponding to the perpendicular distance from the specimen surface to the deepest point of the crack front; and the crack initiation angle (**Figure 46b**), which is the angle between the loading axis and the direction of the crack at initiation are also measured for each individual secondary crack to obtain their distribution to compare between the samples tested in different environments.

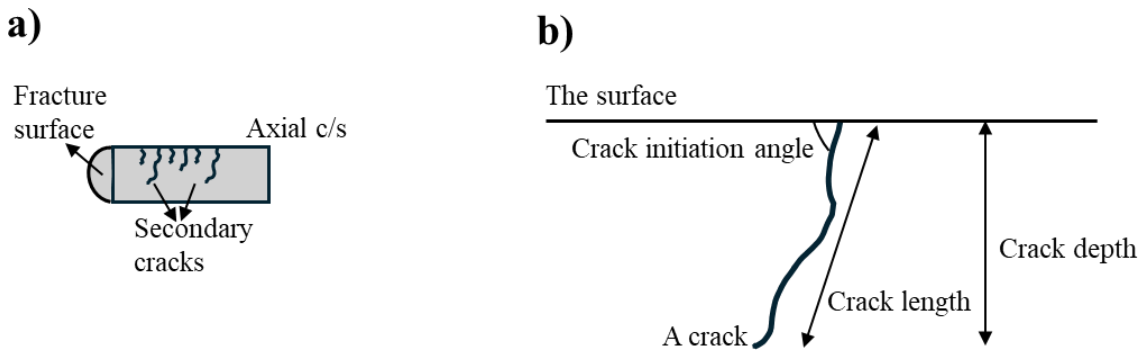

Figure 46: Schematic of the method used to evaluate linear crack density (LCD): (a) axial section of fatigued specimen showing surface secondary cracks, (b) The definition of crack depth, crack length and the crack initiation angle.

III. Low cycle fatigue of Alloy 690TT in air, PWR, and vacuum environment

This chapter focuses exclusively on the experimental results related to the LCF response of Alloy 690TT in air, PWR primary water simulated environment (denoted “PWR environment”) and vacuum, using the as-received material as a baseline. The influence of temperature on fatigue behavior is first assessed under laboratory air conditions. Subsequently, the impact of the PWR environment and strain rate is analyzed to understand environmental degradation mechanisms such as corrosion and possible EAF effects.

These results provide essential insights into the degradation behavior of Alloy 690TT prior to thermal aging and serve as a reference point for evaluating the effects of microstructural evolution in aged conditions presented in later chapters.

Contents

III.1. EFFECT OF THE TEMPERATURE AND STRAIN RATE IN AIR

This section seeks to examine the mechanical behavior of Alloy 690TT under different total strain amplitudes and to investigate the effect of testing temperature on cyclic stress-strain behavior and fatigue life.

Tests carried out at room temperature (RT) consisted of one test per strain amplitude, while tests conducted at 300°C in air involved two tests per strain amplitude (±0.3%, 0.45%, and 0.6%), respectively. Notably, the tests at RT were conducted at a high strain rate of 0.4%/s to speed up the process, given that there is no evident impact of strain rate on the fatigue life of Alloy 690 in air [Chopra, 2018]. The **Figure 47** shows that there is almost no difference in fatigue life at room temperature and 300°C. Those results align with the fatigue lifetime expected from the NUREG/CR-6909 Rev1.

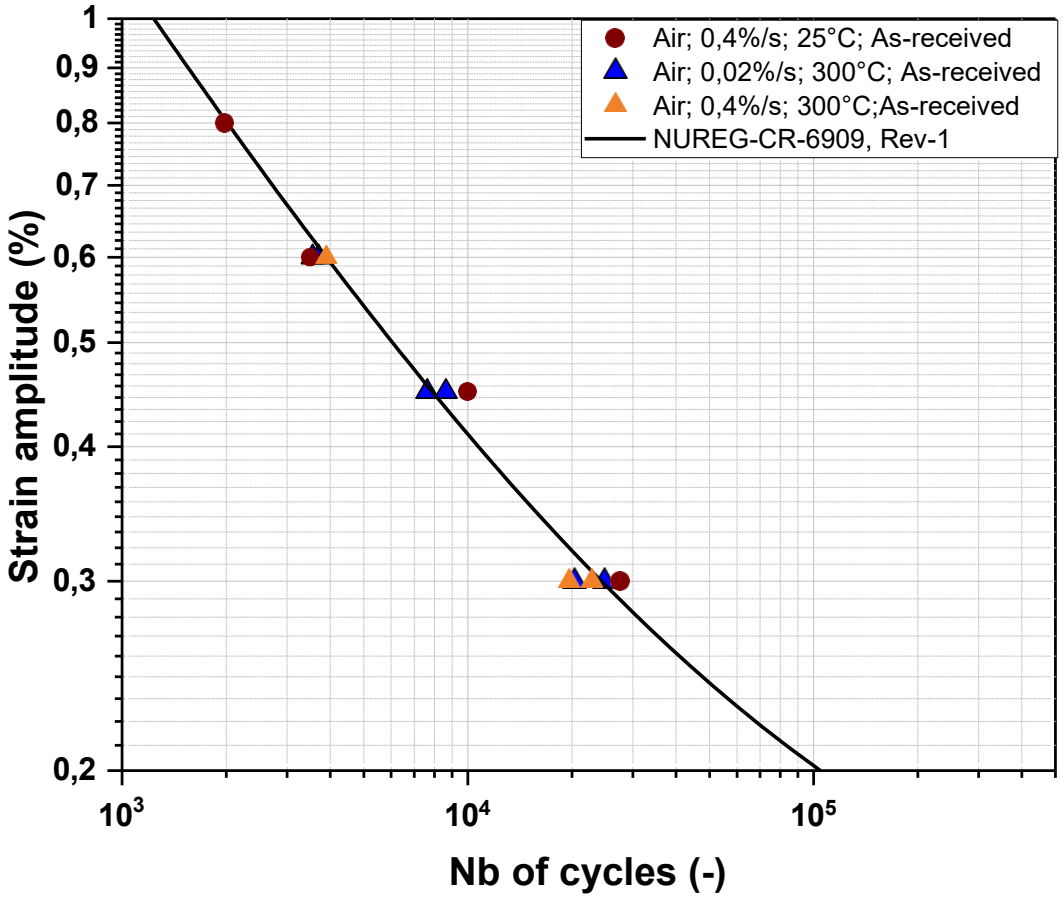

Figure 47*: Influence of the temperature (25°C vs 300°C) and strain rate (0,02%/s vs 0,4%/s) on the strain-life (ε-N) curve of Alloy 690TT in air.*

However, the cyclic stress-strain behavior of the material differs significantly between the two temperatures. Indeed, at room temperature, the alloy starts with a typical primary cyclic hardening, the appearance of peak stress and then a cyclic softening and the final fracture whereas, at 300°C, a continuous hardening, characterized by two distinct hardening rates, is noticed (**Figure 48**). For example, at $\varepsilon_a = 0.6\%$, the first slope is seen between 10 to 100 cycles, and the second slope is seen between 100 to 3500 cycles. Moreover, it can be noticed that the second slope depends on the strain rate: at $\dot{\varepsilon} = 0.4\%/s$ the stress evolves at lower rate, and at failure, it is 20 MPa lower than the test done at $\dot{\varepsilon} = 0.02\%/s$.

It can be noted that this difference in cyclic stress-strain relation between room temperature and 300°C is not present in stainless steels [de Baglion, 2011].

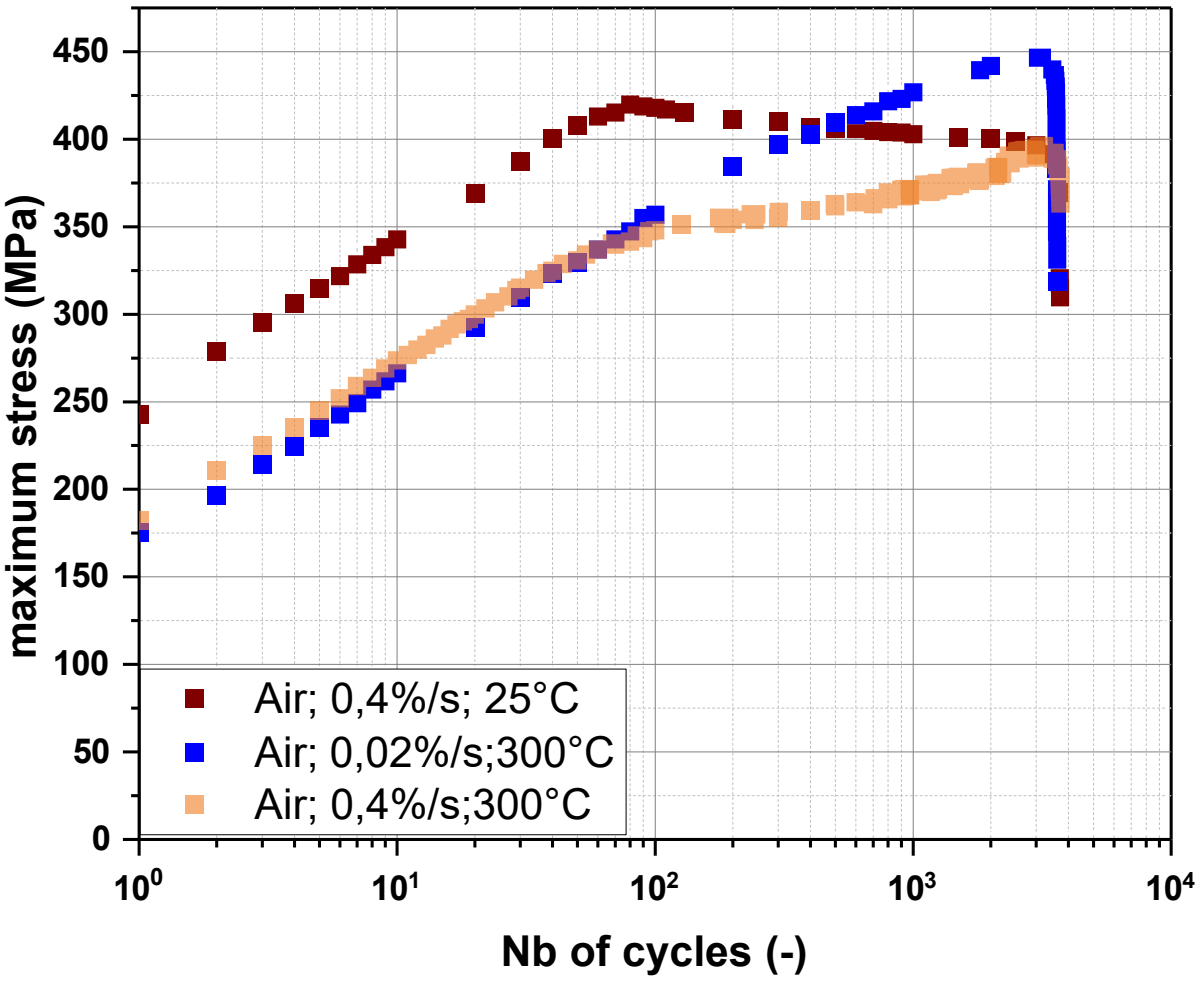

Figure 48: Evolution of the maximum stress during cyclic loading at RT and 300°C in air (ε_a = ±0.6%).

The hysteresis loops recorded at 500 cycles presented in **Figure 49** correspond to the stabilized phase during cycling at 25°C and the secondary hardening phase at 300°C. The alloy was tested at different strain rates (0.4 %/s and 0.02%/s) but at a fixed total strain amplitude of 0.6%.

As already noticed in Figure 48, the maximum stress (σ_{max}) values differ noticeably between straining conditions; at 500 cycles, σ_{max} reaches about 420 MPa at 300 °C with a strain rate of 0.02 %/s, compared to 360 MPa at 0.4 %/s, indicating a pronounced influence of strain rate and temperature on the cyclic stress–strain response.

Additionally, as shown in **Figure 49**, serrated flow associated with the PLC effect is more pronounced at the higher strain rate ($\dot{\varepsilon}$ = 0.4 %/s). This observation confirms that the more evident secondary hardening observed at lower strain rate cannot be attributed to PLC effect and DSA.

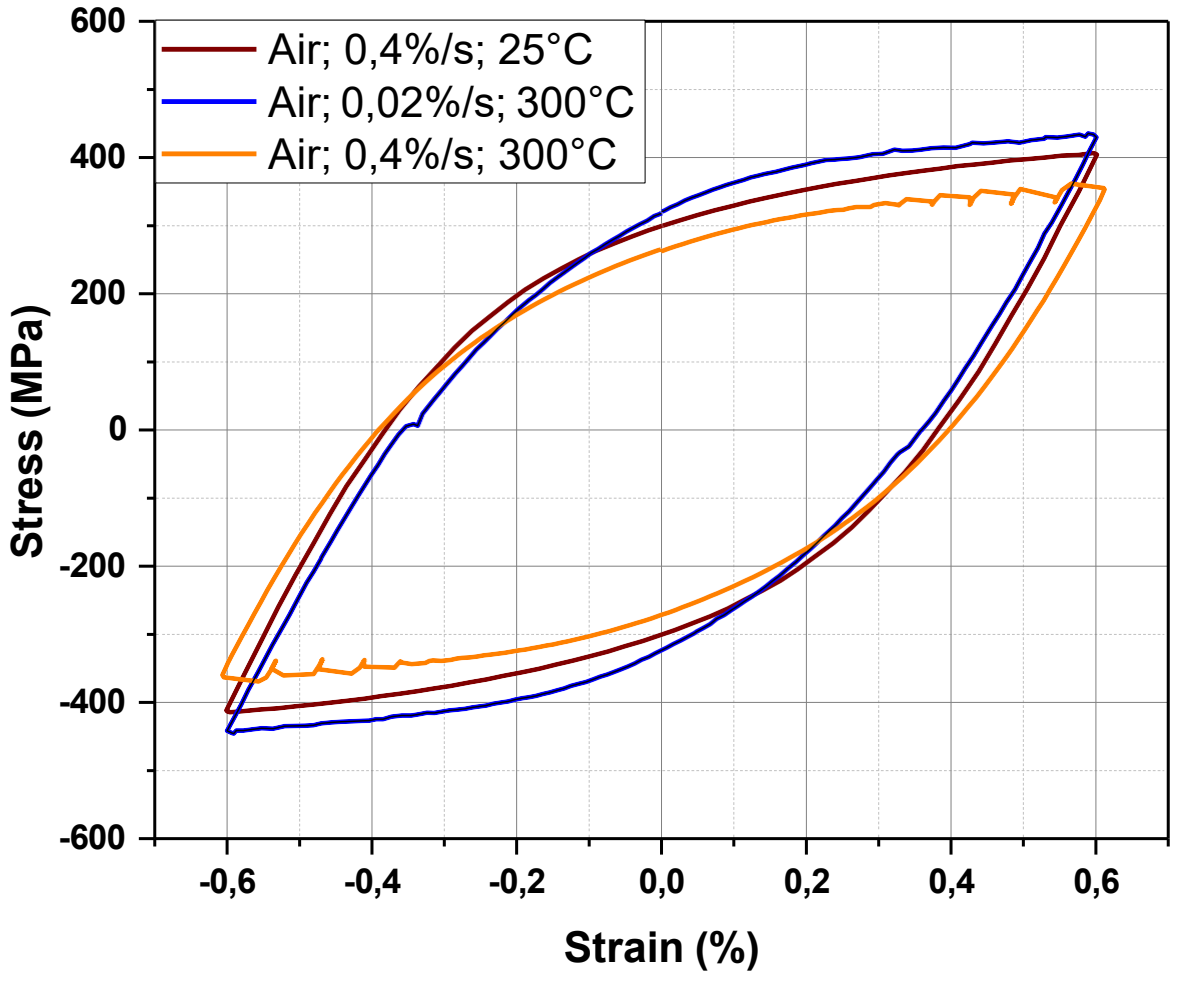

Figure 49: Hysteresis loops from the as-received material tested at 25°C and 300°C (500 cycles) in air (ε_a = 0,6%).

While the differences in maximum stress levels are clear, along with the inverse effect of strain rate on the stress evolution at 300 °C, it remains to be determined whether the plastic strain energy dissipated per cycle, represented by the area enclosed within each hysteresis loop, also varies significantly under these conditions. Although the total strain energy comprises both elastic and plastic components, the elastic portion is largely recoverable and remains relatively constant during low-cycle fatigue. Therefore, the plastic strain energy, corresponding to the irreversible part of the total energy, is used here as a direct measure of cyclic energy dissipation and fatigue damage accumulation. The following analysis examines whether this energy-based response remains stable or exhibits similar temperature-dependent variations.

To calculate the strain energy for tests conducted at a strain amplitude of 0.6%, the plastic strain energy model (W_p) was adopted (**I.3.3.2**). This selection is based on the understanding that, under such high strain amplitudes, the majority of the energy dissipated during each cycle is attributed to plastic deformation. As a result, the W_p model offers a more representative index of fatigue damage compared to models incorporating total or elastic strain energy. This approach is consistent with classical LCF methodologies [Ellyin and Kujawski, 1984], where plastic work is the primary source of material degradation.

The **Figure 50** displays the evolution of the plastic strain energy per cycle W_p for the as-received Alloy 690TT tested at a constant strain amplitude of 0.6%, in air across 25°C and 300°C at a strain rate of 0.4%/s and 0.02%/s. Across all three conditions, the plastic strain energy response remains remarkably constant throughout most of the fatigue life, demonstrating that Alloy 690TT exhibits stable energy dissipation behavior under cyclic loading, even with variations in temperature and strain rate.

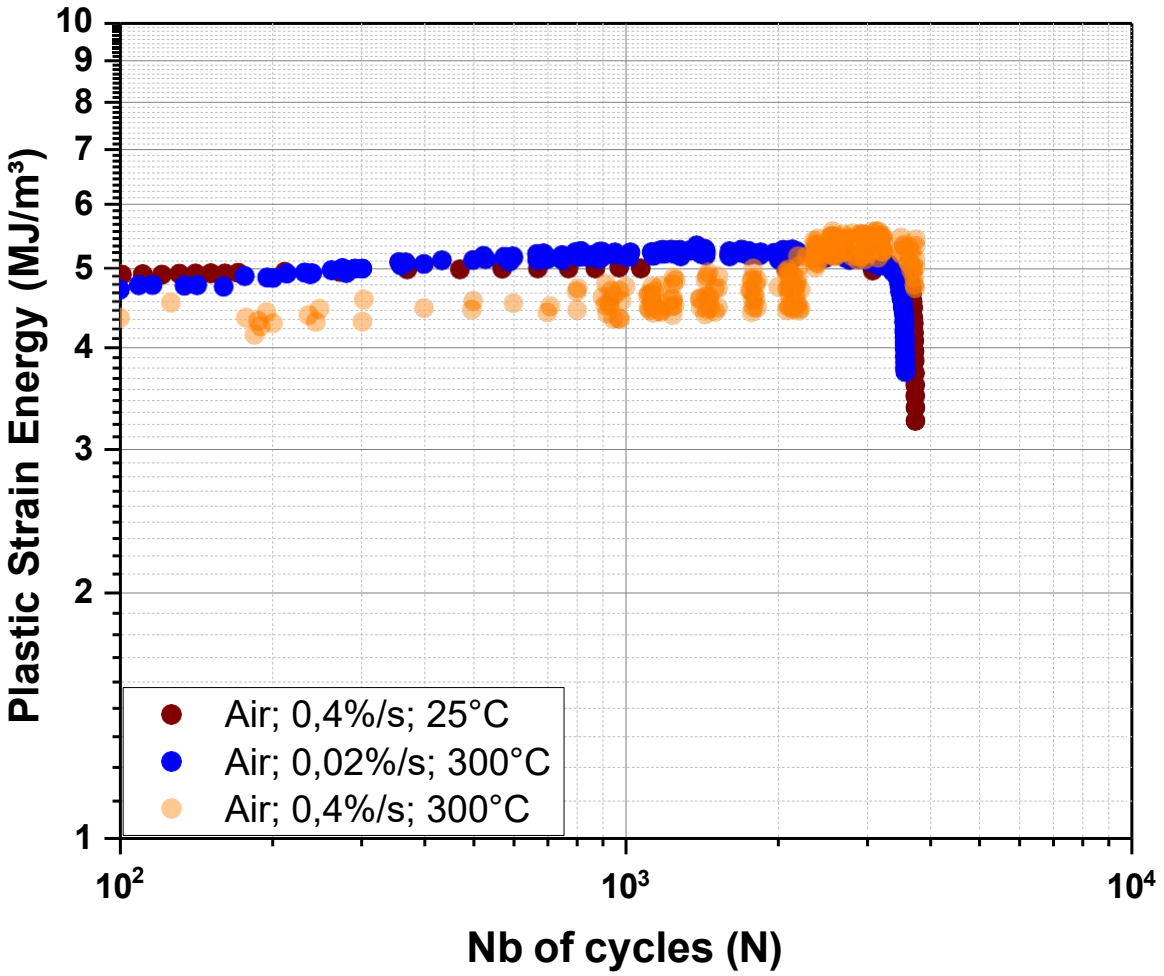

Figure 50: Evolution of plastic strain energy per cycle for the as-received sample at different temperatures and strain rates tested at a 0.6% strain amplitude.

The two cases - 25 °C at 0.4%/s and 300 °C at 0.02%/s - show almost overlapping curves, indicating a negligible influence of temperature on the strain energy evolution. The 300 °C at 0.4%/s case shows a scatter in the data, particularly marked around 800–2000 cycles, with fluctuations in strain energy. Despite the scatter, the upper envelope of this condition aligns well with the other two, indicating comparable energy levels overall. The increased variability might reflect microstructural instabilities at elevated temperature and higher strain rates.

Approaching failure (final 5–10% of life), all three curves sharply drop, showing the expected decrease in strain energy due to crack propagation. The convergence of all three conditions in the final cycles further supports the conclusion that fatigue failure occurs with a nearly similar total plastic strain energy input, regardless of testing temperature and the strain rate in air.

III.1.1. Investigation of the cyclic behavior of Alloy 690TT

Compared to stainless steels, the relationship between the macroscopic cyclic behavior of Alloy 690TT and its microscopic deformation mechanisms is not well documented. Indeed, two distinct phenomena are present while cycling at high temperature but not at room temperature: i) a serrated flow visible on the hysteresis loops (**Figure 49**), ii) a continuous hardening regardless of the applied strain amplitude (**Figure 48**). The mechanism behind this continuous hardening lacks consensus in the literature.

The objective of this section is to investigate the deformation mechanisms of Alloy 690TT at RT and at 300°C in order to explain the difference in stress-strain response. To do so, interrupted tests were performed in air at RT and 300°C at certain intervals of the cycling, i.e., at 30 cycles and 500 cycles at 0.4%/s, where the slopes of cyclic curves are different (**Figure 48**). TEM observations were then performed on foils extracted from the interrupted fatigue tests to investigate the evolution of dislocation structures in Alloy 690TT.

Deformation mechanisms at RT

At room temperature, the deformation microstructure of Alloy 690TT is primarily characterized by dense dislocation tangles (**Figure 53a**) and well-defined cellular dislocation structures (**Figure 53b**). This microstructural arrangement is similar to that typically observed in austenitic stainless steels under comparable loading conditions, where dislocation glide and dynamic recovery dominate the cyclic deformation process. Such cellular structures reflect the rearrangement of dislocations into stable configurations during strain hardening [de Baglion, 2011, Gerland et al., 1997], indicating a comparable deformation mechanism between Alloy 690TT and austenitic steels like 304L.

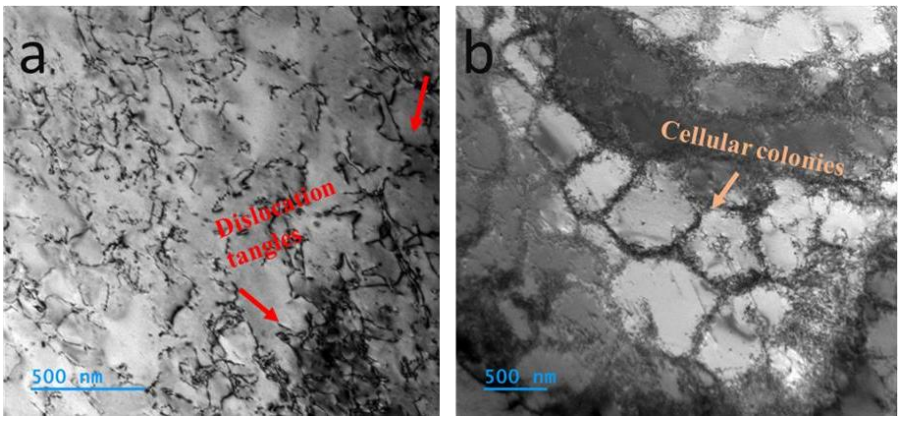

Figure 51: Dislocation structures within the interrupted test specimen tested at ε_a=0.6%, $\dot{\varepsilon} = 0.4$%/s, RT (a) 30 cycles and (b) 500 cycles.

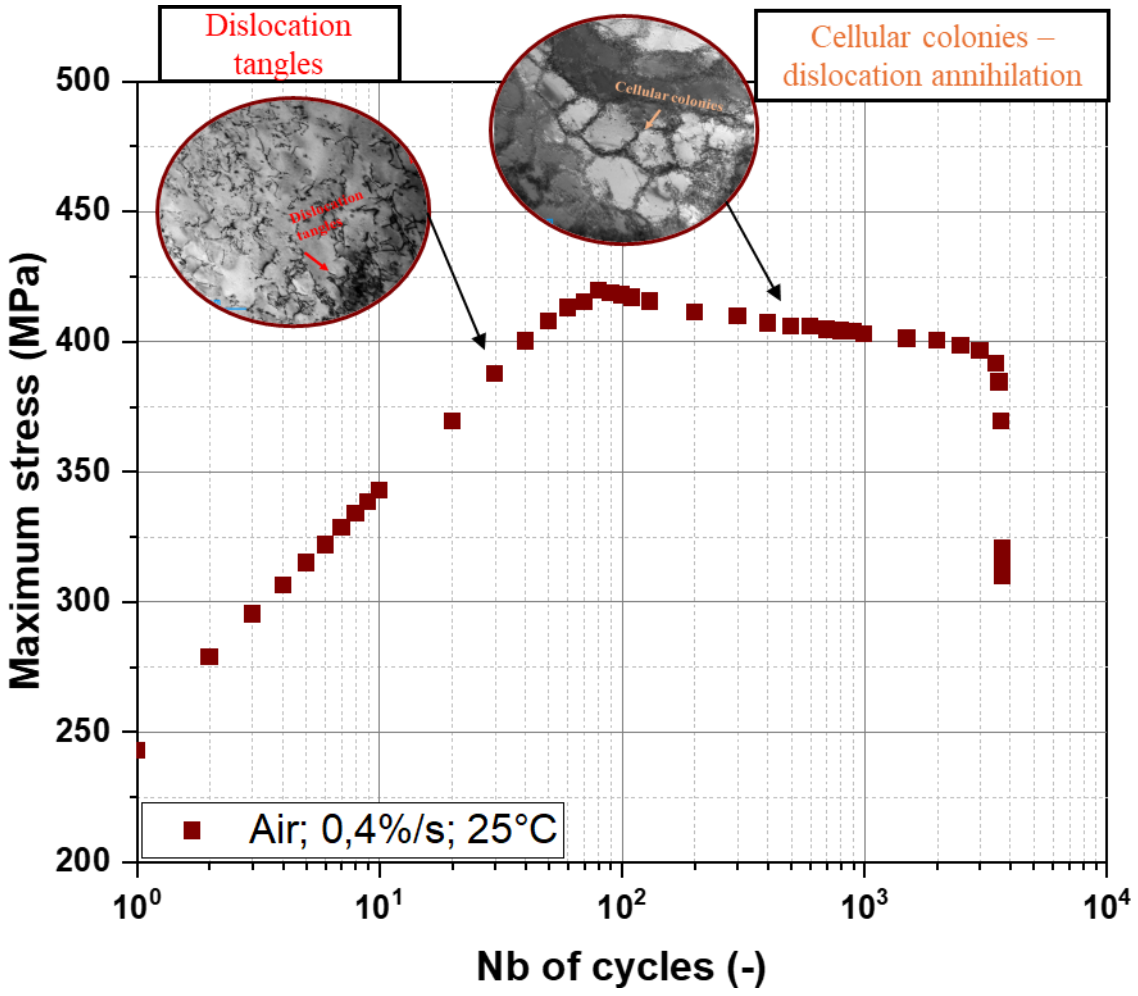

Figure 52: Evolution of the microstructure during cycling at ε_a=0.6% and on the as-received Alloy 690TT at 25°C.

Deformation mechanisms at 300°C

At 300°C, a distinctly different dislocation morphology was revealed, as illustrated in **Figure 53**. Dislocations were observed to be periodically pinned and arranged in linear, planar arrays, suggesting that their motion is temporarily arrested by short-range interactions with diffusing solute atoms like carbon. As the activation energy for the volumic diffusion is around 159 kJ/mol, a fatigue test at 300°C would increases the mobility of carbon at a higher rate, making solute-dislocation pinning kinetically viable.

This accounts for pinned dislocations resulting in the serrated flow in the stress strain curve. while at 300°C the dislocations are pinned and arranged in planar arrays resulting in the stress drop in the form of serrations at 300°C (**Figure 53 (c) and (d)**). According to the literature, in case of austenitic stainless steels, the formation of cellular dislocation colonies, tangled

dislocation structures are the main characteristics observed at RT in air environment [Hong and Lee, 2004], Formation of linear dislocation arrays and also pinned dislocations by forest dislocations are the characteristics of stainless steel tested at 300°C in air environment [de Baglion, 2011, Hong and Lee, 2005]. This behavior is consistent with 316L stainless steel, where slip becomes more planar between 200 °C and 500 °C, forming corduroy structures associated with secondary cyclic hardening [Gerland et al., 1997]. The observation of pinned dislocation and the planar arrays observed confirms that the dislocations patterns in Alloy 690TT and the proof for the activation of DSA at 300°C are similar to the one observed in stainless steels at RT and 300°C but does not provide an explanation for the change in hardening rate noticed during continuous hardening at 300°C. It could be argued that this change of slope is more dependent on the appearance of nano-twins, formation of hardened phases like SRO, or a change in dislocation density during loading [Chai et al., 2013].

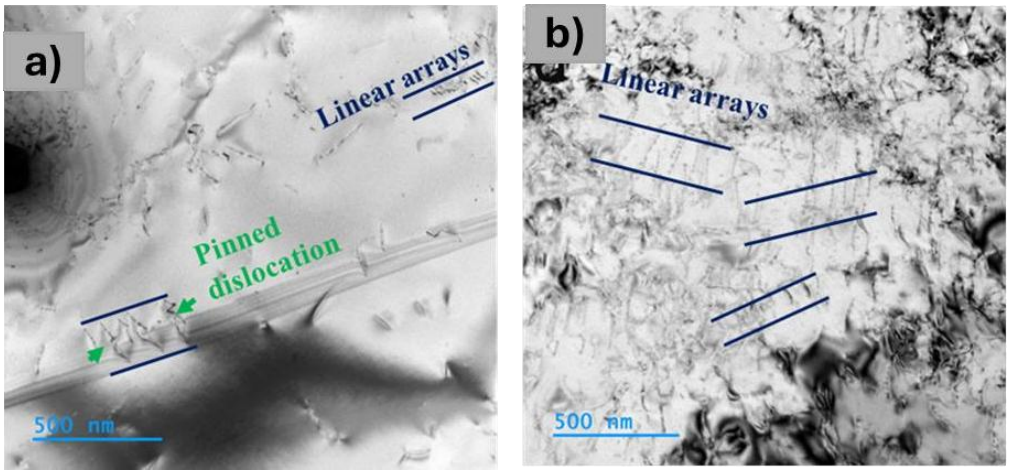

Figure 53: Dislocation structures within the interrupted test specimen tested at ε_a=0.6%, $\dot{\varepsilon}$ = 0.4%/s, 300°C (a) 30 cycles and (b) 500 cycles.

In order to investigate the previous assumption about the appearance of nanotwins during the secondary hardening phase, an interrupted tests was performed up to 3000 cycles at 0.6% strain amplitude and 0.02%/s of strain rate, later the sample was cut axially to extract a FIB foil perpendicular to the loading axis. Thereafter this foil was observed using TEM. These TEM investigations, corresponding with the secondary hardening stage (**Figure 54**). More precisely, **Figure 54a** shows fine twin lamellae, while the corresponding Selected Area Diffraction (**Figure 54b**) confirms their presence through the characteristic splitting of diffraction spots between the matrix and the twin. The main set of reflections corresponds to the parent matrix, while a second one, systematically shifted, originates from the twin lattice. This splitting arises from the crystallographic misorientation between the twin and the matrix, as indicated by the

measured tilt differences (tiltx ≈ 6.4° vs. 4.3°, tilty ≈ 18° vs. 16.5°). Such diffraction evidence demonstrates the coexistence of twin–matrix domains, consistent with the lamellar morphology seen in bright-field TEM. The formation of these nano-twins at 300 °C provides an additional strengthening mechanism during cyclic loading, as twin boundaries act as effective barriers to dislocation motion contributes to the secondary hardening.

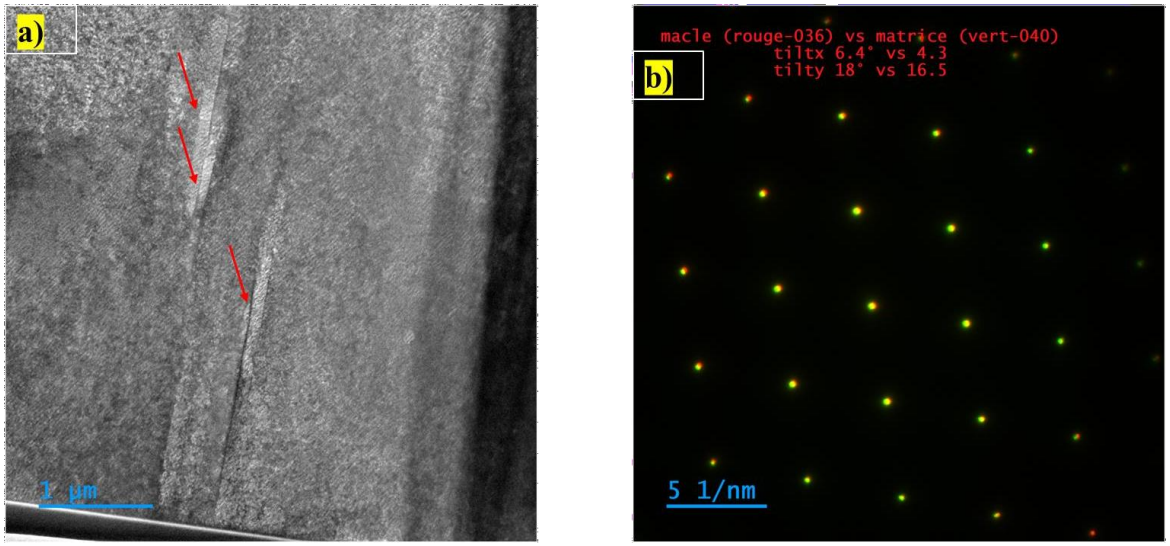

Figure 54: TEM analysis of an interrupted test sample tested at ε_a=0.6%, $\dot{\varepsilon} = 0.4\%/s$, 300°C (a) Bright-field TEM image showing nanoscale deformation twins (red arrows). (b) Corresponding SAD pattern with split diffraction spots, where the green reflections correspond to the matrix and the red reflections to the twins, confirming their crystallographic misorientation (tiltx ≈ 6.4° vs 4.3°, tilty ≈ 18° vs 16.5°).

The evolution of cyclic stress-strain response in Alloy 690TT at 25 °C can be rationalized by the corresponding changes in dislocation structures. During the early cycles, rapid work hardening occurs as dislocations multiply and form dense tangles (**Figure 52).** With continued cycling, these tangles rearrange into cellular colonies, a lower-energy configuration that facilitates dynamic recovery through annihilation of opposite-sign dislocations across cell walls. This structural reorganization reduces the stored dislocation density and promotes partial softening after the initial hardening stage, leading to the observed stabilization and subsequent gradual decrease in peak stress. The formation of dislocation colonies therefore plays a central role in balancing multiplication and annihilation processes, explaining the transition from hardening to cyclic softening at room temperature.

At 300 °C, Alloy 690TT exhibits a fundamentally different dislocation evolution compared to room temperature, consistent with the continuous cyclic hardening observed in the stress response (**Figure 55**). In the early stages of cycling, dislocations are pinned by diffusing solute

atoms, which restricts their mobility and promotes the formation of linear, planar arrays. This arrangement prevents the development of cellular colonies and thus suppresses dynamic recovery through dislocation annihilation, explaining the absence of cyclic softening.

As cycling progresses, the high density of planar dislocations generates strong local shear concentrations along the {111} slip planes. These shear bands frequently extend into stacking faults, which serve as intermediate configurations during cyclic deformation. With continued slip on adjacent planes, stacking faults can thicken and eventually transform into nano-twins, as observed in the later stages of fatigue (**Figure 55**) [Chai et al., 2013].

Overall, the microstructural sequence "dislocation pinning → planar arrays → stacking faults → nano-twins" illustrates the transition from pinned dislocations to defect structures that accommodate plasticity without recovery. This mechanism sustains hardening throughout fatigue life at 300 °C. In contrast, at 25 °C dislocation tangles reorganize into cellular colonies, enhancing dynamic recovery and promoting cyclic softening.

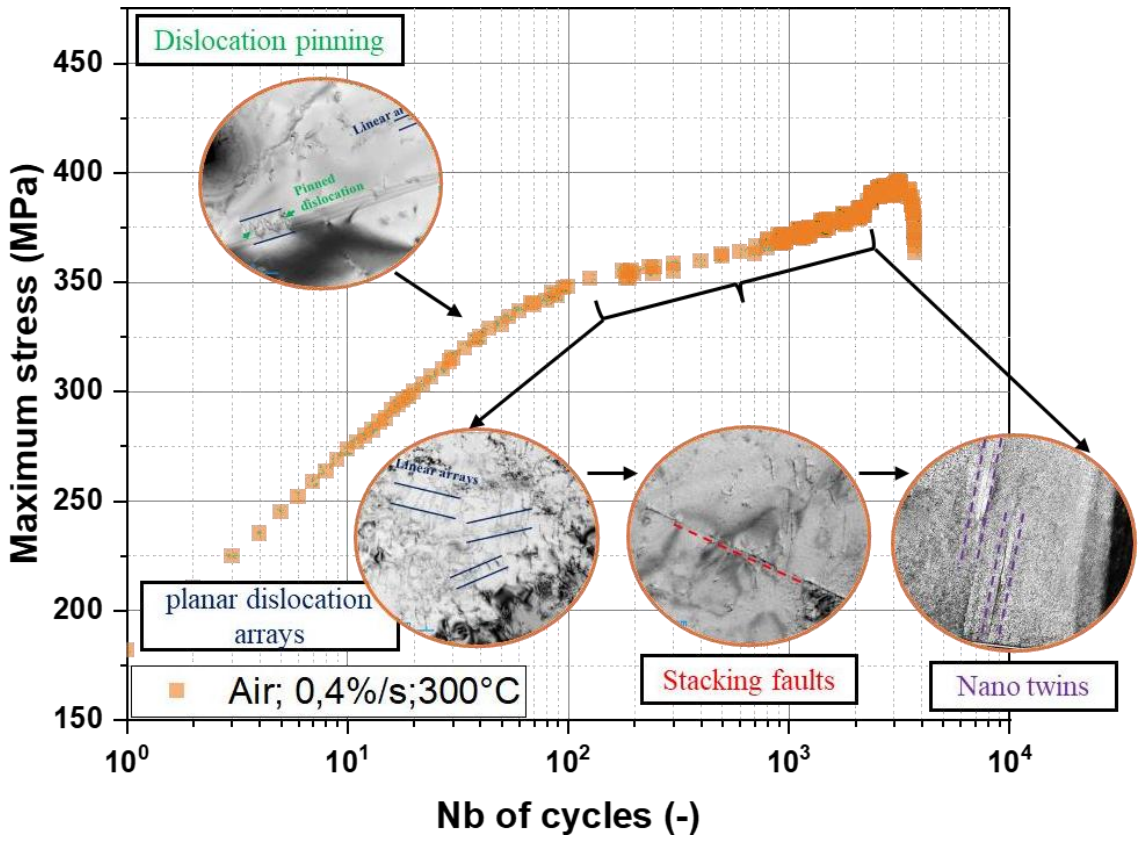

Figure 55: Evolution of the microstructure during cycling at ε_a=0.6% and on the as-received Alloy 690TT at 300°C.

III.2. EFFECT OF ENVIRONMENT ON FATIGUE LIFE

To evaluate the influence of the PWR environment on the fatigue resistance of Alloy 690TT, strain-controlled tests were conducted at various strain amplitudes. An environmental fatigue factor (F_{en}) of 2 was first considered, corresponding to a lifetime in PWR expected to be approximately half that in air. This condition was achieved at a strain rate of 0.02%/s. As shown in **Figure 56**, the PWR environment at this strain rate had a negligible effect on fatigue life compared to air, both at total strain amplitudes of 0.45% and 0.30%.

Subsequently, an additional test was performed at a higher environmental factor, corresponding to F_{en} = 2.5, with a reduced strain rate of 0.004%/s, about five times slower than that used for F_{en} = 2 (0.02%/s). To limit the total test duration, a sawtooth waveform was applied, in which the tensile loading (where the crack remains open and environmental effects are active) was imposed at 0.004%/s, while the compressive part of the cycle was applied more rapidly at 0.04%/s.

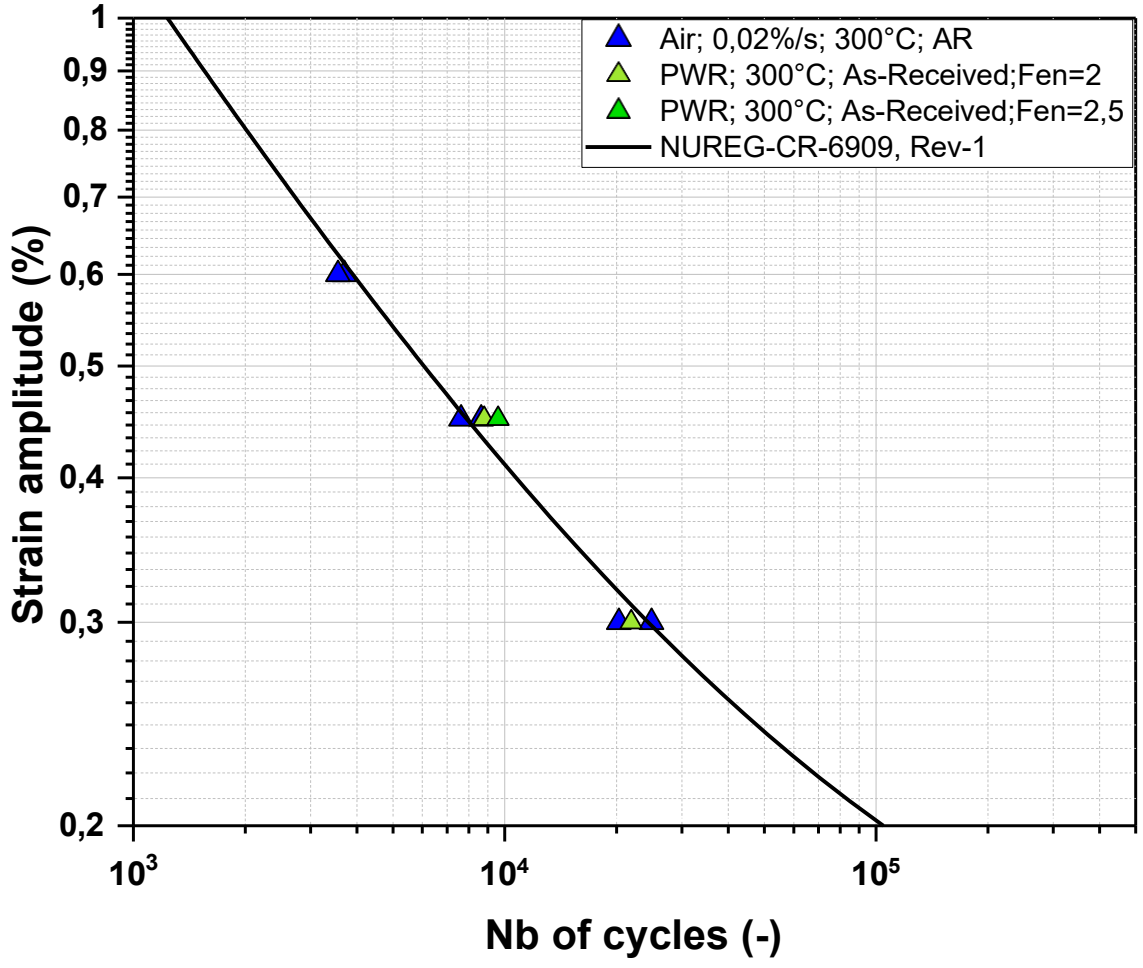

Figure 56: ε-N curve of Alloy 690TT in air and PWR environment at 300°C.

The cyclic behavior of the alloy in the PWR environment shown **Figure 57** is overall similar to the one observed in the air at 300°C. A slight difference is nevertheless observable with an initial stress increase in the PWR environment during the first 100 cycles, presumably resulting from the strain control using the shoulder of the specimen (**II.3.2**). No difference is noticed between the two loading conditions (fast triangle and sawtooth).

Indeed, in the air, the deformation is controlled at a gauge length of 9 mm, and in the PWR environment, it is managed by shoulders at a gauge length of 20 mm; the changes in geometry and strain control may lead to an initial surge in the yield.

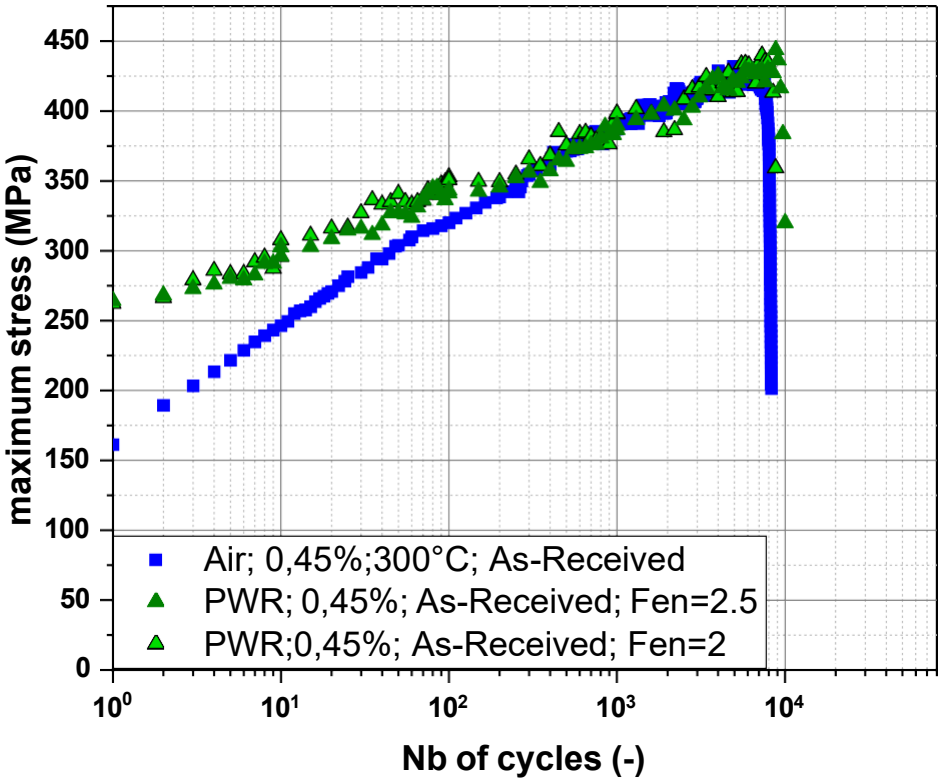

Figure 57: Cyclic behavior of Alloy 690TT during cyclic loading in air and PWR environment at F_{en} = 2 or 2.5.

To confirm the absence of any environmental impact on fatigue life, it is important to estimate the crack initiation life and crack propagation life. In the following, the fatigue crack growth rates are estimated in order to evaluate the crack propagation life as a function of environment.

Based on the previous assumptions the Fatigue Crack Growth Rate (FCGR) with respect to the strain intensity factor ΔK_ε is plotted **(Figure 58)**. In this analysis, the FCGR values were estimated from the striation spacing measured on the fracture surfaces (**II.4.2.1**). The results show that at $\varepsilon_a = 0.45\%$ and at a strain rate of 0.02%/s and at 0.004%/s, the crack growth rates are nearly identical under PWR and air conditions. The comparable fatigue lives observed in air and PWR environments suggest that the environment has little influence on the crack growth kinetics of Alloy 690TT. Under the common assumption that, in austenitic stainless steels, low-cycle fatigue life is largely governed by the propagation stage [de Baglion, 2011], these results are consistent with a similar behavior in Alloy 690TT. However, this interpretation remains indicative rather than conclusive, as no explicit separation between initiation and propagation phases was performed in this study.

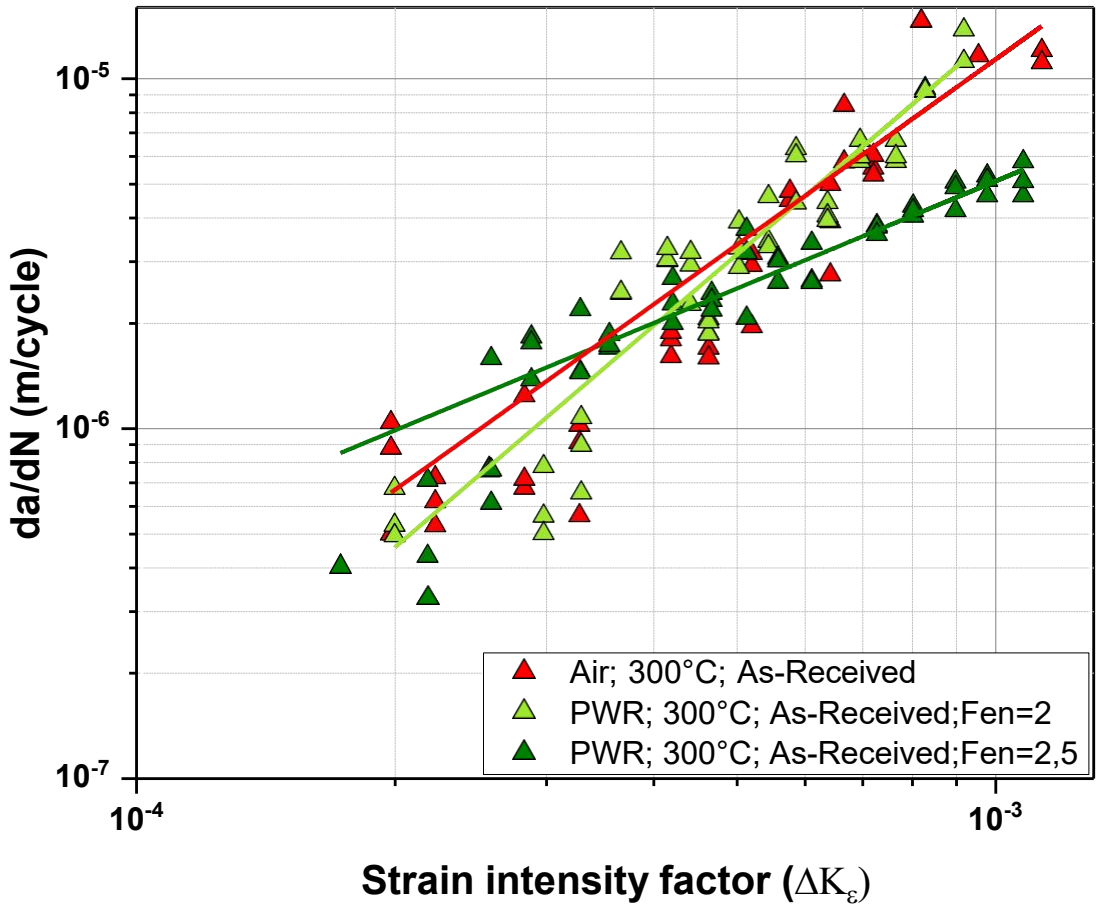

Figure 58: Fatigue crack growth rate curves in air and PWR environment for tests conducted at 0.45% as a function of the strain intensity factor.

III.2.1. Microstructural Characterization of secondary cracks

To gain further insight into the damage mechanisms governing fatigue in Alloy 690TT, a detailed microstructural characterization was performed on the fractured specimens tested in

air and PWR environments. This analysis focused on the initiation and propagation behavior of secondary cracks that developed during cyclic loading. Particular attention was given to the identification of crack initiation sites on the specimen surface, in order to determine the prevailing initiation mode in each environment. The crystallographic orientation of the initiation grains was assessed through Schmid factor analysis to evaluate whether cracks preferentially initiated in grains with high or low slip activity. The extent of surface damage was quantified using the LCD. Additional geometric descriptors, including the distribution of crack lengths, depths, and initiation angles, were compared between air and PWR conditions to evaluate environmental effects on crack morphology. Finally, the propagation behavior of these secondary cracks was examined through EBSD analysis, with KAM maps providing insight into local strain localization and the mode of crack propagation in each environment.

III.2.1.1. Analysis of the initiation

At ε_a = 0.45%, fatigue crack initiation in Alloy 690TT proceeds through distinct microstructural pathways depending on the environment, although the overall fatigue life remains comparable in air and PWR.

In air, at 300°C, initiation occurs predominantly through the development of persistent slip bands (PSBs). The intense cyclic slip at these localized bands produces intrusions and extrusions at the surface, which act as the precursors for Stage I crack nucleation. SEM observations confirmed the presence of PSBs decorated with small surface cracks, indicating a classical slip-driven initiation mechanism.

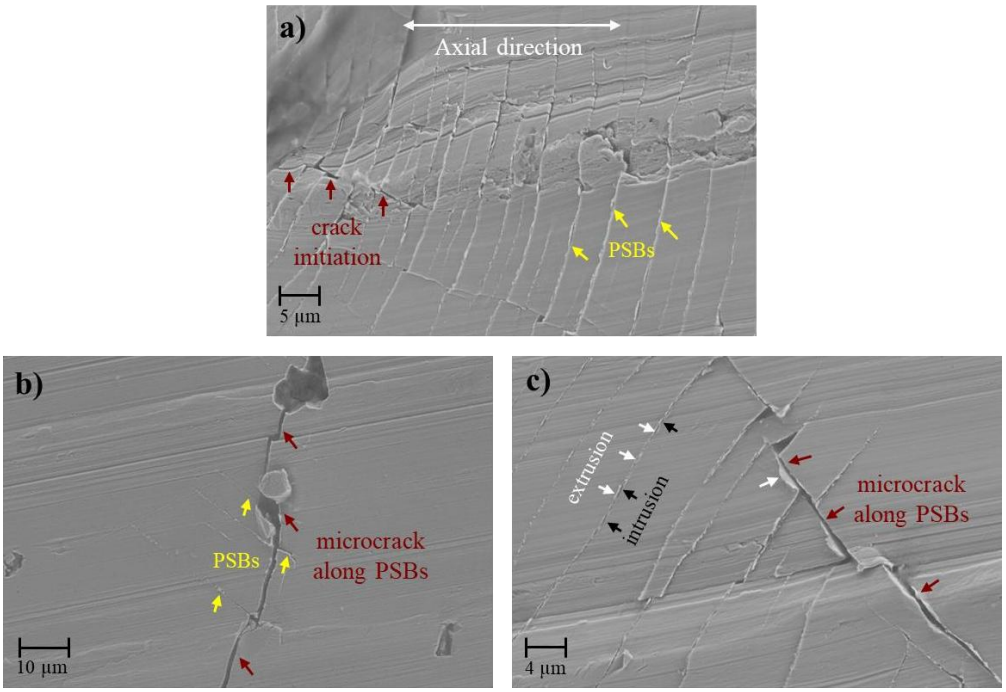

Figure 59: Surface morphologies showing the surface crack initiation features at a ε_a = 0.45% at 300 °C in air: a) crack initiation along PSBs perpendicular to the loading axis, b) Microcrack nucleation and growth along PSBs; c) Formation of intrusions/extrusions at PSBs, serving as preferential sites for microcrack initiation and propagation.

The **Figure 60** presents the surface morphology of Alloy 690TT tested at 0.45% strain amplitude in PWR water at 300 °C, both before and after oxide removal. In the as-tested condition, the surface is largely covered with a continuous oxide film, with needle-like oxide structures and preferential thickening along crack paths. Persistent slip bands (PSBs) are present but remain largely obscured, making it difficult to directly identify slip-driven initiation. After chemical cleaning, the underlying PSBs become clearly visible, confirming that slip localization is active in PWR despite the surface oxide coverage. Microcracks are observed along PSBs as well as at inclusions, with intrusions and extrusions serving as preferential initiation sites.

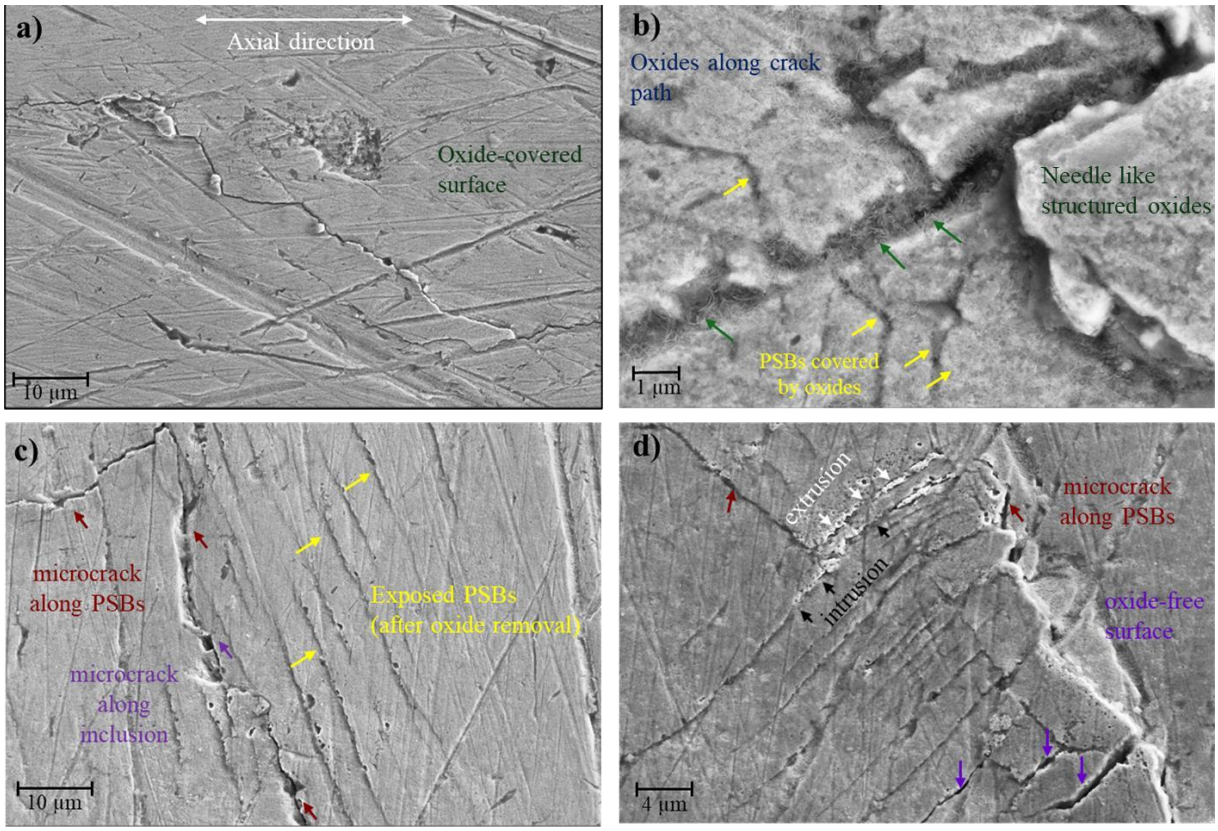

Figure 60: Surface morphologies and crack initiation features at a ε_a = 0.45% at 300 °C in PWR environment: a) Oxide-covered surface; b) Needle-like oxides decorating crack paths and masking PSBs; c) Exposed PSBs and microcracks revealed after oxide removal; d) Microcrack formation along PSBs with clear intrusions/extrusions on the oxide-free surface.

Thus, while both environments share a common dependence on PSBs as preferential initiation sites, the presence of oxides in PWR environment introduces an additional slip–oxidation coupling mechanism. The fact that fatigue life is not significantly reduced in PWR compared to air suggests that, at this strain amplitude, any oxide-assisted initiation mechanism does not accelerate the overall damage accumulation rate.

Schmid factor analysis in air and PWR environments was used to evaluate the role of grain orientation and possible slip irreversibility induced by environmental effects. The **Figure 61** compares cracked and non-cracked grains of the as-received Alloy 690TT tested in both air and PWR environments. The detailed procedure to obtain this Schmid factor is explained in section **II.4.2.4**. In both cases, cracked grains exhibit significantly higher average Schmid factor values compared to non-cracked grains. Specifically, cracked grains were identified as those intersected by the fatigue crack path traced on the EBSD maps, while non-cracked grains were those adjacent to the crack but not intersected. In this analysis, the cracked grains in air and

PWR environments show average Schmid factor values of approximately 0.48 and 0.49, respectively, whereas the non-cracked grains fall around 0.38 in air and 0.41 in the PWR condition. This trend highlights the consistent role of crystallographic orientation in fatigue crack initiation, with grains oriented for higher resolved shear stress being more susceptible to cracking [Mineur, 2000]. Moreover, the similarity in the average Schmid factor values across the two environments suggests that environmental effects have a minimal influence on the crystallographic activation of slip systems during crack initiation in the as-received material. Therefore, the data indicate that the mechanical response, particularly slip activity governed by grain orientation, dominates the early stages of fatigue cracking under both environmental conditions.

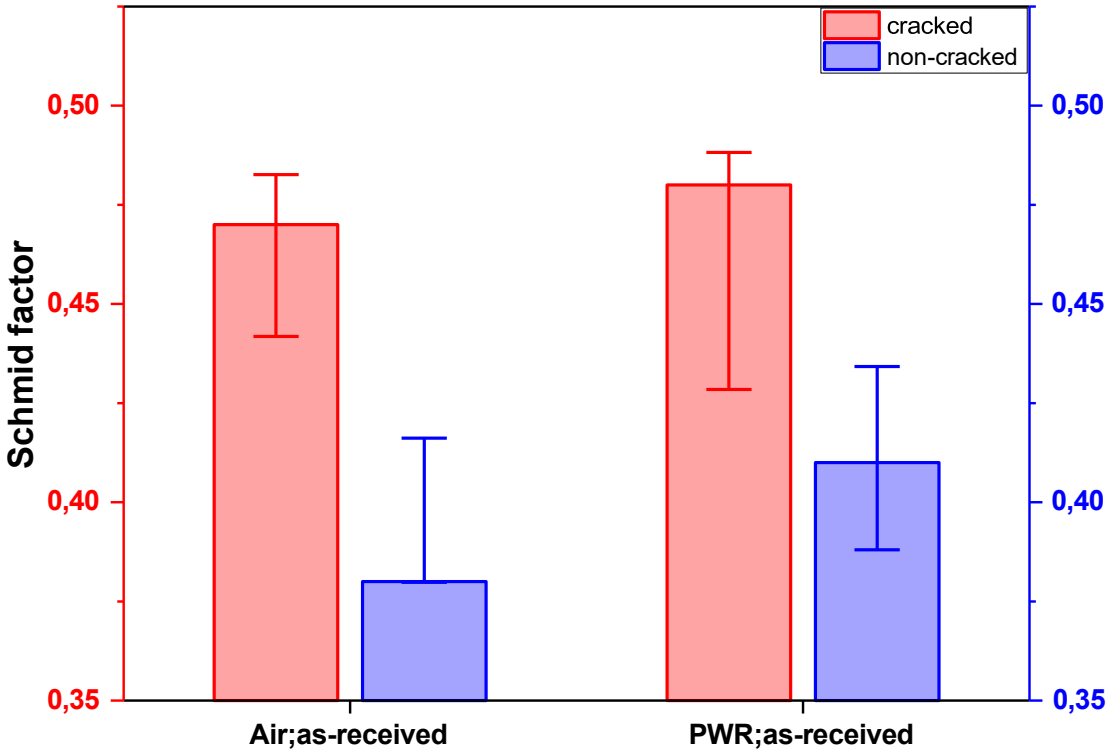

Figure 61: Schmid factor analysis of secondary cracks in the as-received Alloy 690TT between the air and the PWR environment.

The **Figure 62** displays the LCD of Alloy 690TT samples subjected to testing in air and PWR environments, plotted against strain amplitude and determined according to the procedure detailed in section **II.4.2.5**. The data indicates that the secondary crack density is higher in PWR environment than in the air environment. Specifically, the damage at a strain amplitude of 0.45% appears slightly greater than at 0.30% in air, whereas in the PWR environment the opposite trend is observed, with a somewhat higher crack density at 0.30%. However, since

only one specimen per strain amplitude was tested, these differences cannot be considered statistically significant. The overall values remain close, consistent with observations in austenitic stainless steels by [Huin, 2013], where in PWR conditions the linear crack density was ~5 cracks/mm at both strain amplitudes under similar testing conditions.

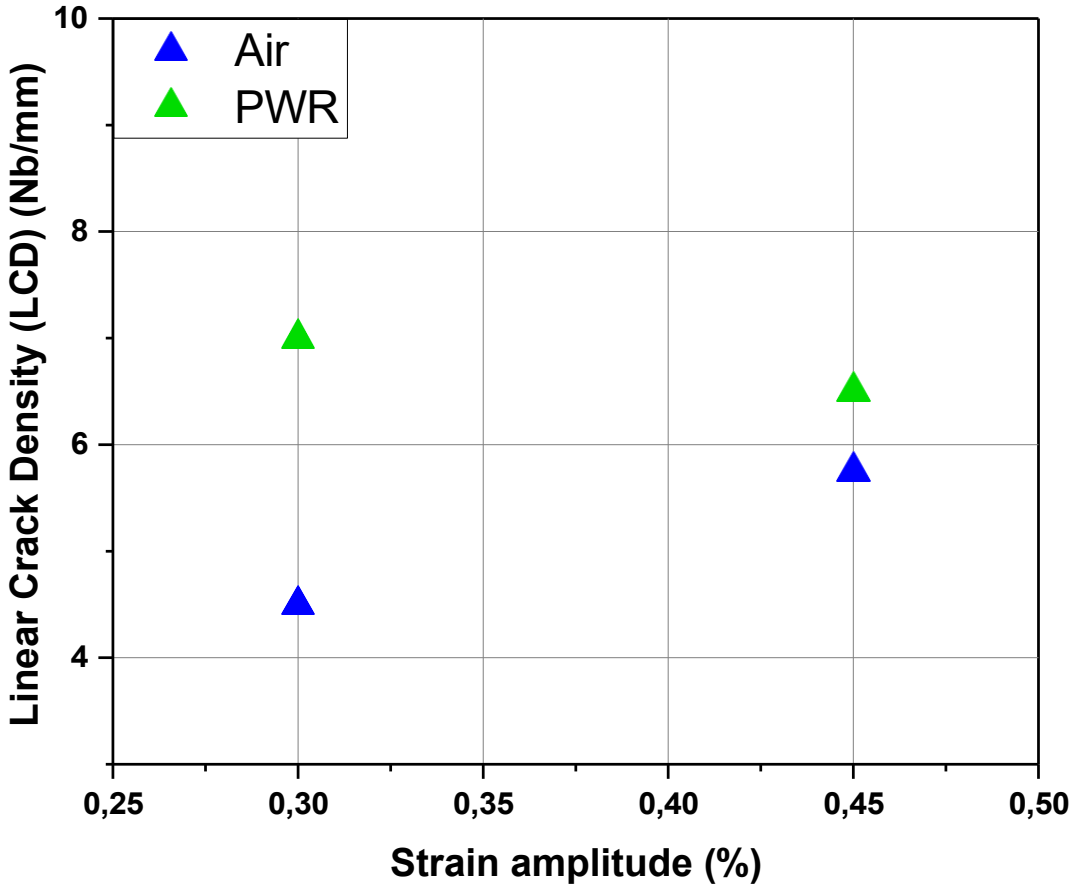

Figure 62: Linear crack density on specimen tested in air and PWR environment at 0.02%/s.

The distribution of crack depth, crack length, and crack initiation angle for as-received Alloy 690TT samples tested in both air and PWR environments are give below.

Concerning crack depth distribution (**Figure 63**), both air and PWR environments show that a majority of cracks have a depth of less than 50 µm and more than 20% are less than 20 µm, with a gradual decrease in probability for deeper cracks (**II.4.2.5**).

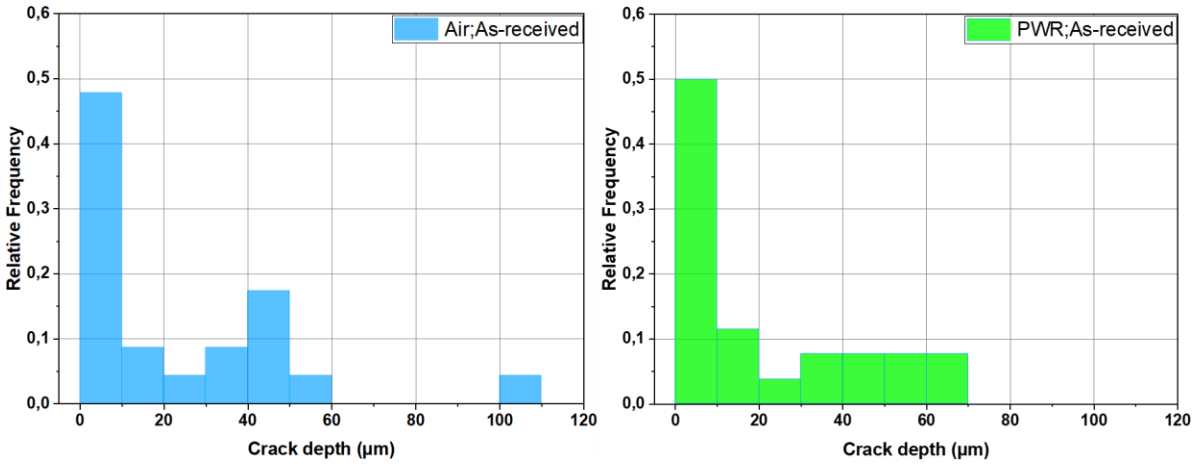

Figure 63: Distribution of the secondary crack depth between the samples tested in air and PWR environment.

The crack length distribution also exhibits similar trends (**Figure 64**), with most cracks measuring under 100 µm in both environments. The crack initiation angle distributions (**Figure 65**) reveal that cracks predominantly initiate at angles between 40° and 60° in both air and PWR, suggesting that the crack initiation mechanisms remain largely unaffected by the testing environment.

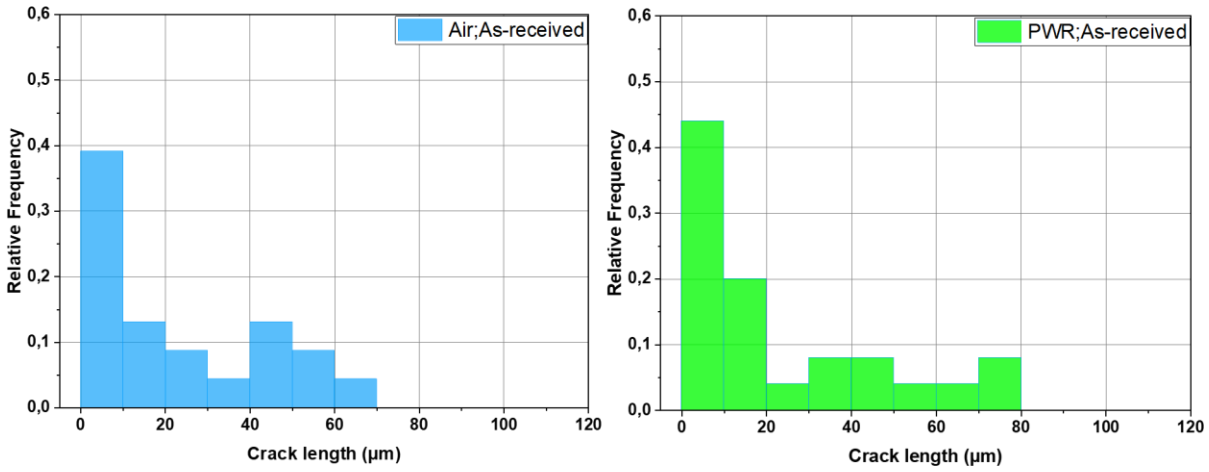

Figure 64: Distribution of the secondary crack length between the samples tested in air and the PWR environment.

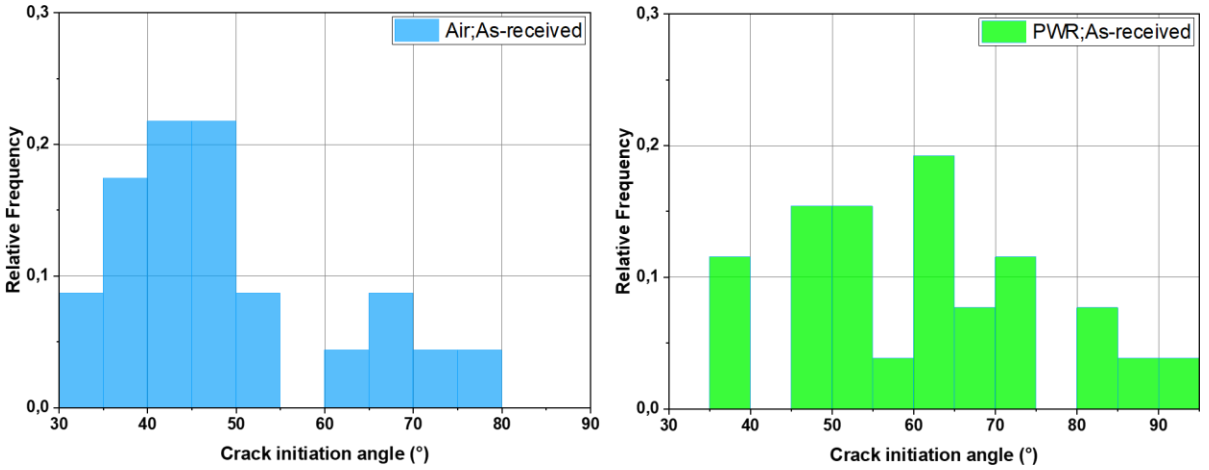

Figure 65: Distribution of the secondary crack initiation angle between the samples tested in air and the PWR environment.

III.2.1.2. Analysis of the propagation

EBSD analysis of crack paths was conducted to evaluate the influence of the environment on crack tip plasticity. An EBSD map of the axial cross-sectional surface with the cracks along the grains is observed (**Figure 66 a and c**). The cracks observed in both environments predominantly followed the {1 1 1} slip plane of the slip system (**Figure 66 a and c**). This behavior was also observed in austenitic stainless steel [Huin, 2013].

In the air environment, the crack path shows features of mixed Stage I and Stage II behavior (**Figure 66a**). Stage I is suggested by segments of the crack path that remain closely aligned

with the {111} slip planes, whereas Stage II is indicated by the transgranular mode of propagation.

However, determining the exact crack initiation mechanism in the Pressurized Water Reactor (PWR) environment remains more complex. Some studies on Alloy 690 and its weld metals have reported the occurrence of intergranular (IG) cracking under high-temperature water exposure, often associated with oxidation-assisted or ductility-dip cracking phenomena [Gao et al., 2020], suggesting that similar mechanisms could potentially contribute to crack initiation under fatigue loading in PWR conditions. Although such processes could potentially contribute to crack initiation under fatigue loading in PWR conditions, the present observations indicate that the initiation mechanism in both air and PWR environments remains predominantly crystallographic. Cracks preferentially initiate along {111} slip planes, and Schmid factor analysis shows that most secondary cracks originate in grains with high Schmid factors (≈0.41) (**Figure 61**), confirming that slip activity is the primary driver of crack initiation.

However, in the PWR environment, oxide formation was observed over the persistent slip bands (PSBs) at the specimen surface, which may promote slip irreversibility and facilitate crack initiation (**Figure 60b**). This suggests that, while the underlying crystallographic nature of initiation seems similar in both environments, the presence of oxides in PWR can modify the local conditions at the surface and may influence the very early stages of fatigue damage. To better understand the interaction between oxides and the PSB initiation mechanism, interrupted tests performed at the earlier cycles would be required . However, **Figure 66 a and c** show that the secondary cracks propagate transgranularly in both air and PWR environments. Only a limited portion of one secondary crack exhibits intergranular propagation, suggesting that while oxidation-assisted effects may locally influence crack paths in PWR, the dominant propagation mode remains transgranular under the present testing conditions.

The KAM images qualitatively suggest a slightly higher level of strain localization in the PWR environment, especially at the specimen surface and along the crack path (**Figure 66(b) and (d)**). Since all specimens were prepared following the same surface-finishing procedure, with controlled surface roughness before testing, the observed differences can be attributed to environmental effects rather than initial surface conditions. the green-highlighted regions in the KAM maps clearly show enhanced local misorientations, reflecting stronger plastic strain gradients near the surface in PWR compared to air. This may be linked to the presence of oxides on the surface in the PWR environment (**Figure 60a**), which can alter the local mechanical response at the surface. For example, by promoting slip irreversibility, enhancing stress concentrations, or inducing local oxide-induced roughness. However, further dedicated

analyses of the metal–oxide interface are required to confirm the relevance of such a mechanism.

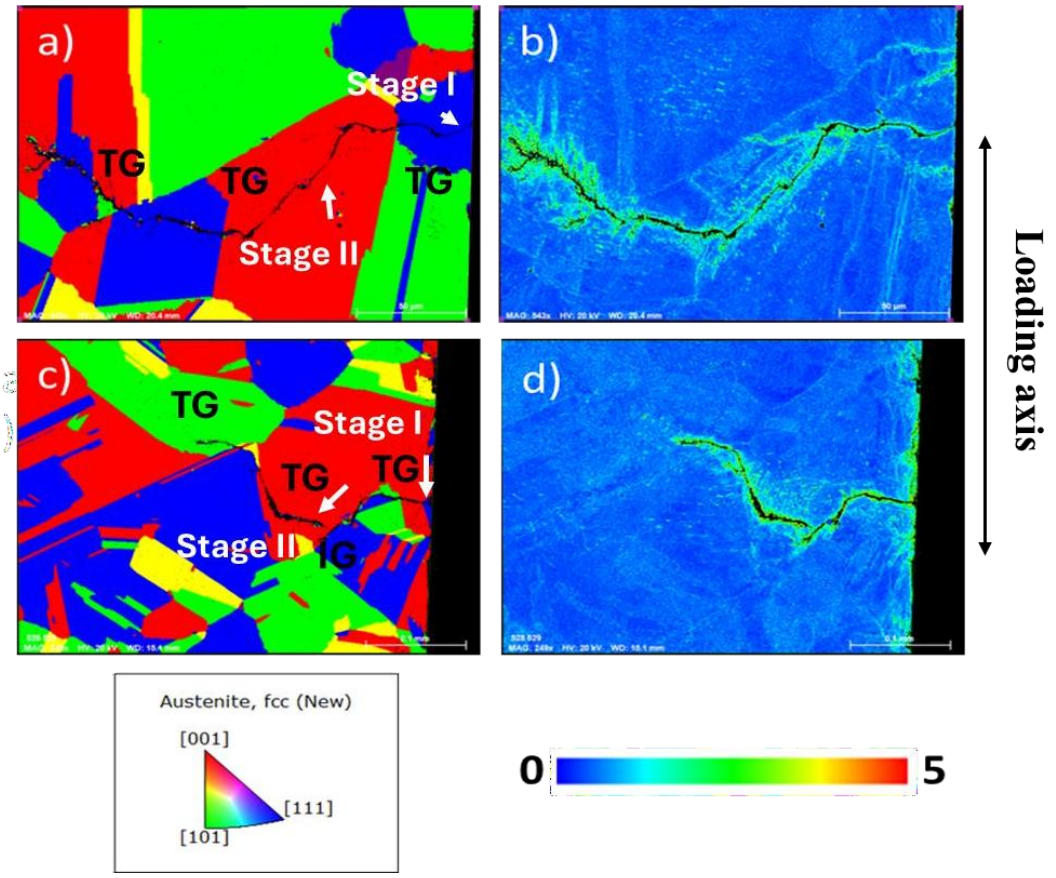

Figure 66: EBSD analysis of the secondary cracks on the failure samples under 0.45% strain amplitude at 300°C in different environments: IPF maps in (a) Air, (c) PWR; KAM maps in (b) Air, (d) PWR.

The **Figure 67** compares the KAM angle distributions measured on the as-received Alloy 690TT surface after low-cycle-fatigue tests conducted in air (blue curve) and in a simulated PWR environment (green curve), specifically in the zone of the secondary cracks as shown in **Figure 66**.

Both distributions are sharply peaked at very low misorientation angles (< 1°) and decay rapidly toward larger angles. The near-perfect overlap of the two curves shows that exposure to the PWR environment during cycling does not measurably increase the overall lattice when compared with testing in air. The slight broadening of the green curve beyond ~0.8° is within the statistical scatter of the measurement and suggests, at most, a marginal increase in localized strain under PWR conditions. Overall, the KAM analysis indicates that the degree of localized

strain around the crack path is broadly similar in air and PWR tests of the as-received material. While this suggests that environmental effects on strain localization are not pronounced, they cannot be ruled out entirely. A comparable analysis in vacuum, where oxidation and corrosion effects are absent, would provide a more definitive baseline for assessing the role of the environment.

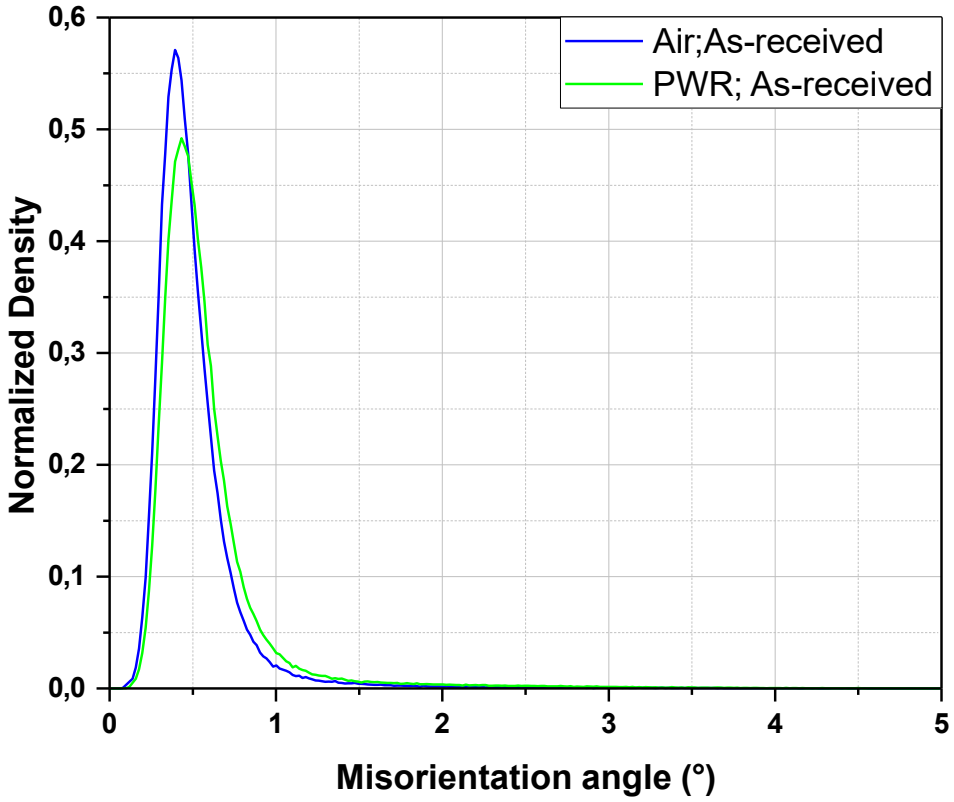

Figure 67: Distribution of the KAM angle of the As-received specimens tested in air and the PWR environment at ε_a = 0.45%; $\dot{\varepsilon}$ = 0.02%/s in the secondary crack zone.

The distributions reveal that the overall patterns in both environments are quite similar, indicating a consistent crack behavior regardless of the testing conditions.

These observations suggest that the fundamental crack growth characteristics for the as-received Alloy 690TT samples do not vary significantly between air and PWR conditions.

The fatigue tests performed in air and PWR environments revealed that the fatigue life of Alloy 690TT remains nearly identical under both conditions, even at the severe PWR environmental condition (F_{en} = 2.5). This observation indicates that, unlike austenitic stainless steels, Alloy 690TT exhibits a very limited environmental sensitivity under low-cycle fatigue.

Two hypotheses can therefore be proposed based on these observations:

- The environment has a negligible effect on the fatigue resistance of Alloy 690TT, or
- The same damage mechanisms are active in both air and PWR conditions.

To clarify these points and isolate the intrinsic material response, additional tests were carried out under vacuum conditions, where no environmental interactions occur.

III.3. FATIGUE BEHAVIOR IN VACUUM

The following section presents the results of fatigue tests performed in vacuum at 300 °C under total strain-controlled conditions ($R_\varepsilon = -1$) using a triangular waveform. The strain amplitudes ranged from ±0.3 % to ±0.6 %, corresponding to the same loading conditions as those used in air and PWR environments. These experiments were conducted to characterize the intrinsic cyclic response of Alloy 690TT in the absence of environmental effects. Particular attention is given to the fatigue life, cyclic stress–strain evolution, and fracture surface observations, in order to directly compare the vacuum results with those obtained in air and PWR environments.

III.3.1. Fatigue life and cyclic behavior in vacuum

The **Figure 68** compares the fatigue life of Alloy 690TT at 300 °C in different environments (air, PWR, and vacuum) with the reference NUREG CR-6909 curve. The results obtained in vacuum (magenta symbols) show significantly longer fatigue lives (by almost a factor of three) than those in both air and PWR environments for the same strain amplitude. This clearly demonstrates that the environment has a detrimental effect on fatigue life. However, the lifetimes measured in air and PWR environments are nearly identical, even up to a F_{en} of 2.5, indicating that the environmental effect is of comparable magnitude in air and PWR environment for Alloy 690TT.

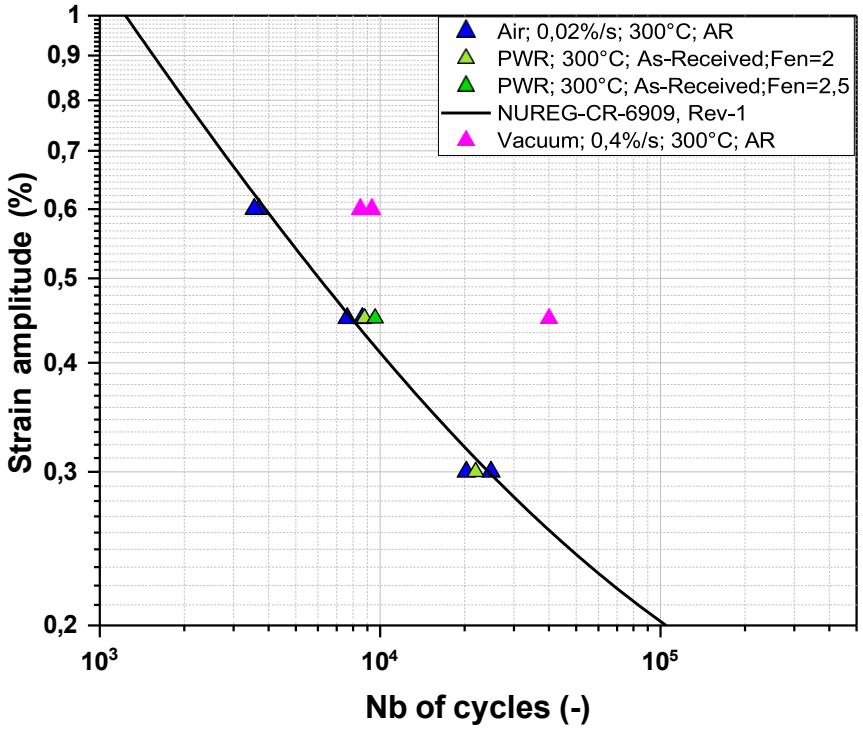

Figure 68: ε-N curve of Alloy 690TT in air, PWR, and vacuum at 300°C.

The **Figure 69** shows the evolution of maximum stress with the number of cycles at 300 °C under a total strain amplitude of 0.6% in air and vacuum environments. In vacuum, the material exhibits a clear two-stage hardening response: an initial primary hardening regime characterized by a rapid increase in maximum stress, followed by a secondary hardening regime with a reduced slope but still a continuous increase. This progressive hardening behavior is sustained over a larger number of cycles (~ 9000 cycles) in vacuum. Additionally, there is an influence of strain rate on the rate of hardening after 100 cycles, which is similar to that of air, i.e., at 0.02%/s, higher hardening occurs, while at 0.4%/s, comparatively lower hardening is observed.

The tests conducted in air follow a similar hardening trend, with both primary and secondary stages evident, but the total life is much shorter (~ 3500 cycles). The similarity of the stress evolution curves in both environments indicates that the underlying cyclic deformation mechanisms, probably a similar dislocation structure as in air at 300°C, dislocation pinning, and planar arrays of dislocation in the secondary hardening phase, as these are not affected by the environment.

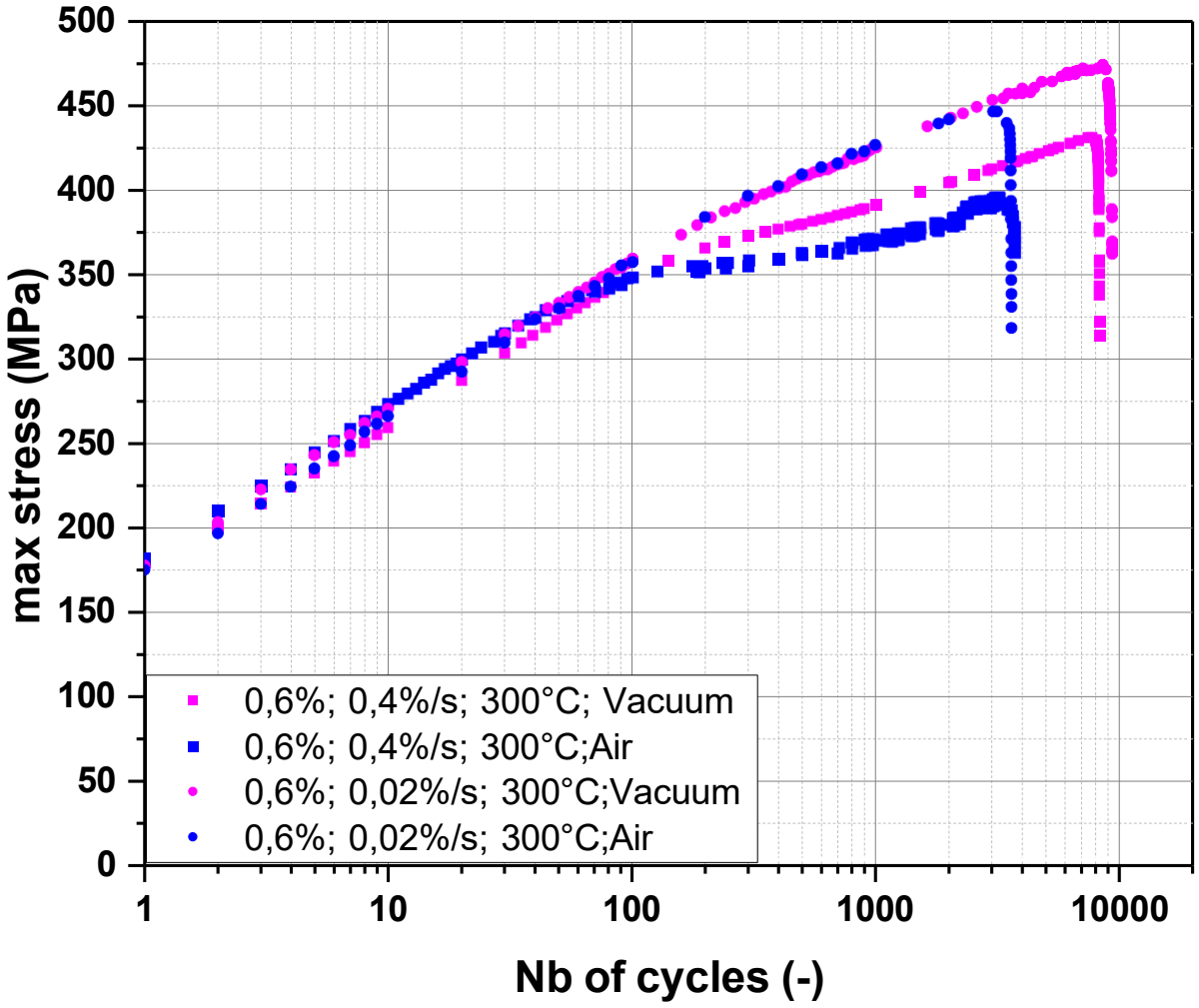

Figure 69: Evolution of maximum stress during cyclic loading in vacuum and air at 300°C at different strain rates.

Figure 70 (a–c) show the overall fracture surfaces of Alloy 690TT tested at 300 °C under strain-controlled conditions (ε_a = 0.45 %, $\dot{\varepsilon}$ = 0.02 %/s) in air, PWR, and vacuum environments, respectively. The corresponding magnified regions, shown in **Figure 70 (d–f)**, highlight the detailed striation morphology for each condition. In air and PWR **(Figure 70 d–e)**, the fracture surfaces exhibit broader and more widely spaced fatigue striations (orange arrows), whereas in vacuum (**Figure 70f**), finer and more closely spaced striations (magenta arrows) are observed. This difference suggests that environmental exposure (air or PWR) may enhance crack-tip

plasticity and oxidation-assisted damage, resulting in larger striation spacing compared to purely mechanical propagation observed in a vacuum.

The evolution of striation spacing with crack depth for these conditions is presented in the following graph, providing a quantitative assessment of the variation in crack growth rate along the propagation path.

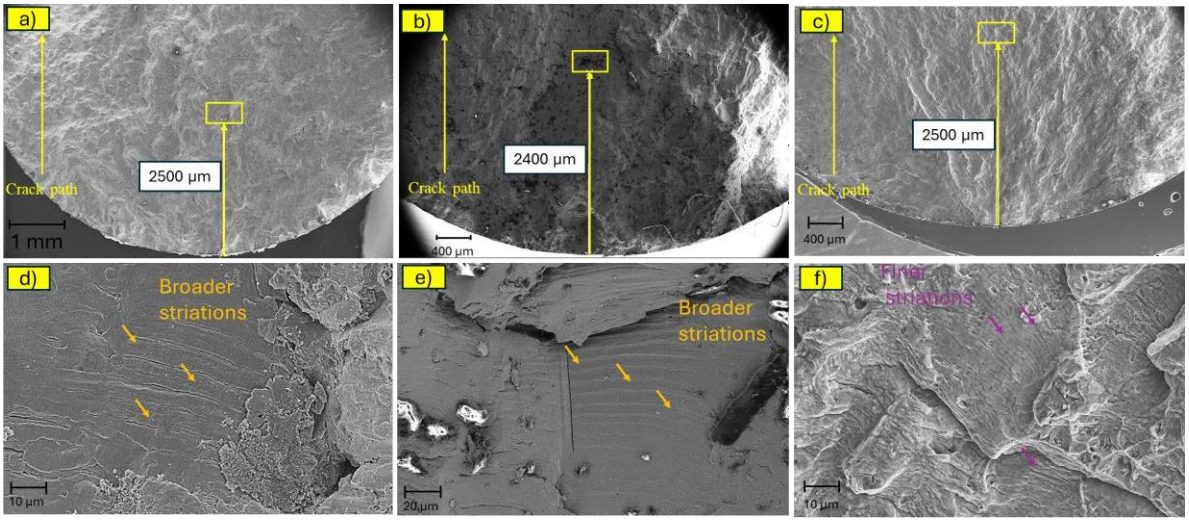

Figure 70: Fracture surfaces of Alloy 690TT tested at ε_a = 0.45%, $\dot{\varepsilon}$ = 0.02%/s, 300°C:in (a, d) air; (b, e) PWR environment; and (c, f) vacuum (orange arrows: striations in air and PWR, magenta arrows: striation in vacuum).

The **Figure 71** shows the variation of striation spacing with crack depth for Alloy 690TT tested at 300 °C in air, PWR water, and vacuum. In vacuum (magenta), the striation spacing remains relatively small and increases only slightly with crack depth, rarely exceeding 3–4 µm even at depths beyond 2000 µm. This indicates that crack advance per cycle is comparatively lower compared to air and PWR. In air (blue) and PWR water (green), the striation spacing increases steadily with crack depth, reaching values of 10–15 µm at depths of ~3000–3500 µm.

Overall, this comparison shows that while Alloy 690TT exhibits finer striations in vacuum, exposure to air and PWR water leads to progressively coarser striations with depth, confirming the accelerating role of environmental interactions in fatigue crack propagation.

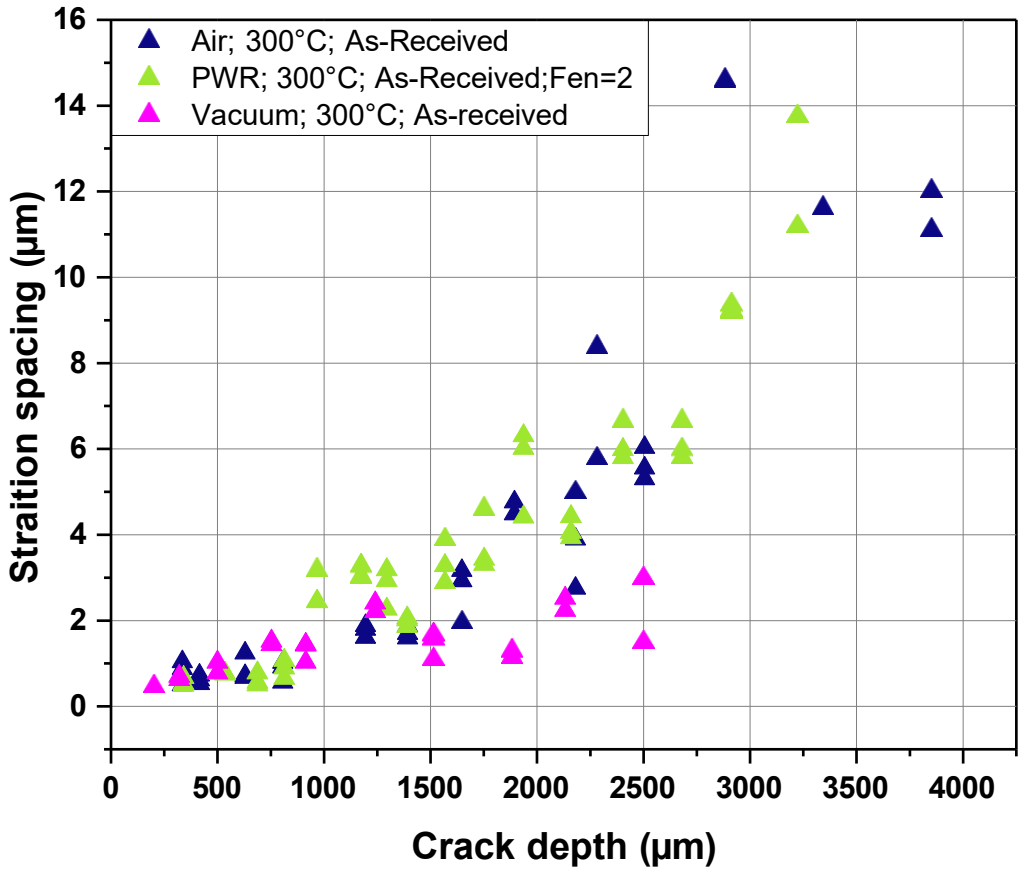

Figure 71: Crack depth vs Striation spacing in air, PWR, and vacuum environment at 0.45%.

The **Figure 72** presents the fatigue crack growth rates of Alloy 690TT at 300 °C in vacuum, air, and PWR environments expressed by the Paris law relation (da/dN vs ΔK_ε) and one sample was considered per condition. In vacuum (magenta symbols), the crack growth rates are consistently the lowest across the ΔK_ε range studied. The fitted Paris slope is only $m \approx 0.0015$, meaning that the crack growth rate is nearly insensitive to ΔK_ε and remains almost constant with increasing driving force. This is consistent with the fractographic observations, where striations in the vacuum condition remain fine and nearly uniform with crack depth. In contrast, in air and PWR the slopes are much steeper ($m \approx 6.718$ and $m \approx 26.288$, respectively), reflecting the fact that striations in these environments widen progressively with crack depth, demonstrating the accelerating effect of environment on crack propagation.

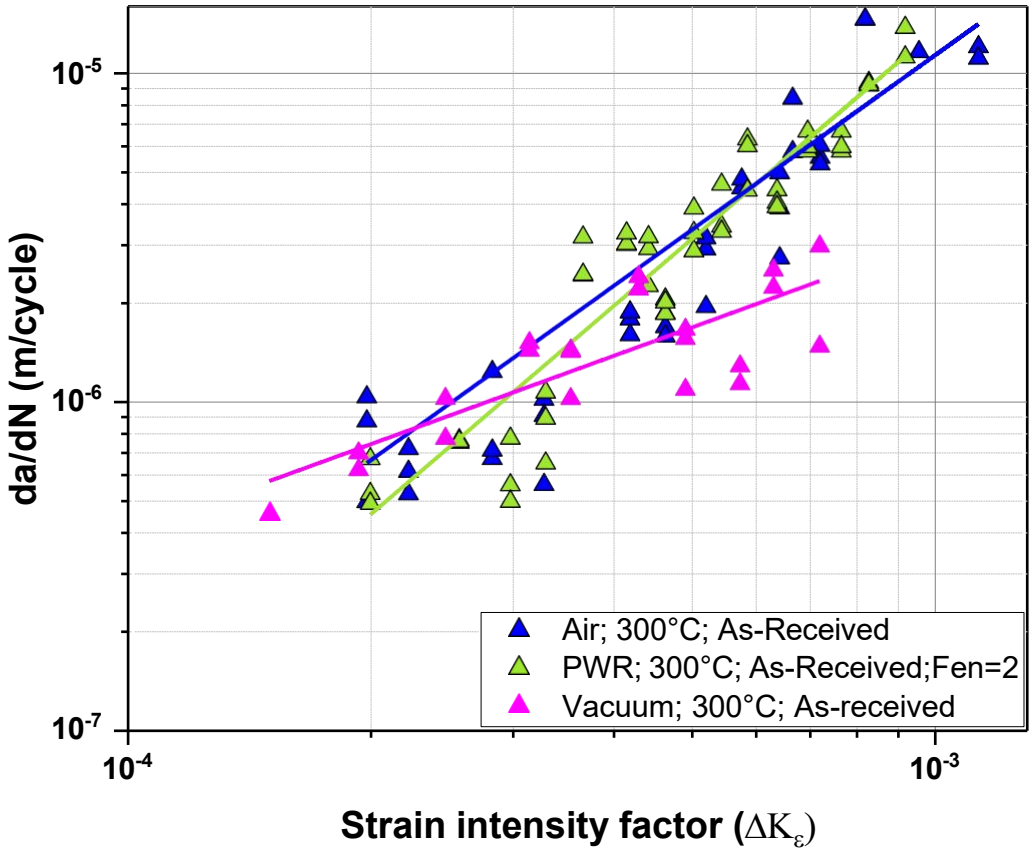

Figure 72: Crack growth rate curves in air, PWR, and vacuum environment for tests conducted at ε_a = 0.45%.

The **Figure 74** compares the linear crack density (LCD) of Alloy 690TT tested at 300 °C in air, PWR water, and vacuum. In both air and PWR environments, the LCD values are significantly higher at 0.45%, with an average of 6 cracks/mm of gauge length observed. By contrast, in vacuum the LCD is much lower (~ 2 cracks/mm), indicating far fewer cracks initiating along the specimen surface.

This clear reduction in crack density in vacuum, despite the significantly longer fatigue life, highlights the suppression of environmental effects such as oxidation, which are enhanced in both air and PWR environments and promote multiple crack initiation sites. In contrast, under vacuum conditions, fatigue damage is primarily governed by intrinsic slip activity and transgranular crack growth, leading to fewer surface cracks and an extended fatigue life.

III.3.2. Microstructural characterization of secondary cracks in vacuum

III.3.2.1. Analysis of the initiation

The Error! Reference source not found. shows the surface features of Alloy 690TT tested in v acuum at 300 °C, emphasizing the role of persistent slip bands (PSBs) in fatigue crack initiation. In the early stage (**Figure 73 a**), well-developed PSBs aligned along crystallographic slip planes are visible, producing distinct slip traces on the specimen surface. These traces are not necessarily parallel to the axial loading direction, reflecting the crystallographic nature of slip in FCC alloys. As cycling progresses, microcracks nucleate preferentially along PSBs, as seen in (**Figure 73 b**). The crack path follows the orientation of the PSBs, which are inclined relative to the loading axis, indicating that initiation is governed by local slip activity rather than global stress direction. At higher magnification (**Figure 73 c**), characteristic intrusions and extrusions are observed along PSBs, resulting from irreversible slip localization. These surface relief features serve as stress concentrators and precursors for crack formation, confirming that fatigue initiation in vacuum occurs predominantly through the PSB mechanism, without interference from environmental oxides as observed in PWR conditions.

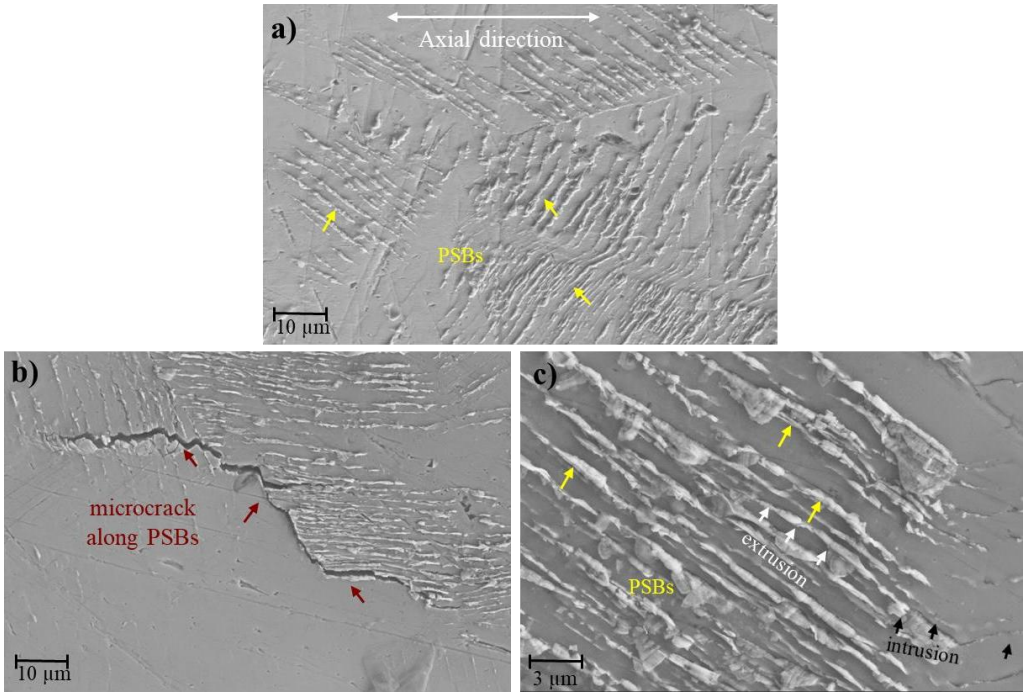

Figure 73: Surface morphologies showing the surface crack initiation features at a ε_a = 0.45% at 300 °C in vacuum: a) Large surface region showing well-defined PSBs; b) Microcrack initiation directly along PSBs ; and c) Higher magnification view of extrusion–intrusions.

The **Figure 74** shows the variation of LCD with strain amplitude for Alloy 690TT tested at 300 °C in air, PWR environment, and vacuum and one sample was considered per condition. The LCD at 0.45% is among the three conditions, with the vacuum tests exhibiting the lowest LCD values (~ 2 cracks/mm), confirming reduced crack nucleation and slower damage accumulation in the absence of environmental interactions. In contrast, both air and PWR environments show significantly higher LCD (~ 6 cracks/mm), reflecting the detrimental influence of the environment on crack initiation. Overall, these results demonstrate that the environment influences surface damage kinetics under low-cycle fatigue conditions at 300 °C.

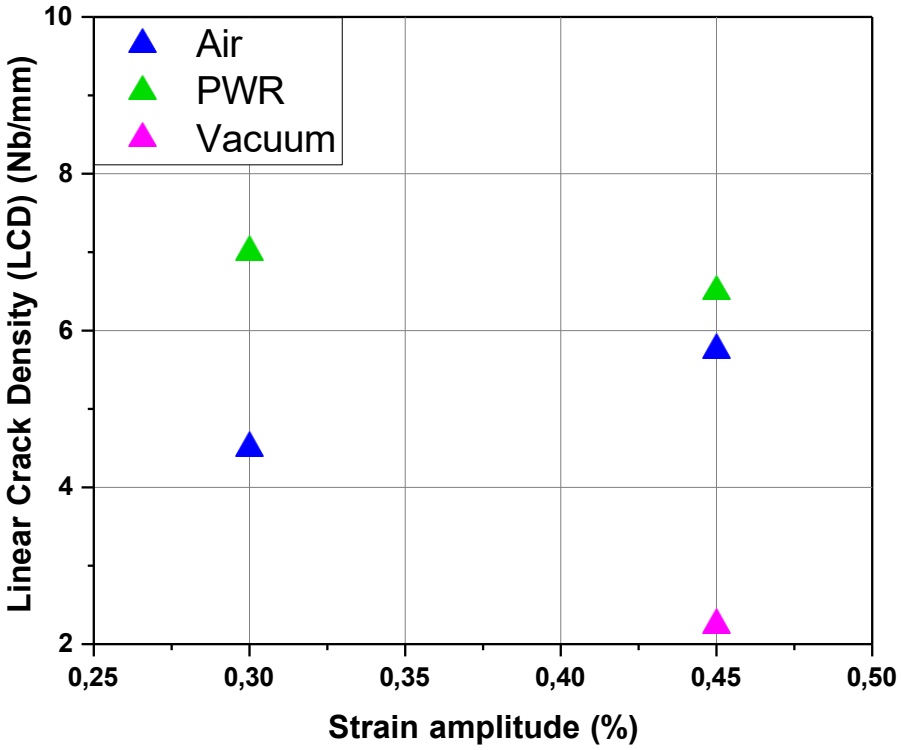

Figure 74: LCD vs strain amplitude tested in air, PWR and vacuum environment at 300° C.

The **Figure 75** shows the distribution of crack depth, crack length, and crack initiation angle for Alloy 690TT tested at 300 °C in vacuum, air, and PWR environments. One sample per condition was considered for this analysis.

In all three environments (air, PWR, and vacuum) (**Figure 75a**), the maximum relative frequency of crack depth occurs in the 0–10 µm range, reaching values of ~0.55. Under vacuum conditions, however, the majority of cracks remain shallow, with ~0.75 of the relative frequency concentrated in the 0–20 µm range, which is higher compared to air and PWR (~0.55–0.65) despite the higher plastic strain energy observed under these conditions. The frequency decreases rapidly with increasing crack depth, falling to ~0.1 for depths above 30

µm. For depths greater than 60 µm, only the air and PWR environments exhibit nonzero frequencies, both below 0.1, while in vacuum no cracks are observed beyond this range.

The **Figure 75b** shows the maximum relative frequency of crack length occurs in the 0–10 µm range, reaching values of ~ 0.40 - 0.55. In vacuum, the majority of cracks remain short consistent with the lower CGR, with ~0.75 of the relative frequency concentrated below 20 µm, which is higher than in air and PWR (~0.60 - 0.65). The frequency decreases rapidly with increasing crack length, dropping to ~0.1 for cracks longer than 30 µm. For crack lengths above 60 µm, only the air and PWR environments exhibit nonzero frequencies, both below 0.1, while in vacuum no cracks are observed beyond this range.

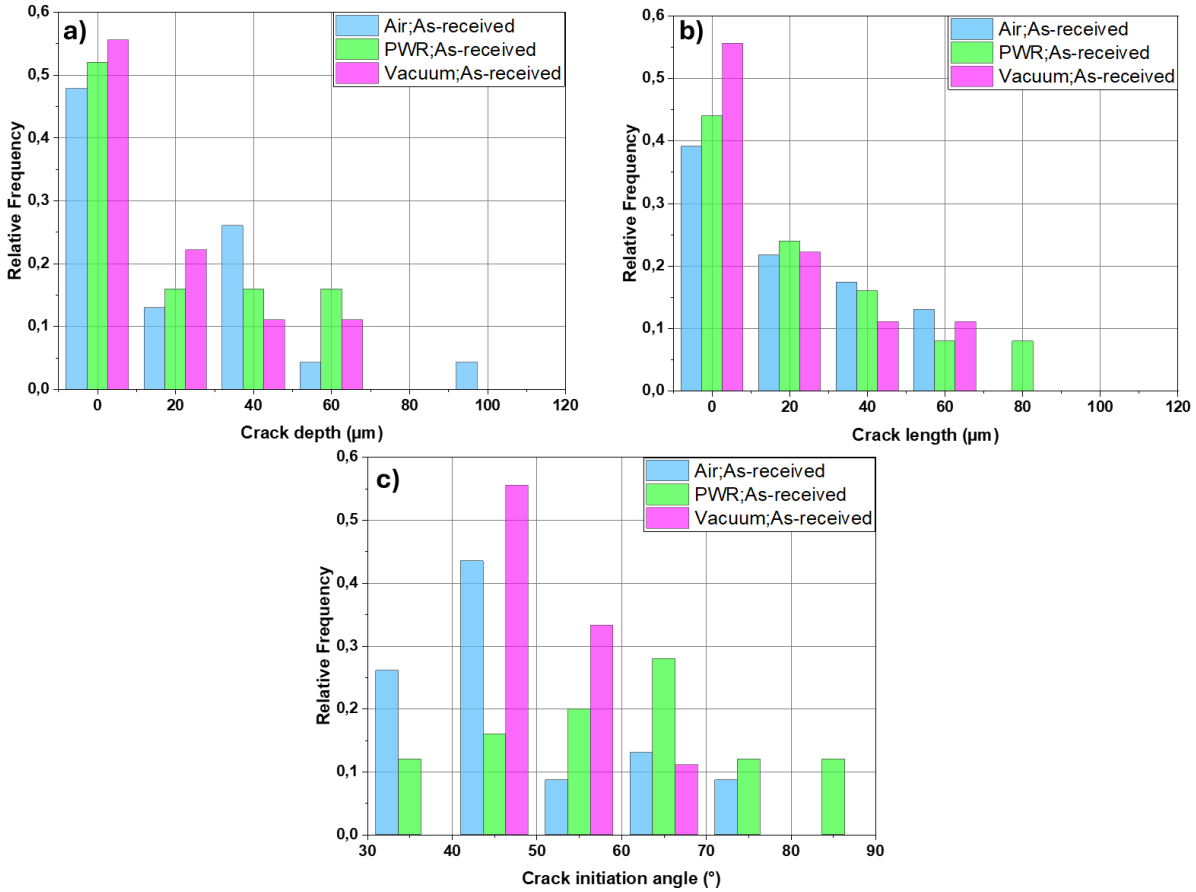

Figure 75: Distribution of secondary (a) cracks depth, (b) crack length and (c) crack initiation angle between the samples tested in air, PWR and vacuum environment at 300°C.

The **Figure 75c** shows the distribution of the crack initiation angle between the three environments. In vacuum, the distribution is strongly concentrated, with a peak at 45° where the relative frequency exceeds ~0.5. In air, the peak occurs at 40° (~0.4), but the distribution is broader, extending up to ~70°, indicating more scattered initiation orientations. In PWR, the

distribution is more dispersed, with a peak at 60° (~0.32) and lower frequencies across other angles. This shows that cracks in vacuum initiate in a more uniform and shear-dominated orientation, while in air and PWR the initiation angles are more widely spread due to environmental interactions influencing local crack nucleation.

III.3.2.2. Analysis of the propagation

In vacuum, the crack path is relatively straight (**Figure 76a**), with propagation occurring through both grains without significant deflection. The EBSD orientation map shows that the crack advances in a more uniform manner, in contrast to the irregular, highly deflected crack trajectories observed in air and especially in PWR (**Figure 66**). The corresponding KAM map (**Figure 76b**) indicates localized strain concentration along the crack path, which appears of similar magnitude to that observed in air, although the interpretation is partly limited by image noise near the crack region. Overall, the crack propagation in vacuum is similar to that in air and the PWR environment, which involves transgranular propagation.

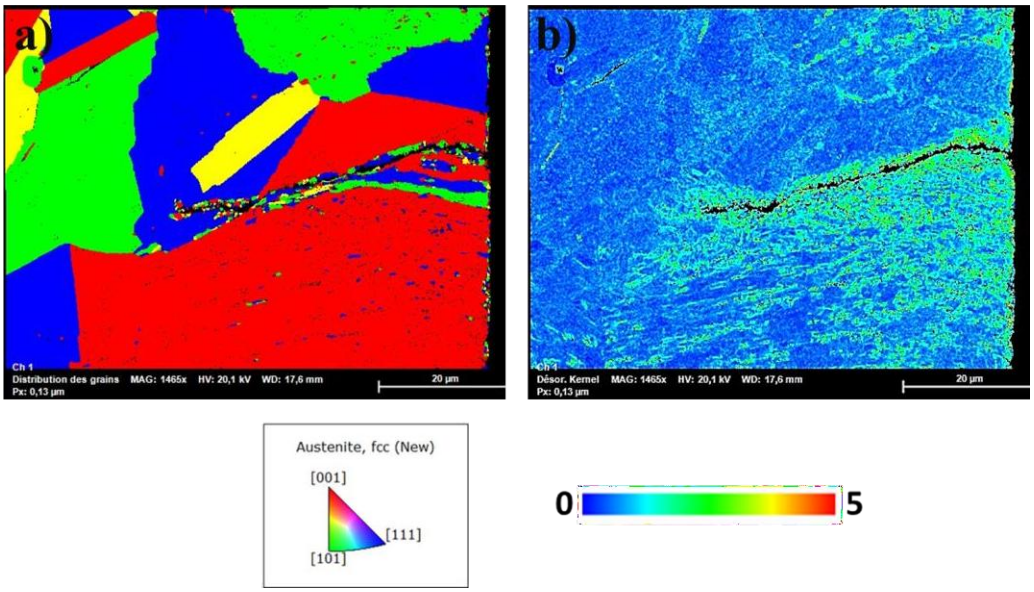

Figure 76: EBSD analysis of the secondary crack on the failure sample under 0.45% strain amplitude at 300°C in vacuum: (a) Inverse pole map, (b) KAM map.

The fatigue tests performed in vacuum demonstrated that the fatigue life of Alloy 690TT is approximately three times higher than that in air and PWR environments. This clearly indicates the detrimental influence of the environment on fatigue resistance. The lower crack growth rates

and the reduced number of surface cracks observed under vacuum conditions further confirm that the environmental effects in air and PWR, such as oxide formation and environmentally assisted crack propagation, contribute to the reduction in fatigue life. However, tests conducted in PWR up to a F_{en} of 2.5 showed no further degradation compared to air, indicating that the environmental effect is similar in both conditions for this alloy.

III.4. SUMMARY

- Cyclic stress-strain behavior
    - At 25°C in air, Alloy 690TT exhibits initial cyclic hardening followed by stabilization, while at 300°C there is continuous cyclic hardening throughout life, attributed to the formation of nano-twins during secondary hardening.
    - The cyclic stress-strain response and dynamic behavior are essentially insensitive to environment, with air, vacuum, and PWR displaying similar trends.
    - In vacuum, hardening trends persist over more cycles due to the extended total lifetime.
- Total fatigue life
    - Fatigue life at 25°C and 300°C in air are comparable, reflecting minimal temperature dependence in total life under the strain rates 0.4%/s – 0.02%/s.
    - No difference in total fatigue life is observed between air and PWR environments for Fen values of 2 and 2.5, confirming similar environmental effects.
    - Lifetimes in vacuum are significantly longer (up to ~3× higher) than in air or PWR. clearly indicating the detrimental influence of the environment (both air and PWR water) on the fatigue life of Alloy 690TT.
- Dynamic strain aging
    - Serrated flow observed in hysteresis loops at 300 °C.
    - TEM revealed planar dislocation arrangements and pinned dislocations at 300 °C, consistent with DSA-like mechanisms.
- Energy-based analysis
    - Energy-based analysis (W_p curves) shows overlap at 25°C (0.4%/s) and 300°C (0.02%/s), and only slight scatter at higher strain rates and cycle numbers; W_p is largely insensitive to both temperature and strain rate for the as-received alloy.
    - In the final 5–10% of life, a sharp drop in W_p marks the onset of rapid crack propagation, indicating failure occurs with similar total plastic energy absorbed across conditions.

- Microstructural characterization
    - Schmid factor analysis reveals cracked grains have consistently higher values (~0.48–0.49) than non-cracked grains (~0.38–0.41), independent of environment.
    - EBSD KAM maps show similar strain localization around cracks for air and PWR, with strong localization near the surface in PWR (related to oxide formation), and localization in vacuum conditions could not be confirmed due to noise in the KAM images; further analysis is needed.
    - Fractography identifies predominantly transgranular fracture in all environments, but vacuum samples show finer, more uniform striation spacing; in air and PWR, striations widen with increasing crack depth.

Overall, the results show that, when referenced to vacuum conditions, both air and PWR environments lead to a comparable reduction in fatigue life, roughly by a factor of three, confirming that environmental effects are of similar magnitude up to $F_{en} = 2.5$. The as-received Alloy 690TT thus exhibits nearly identical fatigue behavior in air and PWR water, with no additional degradation specific to the PWR environment. The combined use of energy-based analysis and detailed microstructural characterization provides a consistent understanding of the unaged fatigue behavior of Alloy 690TT, establishing a solid reference for evaluating the subsequent influence of thermal aging on its mechanical and environmental resistance.

IV. Effect of thermal aging on the microstructure of the Alloy 690TT

This section presents the influence of accelerated thermal aging on the microstructural and mechanical evolution of Alloy 690TT. The analysis focuses on how exposure at 420 °C alters the character of the precipitates and the morphology and chemistry of precipitates within the alloy. Particular attention is given to the coarsening behavior of carbides, the development of short-range ordering (SRO), and their correlation with local hardening effects. The mechanical response is assessed through micro-hardness and nano-indentation measurements to quantify the hardening associated with aging-induced microstructural changes. Together, these investigations provide a detailed understanding of the aging mechanisms governing the long-term stability and performance of Alloy 690TT under nuclear service conditions.

Contents

IV.1. MICROSTRUCTURAL ANALYSIS

Following the detailed investigation of the low-cycle fatigue behavior of the as-received Alloy 690TT, it becomes essential to understand how thermal aging influences the alloy's microstructure, particularly given the alloy's critical role in long-term structural applications in nuclear power plants. As many reactor components approach or exceed 40–60 years of operation, thermal exposure at intermediate temperatures can lead to subtle yet impactful changes in the material's internal structure. These changes may alter mechanical performance and fatigue response.

This chapter investigates the evolution of microstructural features in Alloy 690TT subjected to accelerated thermal aging treatments representative of 40 to 80 years of service at 325°C (**Table 7**). Through a combination of scanning electron microscopy (SEM), transmission electron microscopy (TEM), and hardness measurements, the formation and growth of intergranular and intragranular precipitates, grain boundary alterations, and the possible onset of short-range ordering (SRO) are characterized. Understanding these changes is critical for evaluating the long-term performance and safety margins of structural components made of Alloy 690TT in nuclear environments.

IV.1.1. Grain size and grain boundaries evolution

At 325°C, the actual operating temperature of PWRs, no significant changes in grain size are expected when the Alloy 690TT is exposed to longer durations [Bullens et al., 2018]. However, since the accelerated aging temperature is higher, it is essential to verify whether any changes in grain size occur. Assuming a hypothetical monotonous grain size evolution, it was decided to investigate the maximum aging time of this study to cover all the intermediate times.

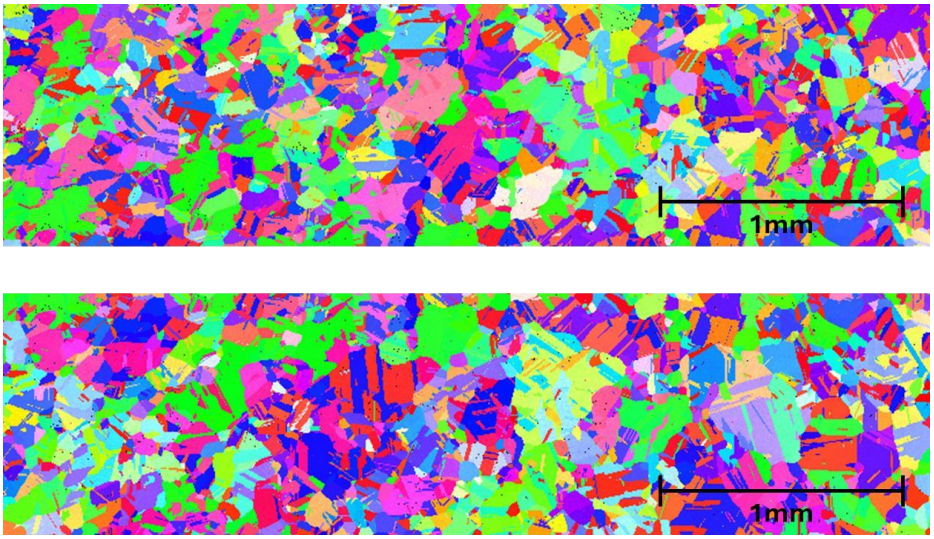

Figure 77: Inverse pole images (IPFZ) from EBSD of the grain structures, a) As-received and b) Aged: 80 years.

The **Figure 78** shows the distribution of grain size before and after 80 years of accelerated aging of the inverse pole images of the microstructure (**Figure 77**). By investigating the maximum aging time, the intermediate aging times are also covered assuming a monotonic evolution. It is observed that the grain size remains constant during the 5400 hours of aging at 420°C. Specifically, the median grain size for both the as-received and aged samples is approximately 75 µm (**Table 8**).

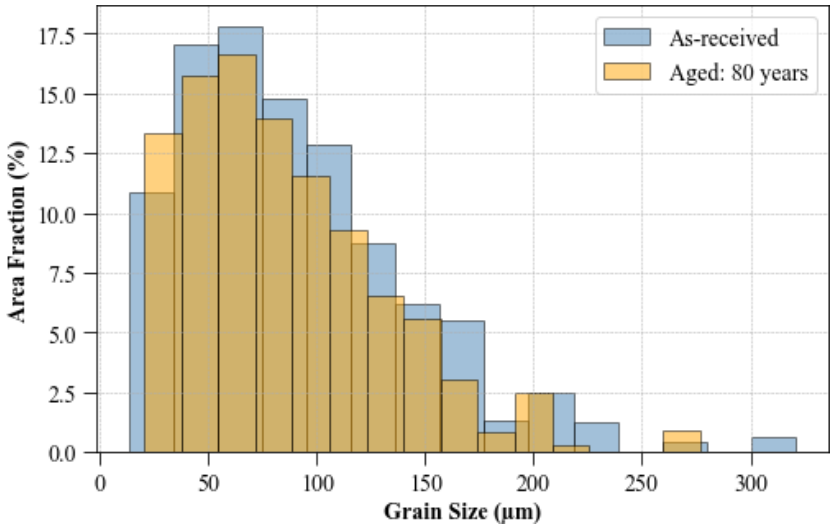

Figure 78: Grain size distribution: before aging and after aging at 420°C for 5400 hours (80 years).

Concerning the evolution of the grain boundaries, the Coincidence Site Lattice (CSL) boundary fractions, such as ∑3 (twin boundaries), ∑5, ∑7, and ∑9, characterized as high-angle grain boundaries are compared before and after accelerated aging in the **Table 8**. It can be observed that the accelerated thermal aging did not modify the proportions of CSL in the material.

Sample	Average Grain size (µm)	Median Grain size (µm)	∑ 3 (%)	∑ 5 (%)	∑ 7 (%)	∑ 9 (%)
As-received	90	75	84	0.1	0.2	8
Aged: 80 years	86	74	85	0.1	0.2	7

Table 8: Summary on the grain size and grain boundary angle of As-received and the Aged sample.

All these results indicate that aging at 420°C has not induced major changes in grain size or boundary characteristics, which aligns with the objective of simulating realistic aging conditions at 325°C.

IV.1.1.1. Intergranular precipitates

While previous studies have qualitatively identified these intergranular precipitates, there is limited quantitative data on their evolution in terms of size, density, and distribution during long-term aging. This lack of detailed measurement limits the ability to fully understand the microstructural evolution, underscoring the importance of systematic analysis.

The **Figure 79** illustrates the evolution of the intergranular precipitates throughout the aging process. Initially (**Figure 79a**) the precipitates are fine and aligned in a narrow, linear pattern along the grain boundaries. As accelerated thermal aging progresses (**Figure 79b, c, d, e**), the precipitates grow, and the grain boundaries exhibit increased waviness. In the literature, this movement of the grain boundaries in Alloy 690TT due to thermal aging is attributed to Diffusion-Induced Grain Boundary Migration (DIGM) [Balluffi and Cahn, 1981, Lim et al., 2019a, Mouginot et al., 2017a, Xue and Marquis, 2022]. Specifically, diffusion of chromium atoms, which tends to form precipitates and oxides near or along the grain boundary, creates a

chemical potential gradient. The chemical potential gradient, created by solute diffusion, drives grain boundary motion to minimize the system's free energy [Persaud et al., 2019, Xue and Marquis, 2022]. It appears in this study that the movement of the grain boundaries does not imply a growth of the grains (**Table 8**).

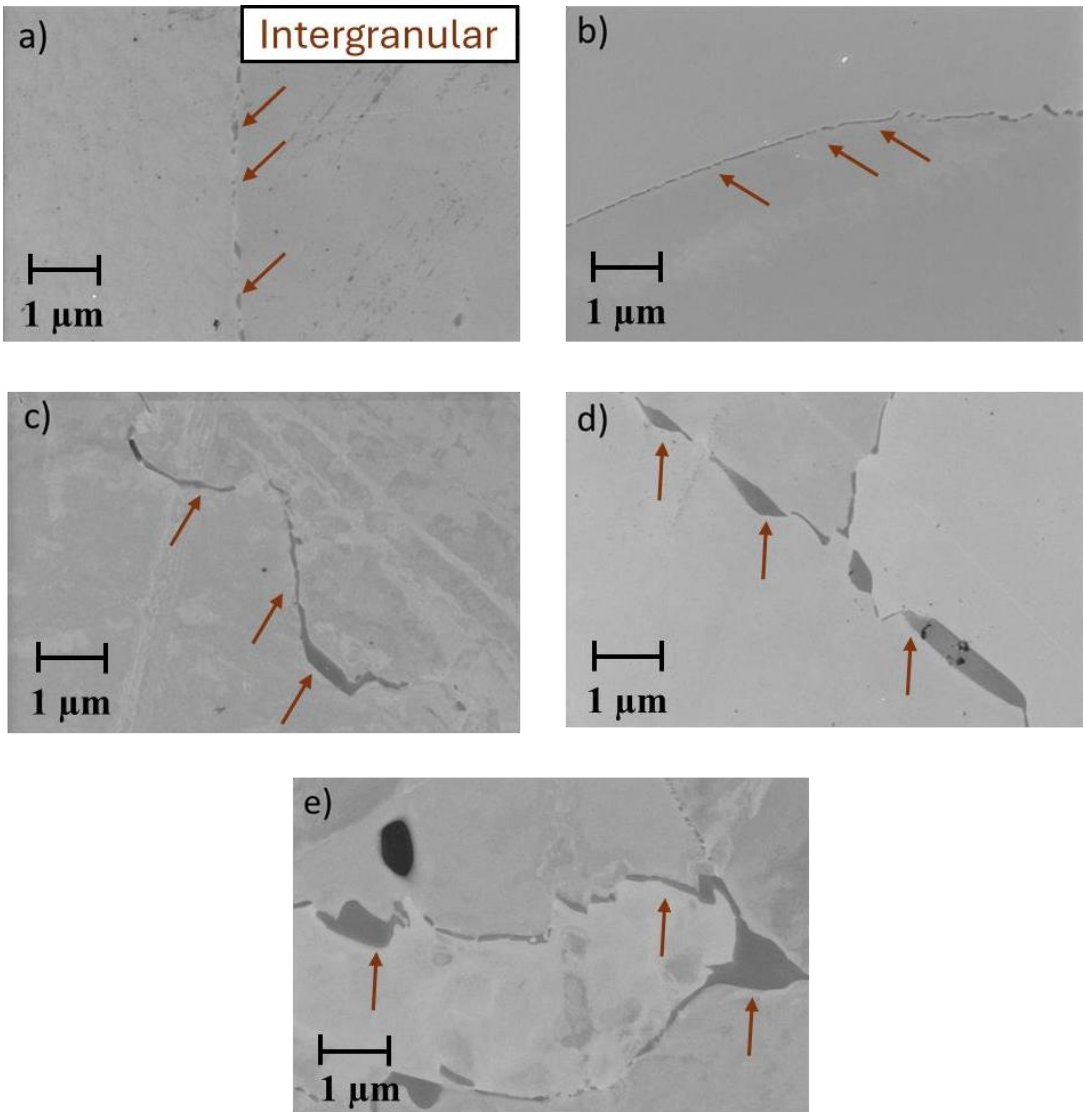

Figure 79: Representative SEM micrographs of $M_{23}C_6$ intergranular precipitates in Alloy 690TT thermally aged at 420°C: a) as-received, b) 20 years, c) 40 years, d) 60 years and e) 80 years (brown arrows indicate intergranular precipitates).

The **Figure 80** and **Figure 81** give a more quantitative view of the intergranular precipitate evolution during accelerated aging. The **Figure 80a** depicts the area occupied by intergranular precipitates. Each square marker represents the average precipitate area, while the error bars correspond to a standard deviation equal to 50% of the mean (coefficient of variation = 0.5).

Initially, from 0 to 30 years, the average area of the intergranular precipitates remains relatively small and stable. However, a steady increase is noticed from 40 to 80 years of accelerated aging. Although a minimum threshold of 0.004 µm² was applied during image processing, the proportional nature of the error calculation causes the lower limits to fluctuate, especially at early aging stages where the mean values are small. In contrast, the upper bounds of the error bars expand more significantly with increasing aging time, particularly after 40 years, as the mean precipitate area increases. This increasing variation reflects the gradual growth of certain precipitates over time, leading to a broader distribution of sizes. The average area reaches approximately 0.1 µm² by 80 years, indicating steady but moderate growth in intergranular precipitate size during thermal aging.

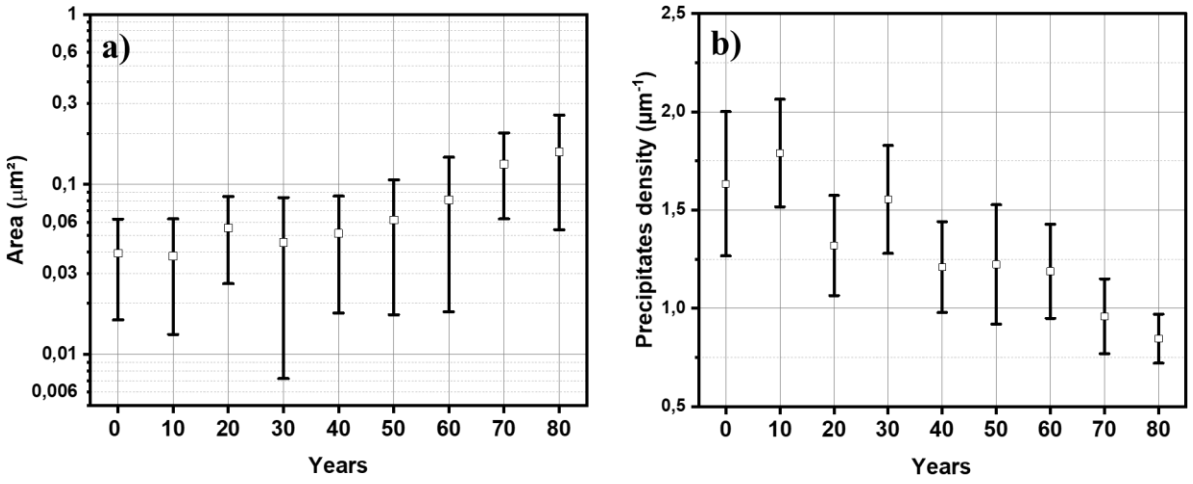

Figure 80 : Representation of a) growth of the area and b) intergranular precipitate density throughout aging.

The **Figure 80b** shows the evolution of precipitate density (µm⁻¹) over thermal aging time from 0 to 80 years. The average density exhibits a gradual decline, starting from approximately 1.75 µm⁻¹ in the unaged sample and reaching about <1.0 µm⁻¹ by 80 years. This trend suggests a reduction in the number of precipitates per unit length with aging, likely due to precipitate growth and the depletion of solute available for new nucleation. The error bars reflect the variability in precipitate distribution across different regions. At early aging times (0–20 years), the error bars are wider, with upper bounds reaching above 2.0 µm⁻¹, indicating a higher degree of heterogeneity in the microstructure. Some regions contain much higher precipitate densities than others. As aging progresses, the length of the error bars decreases, particularly from 60 to 80 years. During this period, both the upper and lower bounds converge more closely around the mean and exhibit shorter error bar lengths compared to the earlier years of aging. This

indicates that the precipitate distribution becomes more uniform over time, with less regional variation in density in the long-term aged alloy.

The **Figure 81** gives more insight into the geometric evolution of the intergranular precipitates. Thus, the **Figure 81a** depicts the evolution of the intergranular precipitate width in the Alloy 690TT during accelerated thermal aging at 420°C over a simulated period of 80 years.

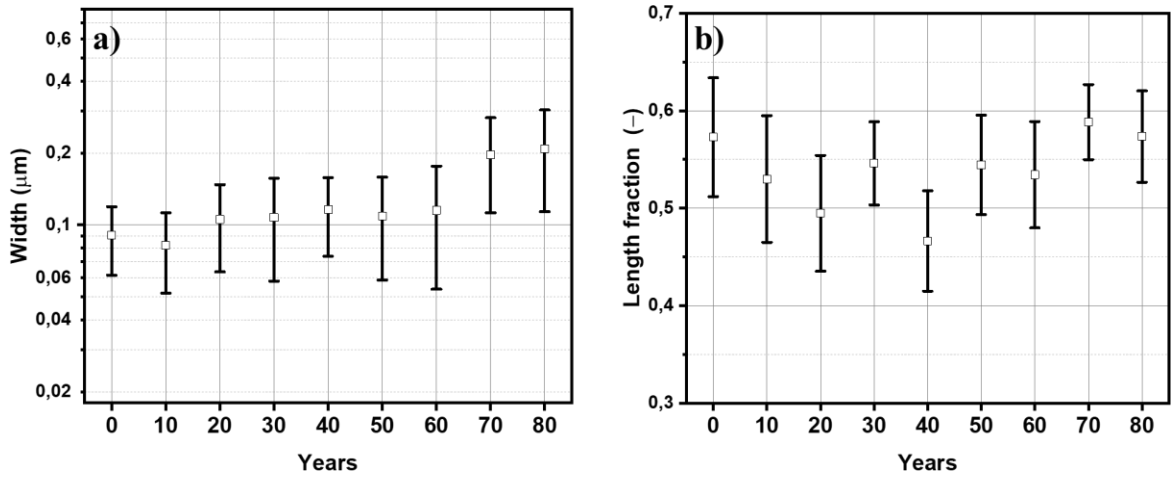

Figure 81 : Representation of a) width and b) length fraction growth of intergranular precipitates during aging.

Throughout this period, the average width of the precipitates remains relatively stable from 0 to 50 years, ranging from 0.09 to 0.1 µm, and it increases from 60 to 80 years to 0.2 µm. This trend is consistent with the corresponding changes in the area of the precipitates during the same timeframe (**Figure 80a**).

The **Figure 81b** tracks the length fraction of intergranular precipitates, indicating the ratio of the precipitate length to the total grain boundary length, and in the event of large-scale DIGM the entire grain boundary length was manually traced. The average values demonstrate minimal variation throughout the aging process (≈ 0.55). This suggests that the overall coverage of intergranular precipitates along the grain boundaries remains constant, indicating a stable distribution over the extended period of thermal exposure. This observation aligns with a Cr diffusion-driven mechanism, where the redistribution of chromium at the grain boundary could contribute to both the waviness of the boundary and the thickening of intergranular precipitates rather than a significant change in their total boundary coverage.

All of those results are consistent with the previous studies reporting a qualitative increase in the size of intergranular precipitates at various temperatures [Alexandreanu et al., 2021, Lee et al., 2015, Li et al., 2013, Mouginot et al., 2017a, Sarver et al., 1988]. For instance, Alloy 690TT aged for 10,000 hours at temperatures of 420°C, 475°C, and 550°C demonstrated this behavior. The size of the precipitates also increased as the temperature was raised [Mouginot et al., 2017a].

To summarize, in the present study, the quantitative evolution of the precipitates characteristics was emphasized. The increase in the average area of intergranular precipitates between 50 and 80 years (**Figure 80a**) indicates the coarsening of precipitates. The area shows a steady rise, highlighting the formation of significantly larger precipitates in the later stages of aging. These larger precipitates contribute to the overall increase in average area. In contrast, **Figure 80b** reveals a decline in precipitate density with aging time. The initial stability of the density up to 30 years suggests a balance between nucleation and coarsening processes. Beyond this point, the steady decrease in density, coupled with the reduced variability in distribution length, indicates that coarsening dominates, leading to fewer but larger precipitates. The decrease in density values from $2\mu m^{-1}$ to $1\mu m^{-1}$ and the convergence toward uniformity in the later stages reflect the progressive homogenization of the microstructure.

IV.1.1.2. Intragranular precipitates

While intergranular precipitation is commonly linked with grain boundary phenomena, intragranular precipitates also play a role in the microstructural evolution of thermally aged Alloy 690TT. These internal features, often forming within grains due to local compositional variations or diffusion processes, can influence the mechanical response and hardening behavior of the alloy. Therefore, a detailed assessment of intragranular precipitate characteristics, such as size and density, is essential to complement the intergranular analysis and build a comprehensive understanding of precipitation behavior during long-term aging.

The **Figure 82** illustrates the evolution of the intragranular precipitate area and density in the Alloy 690TT during accelerated thermal aging at 420°C, simulating a period of 0 (**Figure 82a**) to 80 years (**Figure 82e**) of operation. Visually, the size of the intragranular carbides appears unchanged by aging.

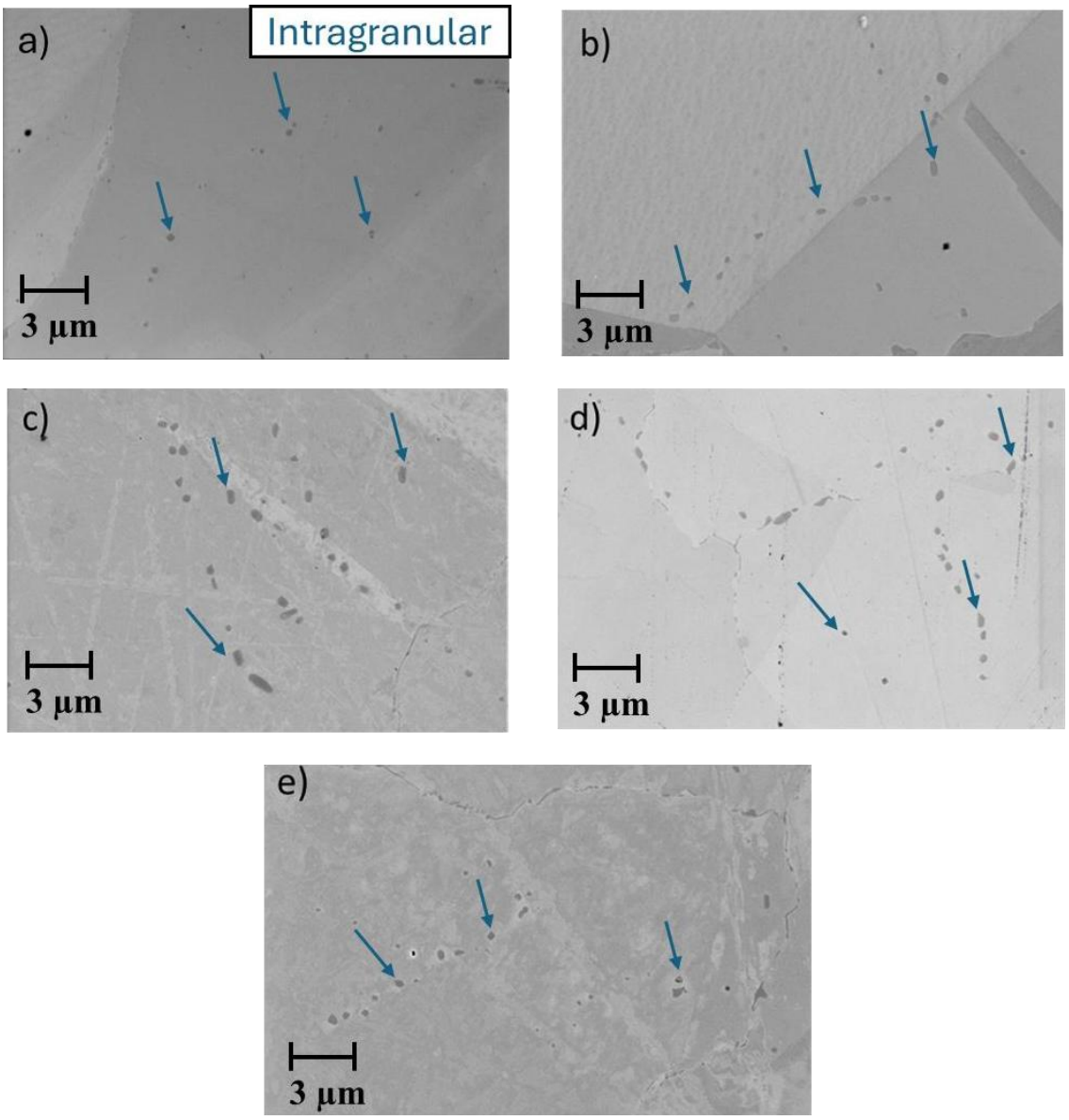

Figure 82: Representative SEM micrographs of $M_{23}C_6$ Intragranular precipitates in Alloy 690TT thermally aged at 420°C: a) as-received, b) 20 years, c) 40 years, d) 60 years and e) 80 years (blue arrows indicate intragranular precipitates).

The **Figure 83** shows a more quantitative analysis of intragranular precipitates as a function of aging duration. It can be seen (**Figure 83a**) that the average area remains relatively stable (≈ 0.05 μm^2), with minimal variation throughout the aging process. Even the lower bond (≈ 0.025 μm^2) and upper bound (≈ 0.07 μm^2) levels of the area intragranular precipitates do not vary much during the entire period of aging. In the case of the precipitate density (**Figure 83b**), the data indicate that the average density remains unchanged (≈ 0.015 μm^{-2}) up to 20 years of accelerated aging. From 30 years onward, there is a noticeable increase in average density (≈ 0.025 μm^{-2}), stabilizing for the remainder of the aging period. The lower and the upper level in

the density of the intragranular precipitates also increase to 0.02 μm^{-2} and 0.028 μm^{-2}, respectively, from 30 – 60 years of aging. In the later aging stages (70–80 years), the error bars begin to narrow, suggesting that the distribution becomes more consistent as the intragranular microstructure reaches a more stable state. The increase in density from 30 years indicates that new precipitates are forming rather than that existing ones are growing significantly.

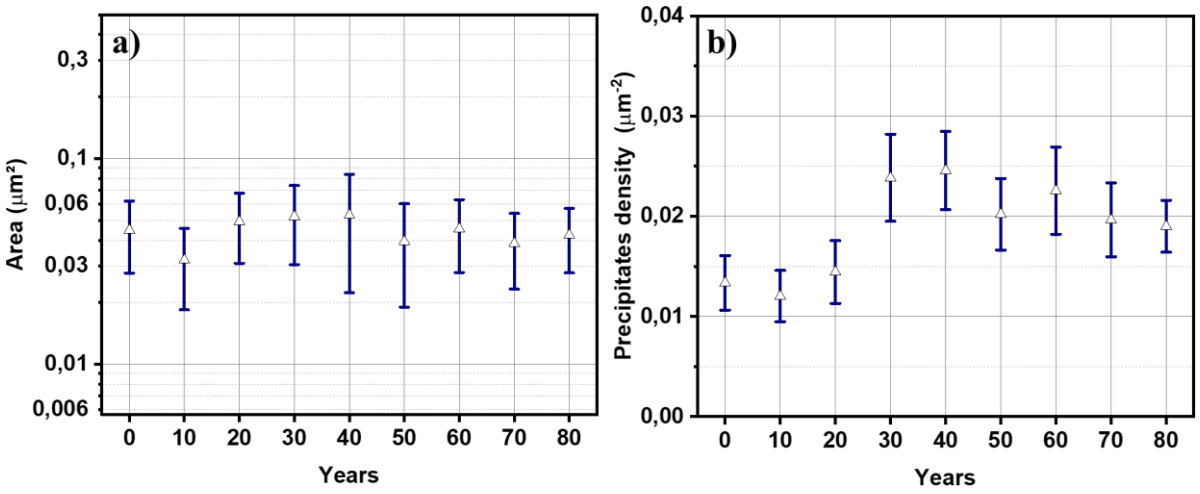

Figure 83 : Representation of a) growth of the area and b) intragranular precipitates density throughout aging.

Overall, these plots indicate that the size of intragranular precipitates in Alloy 690TT remains stable throughout the thermal aging process, exhibiting consistent values with only minor fluctuations, and the increase in density indicates the nucleation of precipitates. In a Ni-based superalloy, the precipitation of $M_{23}C_6$ carbides at grain boundaries during aging depletes carbon from the matrix, limiting the growth of intragranular carbides [Handa, 2014]. Grain boundaries serve as short-circuit diffusion paths, allowing much faster migration of carbon and chromium than through the bulk lattice. This preferential diffusion facilitates the formation and coarsening of intergranular chromium-rich carbides. In contrast, volumetric diffusion within the grain interiors is significantly slower, limiting the growth of intragranular carbides, which tend instead to nucleate but remain fine. For instance, the diffusion coefficient of carbon in nickel at 420 °C is approximately 3.5×10^{-18} m^2/s [Bleu et al., 2019], corresponding to a diffusion distance of roughly 7.5 µm over 4000 hours. Considering that the average grain size of Alloy 690TT is about 75 µm, this distance represents only ~10% of the grain diameter. Such a limited diffusion range confines solute redistribution to the vicinity of grain boundaries, leaving the grain interior largely unaffected. Consequently, while grain boundaries accumulate and promote the growth of coarser intergranular carbides, the grain interiors, characterized by lower

diffusivity and reduced solute availability, develop smaller, more numerous intragranular carbides.

IV.1.2. Evolution of precipitates during aging in the same specimen

Up to this point, precipitate sizes had been measured across various regions and samples aged for different durations. To validate the statistical trends derived from these random-location measurements, a targeted, region-specific analysis was conducted subsequently.

To do so, a specific region of the as-received sample was first marked using micro-indentation. One indentation was made at the top and two at the bottom corners of the region of interest, as indicated by the red boxes (**Figure 84**). Between these reference points, a series of high-magnification SEM images were acquired to document the initial distribution and size of intergranular precipitates highlighted by blue boxes (**Figure 84**).

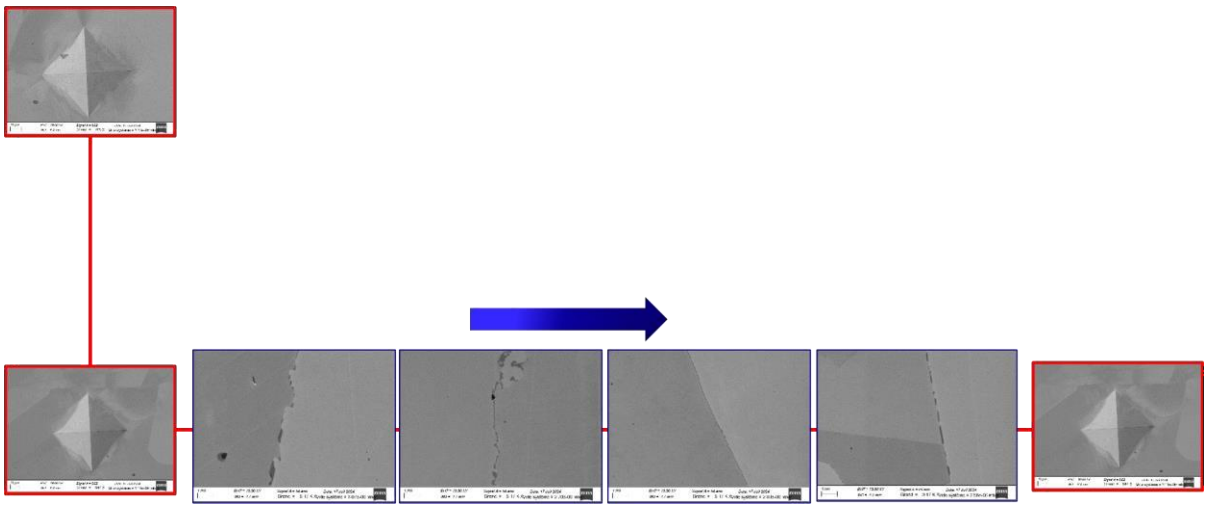

Figure 84: SEM images of intergranular precipitates within the micro-indentations in a specific region of the sample. (red squares: micro-indents, blue squares: intergranular precipitates, blue arrow: direction of the images captured).

Subsequently, the sample was thermally aged to simulate a cumulated period of 60 years of successive aging treatment (equivalent to 4000 hours at 420 °C) in a vacuum-sealed glass container to avoid environmental effects on the precipitates. After aging, the same region, identified by the micro-indentation markers, was relocated, and a new set of SEM images was collected. This approach enabled a direct and precise comparison of the precipitate size and distribution before and after aging.

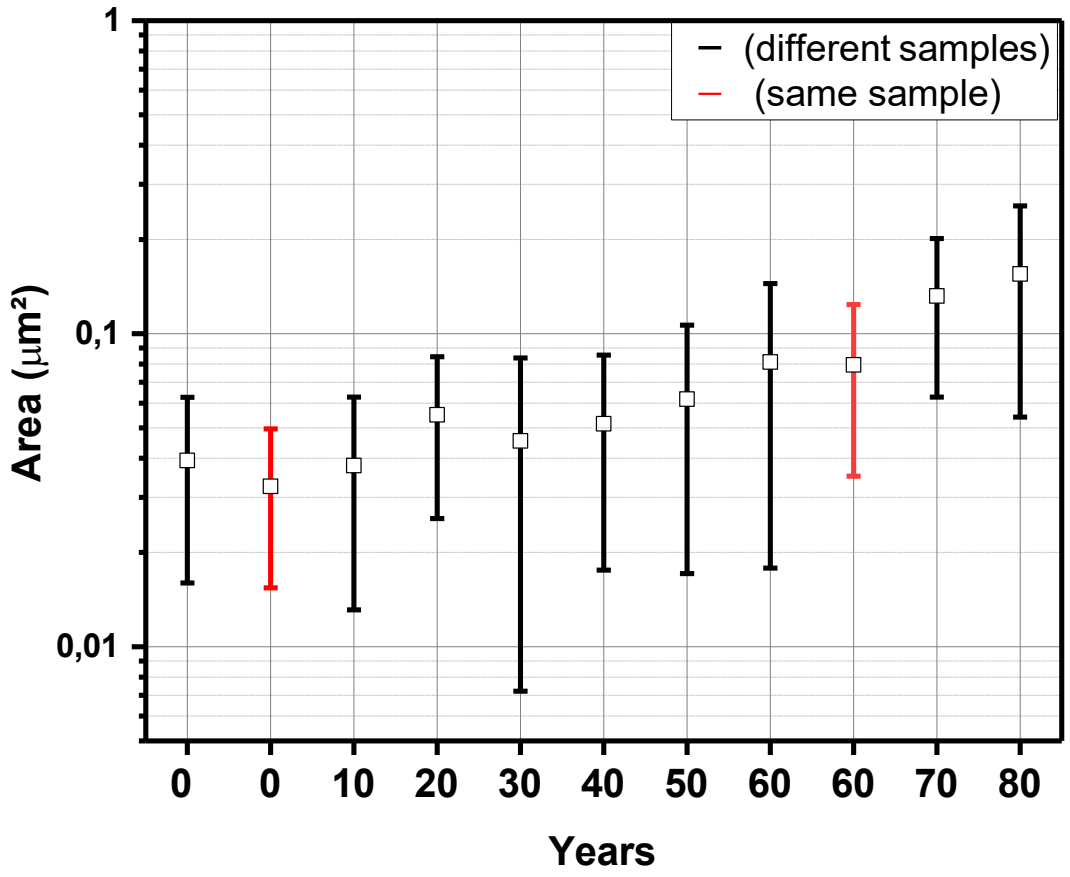

Figure 85: Comparison of the evolution of intergranular precipitates in different samples (black) and the same sample (red).

The **Figure 85** presents the evolution of the intergranular precipitate area in Alloy 690TT as a function of equivalent aging time at 420°C, plotted on a logarithmic scale. The black markers represent statistical measurements performed across different samples and random locations for each aging condition, from 0 years to 80 years. The red markers correspond to a specific, localized region tracked on the same specimen before and after aging: one at 0 years (as-received) and another after 60 years of thermal aging.

At 0 years, the mean precipitate area measured across random samples is approximately 0.04 µm², and the specific localized analysis (red marker) also yields a similar mean value, around 0.03 µm², indicating almost similar consistency at the start. After 60 years of aging, the mean precipitate area from the statistical dataset increases to about 0.08 µm², while the localized site-specific measurement (red marker at 60 years) also shows a mean area around 0.08 µm².

The error bars in both cases indicate a significant scatter, roughly spanning one order of magnitude, reflecting the inherent distribution of precipitate sizes. However, the localized measurements (red markers), taken from the same sample, exhibit comparatively less scatter

than the broader random measurements (black markers). This reduced variability reinforces the consistency of localized measurements and supports the conclusion that aging induces clear and measurable precipitate coarsening.

IV.1.3. Chemistry evolution of the precipitates in the bulk material after aging

The **Figure 86** is a schematic illustration and a SEM micrograph showing the site-specific FIB lift-out procedure used to prepare a thin foil from an aged Alloy 690TT specimen (4000 hours @ 420°C; 60 years @ 325°C). The region of interest (highlighted in yellow) corresponds to intergranular precipitates located in the bulk material and not at the surface.

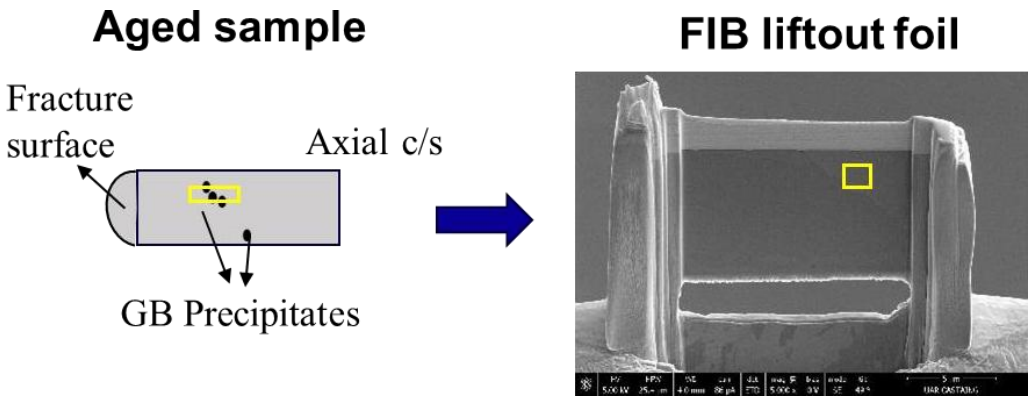

Figure 86: FIB lift-out of a foil with an intergranular precipitate from an aged sample below its surface (4000 hours @ 420°C; 60 years @ 325°C).

The **Figure 87a** shows a representative Bright-Field STEM image of an intergranular precipitate within the thermally-aged Alloy 690TT matrix. The precipitate exhibits a distinct contrast due to its compositional difference from the matrix. The **Figure 87b** presents an overlaid EDS elemental mapping of the same region, illustrating the distribution of key elements (Chromium in red, Nickel in blue, Iron in yellow, Oxygen in light green, and Carbon in cyan).

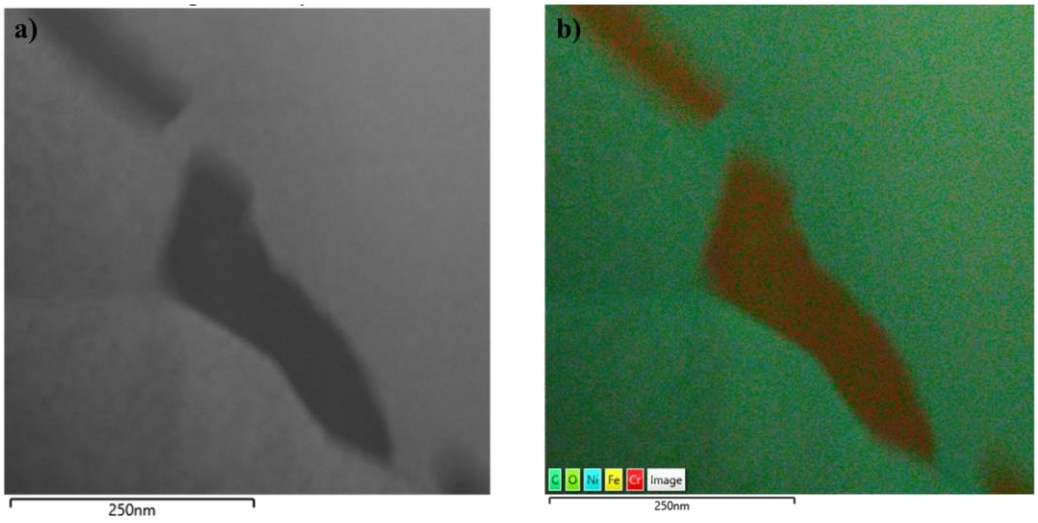

Figure 87: Representative chromium carbide precipitate at a grain boundary below the surface on the aged specimen (4000 hours @ 420°C; 60 years @ 325°C) surface, a) STEM image, b) EDS image in superposition of elements.

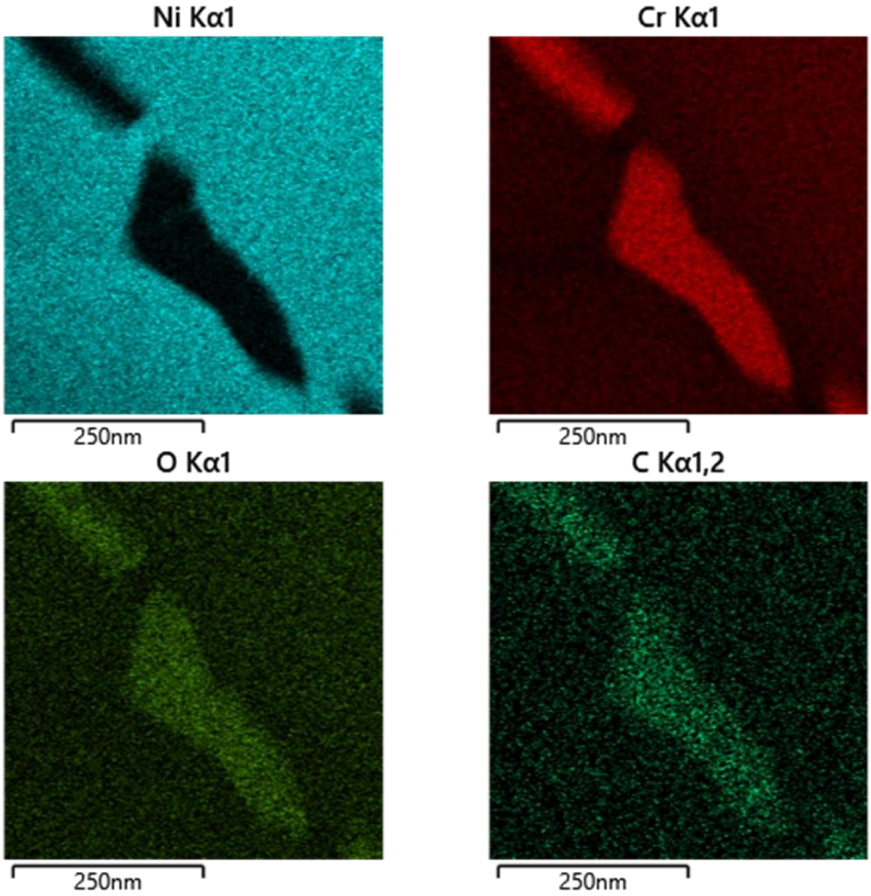

Figure 88: STEM-EDS elemental maps of a intergranular precipitate present below the surface of thermally aged Alloy 690TT (4000 hours @ 420°C; 60 years @ 325°C).

The **Figure 88** displays STEM-EDS elemental maps of the precipitate (**Figure 87**). The chromium (Cr) and carbon (C) are typical from $Cr_{23}C_6$. However, it can be seen that a signal from oxygen (O).

This means that, even though the intergranular carbides are not in contact with the air during accelerated aging, they can be oxidized. Although no study has directly quantified the penetration depth of oxide films along grain-boundary carbides in Alloy 690TT during thermal aging in air at 420 °C, related works on Ni-based alloys provide useful reference points. For instance, in thermally treated Alloy 600TT, specimens exposed to hydrogenated steam at 480 °C for 120 h exhibited intergranular carbide oxidation up to ~2 μm in depth [Langelier et al., 2017]. Similarly, Lim et al. (2019) reported that Alloy 690 specimens exposed to simulated PWR primary water at 325 °C for 3600 h (30 cm^3 H_2/kg H_2O, < 5 ppb O_2) developed oxidized grain-boundary carbides extending up to ~1 μm beneath the surface [Lim et al., 2019a].

IV.2. HARDNESS EVOLUTION

In this section, the effect of microstructural changes on the mechanical properties, particularly hardness, is investigated. Microhardness measurements were employed to assess the evolution of global hardness across the aging durations. Subsequently, nanoindentation was used to probe local variations in hardness at the nanoscale, particularly to characterize the influence of short-range ordering (SRO) within the matrix and in regions adjacent to grain boundaries. This multi-scale hardness evaluation aims to establish a correlation between the evolving microstructure and the material's mechanical response during thermal aging.

IV.2.1. Micro-hardness

The **Figure 89** presents the micro-hardness evolution over different aging periods at 420°C, ranging from 10 years to 80 years, with measurements taken mostly at 20-year intervals. Each data point represents the mean hardness after a specific aging duration, while the error bars illustrate the variability within ±0.5 standard deviations.

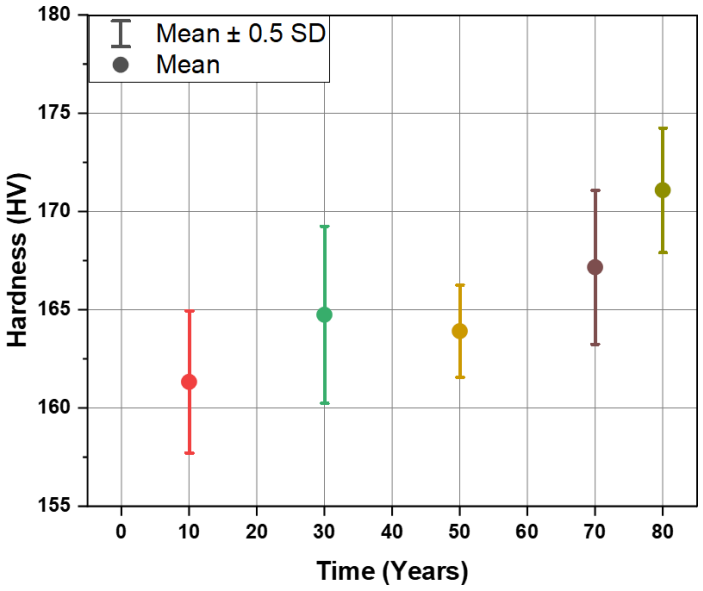

Figure 89 : Evolution of microhardness of the alloy throughout aging at 420°C.

The trend observed in the **Figure 89** indicates that the hardness changes as thermal aging is prolonged. Up to 50 years of accelerated aging, no significant change is noticed in the overall hardness (162 - 165 HV). However, between 50 and 80 years, the hardness increases by 10 HV, likely due to microstructural transformations that occur over time. The varying lengths of the

error bars reflect the repeatability of the hardness measurements across different aging periods. It should be noted that these values of hardness are difficult to compare with data from the literature, as the hardness values reported were obtained from different loads [Huotilainen and Que, 2022, Stephan et al., 2019].

IV.2.2. Nano-indentation Characterization of Short-Range Ordering

Since an increase in global hardness was observed after 50 years of aging, it became necessary to explore the local microstructural origins of this hardening. In particular, the focus was on determining whether this increase is associated with the formation of localized phases or ordering phenomena, such as short-range ordering (SRO). To this end, nano-indentation was employed to resolve spatial variations in hardness at the sub-micron scale, particularly near grain boundaries and within matrix regions. It has been shown that the hardness increase began after accelerated aging of 60 years, and since the French PWRs could be extended to 60 years of operation in the first stage, the study focused on this condition of 60 years of aging.

The **Figure 90** represents the distribution of hardness at the nanoscale for the as-received (**Figure 90a**) and 60 years aged (**Figure 90b**) samples. The dark highlighted lines represent the grain boundaries. In the as-received sample (**Figure 90a**), it appears that the values are relatively uniform, with some slight variation indicated by the color gradients. Within the matrix, some areas in red have a higher hardness (4.45 GPa) that corresponds to the intragranular precipitates. The matrix area with lower hardness (2.8 GPa) are represented in blue. The average hardness of the map is 3.05 GPa, with only limited spatial variation across the scanned region, suggesting a relatively homogeneous microstructure in terms of mechanical response. This uniformity in hardness implies a consistent distribution of phases or precipitates and minimal localized hardening features within the matrix. In contrast, the map for the aged sample (**Figure 90b**) reveals a more pronounced variability and higher hardness values, with distinct regions of higher hardness highlighted in yellow (above 4.66 GPa) and red (4.45 GPa) areas. The maximum hardness recorded above 4.66 GPa has been attributed to an inclusion in the matrix. In addition, the green to red shades regions within the matrix near the grain boundaries indicate hardened zones (indicated by white squares in **Figure 90b**) which exhibit hardness values around 3.833-4.247 GPa. The average hardness of the aged sample has

increased to 3.5 GPa, suggesting substantial microstructural evolution and localized hardening after long-term aging.

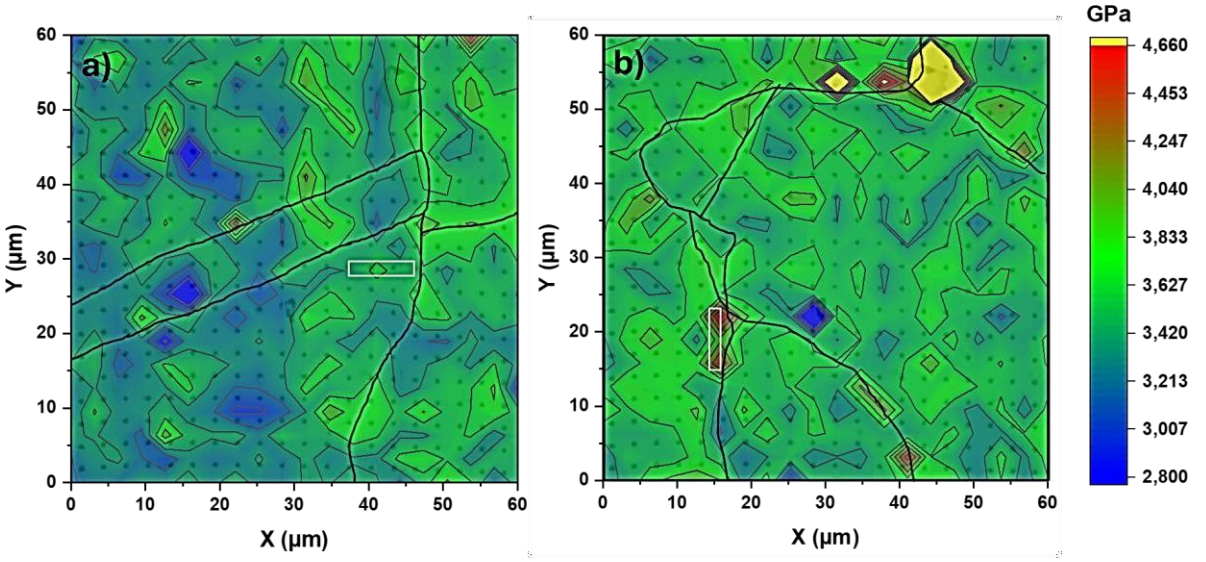

Figure 90: Nano-hardness map of Alloy 690TT: a) As-received and b) Aged at 420°C for 4000 hours (60 years at 325°C) (The black line represents the grain boundaries and the white squares indicate the foil extraction zone near the hardened region).

The variation of hardness near the grain boundary (**Figure 90b**) suggests that aging has led to microstructural changes, such as the formation of nano-precipitates or secondary phases like SRO, which enhance the hardness in specific areas. To verify this assumption, the hardened zone (white square, **Figure 90b**) in the 60 years aged sample was extracted by FIB milling. The foil, oriented perpendicularly to the indentations, is thereafter analyzed by TEM-SAED. In the as-received condition, the region with the highest hardness near the grain boundary (white square, **Figure 90a**) was selected to verify if the slight variation in hardness was due to a microstructural change or due to statistical scattering.

The **Figure 91** shows the TEM images (**Figure 91a, b, c**) associated with the diffraction patterns observed in the as-received (**Figure 91d**) and aged specimens (**Figure 91e, f**). In the as-received sample, a cross-sectional TEM foil was extracted directly beneath the location of maximum hardness (as determined by the nanoindentation map (white square region)). TEM imaging revealed a relatively uniform microstructure, with no evidence of significant dislocation structures or secondary phases (**Figure 91a**). The SAED pattern (**Figure 91d**) acquired from this region along the [011] zone axis displayed sharp and well-defined diffraction spots corresponding to the FCC crystal structure of Austenitic Alloy 690TT. No additional

reflections, such as diffuse scattering or superlattice reflections, were observed, confirming the absence of short-range ordering in that zone. This result indicates that the slight variation of nano hardness (**Figure 90a**) in the as-received sample is probably due to statistical scattering.

For the aged condition, a single TEM foil was prepared from a region containing a nanoindentation imprint corresponding to the maximum hardness zone near the grain boundary. Within this foil, two regions were studied:

A first region near the indent (**Figure 91b**), representing the zone of maximum localized hardening. The SAED pattern obtained from this site along the [011] zone axis (**Figure 91e**) retained the characteristic FCC reflections but also exhibited faint, diffuse satellite reflections positioned between the main Bragg spots, notably near the (-100), (100), and (0-11) reflections. These features are indicative of short-range ordering (SRO) within the FCC matrix, suggesting localized atomic reordering of Ni and Cr atoms, as previously reported in the literature [Wang et al., 2019b]. With an estimated lattice parameter of 3.54 nm, these patterns suggest the formation of Ni_2Cr regions that were recorded in the study conducted by Stephan et al. on the commercial Ni-20Cr-8Fe alloy [Stephan, 2018]. Moreover, the SAED patterns near the hardened zone showed no strong superlattice reflections, indicating the absence of long-range ordered (LRO) phases. The absence of LRO in the current study suggests that the thermal aging conditions used (420°C for up to 4,000 hours) are insufficient for the transition to LRO, which typically requires prolonged exposure or higher temperature [Alexandreanu et al., 2021].

A second region farther from the indent (**Figure 91c**), approximately representing the average hardness zone within the same aged sample. The SAED pattern from this area, recorded along the [–110] zone axis (**Figure 91f**), exhibited a clean FCC diffraction pattern without diffuse reflections. This indicates that SRO formation is spatially localized and does not extend uniformly across the microstructure. The uniform diffraction pattern supports the observation

that only regions with higher nano-hardness (excluding precipitates and inclusions) display structural signatures of ordering.

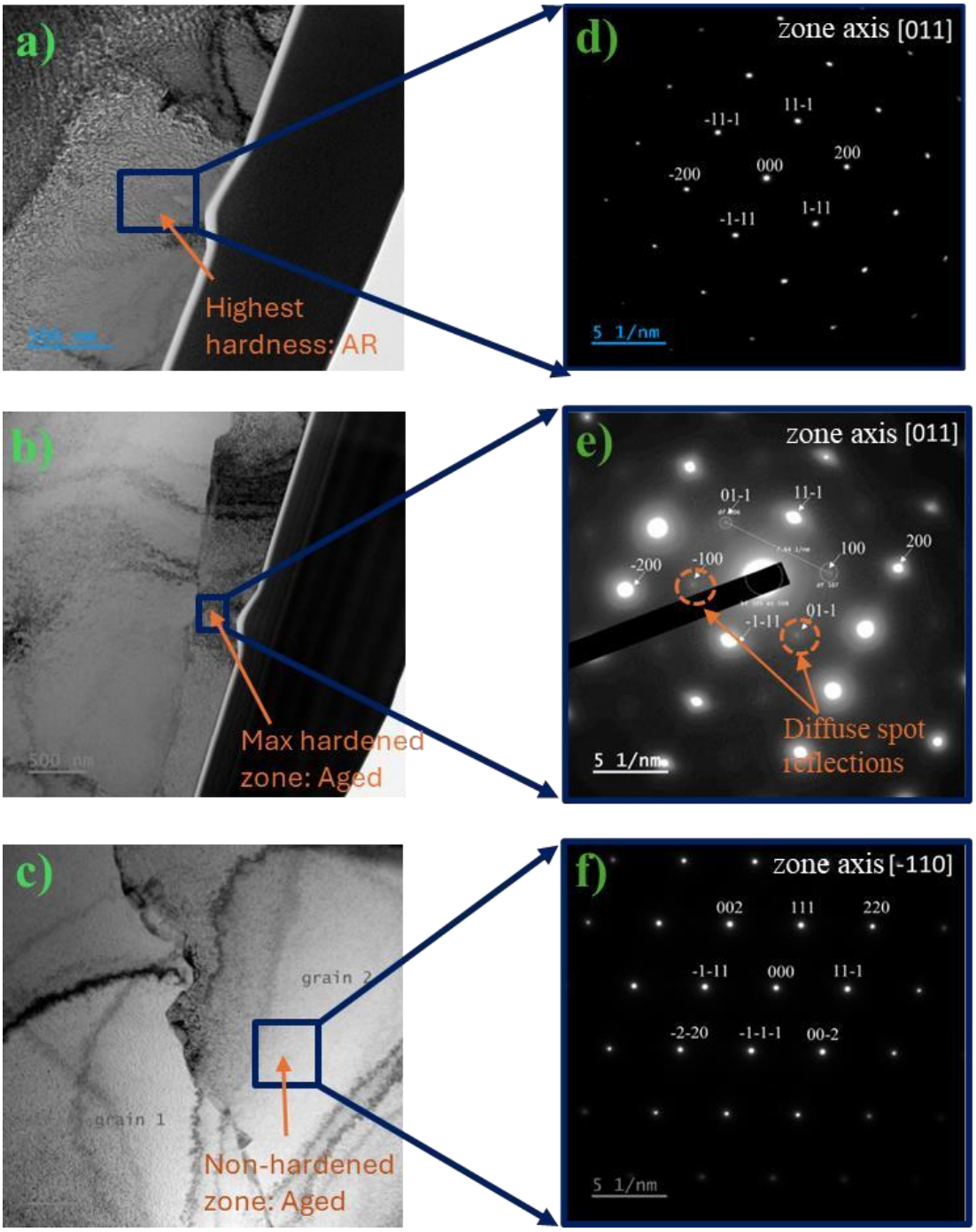

Figure 91: TEM bright field images of the a) highest hardness zone of the as-received material, the b) Maximum hardened zone, and c) non-hardened zone, of the material aged at 420°C for 4000 hours (equivalent to 60 years). SAED patterns of d) the highest hardness zone of the as-received

material, e) the maximum hardened zone, and c) the non-hardened zone of the aged material (orange arrows indicate the soft diffusion spots in the FCC lattice structure).

All of these observations align with findings in the literature indicating the development of SRO during thermal aging at temperatures between 400°C and 475°C, as observed using SAED on alloys such as alloy Ni-20Cr-3.2Al-2.5Fe and model alloy Ni-33Cr [Alexandreanu et al., 2021, Mouginot et al., 2017a, Wang et al., 2019b]. SRO typically arises from local atomic reorganization over short distances, leading to increased hardness in the material. The presence of SRO near the hardened zone directly correlates with an increase in nano-hardness in thermally aged samples. The Ni_2Cr regions are characterized as a harder phase and also act as barriers to dislocation movement, thereby strengthening the alloy [Aerne et al., 2022]. This agrees with the earlier studies highlighting the role of SRO in enhancing hardness during thermal aging [Mouginot et al., 2016, 2019]. Additionally, a study on Ni-20Cr-3.2Al-2.5Fe alloy [Wang et al., 2019b] also demonstrated the development of SRO, even though the aging process was carried out at 475°C for 50 hours. Some studies performed on other nickel alloys discuss the effect of SRO on the material properties, like Ni-Cr-Mo alloys also show SRO formation at temperatures as low as 400°C, affecting mechanical behavior by increasing the elastic modulus [Zhilyakov et al., 2020]. Similarly, Ni-Co-Cr alloys exhibit improved strength due to SRO, which influence dislocations motion and stacking fault width [Naghdi et al., 2023]. In Ni-Al alloys, SRO serves as a precursor to the formation of long-range ordered phases, significantly changing microstructural stability and mechanical performance [Plotnikov et al., 2018].

IV.3. SUMMARY

To simulate the long-term operation of Alloy 690TT in nuclear power plants, accelerated thermal aging was conducted at 420°C. The impact of this accelerated aging on the microstructural evolution and hardness was investigated and quantitatively assessed over time.

- **Grain structure**
  - Accelerated thermal aging did not significantly modify the average grain size or the overall grain boundary character of Alloy 690TT.
  - The grain boundary network (Σ3, Σ5, Σ7, Σ9 boundaries) remained stable throughout aging.

- **Intergranular precipitates**
  - The area fraction of intergranular precipitates increased progressively between 3400 h (~50 years) and 5400 h (~80 years) of aging, primarily due to the growth in their width.
  - The density of intergranular precipitates decreased over the same period, suggesting coarsening and partial coalescence.
  - Chemical analysis using STEM-EDS analysis revealed oxygen enrichment on grain boundary carbides, indicating the formation of chromium oxides (Cr_2O_3) and potential intergranular oxidation.
  - Over long exposures, grain boundaries exhibited a slightly wavy morphology, consistent with diffusion-induced grain boundary migration (DIGM).

- **Intragranular precipitates**
  - The area fraction of intragranular precipitates remained nearly constant during aging, while their density increased from ~1400 h (20 years), indicating continued nucleation within the matrix.

- **Hardness evolution**
  - Vickers microhardness showed a slight global increase after approximately 50 years of equivalent aging, reflecting moderate hardening of the alloy.

- **Nano-indentation and localized hardening**
  - Nano-indentation in the as-received condition revealed uniform hardness across grains, with no distinct hard zones.
  - In aged material (~60 years), localized hardening was observed near grain boundaries, with hardness values higher than in the matrix.

- **Short-Range Ordering (SRO)**
  - TEM combined with SAED revealed additional weak superlattice reflections corresponding to SRO of the Ni_2Cr type in the hardened zones near grain boundaries.
  - The correlation between nano-indentation and TEM confirmed that SRO contributes to local strengthening in the aged material.
  - No evidence of LRO was detected even after 60 years of accelerated aging at 420 °C.

The impact of aging-related changes in the microstructural and mechanical properties on the long-term performance of Alloy 690TT, including its low-cycle fatigue behavior in air and in the PWR medium, will be further assessed.

V. Effect of thermal aging on fatigue behavior of the alloy 690TT

This section investigates how long-term thermal aging influences the low-cycle fatigue response of Alloy 690TT. The study examines the cyclic stress–strain behavior, fatigue crack growth rates, and microstructural damage mechanisms in both air and PWR environments. Emphasis is placed on understanding how aging-induced microstructural changes, such as precipitate coarsening, SRO formation, and grain boundary oxidation, affect plastic strain evolution, crack initiation, and propagation. The combined effects of thermal aging and environment are then discussed to identify the dominant mechanisms governing fatigue degradation in Alloy 690TT.

Contents

V.1. STRAIN-LIFE CURVES

The **Figure 92** shows the comparison between the fatigue life of the as-received and aged samples tested in air and PWR environment. In air, aging leads to a reduction in fatigue life of ~26% at a strain amplitude of 0.6% and ~18% at 0.45%. For the PWR environment, the single aged specimen tested at 0.45% strain amplitude exhibited a ~26% decrease in life compared to the corresponding as-received PWR sample. The fatigue life of aged samples remains well below the NUREG CR-6909 Rev-1 reference curve.

These results confirm that thermal aging reduces the fatigue performance of Alloy 690TT, although the magnitude of the reduction varies slightly with strain amplitude. Additionally, the PWR environment may have a more detrimental effect on the fatigue life; however, additional tests are required to confirm whether there is a systematic combined influence of environment and aging on fatigue life.

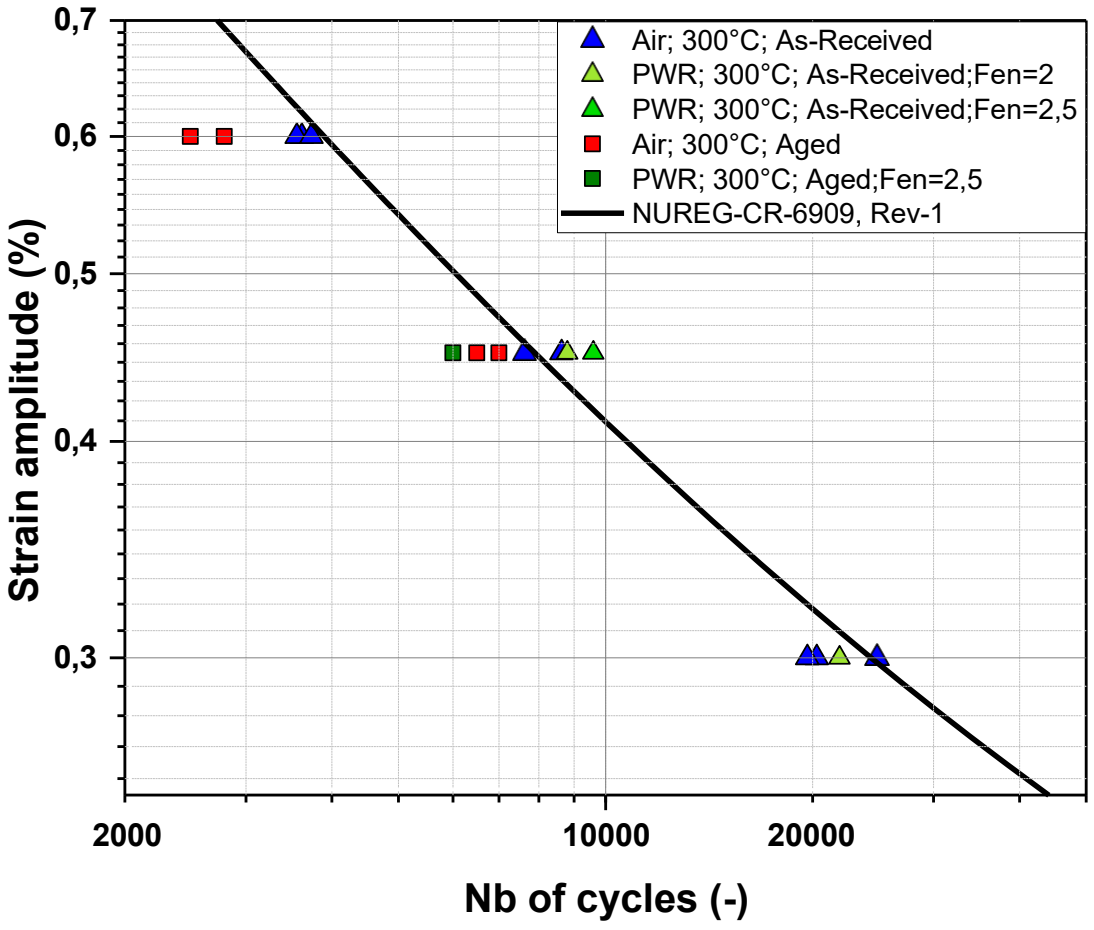

Figure 92: ε-N curve of the as-received and the aged samples tested in air and PWR environment.

V.2. CYCLIC STRESS-STRAIN BEHAVIOR

The cyclic stress–strain response was analyzed to compare the cyclic behavior of as-received and aged Alloy 690TT in air and PWR environments. Moreover, the hysteresis loops give us an information on the evolution of the plastic strain and provide insight into the underlying deformation mechanisms.

V.2.1. Cyclic hardening curves

In air, the aged sample exhibits a noticeably higher stress range and maximum stress per cycle than the as-received sample throughout the test. This difference is especially marked in the early stages (up to about 300 cycles), where the aged sample maintains a ~20 MPa advantage (**Figure 93).** Both conditions show an overall increasing trend in maximum stress with cycling (indicative of cyclic hardening), but the aged sample consistently hardens more than the as-received sample. After approximately 100 cycles, both conditions exhibit a clear change in slope, a sign of secondary hardening. However, the aged material achieves slightly higher peak stresses, indicating greater resistance to cyclic deformation.

Under PWR conditions, the trends are broadly similar: both as-received and aged samples exhibit an initial increase in maximum stress, indicative of cyclic hardening behavior. The aged samples tend to exhibit slightly higher maximum stresses than those in the as-received condition; however, given the level of noise in the EVA signals, it is difficult to confirm this difference with certainty. After the initial cycles, both materials demonstrate a comparable rate of hardening, characterized by similar slope changes at around 100 cycles.

The higher stress values in the aged sample suggest that aging enhances the material's strain-hardening capacity in both environments. This change in hardening behavior in the aged sample may be attributed to microstructural alterations, particularly the formation of a new phase such as Ni_2Cr due to prolonged aging at 420°C (**IV.2.2**). The Ni_2Cr phase likely forms near grain boundaries due to the diffusion of carbon from the matrix, creating vacancies that facilitate this transformation [Verma et al., 2015]. This phenomenon, known as Short Range Ordering (SRO), can enhance the strain-hardening capacity of the material. Further post-treatment analysis is necessary to verify the presence of SRO and its impact on the mechanical properties of the aged sample [Shi et al., 2023].

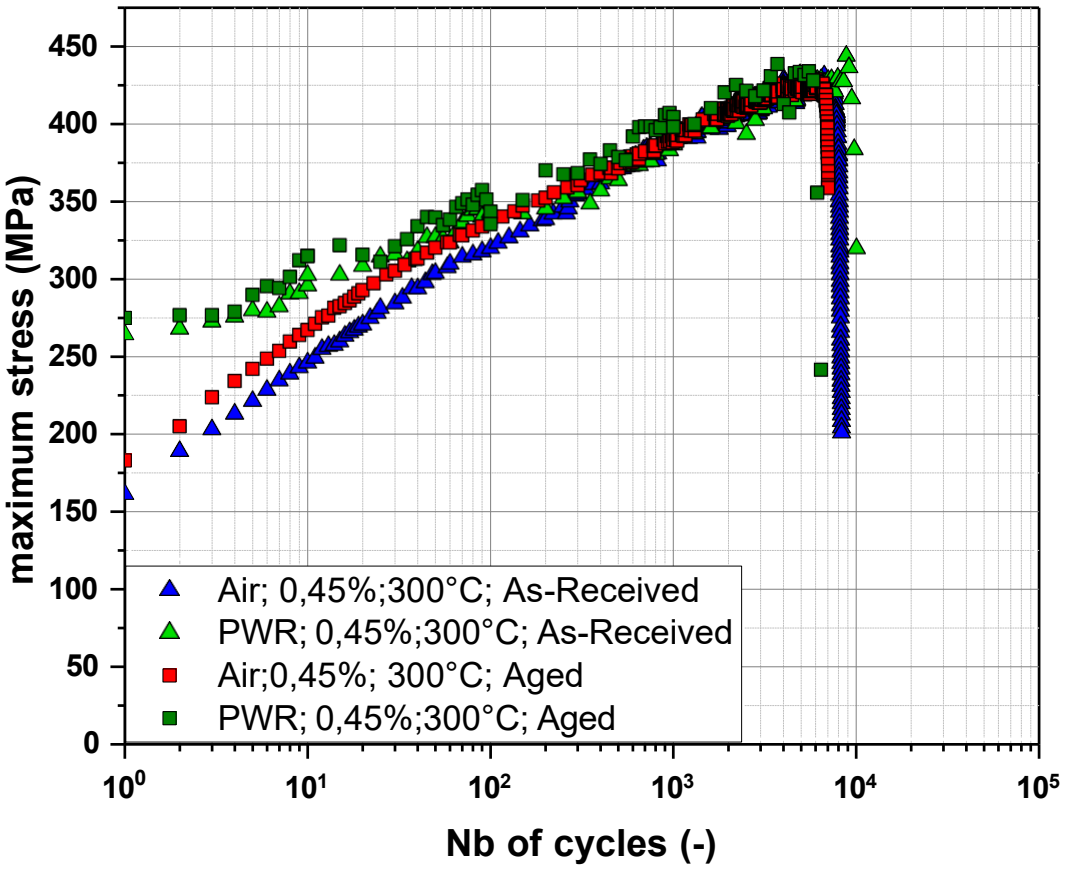

Figure 93: Comparison of the cyclic behavior between as-received and aged Alloy 690TT samples tested at 0.02%/s in the air and at 0.004%/s PWR environment.

V.2.2. Hysteresis loops

The hysteresis loops reveal a clear difference in the total loop area between the aged and as-received samples (**Figure 94**). The aged sample exhibits a larger loop area, indicating greater plastic strain accumulation (**V.2.4**) and higher energy dissipation (**V.2.3**). That may account for the reduced low-cycle fatigue resistance. The hysteresis loops at 300 °C (**Figure 95**) also reveal that the aged samples exhibit more pronounced serrations in the stress response compared with the as-received condition. While the serration intensity remains nearly constant throughout life in the as-received state, it increases progressively with cycling in the aged material, reaching higher magnitudes overall. These serrations reflect intermittent pinning and unpinning of dislocations, indicating stronger DSA activity after thermal aging. This behavior can be attributed to the presence of SRO domains in the aged microstructure, which locally reduce the SFE and promote planar slip. The confinement of dislocation motion along specific {111} planes enhances interactions between dislocations and diffusing solute atoms, thereby intensifying the DSA and the associated PLC effect as deformation proceeds [Shi et al., 2023].

These observations imply that thermal aging promotes microstructural changes that lower resistance to plastic flow under cyclic loading.

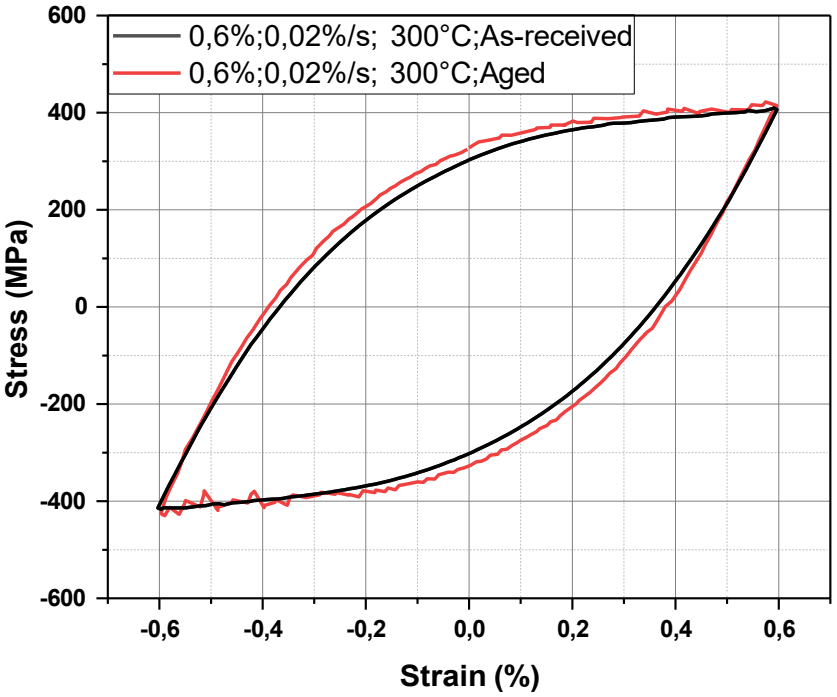

Figure 94: Comparison of the hysteresis loops of as-received and aged Alloy 690TT tested at 300 °C in air after 500 cycles ($\varepsilon_a = \pm 0.6\%$, $\dot{\varepsilon} = 0.02\%/s$).

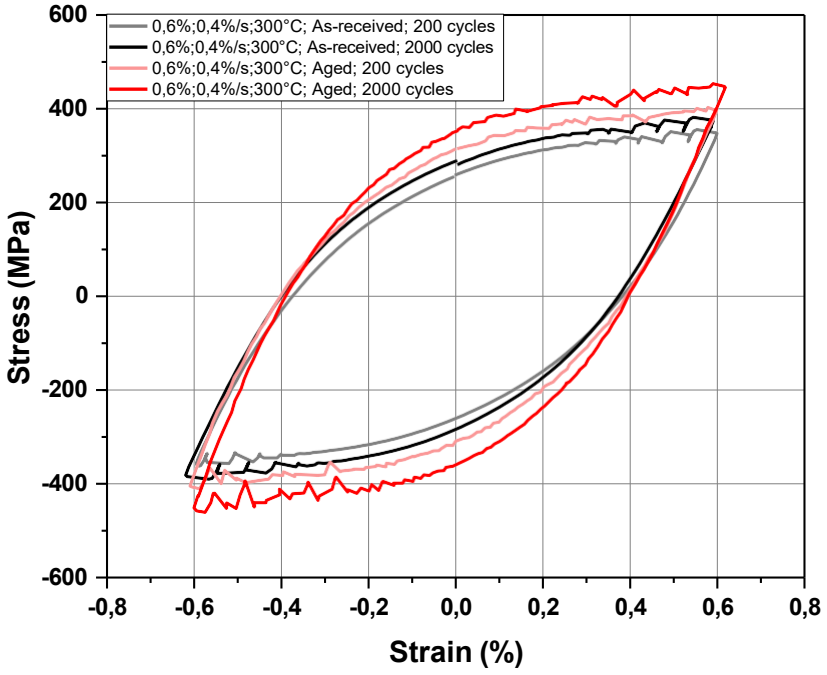

Figure 95: Comparison of the serrations in hysteresis loops of as-received and aged Alloy 690TT tested at 300 °C in air at different cycles ($\varepsilon_a = \pm 0.6$ %, $\dot{\varepsilon} = 0.4$ %/s).

The **Table 9** shows the differences in the yield stress between the as-received and the aged sample tested at 300°C (ε_a = ±0.6%, $\dot{\varepsilon}$ = 0.02%/s). It's clearly witnessed that the initial yield stress at the 1st cycle in the aged specimen is higher than the as-received sample by 34 MPa. Later, at 500 cycles, the difference is still persistent, as the difference was around 24 MPa between the aged and the as-received. These observations clearly explains the higher cyclic hardening behavior in the aged samples.

	σ_y @ 1st cycle (MPa)	**σ_y @ 500th cycle (MPa)**
As-received	202	302
Aged	236	326

Table 9: Evolution of the yield stress between as-received and the 60 years-aged Alloy 690TT at 300°C in air (ε_a = ±0.6%, $\dot{\varepsilon}$ = 0.02%/s).

V.2.3. Evolution of plastics strain energy

The evolution of plastic strain energy with the number of cycles, as shown in **Figure 96**, highlights the influence of thermal aging on energy dissipation.

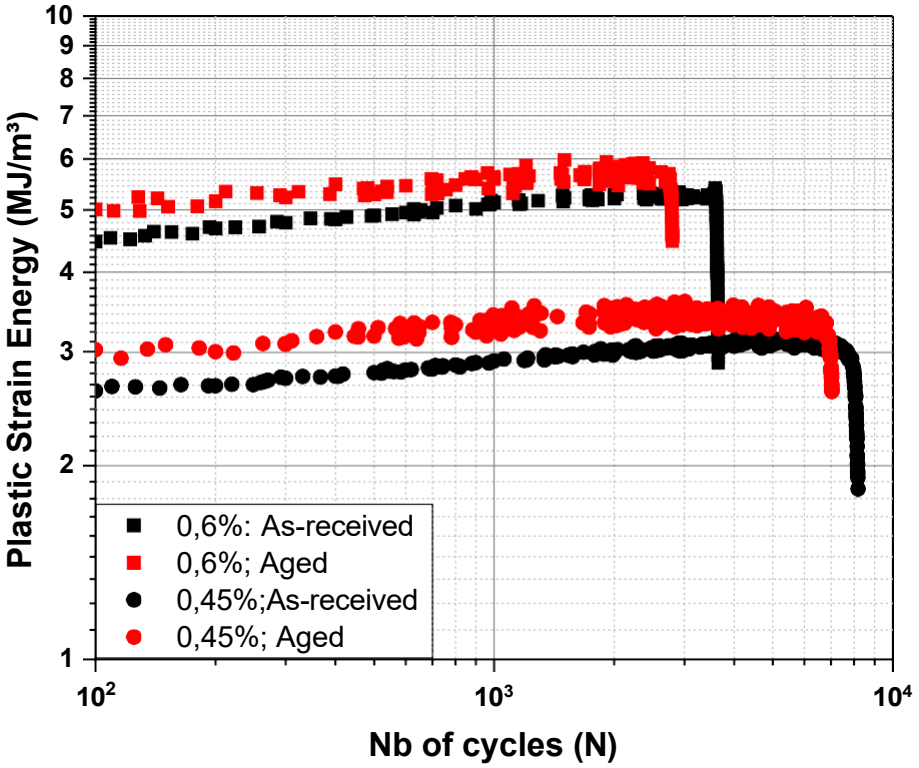

Figure 96: Comparison of the plastic strain energy evolution between as-received and aged samples at different strain amplitudes ($\dot{\varepsilon}$ = 0.02%/s, air 300°C).

At both strain amplitudes (0.45% and 0.6%), the aged specimens consistently exhibit higher plastic strain energy compared to the as-received condition. At 0.45% strain amplitude, during the initial cycles (~100 cycles), the as-received sample dissipates about 2.5 MJ/m³, while the aged sample reaches ~3.0 MJ/m³, representing an increase of nearly 17%. This difference remains throughout the fatigue life, with the aged samples maintaining values between 3.0 and 3.7 MJ/m³, compared to 2.5–3.1 MJ/m³ for the as-received condition. A similar trend is observed at 0.6% strain amplitude, where the as-received condition begins at ~4.5 MJ/m³, while the aged sample shows ~5.0 MJ/m³, again reflecting an increase of approximately 17%. In both strain amplitudes, the final stage of the test is characterized by a sharp drop in plastic strain energy, which corresponds to the onset of rapid crack propagation and the subsequent loss of load-bearing capacity. These results clearly indicate that thermal aging enhances the amount of plastic energy dissipated per cycle, regardless of strain amplitude.

V.2.4. Evolution of plastic strain

The **Figure 97** shows the evolution of the plastic strain amplitude as a function of the number of cycles at a total strain amplitude of 0.6% for both as-received and aged Alloy 690TT. Around the 10th cycle, the plastic strain amplitude is ~0.42% for the as-received condition and ~0.44% for the aged condition. By 100 cycles, the values decrease to ~0.37% for the as-received sample and ~0.40% for the aged one. At 1000 cycles, the aged specimens consistently maintain higher plastic strain amplitudes in the stabilized regime (~0.38–0.40%) compared to the as-received material (~0.35%). This persistent difference indicates that thermal aging increases the level of cyclic plastic strain accommodated during fatigue, thereby accelerating damage accumulation under otherwise identical loading conditions.

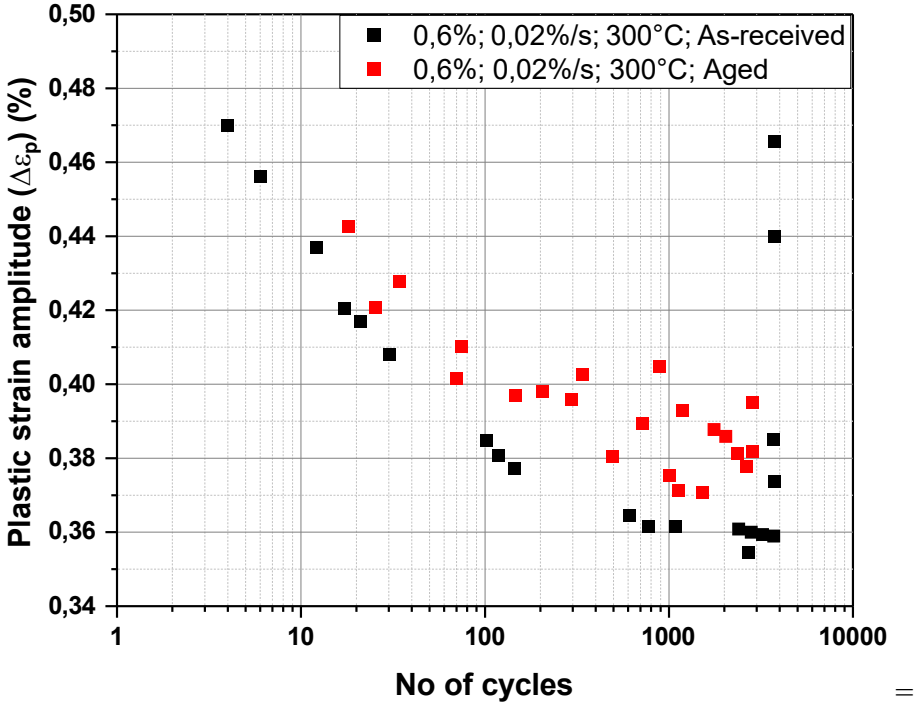

Figure 97: Evolution of plastic strain amplitude with number of cycles; As-received v/s Aged specimen in air at 0.6%, $\dot{\varepsilon}$ = 0.02%/s, air 300°C.

Across air and PWR, the aged Alloy 690TT exhibits, higher maximum cyclic stresses, larger hysteresis loop areas, higher plastic strain energy per cycle, and higher plastic strain amplitude. Taken together, these signatures indicate more plastic work and damage accumulated per cycle in the aged condition. Within an energy-based view (total plastic strain energy to failure), a higher per-cycle W_p necessarily reduces the number of cycles N_f required to reach the critical damage level; hence, the shorter fatigue life.

V.3. FATIGUE CRACK GROWTH RATE ANALYSIS

In this section, the fatigue crack growth rate (FCGR) for Alloy 690TT was derived from striation spacing measurements on fracture surfaces. This approach enables the estimation of the propagation rate under both air and PWR environments.

The **Figure 98** compares the fracture surfaces of Alloy 690TT tested in air under low-cycle fatigue in the as-received (**Figure 98 a, c**) and aged (**Figure 98 b, d**) conditions. The low-magnification images (**Figure 98 a, b**) highlight the overall crack path and initiation zone, with the area of detailed striation analysis marked at ~2500 µm from the initiation site. At higher magnification, the as-received sample (**Figure 98c**) reveals fine, closely spaced striations, indicative of a slower crack advance. In contrast, the aged sample (**Figure 98d**) displays broader striations, pointing to an accelerated propagation process. These qualitative differences illustrate the detrimental influence of thermal aging on the crack growth resistance of Alloy 690TT in air.

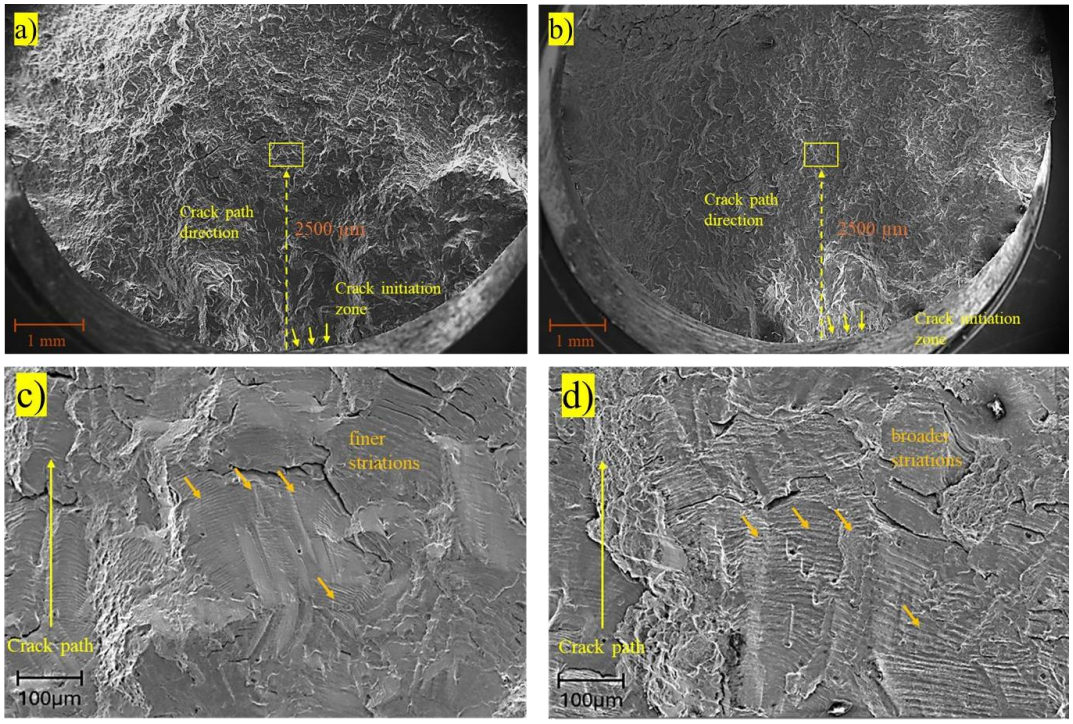

Figure 98: Fracture surfaces of Alloy 690TT tested in air at ε_a = 0.6%, $\dot{\varepsilon}$ = 0.02%/s, air 300°C: (a) as-received and (b) aged specimens showing crack initiation zones and crack paths; (c) higher magnification of as-received with finer striations; (d) higher magnification of aged with broader striations (orange arrows: striations).

The **Figure 99** shows the fracture surfaces of Alloy 690TT tested in the PWR environment, comparing the as-received (**Figure 99 a, c**) and aged (**Figure 99 b, d**) conditions. The low-

magnification views (**Figure 99 a, b**) highlight the fracture surfaces with crack path direction , with striation analysis conducted at ~2000 µm from the initiation site. At higher magnification, the as-received sample (**Figure 99 c**) reveals relatively fine striations, reflecting slower crack advance. In contrast, the aged sample (**Figure 99 d**) displays broader striations, indicative of an accelerated crack growth process under PWR conditions. These qualitative differences emphasize the detrimental effect of thermal aging on crack propagation resistance, which is further exacerbated by the aggressive PWR environment.

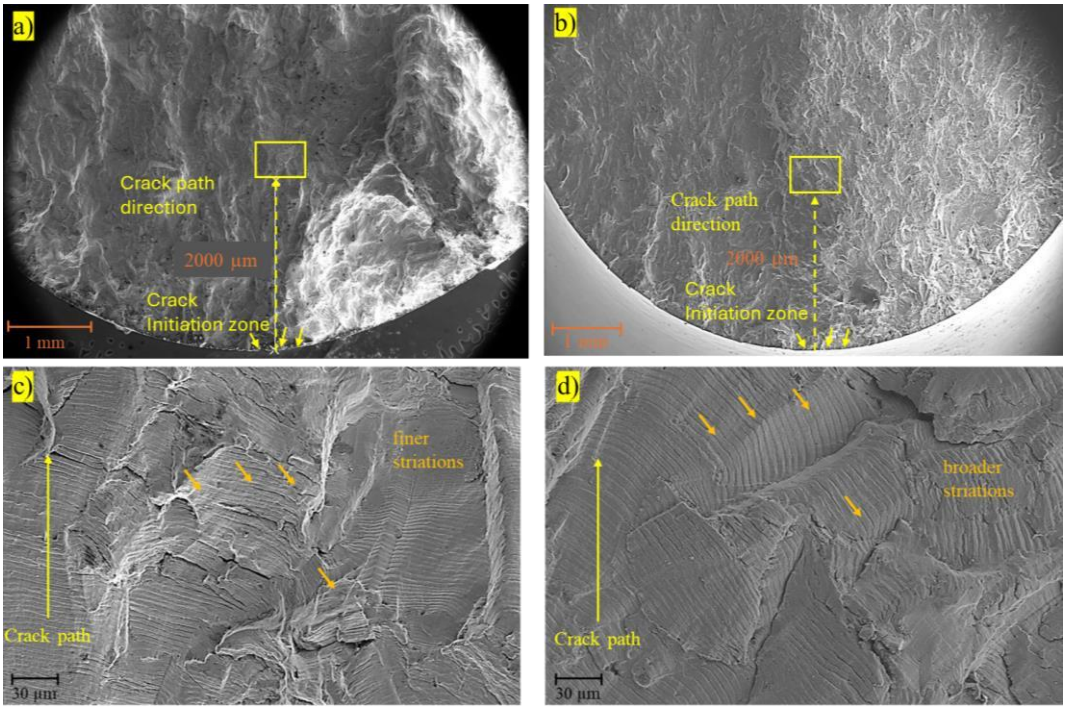

Figure 99: Fracture surfaces of Alloy 690TT tested in the PWR environment at ε_a = 0.45%, $\dot{\varepsilon}$ = 0.004%/s : (a) as-received and (b) aged specimens showing crack initiation zones and crack paths; (c) higher magnification of as-received with finer striations; (d) higher magnification of aged with broader striations.

This **Figure 100** presents the quantitative evolution of the striation spacings as a function of the crack depth for as-received and aged Alloy 690TT in air and in PWR.

In air (ε_a= 0.6%, $\dot{\varepsilon}$ = 0.02%/s), the striation spacing of the aged sample is systematically larger than that of the as-received sample, and the difference increases with crack depth. For a crack depth of ~1000 µm, the striation spacing is ~7 µm for the aged sample compared to ~4 µm for the as-received one. At ~2500 µm, the values increase to ~24 µm for the aged sample and ~20 µm for the as-received one, confirming that aging accelerates crack growth.

In the PWR environment ($\Delta\varepsilon_a$ = 0.45%, $\dot{\varepsilon}$ = 0.004 %/s), the absolute striation spacings are smaller overall, reflecting the slower growth rate. At ~1000 µm crack depth, both aged and as-received specimens show spacings of ~2 µm. Differences appear at larger depths: at ~2000 µm, the striation spacing is ~10 µm in the aged sample versus ~3 µm in the as-received one; and by ~4000 µm, the aged specimen reaches ~25 µm while the as-received specimen remains at ~5 µm.

Taken together, these results demonstrate that thermal aging systematically increases striation spacing and thereby accelerates fatigue crack growth in both air and PWR environments.

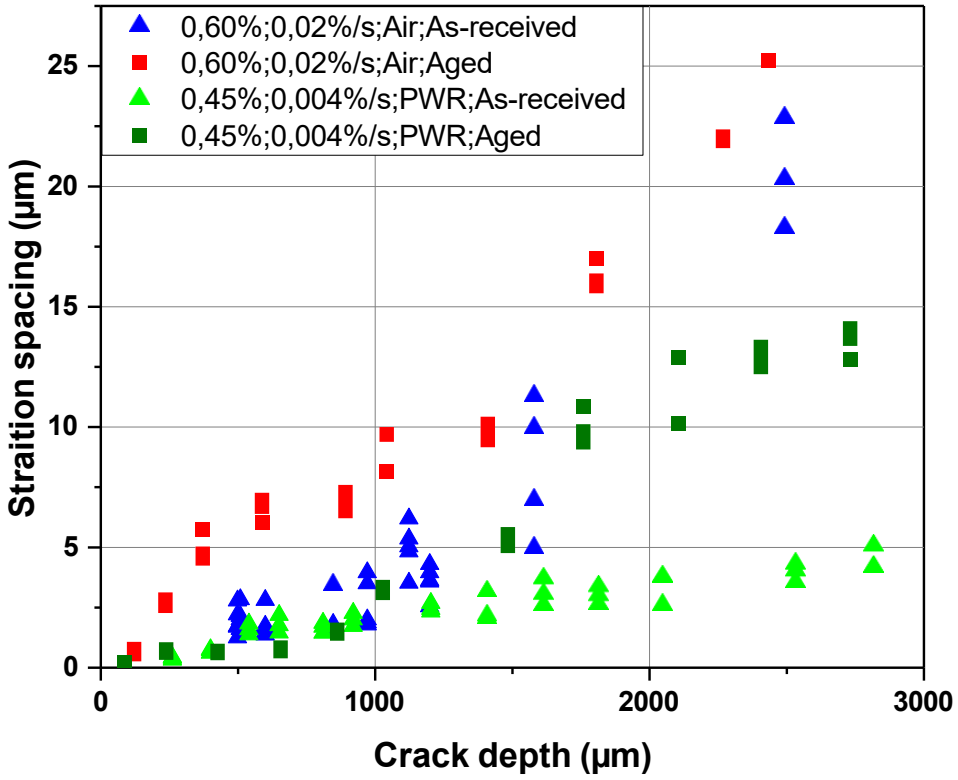

Figure 100: Comparison of the striation spacing with respect to crack depth between as-received and the aged samples in air and PWR environment.

Finally, the fatigue crack growth rate (FCGR) behavior of Alloy 690TT, shown in **Figure 101**, highlights the combined effect of thermal aging and environment on crack propagation. In both air (blue vs. red) and PWR (light green vs. dark green), thermally aged specimens exhibit consistently higher crack growth rates than their as-received counterparts at a given strain

intensity factor range (ΔK_ε). This indicates that aging reduces the intrinsic resistance of the alloy to crack advancement.

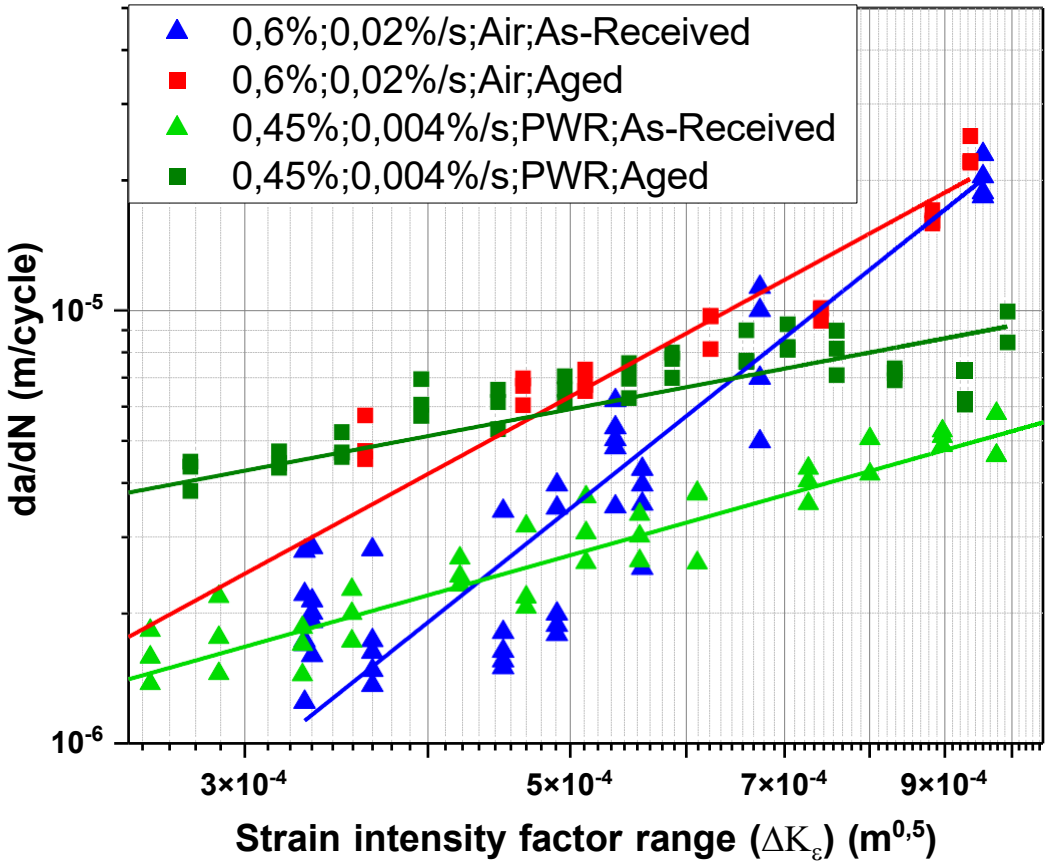

Figure 101: Comparison of the FCGR between as-received and aged samples in air and PWR environment.

The increased crack growth rate in aged samples can be attributed to microstructural changes induced by long-term thermal exposure, including precipitate coarsening and the formation of Ni_2Cr-type phases [Alexandreanu et al., 2024, Yoo et al., 2016]. However, the precise contribution of these microstructural features to the propagation behavior remains uncertain and would require further investigation. In parallel, the larger hysteresis loop areas observed in aged specimens tested in air imply greater plastic energy dissipation per cycle; this translates into more plasticity concentrated at the crack tip and more energy available to drive crack propagation, further accelerating fatigue damage. In the PWR environment, a similar trend of higher crack growth rates, as observed in air, is also seen in aged specimens; however, no prior studies are available on the fatigue behavior of aged Alloy 690TT in both air and PWR. Most published work has focused instead on stress corrosion cracking (SCC). Therefore, the present results provide new insight into the combined effects of aging and PWR environment on fatigue

crack growth. These results of FCGR indicate a degradation in crack growth resistance with aging, regardless of environment.

V.4. MICROSTRUCTURAL DAMAGE EVALUATION ON SECONDARY CRACKS

Secondary cracks were analyzed to assess microstructural fatigue damage in Alloy 690TT under as-received and aged conditions, both in air and PWR environments. Parameters such as crack density, depth, branching, and initiation angle were quantified and correlated with crystallographic factors (e.g., Schmid factor) and local strain localization from EBSD and KAM analyses. This approach allows evaluation of how thermal aging (precipitate coarsening, SRO, local hardening) and environmental effects influence secondary crack morphology, thereby providing insight into fatigue initiation and propagation mechanisms.

V.4.1. Analysis on crack initiation

V.4.1.1. Linear crack density (LCD) and crack branching

The **Figure 102a** and **Figure 102b** displays the linear crack density (LCD) and crack branching density of Alloy 690TT samples, LCD is measured as the number of secondary cracks per millimeter of specimen length, with a total length of 4 mm. The LCD results, plotted against strain amplitude, provide insight into the surface damage characteristics of Alloy 690TT under different test conditions. It compares samples tested under air and PWR environments, distinguishing between as-received and aged conditions.

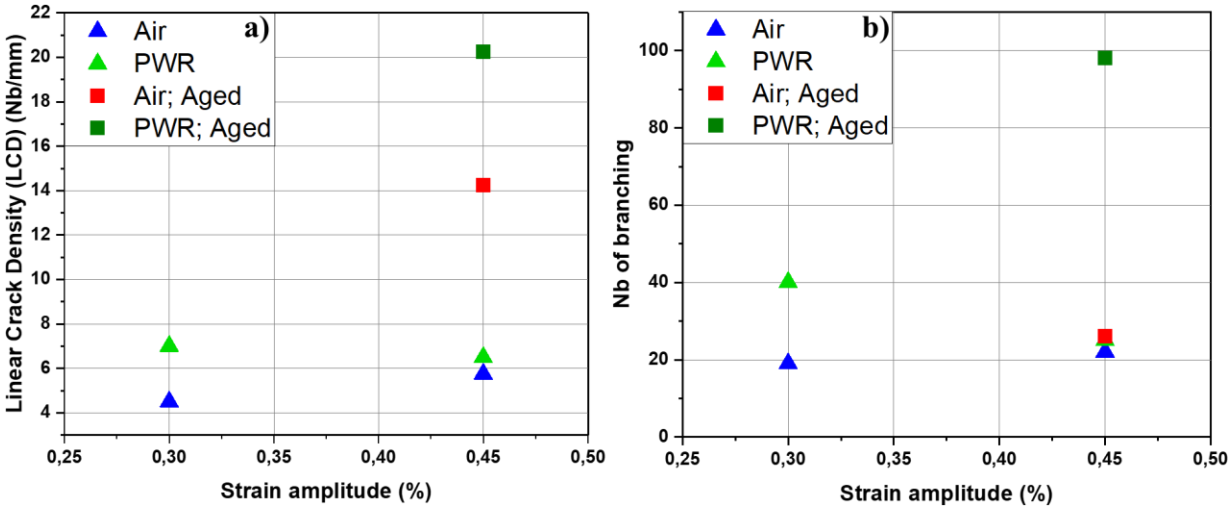

Figure 102: Representation of a) linear crack density (LCD) and b) crack branching of as-received and the aged specimen in air and the PWR environment.

At 0.3% strain amplitude, only as-received samples were tested in both air and PWR environments. In this case, the difference in linear crack density between air and PWR is not significant, indicating that environmental effects on surface cracking are limited in the as-received condition.

At 0.45% strain amplitude, both as-received and aged conditions are available. The aged samples (red and green squares) show a significantly higher LCD than the as-received ones. The aged sample tested in PWR reaches the highest value (~20 cracks/mm), more than 3× that of the as-received PWR sample. The aged sample tested in air also exhibits elevated LCD compared to the as-received air test.

The **Figure 102b** highlights the number of crack branchings as a function of strain amplitude for as-received and aged Alloy 690TT in air and PWR. At 0.3% strain, the difference between air (~20) and PWR (~40) is modest. At 0.45% strain, the aged sample in PWR shows a sharp increase (~100) compared to both as-received and aged conditions (~20–25) in air, highlighting the combined effect of aging and environment on promoting extensive crack branching. The combined effect of aging and environmental conditions therefore appears to accelerate damage accumulation by multiplying crack fronts.

These results indicate that thermal aging significantly enhances the tendency for surface crack formation, especially in the PWR environment. This aligns with observations from crack branching data and supports the notion that aging weakens resistance to fatigue damage initiation and promotes widespread surface cracking, possibly due to degradation at grain boundaries, increased oxidation susceptibility, and microstructural embrittlement.

V.4.2. Damage density quantification

The **Figure 103** and **Figure 104** present the distributions of both crack depth and crack length for as-received and aged Alloy 690TT specimens tested in air and PWR environments.

In air (**Figure 103a**), the aged samples exhibit a larger proportion of short cracks (2–10 μm), accounting for nearly 60% of the total population, compared to around 48% in the as-received condition. Furthermore, approximately 90% of the crack depths in aged samples are confined between 2–40 μm, whereas the as-received condition shows a broader spread, extending up to 60 μm.

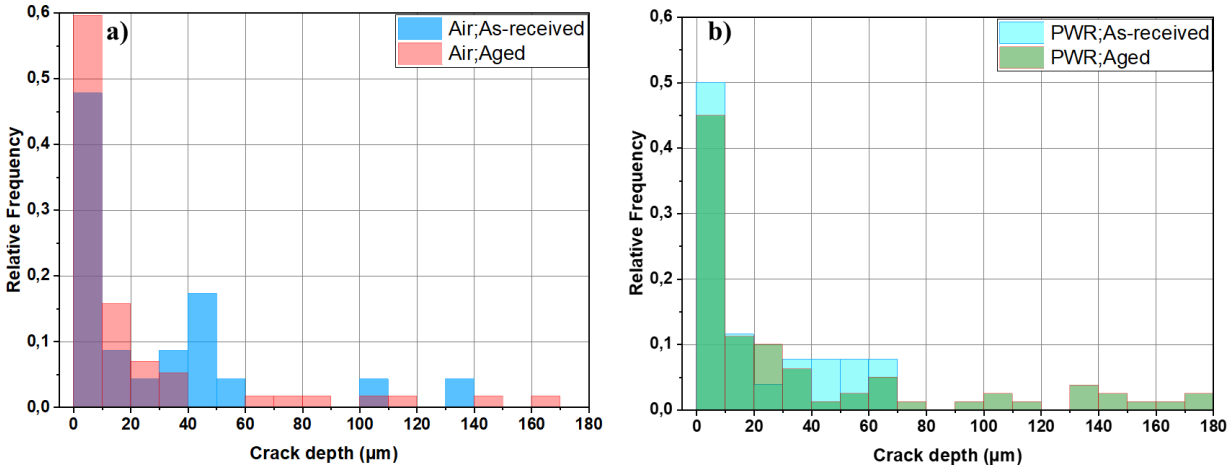

Figure 103: Distribution of crack depth of as-received and the aged specimens tested at ε_a =0.45% in a) air and b) the PWR environment.

This higher percentage of short cracks within the overall density suggests that the aged sample possesses lower resistance to crack initiation, resulting in multiple site initiation.

For the specimens tested in the PWR environment (**Figure 103b**) the crack depth distribution in the as-received sample is almost identical to that observed in the air. The occurrence of short cracks reduces to 45% in the PWR environment, and the distribution of longer cracks (> 40µm) is more widespread. This indicates that crack propagation is more significant in this environment, a phenomenon not observed in the aged specimen tested in air.

A similar trend is evident for crack length: aged specimens in air (**Figure 104a**) show a dense population of short surface cracks (<20 µm), whereas the PWR environment (**Figure 104b**) exhibits a higher crack length, resulting in a reduction of shorter crack lengths. This difference suggests that thermal aging leads to a higher frequency of crack initiation in air, while in the PWR environment, crack propagation also increases, resulting in a shorter fatigue life for the aged alloy under PWR conditions.

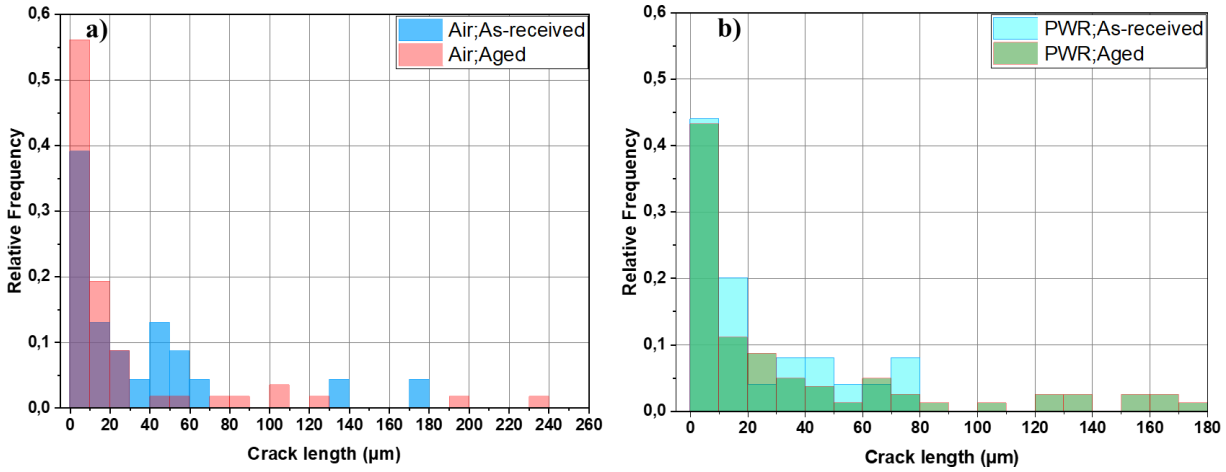

Figure 104: Distribution of crack length of as-received and the aged specimen tested at ε_a = 0.45% in a) air and b) PWR environment.

The **Figure 105** presents the distribution of crack initiation angles for both as-received and aged specimens tested in air and PWR environments.

In air (**Figure 105a**) the initiation angles are centered around 45°, indicating the transgranular crack initiations. However, the aged samples demonstrate a noticeable shift toward higher angles (peaking closer to 50–60°), suggesting that cracks in aged material tend to initiate at more oblique orientations, potentially due to localized formation of secondary phases like SRO or increased stress redistribution around precipitates.

In the PWR environment (**Figure 105b**), both aged and as-received samples exhibit flatter and more uniformly spread angle distributions, indicating more random crack propagation paths. Nonetheless, aged specimens still show a slight bias toward higher angles, similar to the air-tested condition.

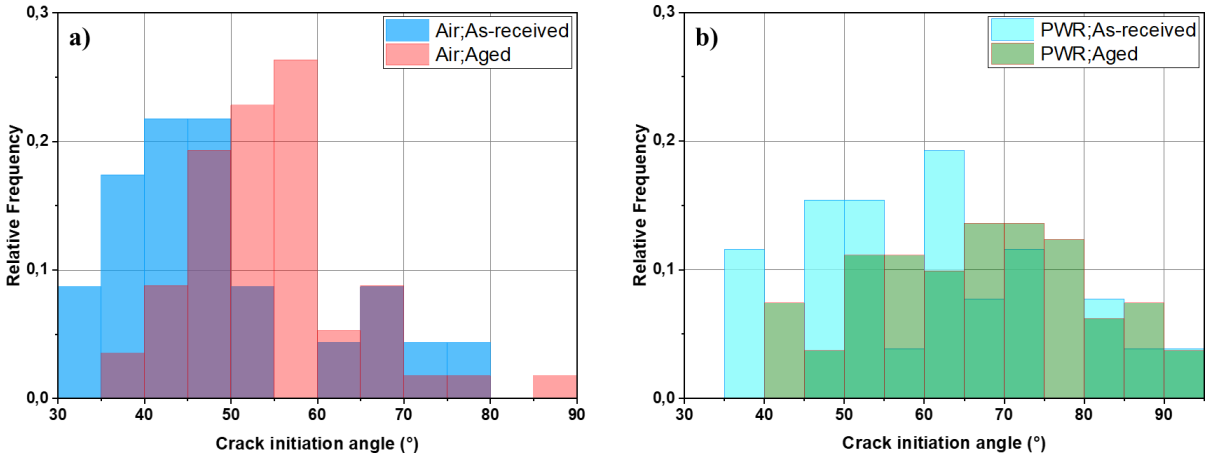

Figure 105: Distribution of crack initiation angle of as-received and the aged specimen tested at 0.45% in a) air and b) the PWR environment.

V.4.3. Schmid factor analysis of secondary cracks

The primary objective of this analysis is to investigate whether crystallographic orientation, represented by the Schmid factor (SF), correlates with fatigue crack initiation in Alloy 690TT under LCF conditions in air and PWR environments, both in the as-received and thermally aged conditions.

By comparing the Schmid factors of the grains that experienced cracking to those of neighboring grains that remained intact (non-cracked), the aim is to identify whether slip system orientation plays a critical role in crack initiation - especially in the context of environmental exposure and microstructural changes (e.g., short-range ordering or carbide formation).

The Schmid factor was calculated using EBSD data from cracked and non-cracked grains. For FCC materials like Alloy 690, the primary slip systems are {111}⟨110⟩ [Jiang et al., 2015, Larrouy et al., 2015]. In this analysis, the Schmid factor was calculated using these slip systems and a uniaxial loading axis aligned along the Z-direction ([0 0 1]), consistent with the axial fatigue loading applied during the tests. This setup allows the evaluation of the contribution of each individual grain orientation to the activation of slip and potential crack nucleation under mechanical loading.

In the as-received condition, both in air and PWR environments, grains where cracks initiated consistently exhibited higher Schmid factors (~0.47–0.48) compared to non-cracked grains (~0.39–0.41) (**Figure 106**).

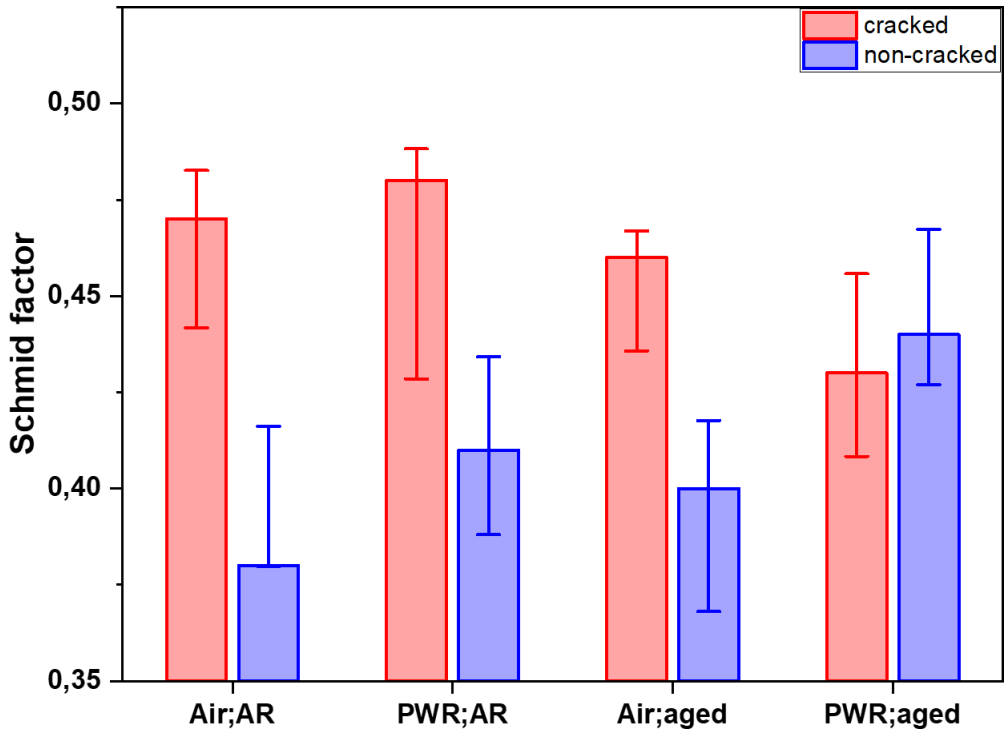

Figure 106: Comparison of Schmid factors between the cracked and the non-cracked grains of the as-received and the aged specimens tested at ε_a = 0.45%, %, $\dot{\varepsilon}$ = 0.02%/s in air and at $\dot{\varepsilon}$ = 0.004%/s the PWR environment.

However, this correlation becomes less distinct in the aged samples. In air, the difference between cracked and non-cracked regions is still present but decreased. In the PWR-aged condition, the average Schmid factor of cracked and non-cracked grains nearly converges (~ 0.44 – 0.45), indicating a reduced influence of crystallographic orientation on crack initiation. This change is likely due to aging-induced microstructural modifications such as short-range ordering (SRO) and carbide precipitation, which alter the local slip resistance and may override the influence of slip orientation alone [Kim et al., 2022]. Moreover, environmental effects in the PWR medium, such as oxidation, may further obscure the role of the Schmid factor.

V.4.4. Analysis of the crack propagation

The **Figure 107** compares the secondary crack propagation modes in as-received and aged Alloy 690TT samples tested at 300 °C in air. In the as-received condition (**Figure 107 a and c**), cracks propagate predominantly in a transgranular (TG) manner, following slip bands across grains. The crack paths are relatively straight, and no significant grain boundary cracking is observed, indicating that the grain boundaries maintain good cohesion and that deformation is primarily controlled by slip activity within grains.

In contrast, the aged condition (**Figure 107 b and d**) exhibits a mixed propagation mode, combining transgranular cracking with localized intergranular (IG) cracking along grain

boundaries. These intergranular regions are typically associated with carbide coarsening and oxidation of carbides resulting from thermal aging, which reduces grain boundary cohesion and promotes crack deflection along weakened interfaces, which are further explained in Section **V.5.2**.

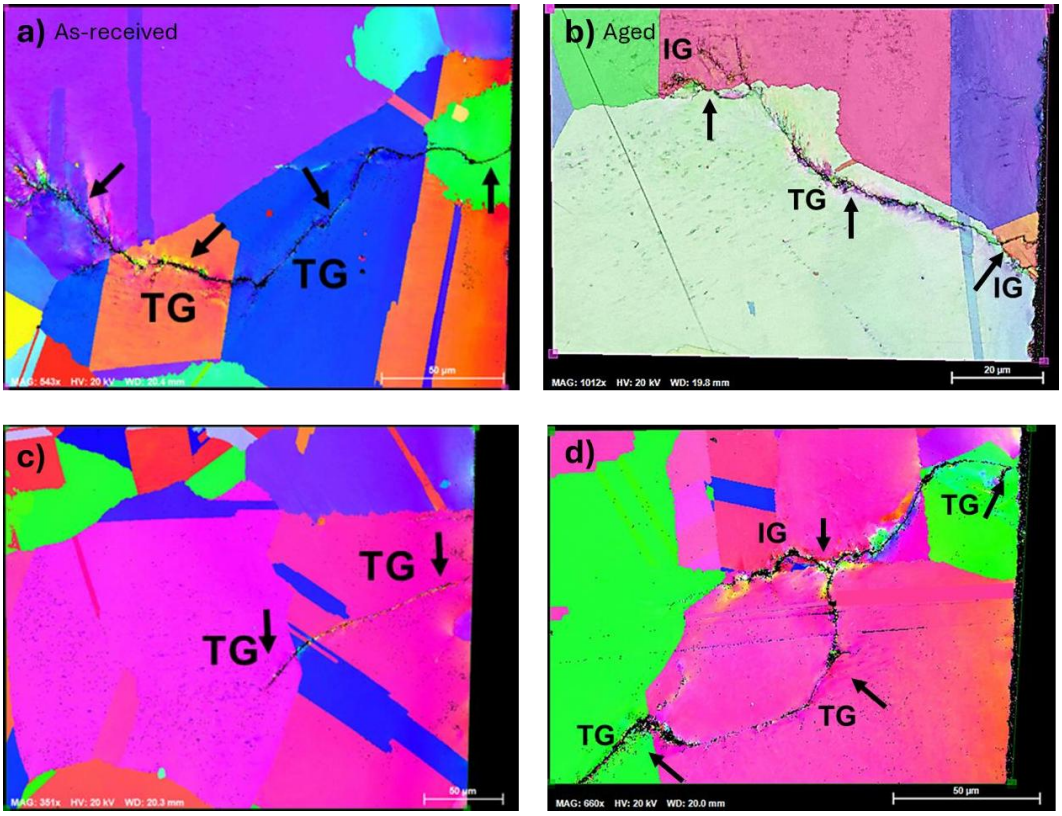

Figure 107: Comparison of secondary crack propagation modes between the (a, c) as-received showing TG propagation and (b, d) aged samples showing mixed mode TG+IG propagation, tested at ε_a = 0.45%, $\dot{\varepsilon}$ = 0.02%/s, 300°C in air.

It can be noted that a similar observation can be done on aged specimens tested in PWR environment (**Figure 108**).

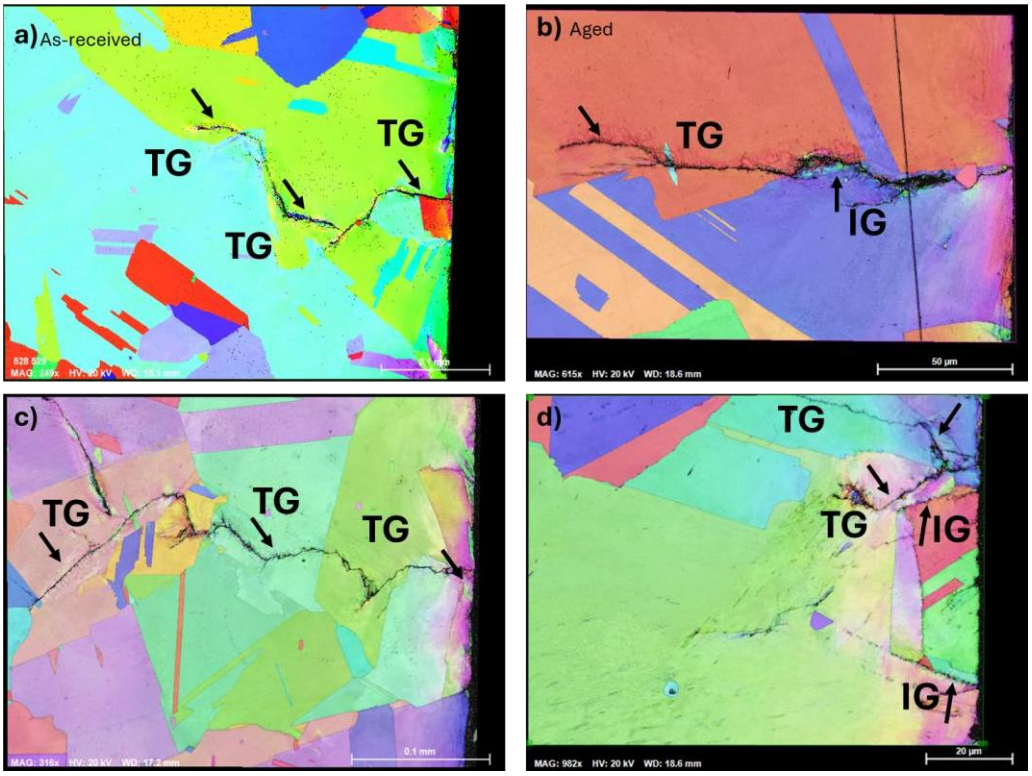

Figure 108: Comparison of secondary crack propagation modes between the (a, c) as-received showing TG propagation and (b, d) aged samples showing mixed mode TG+IG propagation, tested at ε_a = 0.45%, $\dot{\varepsilon}$ = 0.02%/s, 300°C in the PWR environment.

V.4.5. Effect of environment and aging on strain localization

The **Figure 110 a) and c)** shows the images of the secondary cracks of the aged sample tested in air at 0.45%. In comparison with the cracks present on the as-received sample tested in air (**Figure 109a**) the crack path presents a more localised strain around the crack tip, which is also coherent with the higher hysteresis loops (**Figure 94**) and the higher plastic strain accumulation (**Figure 97**). This localization is accompanied by more pronounced development of PSBs in the vicinity of the crack path.

The aged samples tested in PWR environment (**Figure 110b and d**) demonstrate even more pronounced strain localization. The strain is concentrated not only along the primary crack path but also around crack branches, indicating an environment-assisted crack propagation mechanism. The density and distribution of PSBs in these images suggest enhanced slip activity, likely influenced by the corrosive PWR conditions that may reduce cross-slip and increase planar slip [Chen et al., 2019, Tan et al., 2014b]. Moreover, the surface of specimens tested in the PWR environment shows a broader zone of strain localization when compared to those tested in air. This may be due to the formation of surface oxides, which can act as local

stress concentrators and promote slip localization. The effect appears to be more pronounced in the aged condition, as evidenced by the stronger strain localization and more distinct PSB activity observed near secondary cracks (**Figure 110 a–d**), possibly due to oxide-induced changes in surface and microstructure, leading to easier crack initiation and propagation. Overall, the combined effect of thermal aging and environmental exposure contributes to increased susceptibility to localized deformation, facilitating fatigue crack growth under cyclic loading.

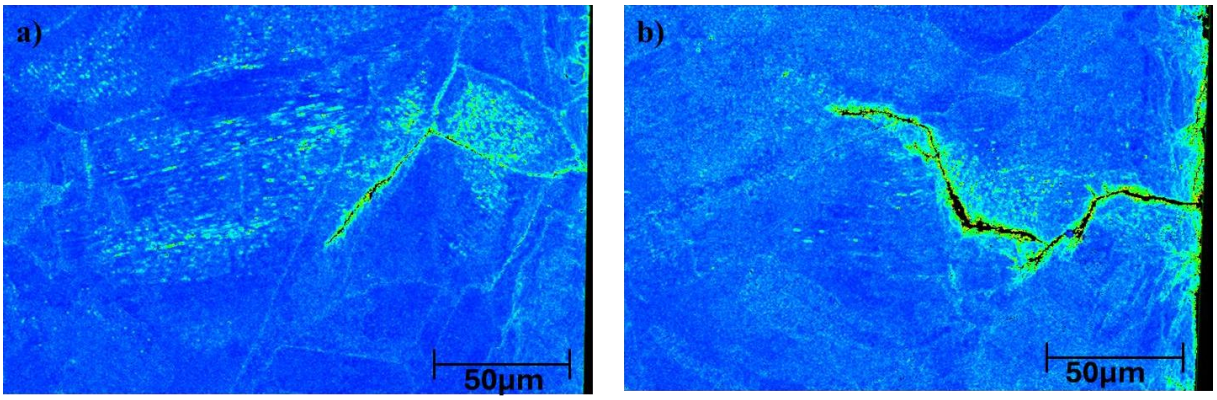

Figure 109: KAM images of secondary cracks of the as-received sample tested at ε_a = 0.45% in a) air, and b) PWR environment.

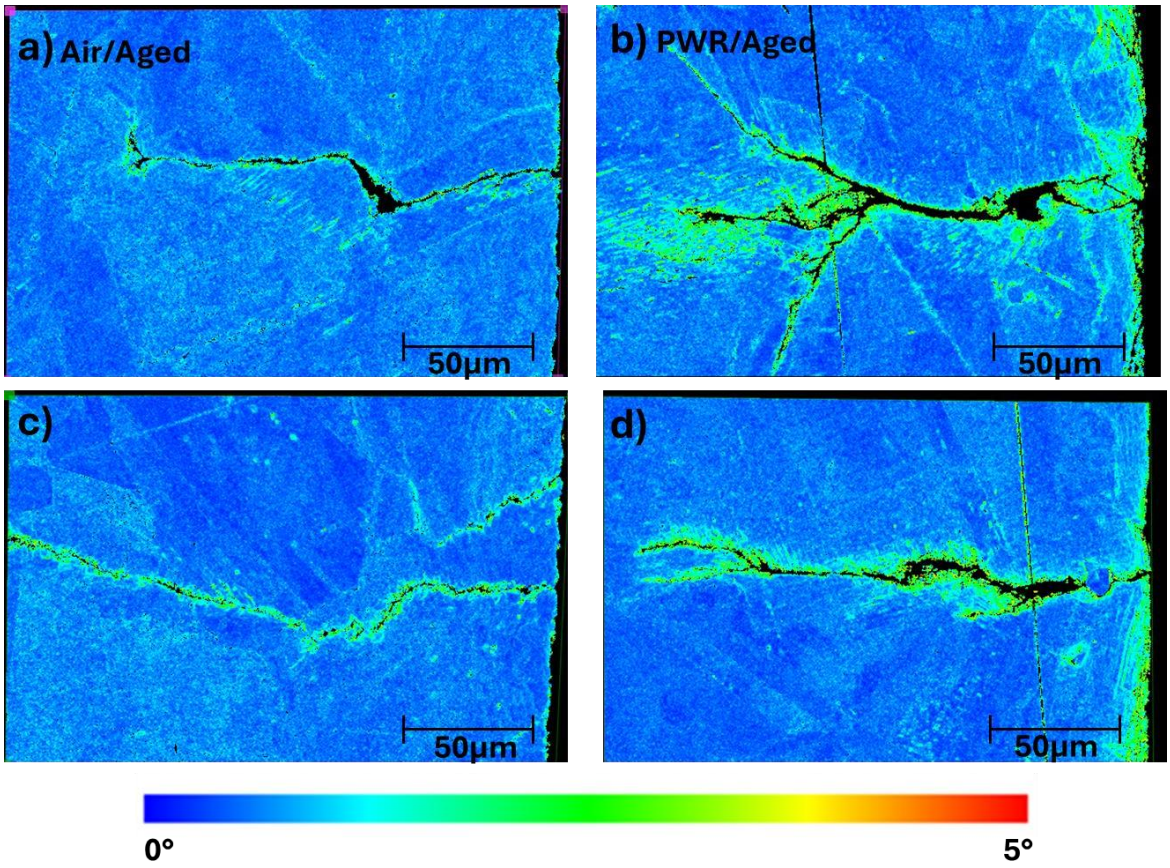

Figure 110: KAM images of the secondary cracks of the aged sample tested at ε_a = 0.45% in a), c) air and b), d) PWR environment.

The misorientation angle histograms (**Figure 111**) were obtained by counting the number of EBSD pixels and sorting them according to their local misorientation angle. This provides a direct measure of the distribution of plastic strain at the microscale.

In air, for the as-received samples, the majority of misorientation angles are concentrated below ~0.7°, with the frequency dropping steeply beyond this value. After thermal aging, a broader distribution is visible, extending up to ~1.2°, with an increased relative frequency in the range 0.5–1°.

In PWR environment, as-received samples show again a peak below ~0.6°, but the distribution extends more gradually. For the aged samples, the histogram develops a distinct tail up to ~1.5°, with a higher fraction of points above 1° compared to both the as-received and the aged-air conditions. This indicates stronger strain localisation and increased lattice rotation in the aged sample tested in PWR environment. It also shows a distinct tailing towards higher misorientation values, signifying more severe plastic accommodation near the crack tips.

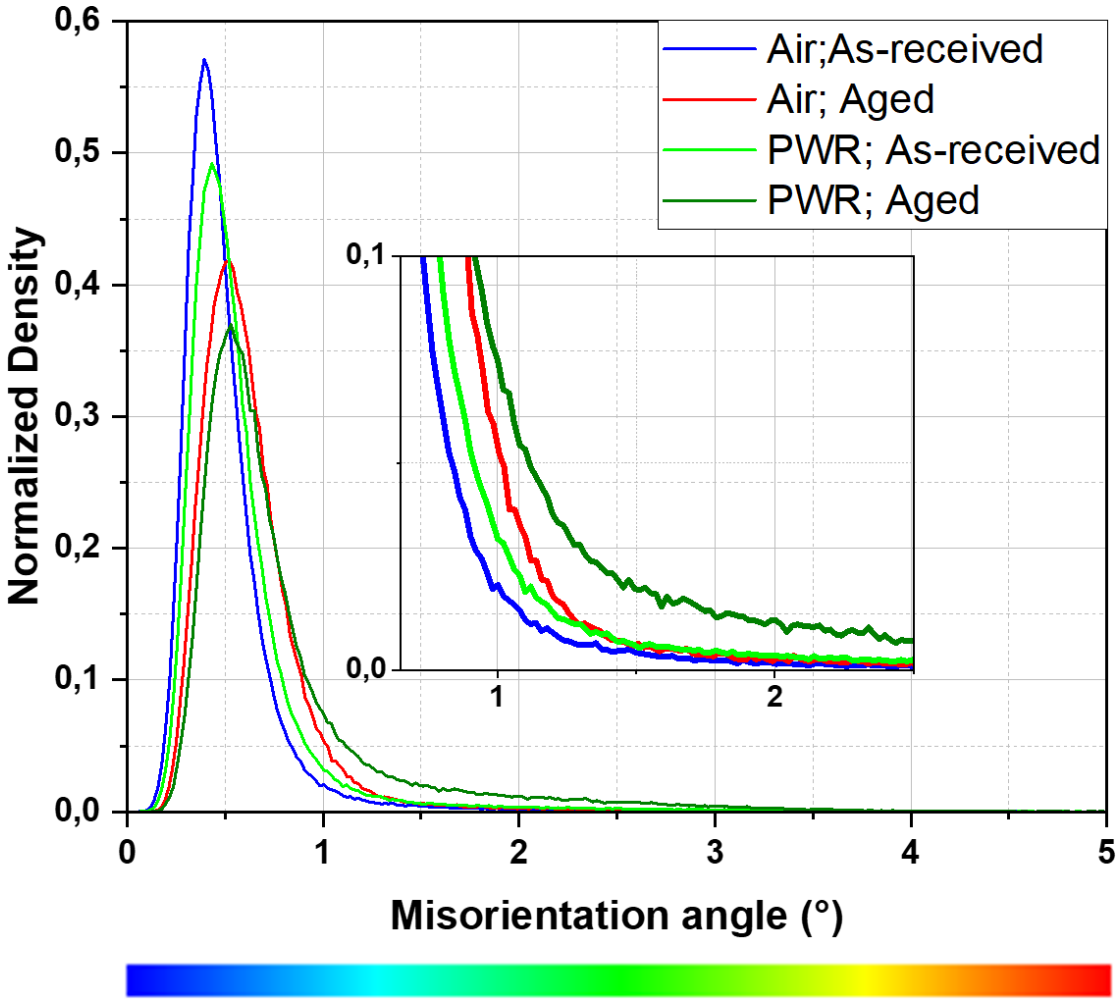

Figure 111: Histogram plot of the misorientation angle of the as-received and the aged samples tested in air and the PWR environment (the color gradient describes misorientation angle from 0° to 5°.

V.5. COUPLED EFFECTS OF THERMAL AGING AND ENVIRONMENT ON THE LCF OF ALLOY 690TT

V.5.1. Effect of thermal aging on cracking characteristics in Alloy 690TT

The **Figure 112** depicts the microstructure of both as-received and aged Alloy 690TT samples, both prior to and after fatigue testing.

Before aging, in the as-received samples, the microstructure shows the presence of precipitates that are firmly integrated into the alloy matrix even after the polishing, with no visible signs of decohesion (**Figure 112a**).

In contrast, after aging, the samples display micro-defect structures within the matrix, indicative of precipitate decohesion (**Figure 112c**). This decohesion occurs despite the samples undergoing polishing processes similar to those of their as-received counterparts.

The decohesion between the matrix and the precipitates could be due to the oxidation of the latest during accelerated thermal aging (**IV.1.3**). Regarding the secondary cracks, the as-received samples predominantly exhibit surface crack initiation, with no evidence of intergranular cracking (**Figure 112b**). Conversely, the aged samples display some cracks that appear to propagate through the precipitates (**Figure 112d**). It remains unclear whether these cracks initiate internally or from another dimension of the material. To investigate this further, Focused Ion Beam (FIB) analysis was used to assess the depth of these internal cracks.

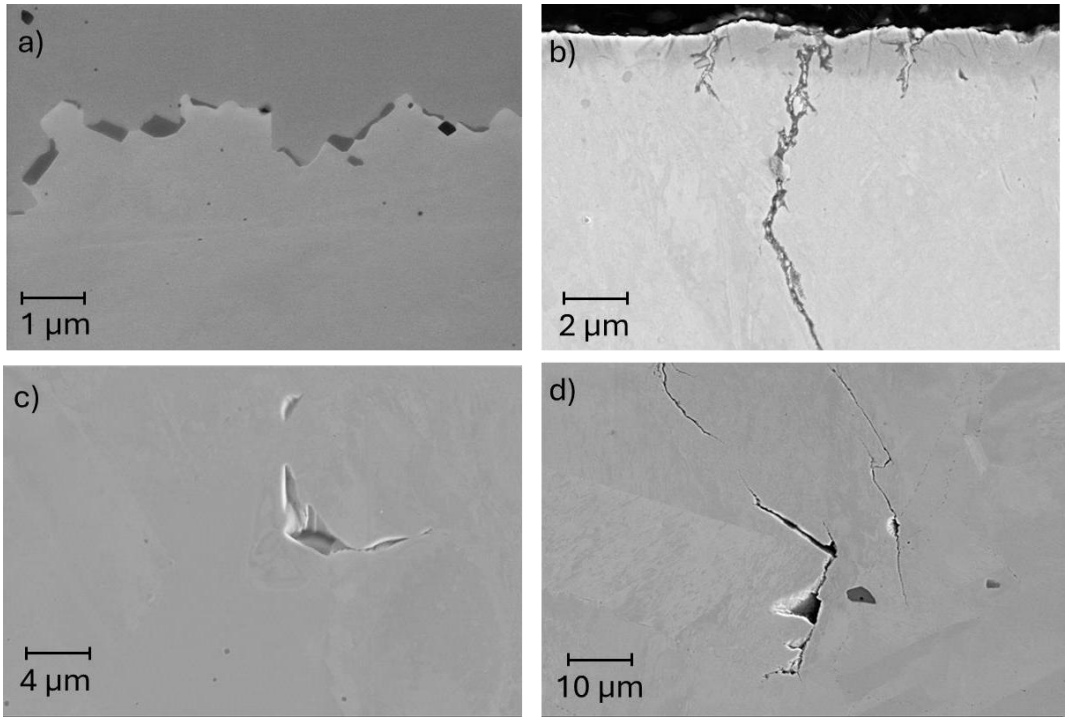

Figure 112: Images of microstructure and cracking characteristics of Alloy 690TT: a) Polished As-received, not tested b) As-received, at failure (8800 cycles) ; c) Polished Aged, decohesion between matrix and precipitates, not tested ; and d) Aged, at failure (6500 cycles) / ε_a = 0.45%, 0.02%/s, 300°C in air.

V.5.2. Chemical analysis of a secondary crack in aged Alloy 690TT

To further investigate the possible role of oxidation in intergranular cracking of aged Alloy 690TT, site-specific thin foils were extracted by FIB from regions containing secondary cracks near the specimen surface. The objective was to characterize the chemical composition along the crack path, particularly at grain boundary carbides, using STEM coupled with EDS. This approach allows precise examination of the crack path and adjacent grain boundary regions to assess whether oxidation or carbide–matrix interactions contribute to intergranular crack propagation, thereby contributing to the reduced crack growth resistance observed in aged samples in air and the PWR environment.

The **Figure 113** shows the axial cross-section of the aged sample tested in air, in which a secondary crack is observed propagating along intergranular carbides near the specimen surface. The region highlighted by the yellow box was selected for FIB lift-out to prepare a site-specific thin foil for STEM–EDS characterization.

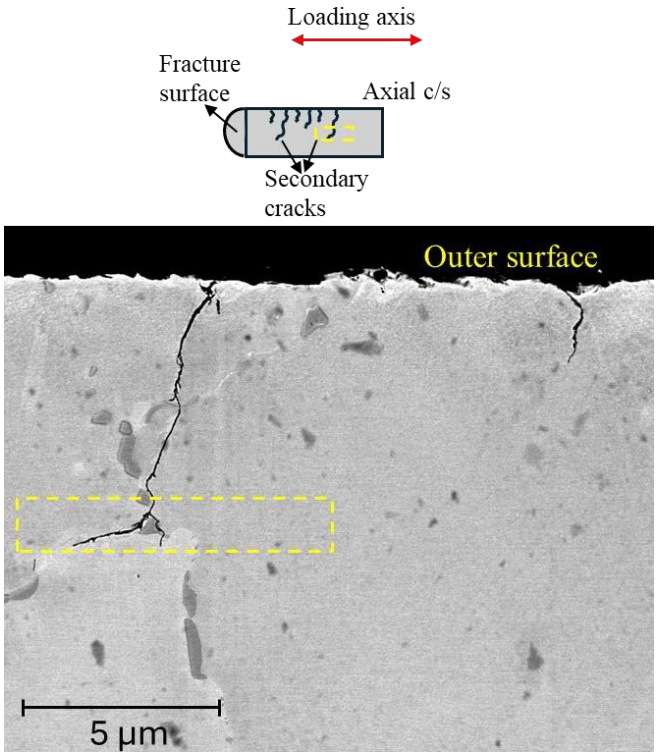

Figure 113: Cross-sectional SEM image of an aged specimen tested at ε_a = 0.45%, $\dot{\varepsilon}$ = 0.02%/s, 300°C in air, showing a secondary crack propagating from the outer surface. The crack exhibits intergranular characteristics, with branching visible along grain boundaries.

The **Figure 114** shows a SEM image of the FIB lift-out from the region of the intergranular crack identified (**Figure 113**). The image highlights a secondary crack intersecting a grain boundary, where the region of interest (marked as Spectre 2) was selected for EDS point analysis.

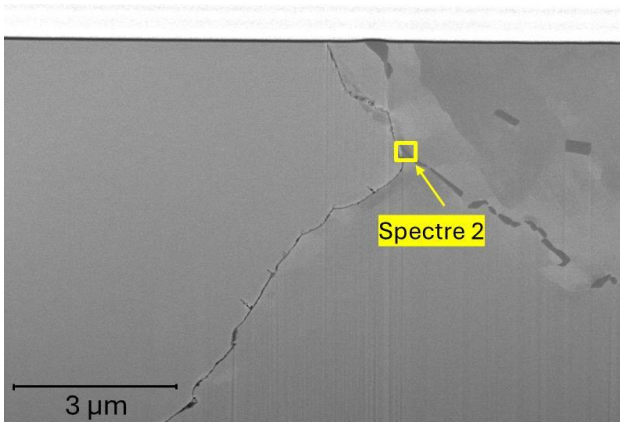

Figure 114: Focused ion beam (FIB) lift-out of a thin lamella from the region ahead of a secondary crack in the aged specimen tested in air, prepared for subsequent STEM-EDS analysis.

The **Figure 115** shows the EDS spectrum acquired from the precipitate region adjacent to the intergranular crack path in the aged Alloy 690TT sample tested in air. The analysis reveals significant oxygen enrichment (~33 at.%), together with peaks corresponding to nickel (Ni), chromium (Cr, ~22 at.%), iron (Fe), and silicon (Si). The resulting O/Cr ratio of approximately 1.5 is consistent with the stoichiometry of Cr_2O_3. This confirms that oxidation occurs preferentially at grain boundary carbides, promoting local decohesion between the matrix and the carbides and facilitating intergranular crack propagation during fatigue.

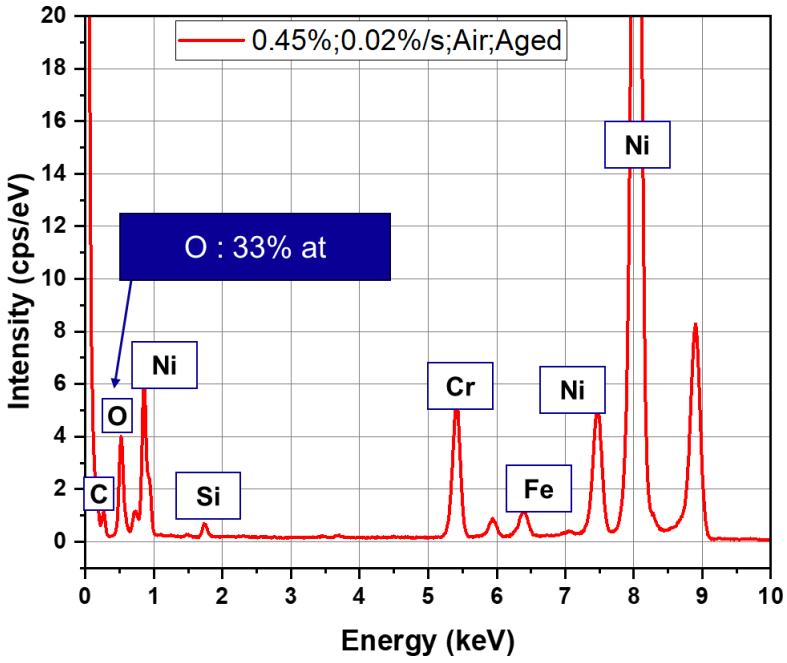

Figure 115: EDS spectrum acquired from the secondary crack surface of the aged Alloy 690TT specimen tested at ε_a = 0.45%, 0.02%/s, 300°C air (Spectre 2).

The **Figure 116** presents the FIB-extracted foil from an aged Alloy 690TT specimen tested in the PWR environment. The thin foil was lifted out from an intergranular secondary crack zone, similar to the region previously examined in the air-tested sample, in order to allow a direct comparison between the two environments. The crack path along the grain boundary is clearly visible, with local branching features typical of intergranular propagation. Specific region of interest, such as Spectre 1, were selected for EDS point to characterize the chemical environment near the crack path.

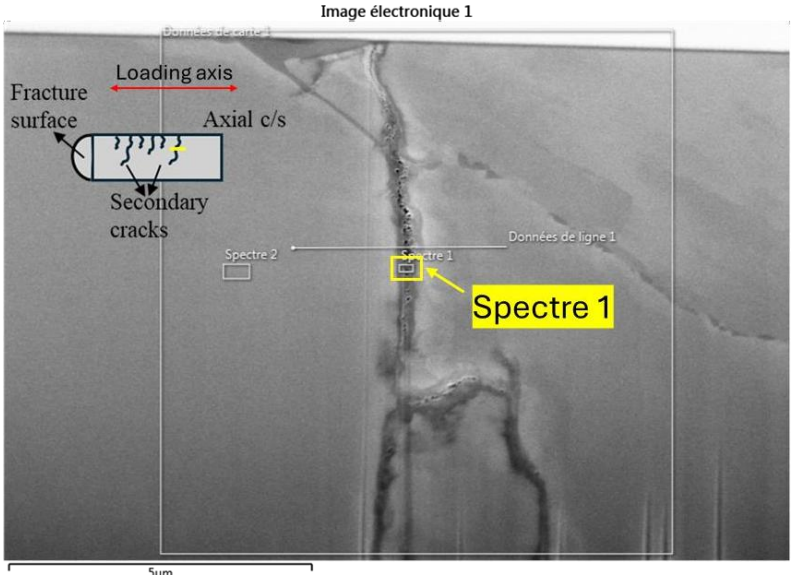

Figure 116: STEM image of a secondary crack extracted by FIB from a aged sample tested at ε_a = 0.45%, $\dot{\varepsilon}$ = 0.004%/s, 300°C in PWR environment.

The comparison between the spectra obtained from aged specimens tested in air (red curve) and PWR environment (green curve) (**Figure 117**) shows that oxygen enrichment occurs along the intergranular crack paths near the precipitates in both cases. The similar oxygen peak intensities (~6 cps/eV, corresponding to ~33 at.% O and an O/Cr ratio close to 1.5) indicate the presence of Cr_2O_3 along grain-boundary carbides, suggesting that the oxidation of precipitate observed near the IG crack is primarily a consequence of the prior thermal aging rather than the PWR environment itself.

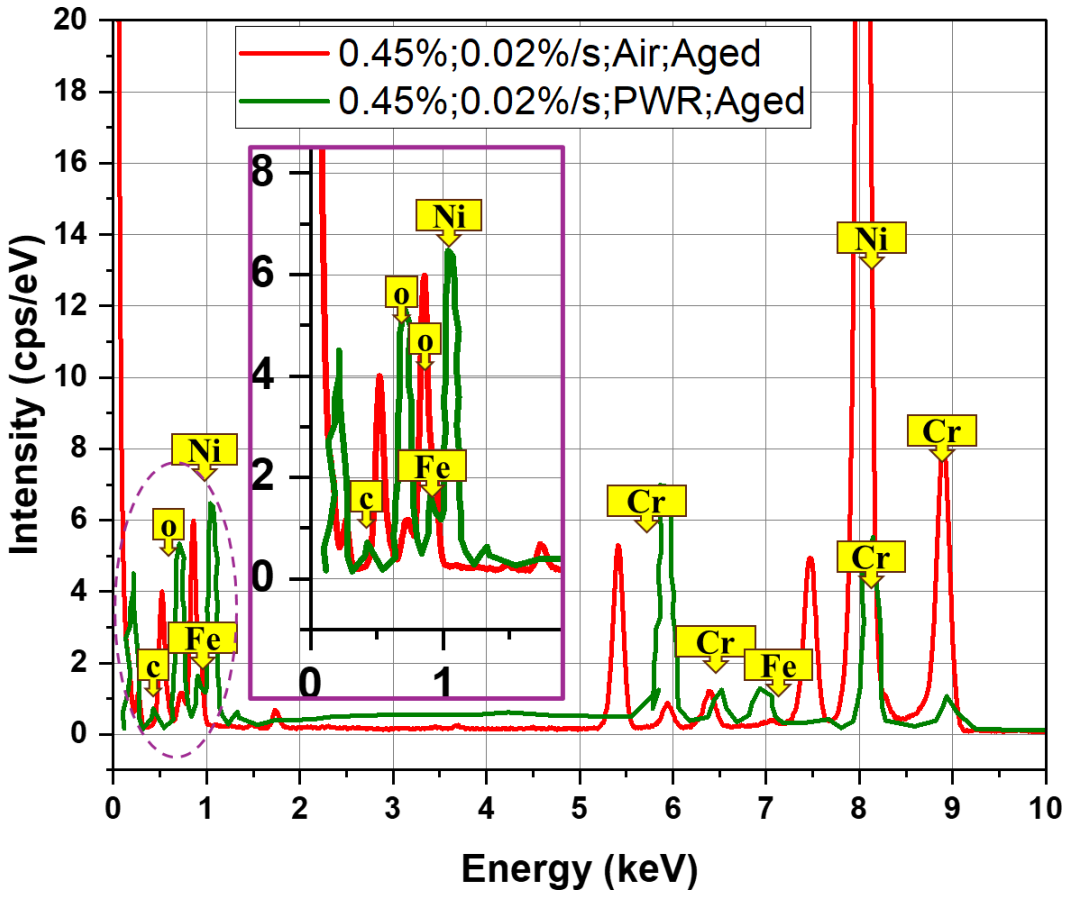

Figure 117: EDS spectrum acquired from the secondary crack surface of the aged Alloy 690TT specimen tested under air and the PWR environment (Spectre 2 and Spectre 1).

The **Figure 118a** shows an example of an intergranular crack extracted by FIB, presents the STEM-EDS superimposed elemental map (**Figure 118b**) in an aged Alloy 690TT specimen tested in the PWR environment. The separate elemental maps (**Figure 119**) reveal strong enrichment of oxygen along the crack path and also beside the precipitate, confirming the presence of Cr-rich oxides. Such oxidation, known to occur preferentially at grain boundary precipitates in aged Alloy 690TT [Feng et al., 2023, Wang, 2023], can weaken boundary cohesion and promote intergranular cracking under cyclic loading. These observations, combined with the EDS spectra, suggest that aging-induced carbide precipitation followed by selective oxidation of the precipitates in the grain boundary plays a key role in interfacial decohesion which leads to intergranular cracking in aged Alloy 690TT.

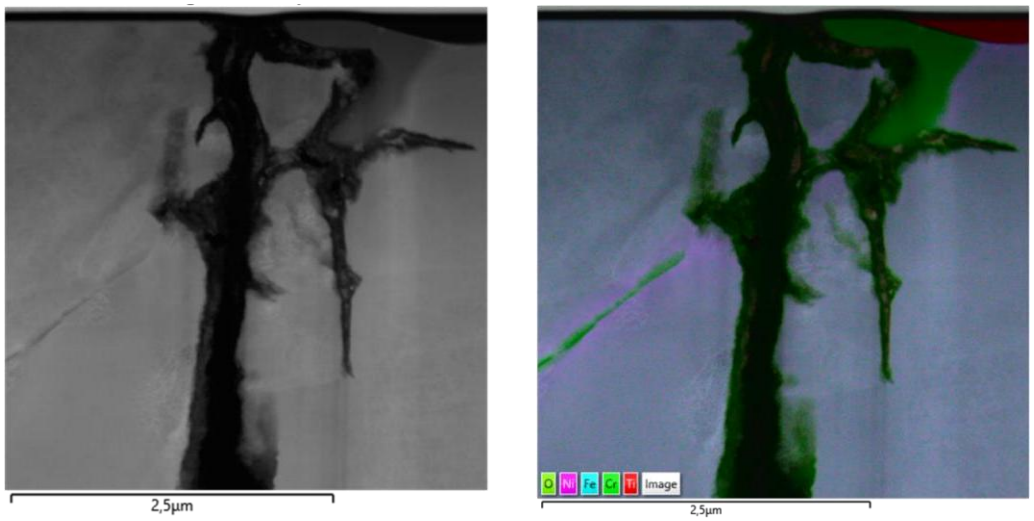

Figure 118: a) STEM image of a secondary crack extracted by FIB, b) Superimposed elemental map from EDS of aged sample tested at ε_a = 0.45%, $\dot{\varepsilon}$ = 0.004%/s, 300°C in PWR environment.

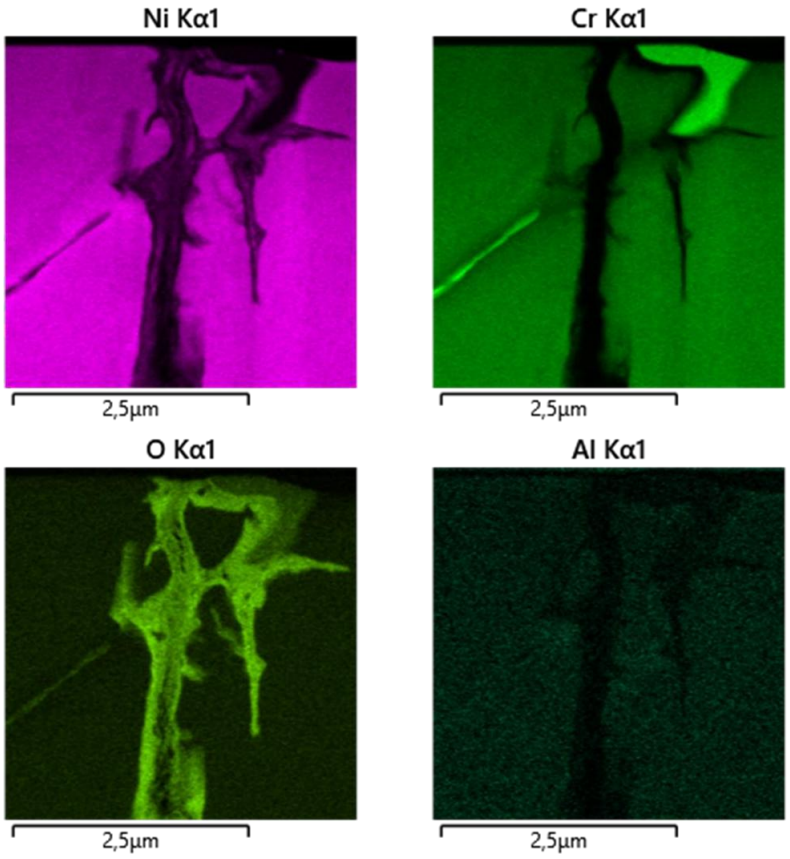

Figure 119: STEM-EDS separate elemental maps of the secondary crack of the aged sample tested at ε_a = 0.45%, $\dot{\varepsilon}$ = 0.004%/s, 300°C in the PWR environment.

V.6. MECHANISM: IMPACT OF THERMAL AGING ON LCF IN AIR OF ALLOY 690TT

Thermal aging at 420°C for 4000h promotes the precipitation and coarsening of intergranular $Cr_{23}C_6$ carbides, the development of SRO within the matrix, and the formation of chromium-rich oxides at GB precipitates and carbide–matrix interfaces. These microstructural changes create locally hardened grain-boundary zones while simultaneously reducing carbides interfacial cohesion through oxidation of carbides.

Under cyclic loading at 300 °C, the aged material exhibits enhanced cyclic hardening and higher plastic strain energy per cycle compared to the as-received condition, indicating greater plastic strain accommodation. Crack initiation occurs through two concurrent pathways:

i) Transgranular (TG) initiation within high-Schmid-factor grains (≈0.41) along {111} slip planes (**Figure 120**).

(ii) Intergranular (IG) initiation at oxidized carbides and weakened GB regions (**Figure 121**).

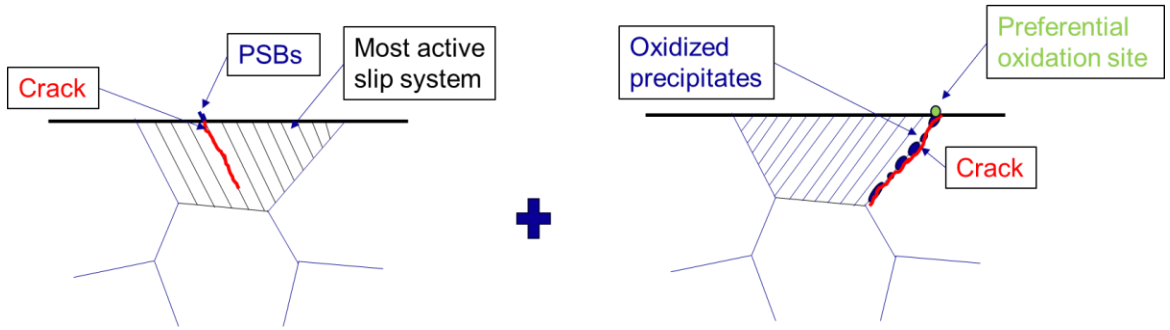

Figure 120: Mechanism of initiation in an aged sample under LCF loading in air at 300°C, showing transgranular and intergranular initiation.

During propagation, cracks exhibit a mixed TG/IG mode, influenced by the mechanical contrast between hardened GB zones and the surrounding matrix. The selective oxidation of GB carbides further assists crack advance along interfaces, promoting oxide-assisted decohesion and accelerated crack growth rates.

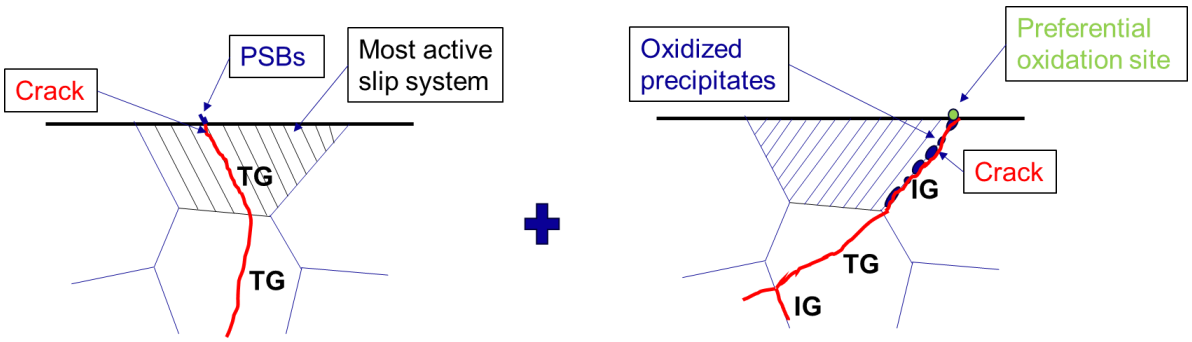

Figure 121: Mechanism of propagation in an aged sample under LCF loading in air at 300°C, showing transgranular and intergranular propagation.

Overall, thermal aging decreases the fatigue resistance of Alloy 690TT by promoting interfacial weakening and oxide-assisted crack propagation, leading to shorter lifetimes in thermally aged samples compared to as-received samples.

V.7. SUMMARY

This part of the study examined the effect of accelerated thermal aging (4000 h at 420 °C, ≈ 60 years under PWR conditions) on the low-cycle fatigue (LCF) behavior of Alloy 690TT in air and PWR environments, with emphasis on the link between microstructural evolution and fatigue response.

- **Cyclic stress–strain behavior:**
  - The aged Alloy 690TT samples exhibit increased cyclic hardening compared to the as-received condition, with an average hardening increment of about 20 MPa at 0.45 % and 0.60 % strain amplitudes.
  - This enhanced hardening could be attributed to microstructural changes during aging, including precipitate coarsening and the formation of SRO phases, which impede dislocation motion.
  - Analysis of hysteresis loops revealed larger PLC in aged compared to as-received, indicating enhanced DSA through SRO formation. Larger loop areas in aged samples compared to as-received, reflecting higher plastic energy dissipation during cyclic loading.
  - The evolution of plastic strain energy shows an overall 17 % increase in total energy dissipation for aged samples, consistent with higher accumulated plastic strain at 0.6 % strain amplitude.
  - These changes in cyclic plasticity accelerate fatigue damage accumulation and lead to a reduction in fatigue life.
- **Total fatigue life:**
  - Thermal aging led to a reduction in fatigue life, averaging ~20 % in air and ~8 % in PWR compared to the as-received condition. Strain-life (ε–N) curves confirmed this degradation, especially at higher strain amplitudes (0.45–0.6 %).
- **Crack Growth Rate:**
  - Fatigue crack growth rates (FCGR) are elevated in aged samples under comparable loading, in both air and PWR environments, evidencing faster crack propagation kinetics post-aging.
- **Microstructural Characterization of secondary cracks:**
  - Aging increases Linear Crack Density (LCD) and promotes crack branching, particularly under PWR conditions.

- Quantitative damage analysis shows that aged materials contain a higher population of short cracks (2–10 μm), indicating decreased resistance to crack nucleation.
- Crack initiation angles shift toward 50–60°, suggesting modified crack trajectories consistent with microstructural degradation.
- In the as-received state, crack initiation occurs preferentially in high-Schmid-factor grains (~0.47–0.48), linking nucleation to slip activity.
- This correlation weakens after aging, where lower Schmid factors (~0.42–0.46) and environmental effects such as SRO formation and carbide precipitation overshadow the influence of crystallographic orientation.

- **Mechanisms of Thermal Aging on LCF**
  - EBSD analyses reveal that fatigue cracks predominantly initiate along {111} slip planes in high-Schmid-factor grains in both air and PWR. However, aging promotes additional crack initiation modes involving grain boundaries or mixed transgranular/intergranular paths initiated at oxidized carbides. STEM-EDS confirms oxygen enrichment and chromium oxide formation (Cr_2O_3) along intergranular carbides, demonstrating that oxidation-assisted decohesion of grain boundary precipitates is active in propagating intergranular cracking in aged Alloy 690TT.

General conclusion and perspectives

GENERAL CONCLUSION

Low cycle fatigue behavior of Alloy 690TT in different environments

The low-cycle fatigue behavior of as-received Alloy 690TT was evaluated in vacuum, air, and PWR primary water environments. The cyclic stress–strain response revealed clear differences with temperature: at 25 °C in air, the alloy exhibited primary hardening followed by stabilization, whereas at 300 °C it showed continuous hardening throughout life. This continuous hardening was consistently observed in all three environments, including in vacuum where the fatigue life is significantly higher. The hysteresis loops recorded at 300 °C in air display serrated flow (PLC effect) that is absent at room temperature. Observations of deformation substructure from tests interrupted at 30 and 500 cycles revealed the presence of pinned dislocations at early stages and of planar dislocation arrays at later stages, confirming the occurrence of DSA. Similar features have been reported in austenitic stainless steels; however, unlike in those alloys, continuous hardening persists in Alloy 690TT. Further testing interrupted at 3000 cycles showed the formation of nano-twins, confirmed by selected-area diffraction in TEM, corresponding to the secondary hardening by acting like a dislocation barrier. The cyclic hardening was similar to a sawtooth signal compared to the triangle signal with a different strain rate, indicating that the cyclic hardening is insensitive to the waveform. The strain rate had an effect on the magnitude of secondary hardening at elevated temperature, which is more pronounced at a lower strain rate (0.02%/s) than at a higher strain rate (0.4%/s).

However, the curves of the plastic energy dissipation per cycle W_p showed excellent overlap at 25 °C (0.4 % s^{-1}) and 300 °C (0.02 % s^{-1}) in air, with only minor deviations at higher strain rates or in the later stages of life. This indicates that W_p is largely insensitive to both temperature and strain rate for the as-received alloy.

In terms of total fatigue life, the results showed that air and PWR environments led to comparable lifetimes up to a theoretical Fen factor of 2.5, whereas significantly longer lives (up to three times higher) were observed in vacuum for the same loading conditions. This confirms that both air and PWR primary water penalize fatigue life relative to the intrinsic baseline defined by vacuum tests. However, no measurable difference was observed between air and PWR, suggesting that the environmental influence under the present test conditions is limited. This similarity may indicate that the environmental impact would be primarily controlled by

bulk diffusion of reactive species (such as oxygen or hydrogen) along cracks or grain boundaries, rather than by surface reaction kinetics, which clearly differ between the two environments. Consequently, the theoretical Fen factor up to 2.5 for this heat (335554) does not correspond to the experimental findings (Fen exp ≈ 1), as the degradation in fatigue life is of similar magnitude in both air and PWR environments.

Microstructural analyses further supported these findings. Thus Schmid factor calculations confirmed that crack initiation preferentially occurred in grains with higher values compared to non-cracked grains, independent of environment. EBSD KAM maps show comparable strain localization patterns near crack tips in both air and PWR environments, with stronger localization near the surface in PWR, likely linked to oxide formation and surface damage. Under vacuum conditions, strain localization could not be reliably quantified due to noise in the KAM data. Fractographic analyses showed predominantly transgranular fracture in all cases; striations remained fine and constant in vacuum, whereas in air and PWR, they progressively widened with crack depth, consistent with environmentally assisted damage.

Overall, this first part demonstrated the intrinsic fatigue response of Alloy 690TT in vacuum, as both air and PWR environments introduce comparable reductions in fatigue life and exhibit similar deformation mechanisms. It is confirmed that environmental effects penalize the fatigue life of the material but remain indistinguishable between the two conditions up to Fen = 2.5, suggesting that similar environmentally assisted mechanisms operate in both environments, although their detailed nature still needs to be elucidated. These findings provide a solid foundation for understanding the fatigue behavior of Alloy 690TT prior to thermal aging and establish a consistent framework for direct comparison with aged materials in the subsequent chapters.

Evolution of the microstructure due to thermal aging

To simulate the long-term operation of Alloy 690TT in nuclear power plants, accelerated thermal aging in air was conducted at 420°C. The impact of this accelerated aging on the microstructural evolution and hardness was investigated and quantitatively assessed over time.

The results indicate that accelerated thermal aging did not significantly affect the grain size or the type of grain boundaries in the studied Alloy 690TT. Nevertheless, some notable changes were observed in intergranular precipitates. In particular, the area occupied by these precipitates increased steadily between 3400 hours (50 years) and 5400 hours (80 years) of accelerated

aging. It appears that this change in area is mostly due to the increase in the width of these precipitates. Conversely, the density of intergranular precipitates decreased from 2700 hours (40 years) to 5400 hours (80 years). Finally, no significant changes occurred in the area of intragranular precipitates, even though their density increased from 1400 hours (20 years) due to the nucleation of precipitates in the matrix. Moreover, thermal aging seems to alter the grain boundary structure over prolonged aging periods by reducing the density of the precipitates, which facilitates the inward and outward movement of the grain boundary toward the matrix. This movement results in a wavy grain boundary structure, possibly attributed to diffusion-induced grain boundary migration (DIGM).

Microhardness testing indicated a slight increase, mostly after 50 years, in the overall hardness of the Alloy 690TT as a result of accelerated thermal aging. Nano-indentation has shown no significantly hardened zones in the as-received material, while some zones near the grain boundaries were harder than the matrix in the 60 years aged material. In the hardened zone of the aged material, transmission electron microscopy coupled with selected area electron diffraction revealed two distinct types of diffraction spots: bright spots, indicating a face-centered cubic crystalline structure, and weaker intensity spots corresponding to a short-range ordering (Ni_2Cr). Hence, coupling nano-indentation and TEM observation established a direct causality between the localized hardness near the grain boundary and the short-range ordering present in this zone. Finally, it can be noted that no evidence of long-range ordering has been found in this alloy after 60 years of accelerated aging at 420°C.

Low cycle fatigue behavior of thermally aged Alloy 690TT in air and PWR environment

This final part of the study investigated the effect of accelerated thermal aging (4000 h at 420 °C, equivalent to approximately 60 years under PWR conditions) on the LCF behavior of Alloy 690TT in both air and PWR environments, with a particular focus on the relationship between microstructural evolution and fatigue response. The results demonstrate that thermal exposure induces significant changes in cyclic deformation behavior, fatigue life, and cracking mechanisms.

From the initial cycles, the aged samples exhibited a higher yield stress compared to the as-received condition. The aged Alloy 690TT specimens also showed enhanced cyclic hardening, with an average hardening increment of about 20 MPa at 0.45 % and 0.60 % strain amplitudes. This increased hardening is attributed to microstructural modifications occurring during thermal exposure, such as precipitate coarsening and the formation of secondary phases like

SRO, which hinder dislocation motion. This effect was corroborated by the more pronounced PLC instabilities observed in aged specimens. Previous studies have reported that SRO can reduce the SFE, thereby promoting planar slip, which in turn enhances DSA and the PLC effect. Analysis of the hysteresis loops revealed larger loop areas in aged samples, indicating greater plastic energy dissipation during cyclic loading. The evolution of plastic strain energy showed an overall increase of about 17 % in aged samples relative to the as-received condition, consistent with higher accumulated plastic strain observed at 0.6 % strain amplitude. These findings suggest that thermally-induced microstructural changes enhance cyclic hardening and plastic energy dissipation, thereby accelerating fatigue damage accumulation and reducing the fatigue life.

Thus thermal aging systematically reduced the total fatigue life, with an average decrease of approximately 20 % in air and about 8 % in the PWR environment relative to the as-received material. The ε–N relationships confirmed this degradation, particularly at higher strain amplitudes (0.45–0.6 %), highlighting that the detrimental effects of aging are more pronounced under severe cyclic deformation. Similarly, FCGR values were found to be higher in aged samples under comparable loading conditions in both environments, confirming that thermal aging promotes faster crack propagation.

Detailed characterization of secondary cracks revealed that aging increases the LCD and enhances crack branching, especially under PWR conditions. Quantitative damage assessment indicated that aged materials contained a greater population of short cracks (2–10 μm), reflecting a decreased resistance to crack nucleation. Crack initiation angles also shifted toward higher values (approximately 50–60°), suggesting a modification in crack trajectories consistent with the observed microstructural degradation. In the as-received condition, crack initiation primarily occurred in grains with higher Schmid factors (~0.47–0.48), indicating a strong correlation between slip activity and crack nucleation. This correlation weakened in aged specimens, where lower Schmid factors (~0.42–0.46) and environmental effects—such as SRO formation and carbide precipitation—appeared to overshadow the influence of crystallographic orientation on crack initiation.

EBSD analyses confirmed that fatigue cracks predominantly initiate along {111} slip planes in high-Schmid-factor grains in both air and PWR environments. However, thermal aging promoted additional crack initiation modes involving grain boundaries and mixed transgranular/intergranular paths, often originating at oxidized carbides. STEM-EDS analysis revealed oxygen enrichment and the formation of Cr_2O_3 along intergranular carbides. These

observations indicate that oxidation-assisted decohesion of grain boundary precipitates plays a critical role in the propagation of intergranular cracking in aged Alloy 690TT.

Taken together, these findings establish that accelerated thermal aging decreases the fatigue resistance of Alloy 690TT and modifies its underlying damage mechanisms. In particular, aging promotes higher plastic strain accumulation, increases crack initiation susceptibility, and enhances oxidation-assisted decohesion processes in air and PWR conditions. These results highlight the importance of considering long-term microstructural evolution when evaluating the fatigue life of Alloy 690TT components, especially beyond 60 years in nuclear reactors.

PERSPECTIVES

This study provides a first comprehensive screening of the parameters influencing the LCF response of Alloy 690TT, including environment (vacuum, air, and PWR primary water), temperature, strain rate, and long-term thermal aging. While the data generated here represent an important step forward, several scientific issues remain open and call for more detailed investigation.

A first open question concerns the environmental effect on fatigue life. The present results suggest comparable fatigue lifetimes in air and PWR water at Fen ≈ 2, but the influence of lower strain rates (<0.004 %/s, corresponding to Fen > 2.5) remains unknown. Additional tests in this regime are necessary to determine whether Alloy 690TT exhibits a reduction in fatigue life similar to that reported for austenitic stainless steels, thereby enabling the development of an experimentally based Fen correlation specific to this alloy.

Further vacuum tests, combined with TEM observations, are needed to clarify the deformation mechanisms in the absence of environmental effects and to better understand the interactions between dislocations, stacking faults, twins, and precipitates. Another important aspect concerns the early stages of fatigue damage. In the present work, the focus was placed exclusively on crack propagation analysis rather than crack initiation. Interrupted tests at very short lifetimes (5–100 cycles), combined with detailed surface and microstructural observations, would therefore be valuable to better understand the mechanisms governing crack initiation in Alloy 690TT. In this context, the role of oxide films formed on the surface or along grain boundaries deserves closer attention. While their involvement in SCC is well established in the literature, their contribution to fatigue crack initiation and propagation under cyclic loading in PWR environments remains poorly understood. Moreover, the present study did not specifically investigate the influence of the environment at the crack tip on the local deformation structure, which represents another important aspect for future work. Incorporating these effects into fatigue crack growth models would significantly improve the predictive accuracy of fatigue life assessments.

The effect of hydrogen in PWR water remains an open question. Advanced analytical techniques such as laser-induced breakdown spectroscopy (LIBS) or micro-analytical TEM could provide valuable insight into hydrogen uptake and its distribution during cyclic loading. Although the EVA setup used in this study does not contain dissolved hydrogen, some hydrogen could still form through surface reactions, even in air, and may influence the local crack-tip

chemistry. This means that the question of hydrogen uptake remains relevant even in the absence of dissolved hydrogen, as such surface-generated hydrogen may act as an additional source. A systematic investigation using sensitive detection and quantification methods is therefore required to better understand the role of hydrogen in the cyclic behavior and damage mechanisms of Alloy 690TT.

The effect of thermal aging likewise requires further exploration, particularly concerning the activation energy, which has not been extensively examined for different metallurgical conditions of the alloy. Although an estimate was derived from the present dataset, its reliability remains uncertain and should be verified through further experiments under varied thermal conditions. The present study provided a quantitative database on precipitate evolution (size, density, and coverage) during accelerated aging at 420 °C and revealed localized hardening near grain boundaries, correlated with the presence of short-range ordering (Ni_2Cr-type). However, the diffusion kinetics governing precipitate growth and the atomic-scale nature of ordered phases were not established. Advanced characterization techniques such as atom probe tomography (APT) or electron energy-loss spectroscopy (EELS) could provide the missing link by resolving the chemistry and lattice configuration of these nanoscale features.

It should also be noted that the accelerated thermal aging performed in this study was conducted in air, whereas in reality aging occurs in the PWR primary environment. To be more representative of service conditions, future work should focus on combined aging and fatigue scenarios, where samples undergo cyclic loading after intervals of thermal exposure in a PWR-simulated environment. Repetitive aging–fatigue sequences would mimic more closely the interplay between constant thermal exposure and operational transients, providing a better assessment of long-term degradation.

Overall, this work establishes a first framework for understanding the interplay between environment, strain rate, temperature, and microstructural aging in Alloy 690TT. Consolidating this database through targeted studies on environmental effects, crack initiation mechanisms, nanoscale ordering, and hydrogen interactions will be essential to resolve the outstanding scientific questions and to provide a reliable basis for fatigue life assessment of PWR components where Alloy 690TT has been used.

References

[Aerne et al., 2023] Aerne, N. J., Sprouster, D. J., Tucker, J. D.: 'Role of Fe in long-range ordered Ni2Cr precipitates in Ni-Cr-Fe model alloys during isothermal aging'; Materials Science and Engineering: A, 877 (2023), 145162. https://doi.org/10.1016/j.msea.2023.145162

[Aerne et al., 2022] Aerne, N., Sprouster, D., Tucker, J.: 'The Formation and Evolution of Ni2cr Precipitates in Ni-Cr Model Alloys as a Function of Stoichiometry'; SSRN Scholarly Paper, Rochester, NY: Social Science Research Network (2022, July 12). https://doi.org/10.2139/ssrn.4160346

[AFCEN. RCC-M, 2022] AFCEN. RCC-M: 'RCC-M'; (2022). Retrieved from https://www.afcen.com/en/rcc-m/194-rcc-m.html

[Alexandreanu et al., 2021] Alexandreanu, B., Chen, Y., Zhang, X., Chen, W.-Y.: 'Effect of thermal aging and irradiation on microstructure and crack growth response of Alloy 690' (No. ANL/LWRS-21/1, 1818506, 170550); (2021), ANL/LWRS-21/1, 1818506, 170550. Retrieved from https://www.osti.gov/servlets/purl/1818506/

[Alexandreanu et al., 2024] Alexandreanu, B., Zhang, X., Chen, W.-Y., Chen, Y.: 'The Effect of Thermal Aging on the Performance of High-Cr Ni-based Alloys in Primary Water Environment' (No. ANL/NSE-23/71); Argonne National Laboratory (ANL) (2024). Retrieved from https://www.osti.gov/biblio/2573022

[Andresen et al., 2016] Andresen, P. L., Berge, P., Chêne, J., Féron, D., Guerre, C., Herms, E., et al.: 'List of contributors'; In D. Féron & R. W. Staehle (Eds.), Stress Corrosion Cracking of Nickel Based Alloys in Water-cooled Nuclear Reactors. Woodhead Publishing (2016), ix. https://doi.org/10.1016/B978-0-08-100049-6.01002-8

[Angeliu and Was, 1990] Angeliu, T. M., Was, G. S.: 'Behavior of grain boundary chemistry and precipitates upon thermal treatment of controlled purity alloy 690'; Metallurgical Transactions A, 21, 8 (1990), 2097–2107. https://doi.org/10.1007/BF02647868

[ASTM B166, 2023] ASTM B166: (2023). https://doi.org/10.1520/B0166-19

[Atas et al., 2024] Atas, M. S., Cengiz, R., Yildirim, M.: 'Microstructural Evolution and Coarsening in Ni–Al–Cr–Co Model Superalloys with Nano γ′-Precipitates: An Experimental and Thermodynamic Investigation'; Metallography, Microstructure, and Analysis, 13, 4 (2024), 582–594. https://doi.org/10.1007/s13632-024-01109-7

[Balluffi and Cahn, 1981] Balluffi, R. W., Cahn, J. W.: ‘Mechanism for diffusion induced grain boundary migration’; Acta Metallurgica, 29, 3 (1981), 493–500. https://doi.org/10.1016/0001-6160(81)90073-0

[Beswick et al., 2025] Beswick, J., McLennan, A., Currie, C., Courtin, S.: ‘INCEFA-SCALE Test Data Compared to Environmental Fatigue Design Curve Methodologies’; In PVP2025. Volume 1: Codes & Standards (2025). https://doi.org/10.1115/PVP2025-154594

[Birnbaum and Sofronis, 1994] Birnbaum, H. K., Sofronis, P.: ‘Hydrogen-enhanced localized plasticity—a mechanism for hydrogen-related fracture’; Materials Science and Engineering: A, 176, 1 (1994), 191–202. https://doi.org/10.1016/0921-5093(94)90975-X

[Bleu et al., 2019] Bleu, Y., Barnier, V., Christien, F., Bourquard, F., Loir, A.-S., Garrelie, F., Donnet, C.: ‘Dynamics of carbon diffusion and segregation through nickel catalyst, investigated by in-situ XPS, during the growth of nitrogen-doped graphene’; Carbon, 155 (2019), 410–420. https://doi.org/10.1016/j.carbon.2019.08.084

[Bullens et al., 2018] Bullens, A. L., Bautista, E., Jaye, E. H., Vas, N. L., Cain, N. B., Mao, K., et al.: ‘Comparative Thermal Aging Effects on PM-HIP and Forged Inconel 690’; JOM, 70, 10 (2018), 2218–2223. https://doi.org/10.1007/s11837-018-2818-z

[Carpinteri, 1993] Carpinteri, A.: ‘Shape change of surface cracks in round bars under cyclic axial loading’; International Journal of Fatigue, 15, 1 (1993), 21–26. https://doi.org/10.1016/0142-1123(93)90072-X

[Chaboche, 1989] Chaboche, J. L.: ‘Constitutive equations for cyclic plasticity and cyclic viscoplasticity’; International Journal of Plasticity, 5, 3 (1989), 247–302. https://doi.org/10.1016/0749-6419(89)90015-6

[Chai et al., 2013] Chai, G., Liu, P., Zhou, N., Frodigh, J.: ‘Low and High Cycle Fatigue Behavior of Nickel-base Alloy at High Temperatures’; Procedia Engineering, 55 (2013), 671–676. https://doi.org/10.1016/j.proeng.2013.03.313

[Chen et al., 2019] Chen, J., Nurrochman, A., Hong, J.-D., Kim, T. S., Jang, C., Yi, Y.: ‘Comparison of oxide layers formed on the low-cycle fatigue crack surfaces of Alloy 690 and 316 SS tested in a simulated PWR environment’; Nuclear Engineering and Technology, 51, 2 (2019), 479–489. https://doi.org/10.1016/j.net.2018.10.007

[Chopra, 2018] Chopra, O.: ‘Effect of LWR Water Environments on the Fatigue Life of Reactor Materials (NUREG/CR-6909, Revision 1’; (2018). Retrieved 29 September 2023, from https://www.nrc.gov/reading-rm/doc-collections/nuregs/contract/cr6909/r1/index.html

[Chopra, 2007] Chopra, O. K.: ‘The Effect of LWR Coolant Environments on the Fatigue Life of Reactor Materials | Request PDF’; (2007). Retrieved 9 October 2023, from https://www.researchgate.net/publication/267610460_The_Effect_of_LWR_Coolant_Environments_on_the_Fatigue_Life_of_Reactor_Materials

[Chopra and Shack, 2008] Chopra, O. K., Shack, W. J.: ‘The Effect of LWR Coolant Environments on the Fatigue Life of Reactor Materials’; Presented at the ASME 2006 Pressure Vessels and Piping/ICPVT-11 Conference, American Society of Mechanical Engineers Digital Collection (2008), 191–204. https://doi.org/10.1115/PVP2006-ICPVT-11-93889

[Coffin, 2022] Coffin, L. F., Jr.: ‘A Study of the Effects of Cyclic Thermal Stresses on a Ductile Metal’; Transactions of the American Society of Mechanical Engineers, 76, 6 (2022), 931–949. https://doi.org/10.1115/1.4015020

[Cowley, 1950] Cowley, J. M.: ‘An Approximate Theory of Order in Alloys’; Physical Review, 77, 5 (1950), 669–675. https://doi.org/10.1103/PhysRev.77.669

[de Baglion, 2011] de Baglion, L.: ‘Comportement et endommagement en fatigue oligocyclique d’un acier inoxydable austénitique 304L en fonction de l’environnement (vide, air, eau primaire REP) à 300°C.’ (Phd thesis); ISAE-ENSMA Ecole Nationale Supérieure de Mécanique et d’Aérotechique - Poitiers (2011, June 16). Retrieved from https://theses.hal.science/tel-00623190

[Delabrouille et al., 2009] Delabrouille, F., Renaud, D., Vaillant, F., Massoud, J.: ‘Long Range Ordering of Alloy 690, 14th Intl’; Presented at the Conference on Environmental Degradation of Materials in Nuclear Power Systems, Virginia Beach, VA, USA (2009).

[Diánez et al., 2016] Diánez, M. J., Donoso, E., Criado, J. M., Sayagués, M. J., Díaz, G., Olivares, L.: ‘Study by DSC and HRTEM of the aging strengthening of Cu–Ni–Zn–Al alloys’; Materials & Design, 92 (2016), 184–188. https://doi.org/10.1016/j.matdes.2015.12.030

[Duarte et al., 2020] Duarte, L., Andrade, A. C., Bettge, D.: ‘Fractographic Analysis of Fatigue Striations Formation under different Microstructures and Loading Conditions’; Practical Metallography, 57, 12 (2020), 869–886. https://doi.org/10.3139/147.110668

[Dutta and Tewari, 1999] Dutta, R. S., Tewari, R.: ‘Microstructural and corrosion aspects of alloy 690’; British Corrosion Journal, 34, 3 (1999), 201–205. https://doi.org/10.1179/000705999101500851

[Dutta et al., 2007] Dutta, R. S., Tewari, R., De, P. K.: ‘Effects of heat-treatment on the extent of chromium depletion and caustic corrosion resistance of Alloy 690’; Corrosion Science, 49, 2 (2007), 303–318. https://doi.org/10.1016/j.corsci.2006.05.043

[Ellyin, 1997] Ellyin, F.: ‘Phenomenological approach to fatigue life prediction under uniaxial loading’; In F. Ellyin (Ed.), Fatigue Damage, Crack Growth and Life Prediction. Dordrecht: Springer Netherlands (1997), 77–144. https://doi.org/10.1007/978-94-009-1509-1_3

[Ellyin and Kujawski, 1984] Ellyin, F., Kujawski, D.: ‘Plastic Strain Energy in Fatigue Failure’; Journal of Pressure Vessel Technology, 106, 4 (1984), 342–347. https://doi.org/10.1115/1.3264362

[Feng et al., 2023] Feng, X., Zhang, S., Liu, P., Kuang, W.: ‘The structure dependence of grain boundary passivation of Alloy 690 in high temperature water’; Acta Materialia, 261 (2023), 119368. https://doi.org/10.1016/j.actamat.2023.119368

[Gao et al., 2020] Gao, J., Tan, J., Jiao, M., Wu, X., Tang, L., Huang, Y.: ‘Role of welding residual strain and ductility dip cracking on corrosion fatigue behavior of Alloy 52/52M dissimilar metal weld in borated and lithiated high-temperature water’; Journal of Materials Science & Technology, 42 (2020), 163–174. https://doi.org/10.1016/j.jmst.2019.10.012

[Gault et al., 2012] Gault, B., Moody, M. P., Cairney, J. M., Ringer, S. P.: ‘Atom Probe Microscopy and Materials Science’; In B. Gault, M. P. Moody, J. M. Cairney & S. P. Ringer (Eds.), Atom Probe Microscopy. New York, NY: Springer (2012), 299–311. https://doi.org/10.1007/978-1-4614-3436-8_9

[Gerland et al., 1997] Gerland, M., Alain, R., Ait Saadi, B., Mendez, J.: ‘Low cycle fatigue behaviour in vacuum of a 316L-type austenitic stainless steel between 20 and 600°C—Part II: Dislocation structure evolution and correlation with cyclic behaviour’; Materials Science and Engineering: A, 229, 1 (1997), 68–86. https://doi.org/10.1016/S0921-5093(96)10560-8

[Guerre et al., 2016] Guerre, C., Laghoutaris, P., Chêne, J., Marchetti, L., Molins, R., Duhamel, C., Sennour, M.: ‘Stress Corrosion Cracking of Alloy 600 in PWR Primary Water : Influence of Chromium, Hydrogen and oxygen Diffusion’; In J. T. Busby, G. Ilevbare & P. L. Andresen (Eds.), Proceedings of the 15th International Conference on Environmental Degradation of

Materials in Nuclear Power Systems — Water Reactors. Cham: Springer International Publishing (2016), 1477–1490.

[H. Xu, 2004] H. Xu, X.: 'Materials Reliability Program: Resistance to Primary Water Stress Corrosion Cracking of Alloy 690 in Pressurized Water Reactors (MRP-258)'; (2004). Retrieved 6 November 2024, from https://www.epri.com/research/products/1019086

[Handa, 2014] Handa, S. S.: 'Precipitation of Carbides in a Ni-based Superalloy'; (2014). Retrieved from https://www.semanticscholar.org/paper/Precipitation-of-Carbides-in-a-Ni-based-Superalloy-Handa/cab3b55076c682c42ca7813bdf7ef56d7c6d5df0

[Hänninen et al., 2005] Hänninen, H., Ivanchenko, M., Yagodzinskyy, Y., Nevdacha, V., Ehrnstén, U., Aaltonen, P.: 'DYNAMIC STRAIN AGING OF NI-BASE ALLOYS INCONEL 600 AND 690'; (2005).

[Hata et al., 2000] Hata, S., Shindo, D., Mitate, T., Kuwano, N., Matsumura, S., Oki, K.: 'HRTEM image contrast of short range order in Ni4Mo'; Micron, 31, 5 (2000), 533–538. https://doi.org/10.1016/S0968-4328(99)00134-1

[He et al., 2024] He, M., Davids, W. J., Breen, A. J., Ringer, S. P.: 'Quantifying short-range order using atom probe tomography'; Nature Materials, 23, 9 (2024), 1200–1207. https://doi.org/10.1038/s41563-024-01912-1

[Hong et al., 2014] Hong, J.-D., Lee, J., Jang, C., Kim, T. S.: 'Low cycle fatigue behavior of alloy 690 in simulated PWR water—Effects of dynamic strain aging and hydrogen'; Materials Science and Engineering: A, 611 (2014), 37–44. https://doi.org/10.1016/j.msea.2014.05.069

[Hong and Lee, 2004] Hong, S.-G., Lee, S.-B.: 'Dynamic strain aging under tensile and LCF loading conditions, and their comparison in cold worked 316L stainless steel'; Journal of Nuclear Materials, 328, 2 (2004), 232–242. https://doi.org/10.1016/j.jnucmat.2004.04.331

[Hong and Lee, 2005] Hong, S.-G., Lee, S.-B.: 'Mechanism of dynamic strain aging and characterization of its effect on the low-cycle fatigue behavior in type 316L stainless steel'; Journal of Nuclear Materials, 340, 2 (2005), 307–314. https://doi.org/10.1016/j.jnucmat.2004.12.012

[Howe et al., 2022] Howe, B., Mann, J., Que, Z., Huotilainen, C., Scenini, F., Burke, G.: 'Development of a Robust Procedure for the Evaluation of Striation Spacings in Low Cycle Fatigue Specimens Tested in a Simulated PWR Environment'; In PVP2022. Volume 4A: Materials and Fabrication (2022). https://doi.org/10.1115/PVP2022-84027

[Huang et al., 2013] Huang, F., Wang, J., Han, E.-H., Ke, W.: 'Microstructural characteristics of the oxide films formed on Alloy 690 TT in pure and primary water at 325°C'; Corrosion Science, 76 (2013), 52–59. https://doi.org/10.1016/j.corsci.2013.06.023

[Huin, 2013] Huin, N.: 'Effets d'environnement sur la fatigue de l'acier inoxydable 304L en milieu primaire REP sous chargement cyclique' (Phd thesis); ISAE-ENSMA Ecole Nationale Supérieure de Mécanique et d'Aérotechique - Poitiers (2013, February 19). Retrieved from https://theses.hal.science/tel-00835093

[Huotilainen et al., 2019] Huotilainen, C., Ehrnstén, U., Ahonen, M., Hänninen, H.: 'Effect of thermal aging on microstructure and hardness of industrial heats of Alloy 690'; Presented at the 19th International Conference on Environmental Degradation of Materials in Nuclear Power Systems - Water Reactors, EnvDeg 2019 (2019), 156–164.

[Huotilainen and Que, 2022] Huotilainen, C., Que, Z.: 'Effect Of Thermal Aging On The Microstructure And Mechanical Properties Of High-Ni And Ni-Base Alloys'; (2022). Retrieved from https://store.ampp.org/effect-of-thermal-aging-on-the-microstructure-and-mechanical-properties-of-high-ni-and-ni-base-alloys

[Ikram and Shaukat, 1993] Ikram, N., Shaukat, A.: 'Resistivity change due to short-range order and size-effect correction in Ni-Al alloys'; Journal of Physics and Chemistry of Solids, 54, 6 (1993), 747–750. https://doi.org/10.1016/0022-3697(93)90136-F

[Ivanchenko, 2010] Ivanchenko, M.: 'Dynamic strain aging of austenitic stainless steels and Ni-base alloys'; Aalto-yliopiston teknillinen korkeakoulu (2010). Retrieved from https://aaltodoc.aalto.fi:443/handle/123456789/4872

[Jang et al., 2013] Jang, C., Jang, H., Hong, J.-D., Cho, H., Kim, T. S., Lee, J.-G.: 'ENVIRONMENTAL FATIGUE OF METALLIC MATERIALS IN NUCLEAR POWER PLANTS – A REVIEW OF KOREAN TEST PROGRAMS'; Nuclear Engineering and Technology, 45, 7 (2013), 929–940. https://doi.org/10.5516/NET.07.2013.040

[Jiang et al., 2015] Jiang, R., Gao, N., Reed, P. A. S.: 'Influence of orientation-dependent grain boundary oxidation on fatigue cracking behaviour in an advanced Ni-based superalloy'; Journal of Materials Science, 50, 12 (2015), 4379–4386. https://doi.org/10.1007/s10853-015-8992-2

[Kamaya, 2015] Kamaya, M.: 'Low Cycle Fatigue Crack Growth Prediction for Stainless Steel by Strain Intensify Factor'; Journal of the Society of Materials Science, Japan, 64 (2015), 902–909. https://doi.org/10.2472/jsms.64.902

[Kim et al., 2022] Kim, J.-M., Kim, S.-J., Kang, J.-H.: ‘Effects of short-range ordering and stacking fault energy on tensile behavior of nitrogen-containing austenitic stainless steels’; Materials Science and Engineering: A, 836 (2022), 142730. https://doi.org/10.1016/j.msea.2022.142730

[Kim et al., 2000] Kim, S., Kuk, I. H., Kim, J. S.: ‘Order–disorder reaction in Alloy 600’; Materials Science and Engineering: A, 279, 1 (2000), 142–148. https://doi.org/10.1016/S0921-5093(99)00640-1

[Kim et al., 2015] Kim, Y. S., Maeng, W. Y., Kim, S. S.: ‘Effect of short-range ordering on stress corrosion cracking susceptibility of Alloy 600 studied by electron and neutron diffraction’; Acta Materialia, 83 (2015), 507–515. https://doi.org/10.1016/j.actamat.2014.10.009

[Kuang et al., 2017] Kuang, W., Song, M., Wang, P., Was, G. S.: ‘The oxidation of alloy 690 in simulated pressurized water reactor primary water’; Corrosion Science, 126 (2017), 227–237. https://doi.org/10.1016/j.corsci.2017.07.004

[Langelier et al., 2017] Langelier, B., Persaud, S. Y., Korinek, A., Casagrande, T., Newman, R. C., Botton, G. A.: ‘Effects of boundary migration and pinning particles on intergranular oxidation revealed by 2D and 3D analytical electron microscopy’; Acta Materialia, 131 (2017), 280–295. https://doi.org/10.1016/j.actamat.2017.04.003

[Larrouy et al., 2015] Larrouy, B., Villechaise, P., Cormier, J., Berteaux, O.: ‘Grain boundary–slip bands interactions: Impact on the fatigue crack initiation in a polycrystalline forged Ni-based superalloy’; Acta Materialia, 99 (2015), 325–336. https://doi.org/10.1016/j.actamat.2015.08.009

[Lee et al., 2015] Lee, T.-H., Lee, Y.-J., Joo, S.-H., Nersisyan, H. H., Park, K.-T., Lee, J.-H.: ‘Intergranular M23C6 Carbide Precipitation Behavior and Its Effect on Mechanical Properties of Inconel 690 Tubes’; Metallurgical and Materials Transactions A, 46, 9 (2015), 4020–4026. https://doi.org/10.1007/s11661-015-3003-4

[Lee et al., 2016] Lee, T.-H., Suh, H.-Y., Han, S.-K., Noh, J.-S., Lee, J.-H.: ‘Effect of a heat treatment on the precipitation behavior and tensile properties of alloy 690 steam generator tubes’; Journal of Nuclear Materials, 479 (2016), 85–92. https://doi.org/10.1016/j.jnucmat.2016.06.038

[Li et al., 2013] Li, H., Xia, S., Zhou, B., Peng, J.: ‘The growth mechanism of grain boundary carbide in Alloy 690’; Materials Characterization, 81 (2013), 1–6. https://doi.org/10.1016/j.matchar.2013.04.005

[Li et al., 2023a] Li, Y., Wei, Y., Wang, Z., Liu, X., Colnaghi, T., Han, L., et al.: ‘Quantitative three-dimensional imaging of chemical short-range order via machine learning enhanced atom probe tomography’; Nature Communications, 14, 1 (2023a), 7410. https://doi.org/10.1038/s41467-023-43314-y

[Li et al., 2022] Li, Z. H., Hong, C., Zhao, Y. G., Hu, Y., Lu, Y. H., Shoji, T.: ‘Cyclic deformation behavior and cracking mechanism of Inconel Alloy 690TT steam generator tube at elevated temperature’; Materials Characterization, 190 (2022), 111935. https://doi.org/10.1016/j.matchar.2022.111935

[Li et al., 2023b] Li, Z. H., Lu, Y. H., Hong, C., Zhao, Y. G., Han, Y. M., Shoji, T.: ‘Corrosion fatigue damage mechanism and life evaluation of Inconel Alloy 690TT steam generator tube in high temperature pressurized water’; Corrosion Science, 212 (2023b), 110953. https://doi.org/10.1016/j.corsci.2022.110953

[Li et al., 2024] Li, Z. H., Lu, Y. H., You, L., Zhang, X. F., Wang, L., Tian, D. H., et al.: ‘Effect of temperature on corrosion fatigue behavior of Inconel Alloy 690TT steam generator tube’; Corrosion Science, 227 (2024), 111741. https://doi.org/10.1016/j.corsci.2023.111741

[Lim et al., 2014] Lim, Y., Kim, D.-J., Hwang, S., Kim, H., Kim, S. W.: ‘M23C6 precipitation behavior and grain boundary serration in Ni-based Alloy 690’; Materials Characterization, 96 (2014), 28–39. https://doi.org/10.1016/j.matchar.2014.07.008

[Lim et al., 2019a] Lim, Y. S., Kim, D. J., Kim, S. W., Hwang, S. S., Kim, H. P.: ‘Characterization of internal and intergranular oxidation in Alloy 690 exposed to simulated PWR primary water and its implications with regard to stress corrosion cracking’; Materials Characterization, 157 (2019a), 109922. https://doi.org/10.1016/j.matchar.2019.109922

[Lim et al., 2019b] Lim, Y. S., Kim, D. J., Kim, S. W., Kim, H. P.: ‘Crack growth and cracking behavior of Alloy 600/182 and Alloy 690/152 welds in simulated PWR primary water’; Nuclear Engineering and Technology, 51, 1 (2019b), 228–237. https://doi.org/10.1016/j.net.2018.09.011

[Liu et al., 2015] Liu, R., Zhang, Z. J., Zhang, P., Zhang, Z. F.: 'Extremely-low-cycle fatigue behaviors of Cu and Cu–Al alloys: Damage mechanisms and life prediction'; Acta Materialia, 83 (2015), 341–356. https://doi.org/10.1016/j.actamat.2014.10.002

[Marceau et al., 2015] Marceau, R. K. W., Ceguerra, A. V., Breen, A. J., Palm, M., Stein, F., Ringer, S. P., Raabe, D.: 'Atom probe tomography investigation of heterogeneous short-range ordering in the 'komplex' phase state (K-state) of Fe–18Al (at.%)'; Intermetallics, 64 (2015), 23–31. https://doi.org/10.1016/j.intermet.2015.04.005

[Marucco, 1991] Marucco, A.: 'Effects of Composition on the Order-Disorder Transformation in Ni-Cr Based Alloys'; Key Engineering Materials, 48 (1991), 77–90. https://doi.org/10.4028/www.scientific.net/KEM.48.77

[Matt, 2011] Matt, O.: 'Microstructural Characterizations of Alloy 690: Key Examples.'; Presented at the NRC – Industry, Rockville. (2011).

[Meng et al., 2010] Meng, F., Wang, J., Han, E.-H., Ke, W.: 'The role of TiN inclusions in stress corrosion crack initiation for Alloy 690TT in high-temperature and high-pressure water'; Corrosion Science, 52, 3 (2010), 927–932. https://doi.org/10.1016/j.corsci.2009.11.015

[Mineur, 2000] Mineur, M.: 'Conditions locales d'amorçage des fissures de fatigue dans un acier inoxydable de type 316L : aspects cristallographiques (EBSD)' (PhD Thesis); (2000). Retrieved from http://www.theses.fr/2000POIT2266

[Mitchell, 1996] Mitchell, M. R.: 'Fundamentals of Modern Fatigue Analysis for Design'; In ASM Handbook Committee (Ed.), Fatigue and Fracture (Vol. 19). ASM International (1996), 0. https://doi.org/10.31399/asm.hb.v19.a0002364

[Moss and Was, 2012] Moss, T. E., Was, G. S.: 'Dynamic Strain Aging of Nickel-Base Alloys 800H and 690'; Metallurgical and Materials Transactions A, 43, 10 (2012), 3428–3432. https://doi.org/10.1007/s11661-012-1335-x

[Mouginot et al., 2019] Mouginot, R., Sarikka, T., Ehrnstén, U., Hänninen, H.: 'Nanoindentation study of short-range ordering'; Materials Research Express, 6, 4 (2019), 045052. https://doi.org/10.1088/2053-1591/aafeaf

[Mouginot et al., 2016] Mouginot, R., Sarikka, T., Ehrnstén, U., Kim, Y. S., Kim, S. S., Hänninen, H.: 'Short-range ordering of Alloy 690 aged for 10 000 h at 420, 475 and 550 °C: BALTICA X - International Conference on Life Management and Maintenance for Power Plants'; Baltica X (2016).

[Mouginot et al., 2017a] Mouginot, R., Sarikka, T., Heikkilä, M., Ivanchenko, M., Ehrnstén, U., Kim, Y. S., et al.: 'Thermal ageing and short-range ordering of Alloy 690 between 350 and 550 °C'; Journal of Nuclear Materials, 485 (2017a), 56–66. https://doi.org/10.1016/j.jnucmat.2016.12.031

[Mouginot et al., 2017b] Mouginot, R., Sarikka, T., Heikkilä, M., Ivanchenko, M., Ehrnstén, U., Kim, Y. S., et al.: 'Thermal ageing and short-range ordering of Alloy 690 between 350 and 550 °C'; Journal of Nuclear Materials, 485 (2017b), 56–66. https://doi.org/10.1016/j.jnucmat.2016.12.031

[MRP-241, 2008] MRP-241: 'Materials Reliability Program: Guidelines for Thermally Treated Alloy 690 Pressure Vessel Nozzles (MRP-241)' (No. 1015007);. EPRI, Palo Alto, CA (2008).

[Mu and Aubin, 2010] Mu, P., Aubin, V.: 'Microcrack initiation in low-cycle fatigue of an austenitic stainless steel'; Procedia Engineering, 2, 1 (2010), 1951–1960. https://doi.org/10.1016/j.proeng.2010.03.210

[Naghdi et al., 2023] Naghdi, A. H., Karimi, K., Poisvert, A. E., Esfandiarpour, A., Alvarez, R., Sobkowicz, P., et al.: 'Dislocation plasticity in equiatomic NiCoCr alloys: The effect of short-range order'; Physical Review B, 107, 9 (2023), 094109. https://doi.org/10.1103/PhysRevB.107.094109

[Paris and Erdogan, 1963] Paris, P., Erdogan, F.: 'A Critical Analysis of Crack Propagation Laws'; Journal of Basic Engineering, 85, 4 (1963), 528–533. https://doi.org/10.1115/1.3656900

[Peng, 2021] Peng, Z.: 'Fatigue d'un acier inoxydable austénitique 304L : étude des effets de l'environnement (air/eau primaire rep) à 300°c, de la contrainte moyenne et de l'état de surface' (phdthesis); ISAE-ENSMA Ecole Nationale Supérieure de Mécanique et d'Aérotechique - Poitiers (2021, February 9). Retrieved from https://theses.hal.science/tel-03232355

[Persaud et al., 2019] Persaud, S. Y., Langelier, B., Eskandari, A., Zhu, H., Botton, G. A., Newman, R. C.: 'Advanced Characterization of Oxidation Processes and Grain Boundary Migration in Ni Alloys Exposed to 480 °C Hydrogenated Steam'; In J. H. Jackson, D. Paraventi & M. Wright (Eds.), Proceedings of the 18th International Conference on Environmental Degradation of Materials in Nuclear Power Systems – Water Reactors. Cham: Springer International Publishing (2019), 375–398. https://doi.org/10.1007/978-3-030-04639-2_24

[Plotnikov et al., 2018] Plotnikov, E. Y., Mao, Z., Baik, S.-I., Yildirim, M., Li, Y., Cecchetti, D., et al.: 'A Correlative Four-Dimensional Study of Phase Separation at the Subnanoscale to

Nanoscale of a Ni-Al Alloy'; arXiv (2018, November 19). https://doi.org/10.48550/arXiv.1808.02629

[Polák and Man, 2014] Polák, J., Man, J.: 'Mechanisms of extrusion and intrusion formation in fatigued crystalline materials'; Materials Science and Engineering: A, 596 (2014), 15–24. https://doi.org/10.1016/j.msea.2013.12.005

[Poulain, 2015] Poulain, T.: 'Fatigue oligocyclique d'un acier inoxydable austénitique 304L : influence de l'état de surface et de signaux de chargement en milieu eau primaire REP' (Phd thesis); ISAE-ENSMA Ecole Nationale Supérieure de Mécanique et d'Aérotechique - Poitiers (2015).

[Poulain et al., 2016] Poulain, T., Mendez, J., Hénaff, G., de Baglion, L.: 'Characterization of Damage During Low Cycle Fatigue of a 304L Austenitic Stainless Steel as a Function of Environment (Air, PWR Environment) and Surface Finish (Polished, Ground)'; Procedia Engineering, 160 (2016), 123–130. https://doi.org/10.1016/j.proeng.2016.08.871

[R. C. Boettner et al., 1965] R. C. Boettner, C. Laird, A. J. McEvily: 'Institute of Metals Division - Crack Nucleation and Growth in High Strain-Low Cycle Fatigue'; The American Institute of Mining, Metallurgical, and Petroleum Engineers (1965).

[Rudling, 2007] Rudling, P.: 'Welding of Zirconium alloys'; Skultuna Adv. Nucl. Technol. Int. Eur. AB (2007), 8–9.

[Sarver et al., 1988] Sarver, J. M., Crum, J. R., Mankins, W. L.: 'Carbide Precipitation and SCC Behavior of Inconel Alloy 690'; Corrosion, 44, 5 (1988), 288–289. https://doi.org/10.5006/1.3583939

[Schijve, 2009] Fatigue Crack Growth. Analysis and Predictions: In Fatigue of Structures and Materials. Dordrecht: Springer Netherlands (2009), 209–256. https://doi.org/10.1007/978-1-4020-6808-9_8

[Schönfeld, 1999] Schönfeld, B.: 'Local atomic arrangements in binary alloys'; Progress in Materials Science, 44, 5 (1999), 435–543. https://doi.org/10.1016/S0079-6425(99)00005-5

[Shi et al., 2023] Shi, S., Li, H., Cui, J., Chen, X.: 'Impact of dynamic strain aging on multiaxial low cycle fatigue behavior of nickel-based alloy 690 at 350 °C'; International Journal of Fatigue, 170 (2023), 107547. https://doi.org/10.1016/j.ijfatigue.2023.107547

[Skelton and Haigh, 1978] Skelton, R. P., Haigh, J. R.: ‘Fatigue crack growth rates and thresholds in steels under oxidising conditions’; Materials Science and Engineering, 36, 1 (1978), 17–25. https://doi.org/10.1016/0025-5416(78)90191-X

[Song et al., 2018] Song, M., Yang, Y., Wang, M., Kuang, W., Lear, C. R., Was, G. S.: ‘Probing long-range ordering in nickel-base alloys with proton irradiation’; Acta Materialia, 156 (2018), 446–462. https://doi.org/10.1016/j.actamat.2018.06.043

[Song et al., 2017] Song, X., Tang, L., Chen, Z., Zhou, R.: ‘Micro-mechanism during long-term creep of a precipitation-strengthened Ni-based superalloy’; Journal of Materials Science, 52, 8 (2017), 4587–4598. https://doi.org/10.1007/s10853-016-0703-0

[Sourabh and Singh, 2023] Sourabh, K., Singh, J. B.: ‘Tensile Behavior of Alloy 690 in the Dynamic Strain Aging Regime’; Journal of Materials Engineering and Performance, 32, 7 (2023), 2932–2949. https://doi.org/10.1007/s11665-022-07314-1

[Stahlmann, 2013] Stahlmann, A.: ‘Experimental and numerical modeling of scour at offshore wind turbines’; (2013). https://doi.org/10.15488/8173

[Stephan, 2018] Stephan, B.: ‘Etude cinétique et microstructurale de la transformation ordre-désordre dans les alliages Ni2Cr à faible teneur en fer’ (These de doctorat); Université de Lille (2018-2021) (2018, February 15). Retrieved from https://theses.fr/2018LILUR004

[Stephan et al., 2019] Stephan, B., Jacob, D., Delabrouille, F., Legras, L.: ‘A Kinetic Study of Order-Disorder Transition in Ni–Cr Based Alloys’; In J. H. Jackson, D. Paraventi & M. Wright (Eds.), Proceedings of the 18th International Conference on Environmental Degradation of Materials in Nuclear Power Systems – Water Reactors. Cham: Springer International Publishing (2019), 233–249. https://doi.org/10.1007/978-3-030-04639-2_15

[Suresh, 1998] Suresh, S.: ‘Fatigue of Materials’; (2nd ed.). Cambridge: Cambridge University Press (1998). https://doi.org/10.1017/CBO9780511806575

[Tan et al., 2016a] Tan, J., Liu, X. Q., Xu, X., Han, E.-H., Wu, X., wang, xiang: ‘Environmentally Assisted Fatigue Evaluation Model of Alloy 690 Steam Generator Tube in High-Temperature Water’; Corrosion, 72 (2016a). https://doi.org/10.5006/1803

[Tan et al., 2014a] Tan, J., Wu, X., Han, E.-H., Ke, W., Liu, X., Meng, F., Xu, X.: ‘Corrosion fatigue behavior of Alloy 690 steam generator tube in borated and lithiated high temperature water’; Corrosion Science, 89 (2014a), 203–213. https://doi.org/10.1016/j.corsci.2014.08.027

[Tan et al., 2014b] Tan, J., Wu, X., Han, E.-H., Ke, W., Liu, X., Meng, F., Xu, X.: 'Corrosion fatigue behavior of Alloy 690 steam generator tube in borated and lithiated high temperature water'; Corrosion Science, 89 (2014b), 203–213. https://doi.org/10.1016/j.corsci.2014.08.027

[Tan et al., 2014c] Tan, J., Wu, X., Han, E.-H., Ke, W., Liu, X., Meng, F., Xu, X.: 'Role of TiN inclusion on corrosion fatigue behavior of Alloy 690 steam generator tubes in borated and lithiated high temperature water'; Corrosion Science, 88 (2014c), 349–359. https://doi.org/10.1016/j.corsci.2014.07.059

[Tan et al., 2016b] Tan, J., Wu, X., Han, E.-H., Liu, X., Xu, X., Sun, H.: 'The effect of dissolved oxygen on fatigue behavior of Alloy 690 steam generator tubes in borated and lithiated high temperature water'; Corrosion Science, 102 (2016b), 394–404. https://doi.org/10.1016/j.corsci.2015.10.032

[Toth et al., 2013] Toth, L. S., Biswas, S., Gu, C., Beausir, B.: 'Notes on representing grain size distributions obtained by electron backscatter diffraction'; Materials Characterization, 84 (2013), 67–71. https://doi.org/10.1016/j.matchar.2013.07.013

[Vainionpää et al., 2025] Vainionpää, A., Ferreirós, P. A., Seppänen, T., Que, Z.: 'Microstructural insights into effects of pressurized water reactor environment and cyclic loading parameters on the low cycle fatigue behavior of 316L stainless steel'; International Journal of Fatigue, 198 (2025), 109016. https://doi.org/10.1016/j.ijfatigue.2025.109016

[Verma et al., 2015] Verma, A., Singh, J. B., Wanderka, N., Chakravartty, J. K.: 'Delineating the roles of Cr and Mo during ordering transformations in stoichiometric Ni2(Cr1− *x*,Mo*x*) alloys'; Acta Materialia, 96 (2015), 366–377. https://doi.org/10.1016/j.actamat.2015.06.022

[Volpe et al., 2022] Volpe, L., Bertali, G., Scenini, F., Burke, M. G.: 'Effect of temperature on the preferential intergranular oxidation susceptibility of thermally-treated Alloy 600'; Corrosion Science, 207 (2022), 110565. https://doi.org/10.1016/j.corsci.2022.110565

[Wang, 2023] Wang, J.: 'Revealing the Superior Oxidation Resistance of a Nickel-Based Alloy in High-Temperature Steam Through Advanced Characterization'; SSRN Scholarly Paper, Rochester, NY: Social Science Research Network (2023, November 21). https://doi.org/10.2139/ssrn.4639591

[Wang et al., 2017] Wang, M., Pang, J. C., Li, S. X., Zhang, Z. F.: 'Low-cycle fatigue properties and life prediction of Al-Si piston alloy at elevated temperature'; Materials Science and Engineering: A, 704 (2017), 480–492. https://doi.org/10.1016/j.msea.2017.08.014

[Wang et al., 2022] Wang, N., Yu, H., Zhao, P., Zhang, J.-M., Gong, J.-G., Xuan, F.-Z.: 'Cyclic deformation response of austenitic Ni-based alloy: Mechanical behavior, internal stress evolution and microstructural feature'; Materials Science and Engineering: A, 850 (2022), 143522. https://doi.org/10.1016/j.msea.2022.143522

[Wang et al., 2019a] Wang, Y., Jiang, D., Yu, W., Huang, S., Wu, D., Xu, Y., Yang, X.: 'Short-range ordering in a commercial Ni-Cr-Al-Fe precision resistance alloy'; Materials & Design, 181 (2019a), 107981. https://doi.org/10.1016/j.matdes.2019.107981

[Wang et al., 2019b] Wang, Y., Jiang, D., Yu, W., Huang, S., Wu, D., Xu, Y., Yang, X.: 'Short-range ordering in a commercial Ni-Cr-Al-Fe precision resistance alloy'; Materials & Design, 181 (2019b), 107981. https://doi.org/10.1016/j.matdes.2019.107981

[Xiao et al., 2015] Xiao, J., Qiu, S. Y., Chen, Y., Lin, Z. X., Xu, Q., Xie, H. Y.: 'Effects of dissolved oxygen on corrosion fatigue cracking of Alloy 690(TT) in pressurized water reactor environments'; International Journal of Fatigue, 74 (2015), 65–70. https://doi.org/10.1016/j.ijfatigue.2014.12.007

[Xu and Shoji, 2015] Xu, J., Shoji, T.: 'The corrosion behavior of Alloy 52 weld metal in cyclic hydrogenated and oxygenated water chemistry in high temperature aqueous environment'; Journal of Nuclear Materials, 461 (2015), 10–21. https://doi.org/10.1016/j.jnucmat.2015.02.033

[Xue and Marquis, 2022] Xue, F., Marquis, E. A.: 'Role of diffusion-induced grain boundary migration in the oxidation response of a Ni-30 Cr alloy'; Acta Materialia, 240 (2022), 118343. https://doi.org/10.1016/j.actamat.2022.118343

[Yoo et al., 2016] Yoo, S. C., Choi, K. J., Kim, T., Kim, S. H., Kim, J. Y., Kim, J. H.: 'Microstructural evolution and stress-corrosion-cracking behavior of thermally aged Ni-Cr-Fe alloy'; Corrosion Science, 111 (2016), 39–51. https://doi.org/10.1016/j.corsci.2016.04.051

[Young, G. A. and Eno, D. R., 2014] Young, G. A., Eno, D. R.: 'Long range ordering in model Ni-Cr-X alloys'; Conference on Contribution of Materials Investigations and Operating Experience to LWRs' Safety, Performance and Reliability. Fontevraud 8), Avignon (France) (2014).

[Young and Tucker, 2013] Young, G., Tucker, J.: 'The kinetics of long range ordering in Ni-Cr and Ni-Cr-Fe alloys | Advanced Technology and Manufacturing Institute (ATAMI) | Oregon

State University’; 16th International Conference on Environmental Degradation of Materials in Nuclear Power Systems - Water Reactors. Asheville, NC (2013, August).

[Zhai et al., 2019] Zhai, Z., Toloczko, M., Bruemmer, S.: ‘Crack Initiation for Alloy 600 and Alloy 690 During Constant Load Tests in Simulated Pressurized Water Reactor Primary Water’; Presented at the CORROSION 2019 (2019), NACE-2019-13383.

[Zhang et al., 2017] Zhang, F. X., Zhao, S., Jin, K., Xue, H., Velisa, G., Bei, H., et al.: ‘Local Structure and Short-Range Order in a NiCoCr Solid Solution Alloy’; Physical Review Letters, 118, 20 (2017), 205501. https://doi.org/10.1103/PhysRevLett.118.205501

[Zhang et al., 2021] Zhang, J., Liu, L., Huang, T., Chen, J., Cao, K., Liu, X., et al.: ‘Coarsening kinetics of γ′ precipitates in a Re-containing Ni-based single crystal superalloy during long-term aging’; Journal of Materials Science & Technology, 62 (2021), 1–10. https://doi.org/10.1016/j.jmst.2020.05.034

[Zhang et al., 2023] Zhang, Y. J., Han, D., Li, X. W.: ‘Short-range ordering plays a determining role in the low-cycle fatigue life improvement of fcc metals: A conclusive study on low solid-solution hardening Ni-Cr alloys’; Journal of Materials Science & Technology, 156 (2023), 157–171. https://doi.org/10.1016/j.jmst.2023.01.036

[Zhang et al., 2011] Zhang, Z., Wang, J., Han, E.-H., Ke, W.: ‘Influence of dissolved oxygen on oxide films of Alloy 690TT with different surface status in simulated primary water’; Corrosion Science, 53, 11 (2011), 3623–3635. https://doi.org/10.1016/j.corsci.2011.07.012

[Zhilyakov et al., 2020] Zhilyakov, A. Yu., Belikov, S. V., Gibadullina, A. F., Polovov, I. B., Ilikbaev, I. V.: ‘Relation Between Short-Range and Long-Range Ordering and Physical Properties of Corrosion-Resistant Alloys of the Ni – Cr – Mo System’; Metal Science and Heat Treatment, 61, 11 (2020), 792–797. https://doi.org/10.1007/s11041-020-00502-7

VI. Annexe 1: SHOULDER TO GAUGE LENGTH RATIO

In strain-controlled LCF testing, precise control of the strain within the gauge section is essential, as it directly governs the measured fatigue life. In the present EVA setup, it is not possible to attach a knife-edge extensometer directly on the gauge length because of the environmental and geometric constraints. Instead, an eddy-current extensometer is used to measure strain between the specimen shoulders. Therefore, a shoulder-to-gauge factor (S2G) is required to convert the strain measured at the shoulders into the actual strain experienced in the gauge region. This factor was determined both experimentally and numerically to ensure accurate strain control during testing.

Modeling the cyclic behavior of Alloy 690TT

However, a numerical simulation using CASTEM was performed to determine the S2G factor instead of relying on experimental calibration. This approach eliminates the need for multiple extensometer setups in testing.

To capture the cyclic plasticity and strain evolution characteristics of Alloy 690TT, the Chaboche nonlinear kinematic hardening model was employed [Chaboche, 1989]. This model is well-suited for materials that exhibit Bauschinger effects and cyclic hardening/softening. Before implementing the model, it was necessary to verify that Alloy 690TT exhibits Masing behavior, meaning that its cyclic stress-strain curve can be scaled from a single master curve. This verification was achieved by plotting hysteresis loops from LCF tests at 300°C in air, where the similarity of loop shapes at different strain amplitudes confirmed Masing behavior.

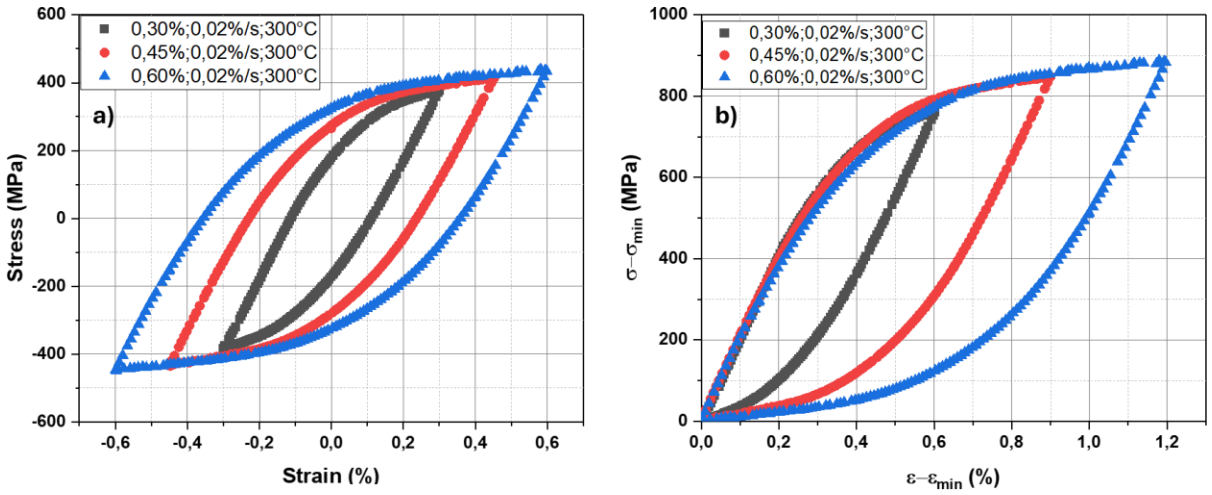

Figure 122: Experimental Hysteresis loops at different strain amplitude in air, a) Individual stress-strain loops, b) Loops following master curve: Masing behavior.

To simulate this cyclic behavior, the Chaboche Model 2 was used, as it incorporates both isotropic and kinematic hardening components, allowing accurate representation of cyclic hardening and mean stress relaxation. However, in the present case, the experimental results show that the yield stress remains nearly constant during cycling; therefore, the isotropic hardening term was neglected, and only kinematic hardening was considered. The governing equation is given below:

The yield criterion is given by,

$$J_2(\sigma - X) = R(p) \tag{1}$$

Where,

- σ = Stress tensor
- $X=X_1+X_2$ = Total backstress (sum of two kinematic hardening components)
- $R(p)$ = Isotropic hardening function
- J_2 = Second invariant of the deviatoric stress tensor

The equation for the evolution of the kinematic hardening is given by,

$$dX_1 = C_1 . (\frac{2}{3} A_1 \emptyset(p) d\epsilon^p - X_1 dp) \quad (2)$$

$$dX_2 = C_2 . (\frac{2}{3} A_2 \emptyset(p) d\epsilon^p - X_2 dp) \quad (3)$$

Where,

- dX_1 and dX_2 = Change in backstress component
- A_1, C_1 and A_2, C_2= Material parameters controlling kinematic hardening
- $d\epsilon^p$ = Incremental plastic strain tensor
- dp = Incremental equivalent plastic strain
- $\phi(p) = 1$ = Recall function controlling strain memory

The parameters derived from the experimental hysteresis loops of the test at 0.3% in air at 300°C are given in the **Table 10**,

E (MPa)	γ [-]	**R_0 (MPa)**	**A_1 (MPa)**	**C_1 [-]**	**A_2 (MPa)**	**C_2 [-]**	ϕ
201260	0.3	227	127	2246	224	15	1

Table 10: Parameters obtained from the experimental hysteresis loops of Alloy 690TT tested at 0.3% strain amplitude in air at 300 °C, used for calibration of the Chaboche model.

In this finite element modeling, a cylindrical uniaxial specimen is analyzed using a simplified axisymmetric approach. The axisymmetric geometry of EVA sample is modelled as shown in **Figure 123**. GL represents the gauge length of the sample, with a diameter of 9 mm and a height of 12.5 mm. The model, depicted in **Figure 123**, comprises 385 QUA8 elements (8-node quadrilaterals), and symmetry is achieved by imposing a zero displacement (Uz = 0) along the symmetry plane (blue line), while a zero-radial displacement (Ur = 0) is maintained along the axis of revolution (red line). A controlled displacement is applied to the upper boundary (green arrows) to manage specimen deformation. The displacement follows a triangular waveform, replicating experimental conditions, and a total of 10 cycles are imposed to ensure the stabilization of stress values in the simulation.

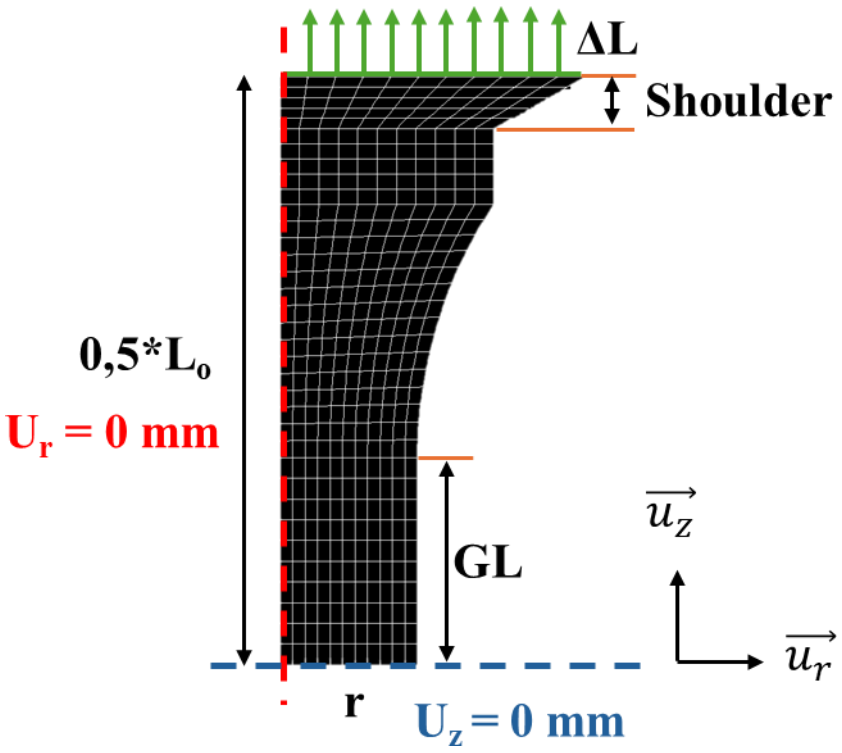

Figure 123: Finite element mesh and boundary conditions of the axisymmetric uniaxial specimen.

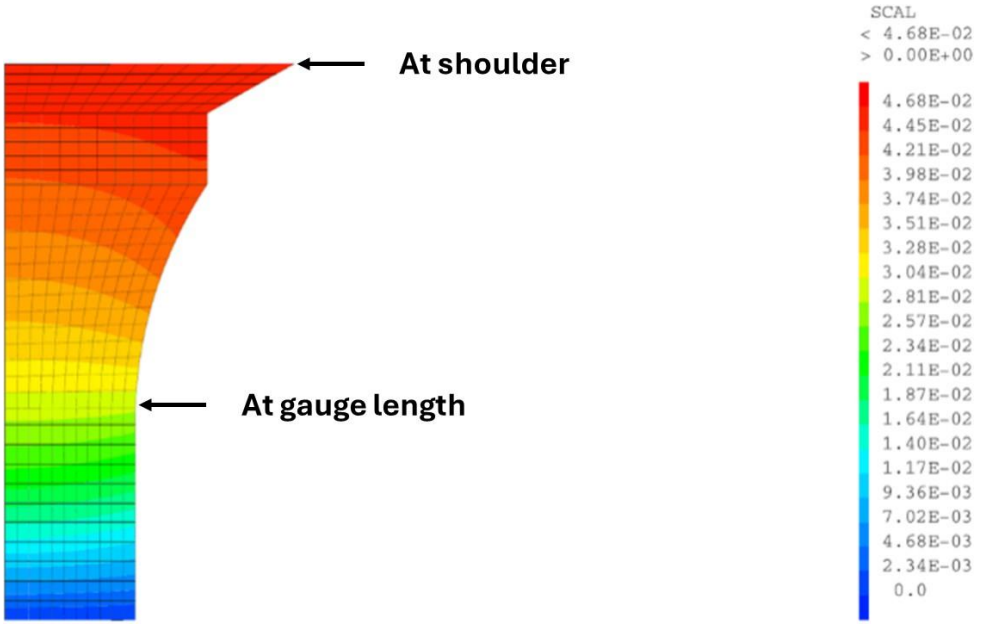

Figure 124: Contour plot of vertical displacement in the axisymmetric uniaxial specimen.

During the post-processing of the results from the simulation, the change in displacement values at the shoulder and the gauge length is tracked to measure the shoulder-to-gauge (S2G) factor (**Figure 124**). The S2G factor is defined as the change in displacement at the shoulder relative to the change in displacement at the gauge length. This S2G factor depends on the strain amplitude applied during the test. In this case, the strain rate is not taken into account because only the final deformation is considered to calculate the S2G factor. The **Figure 125** describes the deformation signals at the shoulder and the gauge length for a strain amplitude of 0.45% at 300°C. By comparing the amplitude of the deformation signals, the S2G factor is found to be 1.44.

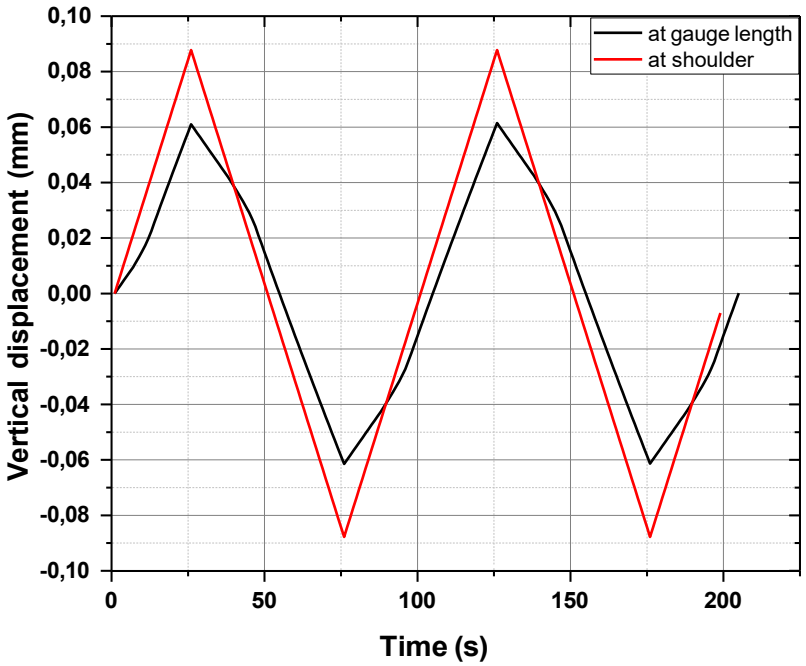

Figure 125: Vertical displacement measured at the shoulder and at the gauge length of the specimen, for the strain amplitude 0.45% at 300°C using simulation.

Experimental validation of S2G

To verify the S2G factor obtained from the simulation, a comparison was made between the numerical and experimental measurements of axial displacement at the shoulders and within the gauge section. Two extensometers were used for this purpose: an eddy-current extensometer positioned on the shoulders and a clip-on extensometer mounted directly on the gauge length. The tests were conducted at room temperature under strain-controlled conditions using a triangular waveform at a strain amplitude of 0.45%. During each cycle, the displacements recorded by both extensometers were continuously monitored and synchronized through the

EVA control system. The ratio between the total displacement measured at the shoulders and the local displacement in the gauge section was then calculated to obtain the experimental S2G factor. Several loading–unloading cycles were repeated to ensure measurement repeatability, and the resulting experimental factor was compared with the value derived from finite element simulation for validation.

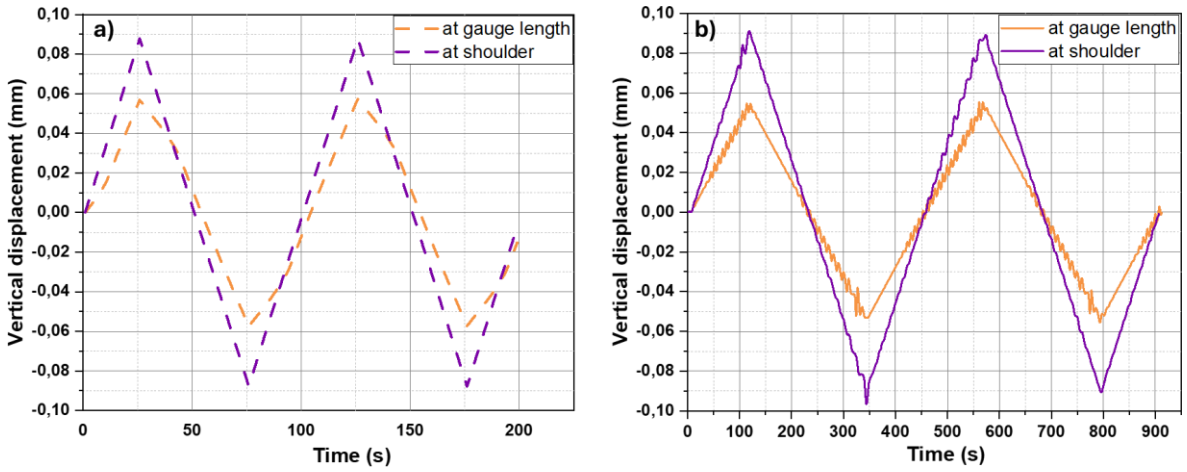

Figure 126: Validation test to verify the S2G factor at room temperature, comparison between a) Simulation and b) Experimental at 0.45%.

The simulation results indicated a vertical displacement of 0.057 mm at the gauge length, while the experimental results recorded a displacement of 0.055 mm, both corresponding to an applied displacement of 0.087 mm at the shoulder (**Figure 126**). The S2G factor calculated from the simulation was 1.53, while the experimental S2G factor was 1.57, demonstrating close agreement with a deviation of only 2.5% between the two measurements. This confirms that the S2G factor determined using the finite element method remains valid at 300°C as well. The **Figure 127** compares the S2G values reported by various laboratories for different specimen geometries, mainly based on stainless steel data. The results show that the S2G values are very consistent across studies. This agreement supports the reliability of the S2G estimation used in the present work.

		FEM calculation			Measurement @ N25/2
Geometry	**Strain amplitude**	**JRC**	**CIEMAT**	**IRSN**	**SCK.CEN**
JRC (304L SS, in air, at ?°C)	0,30%	1,53			
	0,60%	1,49			
SCK.CEN (304L SS, in air, at 300°C)	0,30%	1,55	1,52		1,51
	0,60%	1,48	1,46		1,46
CIEMAT (304L SS)	0,30%		2,67		
	0,60%		2,17		
ASNR (Alloy 690, in air, at 300°C)	0,30%			1,53	
	0,45%			1,44	
	0,60%			1,41	
ASNR (Alloy 690, in air, at RT)	0,45%			1,53	1,57

Figure 127: Summary of the shoulder-to-gauge factor at different amplitudes from various laboratories.

COMPRÉHENSION DE L'INFLUENCE DU VIEILLISSEMENT THERMIQUE ET DE L'ENVIRONNEMENT DU MILIEU PRIMAIRE REP SUR LE COMPORTEMENT EN FATIGUE OLIGOCYCLIQUE DE L'ALLIAGE 690TT

L’extension de la durée de vie des réacteurs nucléaires français au-delà de quarante ans représente un défi majeur pour garantir une exploitation sûre et fiable à long terme. Le maintien d’un haut niveau de sûreté nécessite une compréhension approfondie et une maîtrise des phénomènes de vieillissement des matériaux du circuit primaire. En service, les transitoires thermiques dans un milieu chimiquement actif peuvent induire de la fatigue assistée par l’environnement (EAF), tandis qu’une exposition prolongée à haute température favorise le vieillissement thermique. Si la majorité des composants du circuit primaire sont constitués d’aciers inoxydables, certaines pièces critiques telles que les tubes de générateurs de vapeur et les buses des mécanismes de commande de grappes sont fabriquées en alliage 690, un alliage à base de nickel. Comparé aux nombreuses études consacrées à l’EAF des aciers inoxydables, le comportement en fatigue de l’alliage 690 a fait l’objet de beaucoup moins de recherches. Cette thèse s’intéresse au comportement en fatigue de l’alliage 690TT à 300 °C sous vide, en air et en environnement d’eau primaire de réacteur à eau pressurisée (REP). Les essais ont été réalisés afin d’évaluer les effets de l’environnement et la survenue d’un vieillissement dynamique par déformation (DSA) à différentes vitesses de déformation, en lien avec des analyses microstructurales des structures de dislocations et des mécanismes de déformation. Les résultats montrent que, jusqu’à un facteur environnemental Fen = 2,5, la durée de vie en fatigue reste du même ordre de grandeur en air et en milieu REP. Une partie importante du travail porte sur les effets du vieillissement thermique accéléré (4000 h à 420 °C, équivalant à environ 60 ans en conditions REP) sur la microstructure et la réponse en fatigue de l’alliage 690TT. Le grossissement des carbures inter- et intragranulaires, l’évolution de la dureté et la formation d’un ordre à courte distance (SRO) ont été caractérisés par des techniques avancées telles que la microscopie électronique en transmission (MET) et la diffraction électronique (SAED). Des mesures locales de nanoindentation ont permis de corréler les évolutions microstructurales aux propriétés mécaniques. Les essais de fatigue réalisés sur les échantillons vieillis, en air et en milieu REP, ont révélé une réduction de la durée de vie par rapport à l’état initial. Les analyses MET-EDX ont mis en évidence l’oxydation des carbures situés aux joints de grains comme l’un des principaux mécanismes de dégradation, favorisant la fissuration intergranulaire et accélérant la rupture. Dans l’ensemble, cette étude apporte de nouveaux éléments de compréhension sur les effets couplés de l’environnement et du vieillissement thermique sur le comportement en fatigue oligocyclique de l’alliage 690TT, contribuant à une meilleure prédiction de la durée de vie et à l’évaluation de la sûreté des composants nucléaires en service prolongé.

Mot clés: Alliages chrome-fer-nickel—Effets des hautes températures, Alliages chrome-fer-nickel—Fatigue, Alliages chrome-fer-nickel—Fissuration, Carbures—Oxydation, Contraintes thermiques, Dislocations dans les métaux, Durée de vie (ingénierie), Microscopie électronique en transmission, Nanoindentation, Réacteurs à eau sous pression.

UNDERSTANDING THE INFLUENCE OF THERMAL AGING AND PWR PRIMARY WATER ENVIRONMENT ON THE LOW-CYCLE FATIGUE BEHAVIOR OF ALLOY 690TT

Extending the operating life of French nuclear reactors beyond 40 years represents a major challenge for ensuring safe and reliable long-term operation. Maintaining a high level of safety requires a thorough understanding and control of material aging phenomena within the primary circuit. During service, thermal transients in a chemically active medium can induce Environmentally Assisted Fatigue (EAF), while prolonged exposure to elevated temperatures promotes thermal aging. Although many primary-loop components are made of stainless steels, critical parts such as steam generator tubes and control rod drive mechanism nozzles are made from Alloy 690, a nickel-based alloy. Compared to the extensive research on EAF in stainless steels, the fatigue behavior of Alloy 690 has received considerably less attention. This thesis investigates the fatigue behavior of as-received Alloy 690TT at 300 °C under vacuum, air, and Pressurized Water Reactor (PWR) environments. Tests were performed to assess environmental effects and the occurrence of dynamic strain aging (DSA) at various strain rates, complemented by microstructural analyses of dislocation structures and deformation mechanisms. The results show that, up to an environmental correction factor of Fen = 2.5, the fatigue life remains of the same order of magnitude in air and PWR water. A major part of the work focuses on the effects of accelerated thermal aging (4000 h at 420 °C, equivalent to ~60 years under PWR conditions) on the microstructure and fatigue response of Alloy 690TT. The coarsening of intergranular and intragranular carbides, hardness evolution, and formation of short-range ordering (SRO) were characterized using advanced techniques, including Transmission Electron Microscopy (TEM) and Selected Area Electron Diffraction (SAED). Local nanoindentation measurements were used to correlate microstructural changes with mechanical properties. Fatigue tests on aged samples, conducted in both air and PWR environments, revealed a reduction in fatigue life relative to the as-received condition. TEM-EDX analyses revealed oxidation of carbides at grain boundaries as one of the degradation mechanisms, which promotes intergranular cracking and accelerates failure. Overall, this study provides new insights into the coupled effects of environment and thermal aging on the low-cycle fatigue behavior of Alloy 690TT, contributing to improved life prediction and safety assessment of nuclear components operating under extended service conditions.

Keywords: Chromium-iron-nickel alloys – effect of high temperatures, chromium-iron-nickel alloys – fatigue, chromium-iron-nickel alloys – cracking, carbides – oxidation, thermal stresses, dislocations in metals, service life (engineering), transmission electron microscopy, nanoindentation, pressurized water reactors